Universiteit Antwerpen

Faculteit Wetenschappen

Departement Chemie

Exploring the boundaries of cryospectroscopy:

A new approach towards separating monomer and complex spectra

---

Proefschrift voorgelegd tot het behalen van de graad

Doctor in de wetenschappen: Chemie

aan de Universiteit Antwerpen, te verdedigen door

Liene De Beuckeleer

Promotor: Prof. dr. W.A. Herrebout

Antwerpen, 2015

Table of contents

Chapter 1

Introduction

The research group Molecular Spectroscopy has been studying the infrared spectra of solutions in cryogenic solvents such as liquid argon, krypton and xenon since the early nineties. The research has evolved from applications towards conformational equilibria in small organic molecules to studying complexation equilibria involving weak intermolecular hydrogen and halogen bonding interactions. In contrast to classical solutions, the cryosolutions offer the possibility to study complexation equilibria at relatively low temperatures, using a chemically inert environment in which only weak solute-solvent interactions are expected to occur. The relatively low temperatures used during these experiments shift the chemical equilibrium towards the complex, which is favorable when studying weak interactions. The weakly interacting environment combined with the low temperatures used, leads to small bandwidths and thus facilitates the detection of complex bands only slightly shifted from the monomer modes. Moreover, since most cryosolutions are in thermodynamic equilibrium, these solutions are also ideally suited for the determination of the relative stability of the formed complexes.

Early on in the study of cryosolutions, in 1992, van der Veken and De Munck published on the observation of weak, unexpected, transitions in the spectra of HCl dissolved in liquid noble gases.[1] As illustrated in Figure 1.1, copied from this study, it was noticed that upon increasing the concentration of HCl new absorption bands appeared on the low-wavenumber side of the monomer band. As these bands were found to be concentration and temperature dependent it was suggested that they were due to oligomers of HCl in which two, three or four HCl molecules were held together by Cl–H···Cl hydrogen bonds, which can be described as $(HCl)_n$. Two different approaches were applied to rationalize these new features. Firstly, the phenomenon was analyzed by subjecting it to a factor analysis [2]. However, as this technique led to unsatisfying results it was abandoned and a band profile analysis was performed instead. In this second method, the contributions of the monomer and the oligomeric species were firstly approximated by a subtracting procedure. This implies that a rescaled spectrum of a highly diluted solution, which is assumed to only contain monomer features, was subtracted from spectra of solutions containing larger amounts of HCl and a recorded under similar circumstances. Subsequently, the difference

spectra were least-squares fitted using a series of Gauss-Lorentz sum profiles. This way the analysis of the spectra obtained in a concentration study allowed assigning the different band features to dimers, trimers, and tetramers.[1] It should be noted that in the subtraction procedure the spectra need to be isothermal. A change in temperature causes a band to shift and to change shape, which makes it impossible to subtract spectra recorded at different temperatures.

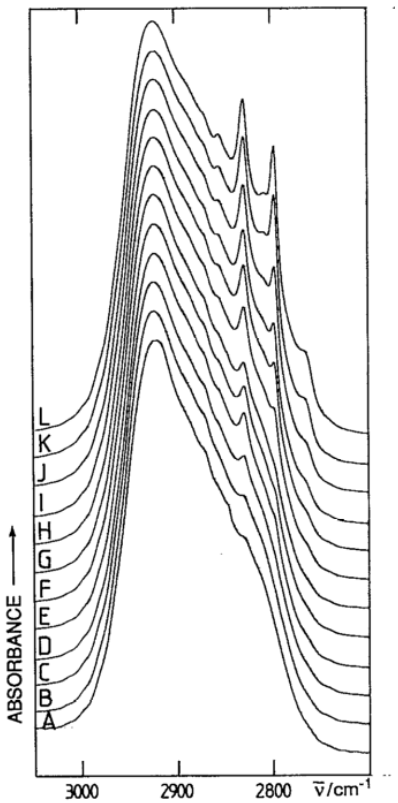

Figure 1.1 The HCl stretching region of solutions of HCl dissolved in liquid argon at 103 K at different concentrations [1]

The observation of the HCl features gave rise to a research line that was focused on the study of weakly bound molecular complexes, in which, among other, unsaturated hydrocarbons such as ethene and pseudo-unsaturated hydrocarbons such as cyclopropane and cyclopropene interact with HCl and BF_3.[3-5] In these investigations the overlapping bands of monomers and heterocomplexes, complexes that consist of

different kind of molecules, separated by least-squares band fitting using Gauss/Lorentz sum functions. During these studies it was realized that in order to observe weak complex bands overlapping with larger bands, scaled monomer spectra from both components should be subtracted from the mixture spectra. From then on the use of the subtraction became common practice.

In the beginning of the 21st century the main focus within the research line focusing on weakly interacting molecules has been on the study of van der Waals complexes[6], blue shifting hydrogen bonding[7] and more recently halogen bonding[8,9] and hydrogen bonding by anesthetics[10,11]. In the latter investigations a halogen bond donor or an anesthetic was mixed with a variety of Lewis bases that are considered to be simple model systems occurring as building blocks of larger biomolecules and crystals. During the measurements the Lewis bases ammonia (NH_3) and pyrrole (C_4H_5N) showed oligomeric features similar to the HCl system. As the appearance of bands due to self-association complicates also the experimental spectra it was seen as a drawback to study heterocomplexes. However it opened up to a new research line to study the self-associating behavior of molecules in cryosolutions. It was soon realized that the current methodology for heterocomplexes was not suited to study the formation of homocomplexes. In the spectrum of the highly diluted solution used for the subtraction procedures, a weak feature due to dimers can be observed. The appearance of this feature necessarily leads to an underestimation of the dimer contribution in the subtracted spectrum. The data also illustrated that even for small concentrations, additional features do to oligomeric species are present and the general requirement of a monomer only contribution introduced in the analysis is difficult to achieve. Furthermore it was also observed that results of least-squares band fitting procedures used before depend strongly on the initial parameters chosen and thus can be severely biased by the end-user. These observations triggered us to develop and validate new numerical methods to analyze spectra of molecules showing self-associating behavior in cryosolvents.

The first goal of this PhD project is thus investigating a new and robust methodology to analyze the isothermal spectra of self-associating species and to determine the separate spectra of the oligomers present in the solution. In this method polynomials are

least-squares fitted to the data of an isothermal concentration study with the purpose of mimicking the relation the relation between monomer concentrations and measured absorbances at every wavenumber. Each term of the polynomial determines the contribution of the monomer or homocomplex in the solution. Because the self-association of HCl in liquid noble gasses has been thoroughly studied before, it is considered to be an ideal system to validate any new methodologies developed. The development and validation of the methodology with HCl in liquid argon is discussed in Chapter 3. To further rationalize the possibilities and limitations of the models developed, more testing involving other self-associating species is required. Therefore the new methodology is used in Chapter 4 to 5 to analyze the spectra of solutions of NH_3 and ND_3, pyrrole for which self-association has been noticed before. Chapter 6 looks into the formation of acetone homocomplexes held together by long-range dipole-dipole interactions. Although previous studies have indicated the existence of acetone dimers, only limited experimental evidence is available. In this study the spectroscopic results are complemented with theoretical calculations in which structural and spectroscopic properties of possible complexes are predicted using *ab initio* calculations. In addition experimental data on the relative stability of the complexes can be determined and more information on the solvatation can be obtained by carrying out Monte Carlo simulations. A short description of these latter calculations can be found in Chapter 2.

The second goal of the recent investigations is to extend the developed methodology to study spectra of mixtures of species to be able to separate the spectra of monomers and hetero and homocomplexes in the cryosolutions. In the first part of Chapter 7 the methodology is adapted and tested on the spectra of mixtures of dimethyl ether and CF_3X (with X = I or Br) in liquid argon. These systems have already been thoroughly studied and are known to form a heterodimer. Thereafter, the complexation of the acetone and CF_3I are investigated.

In the beginning of this PhD investigation a lack of expertise on how to treat multi overlapping bands caused these experiments to lie past the boundary of cryospectroscopy. In this work the boundaries are being explored and we attempt to push these boundaries forward by developing a new methodology.

A key element in implementation of the new methodology is the innovation of the experimental set-up. The introduction of a cryostat controlled by a proportional-integral-derivative (PID) controller, developed by J. Dom in the framework of his PhD thesis[11], allows spectra to be recorded with a much higher temperature stability (±0.05 K) than before. Consequently it becomes possible to record large data sets of spectra with different concentrations recorded at the same temperature which was not possible with earlier temperature controller systems. More details about the experimental set-up can be found in Chapter 2.

References

[1] B. J. van der Veken and F. R. De Munck, J. Chem. Phys., 97 (1992) 3060-3071.

[2] E. R. Malinowski, *Factor Analysis in Chemistry*, 3rd ed., John Wiley & Sons, Inc., New York, 2002.

[3] G. Everaert, *Van der Waals molecules of some Lewis acids with bases containing π or pseudo-π systems: a cryospectroscopic and computational approach* PhD thesis, University of Antwerp, 2002.

[4] R. Szostak, W. A. Herrebout and B. J. van der Veken, Physical Chemistry Chemical Physics, 2 (2000) 3983-3991.

[5] W. A. Herrebout, R. Szostak and B. J. van der Veken, The Journal of Physical Chemistry A, 104 (2000) 8480-8488.

[6] P. Van Ginderen, *Studie van de Van der Waals complexen gevormd tussen zwakke Lewiszuren en verschillende Lewisbasen in vloeibare edelgassen*, PhD thesis, University of Antwerp, 2005.

[7] S. N. Delanoye, *Cryospectroscopic study of proper and improper C–H···O hydrogen bonds : the Van der Waals complexes of dimethyl ether, acetone and oxirane with diverse proton donors* PhD thesis, University of Antwerp, 2004.

[8] D. Hauchecorne, *C–X···Y Halogen bonding: a spectroscopic study*, PhD thesis, University of Antwerp, 2011.

[9] N. Nagels, *Building cryospectroscopic bridges: halogen bonding, hydrogen bonding and lone pair···π interactions*, PhD thesis, University of Antwerp, 2013.

[10] B. Michielsen, *Molecular interactions with halothane a spectroscopic study*, PhD thesis, University of Antwerp, 2011.

[11] J. J. Dom, *Anaesthetics directed via weak hydrogen bonds? An infrared and Raman spectroscopic study towards target molecules and computational accuracy*, PhD thesis, University of Antwerp, 2011.

Chapter 2

Experimental and computational methods

2.1 Infrared spectroscopy of cryosolutions[1]

In this paragraph only the specific characteristics used in the measurements performed in the following chapters are discussed. A more detailed description of the equipment can be found in the literature.[1]

2.1.1 Cryosolutions

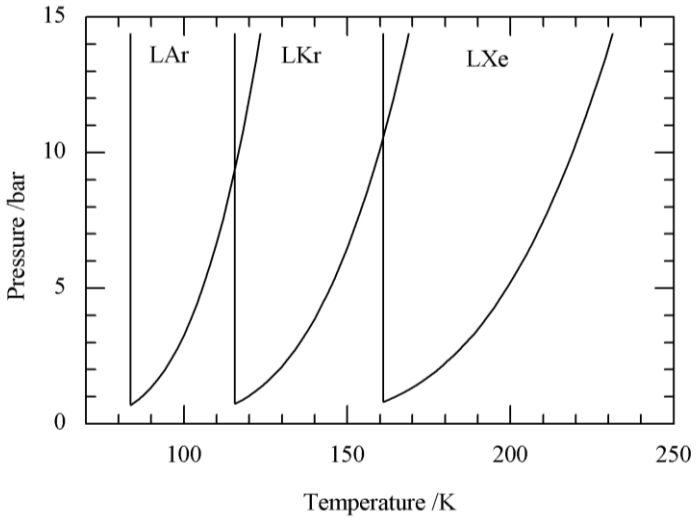

Figure 2.1 Liquid lines of different noble gases used.[2]

Solutions in liquefied noble gases are an ideal medium to study molecular complexes held together by weak and medium-strong interactions. Because cryosolutions in general are in thermodynamical equilibrium they are ideally suited to determine thermodynamical and other physical properties. Furthermore they create a weakly interacting environment that, combined with the low temperatures used, leads to small bandwidths and thus facilitates the detection of complex bands only slightly shifted from the monomer modes. But the main obstacle to using liquefied inert gases as solvents is their limited solubility. As the solubility is dependent on the polarizability of the gas, only a small amount of molecules dissolve in liquid argon (LAr), while substantially more compounds dissolve in liquid krypton (LKr) and even more in liquid xenon (LXe). A second obstacle is related to the fact that at atmospheric pressure the liquid ranges of the rare gases are very narrow, varying from 3.3 K for LAr to 3.8 K for

LXe. As a sufficiently broad temperature interval is required in the determination of interaction enthalpies, the use of higher pressures is essential as illustrated in Figure 2.1. While studying weakly interacting molecules one always has to find the right balance between temperature, pressure and solubility.

2.1.2 Experimental set-up

Figure 2.2 illustrates the experimental set-up for infrared experiments of cryosolutions used for all experiments documented in this thesis. It consists of (1) a pressure manifold to fill and evacuate the cell and to monitor the amount of solute gas in a particular experiment, (2) the liquid cell, (3) temperature regulator and (4) the spectrometer. These components are discussed in the following paragraphs.

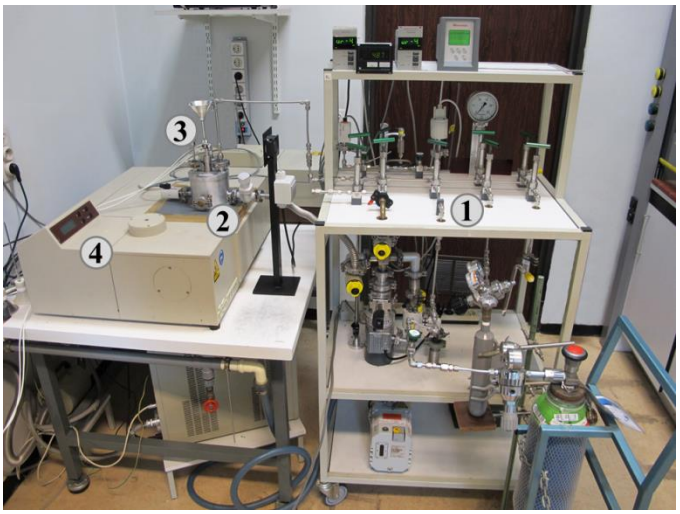

Figure 2.2 Overview of an experimental set-up for infrared experiments.

(1) *The pressure manifold* consists of Swagelok SS-4H or SS-4UK bellow valves interconnected with 1/4" stainless steel tubes. The manifold allows the handling of pressures up to 145 bar and it can be evacuated to 10^{-6} bar, using a combination of a rotation and diffusion pump. To monitor the pressure, the manifold is equipped with 3 types of manometers. A Pirani vacuum meter is used to check the vacuum in the manifold and in the actual cell, the capacitance manometer serves to monitor the amount of gas used in a particular experiment and a Bourdon manometer is used to control the pressure of the solvent gas. All pressure meters can be isolated from the

manifold using bellow valves. Further, the manifold has several inlets to which sample tubes or gas cylinders can be attached in order to admit solutes and solvent gasses to the system. A schematic overview of the manifolds' construction is shown in Figure 2.3.

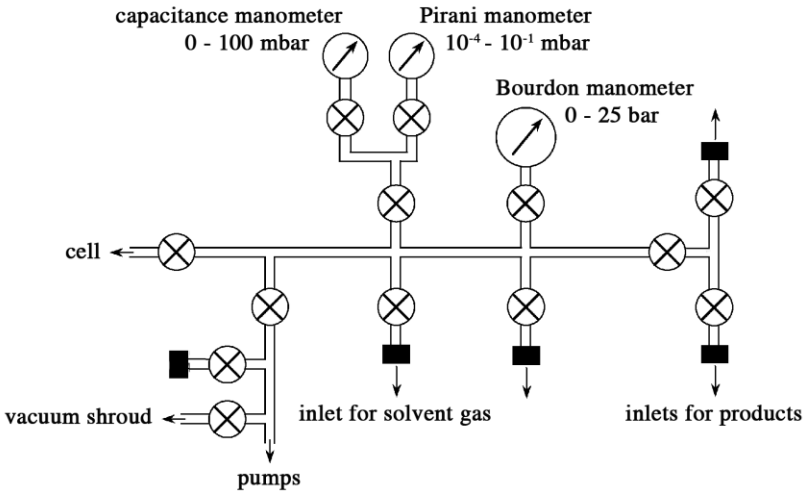

Figure 2.3 Schematic overview of the pressure manifold

(2) *The liquid cell,* depicted in Figure 2.4, consists of a brass body on which infrared windows are fixed using an indium gasket. The cell is designed to withstand an internal pressure of 15 bar at 80 K and can be used in different temperature intervals, ranging from 93 to 125 K for LAr, from 120 to 155 K for LKr, and from 152 to 223 K for LXe. The filling and evacuating of the cell is performed using a 1/8" stainless steel tube brazed into the cell body and connected to the pressure manifold. A second tube is connected to a safety relief valve.

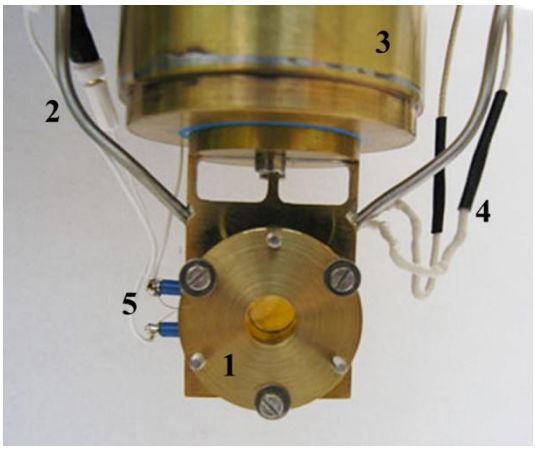

Figure 2.4 The 10 mm liquid cell with Si windows (1) with two stainless steel tubes (2) brazed into the body to fill and evacuate the cell and to foresee a safety relief valve. To control and stabilize the temperature the cell is provided with a LN_2 dewar (3), a heating cartridge (4) and a Pt-100 thermoresistor (5).

The research group has several cells available with path lengths between 10 mm and 40 mm. When measuring weak bands, e.g. when studying compounds with limited solubility, a longer path length is preferred so that the intensity of these bands is still sufficient. On the other hand, short path lengths are useful when studying weak complexes, so that higher concentrations can be used. Since self-association occurs more easily in higher concentrated solutions, a shorter path length is preferred and the 10 mm cell is used throughout all experiments in this thesis. The material of the infrared window can also be varied as long as the material is of sufficient strength to withstand the high pressures and low temperatures. In this work it was chosen to use Si windows, because Si is quite strong and transparent through most of the infrared region. Unfortunately, silicon has a fairly high index of refraction. Therefore, substantial reflections may occur so the actual transmittance of the cell is rather low. To avoid internal reflections in the windows and to avoid the resulting interference fringes, the Si windows are slightly wedged.

The actual cell is suspended in a vacuum shroud to avoid condensation of H_2O and CO_2 onto the outside of the cell. The vacuum shroud is equipped with KBr windows for the mid-infrared region, hermetically sealed to the vacuum spectrometer and connected to the vacuum pumps through the pressure manifold.

(3) *Temperature control.* The quality of spectra increases if the temperature can remain stable during the time of the measurement. Therefore, the research group has constructed a design in which the cell is connected to a liquid N_2 (LN_2) Dewar with three cold bridges and equipped with heating cartridge and a Pt-100 thermoresistor, as can be seen in Figure 2.4. The temperature of the cell body is measured using a Pt-100 thermoresistor and the SunRod electric 30 W minicartridge heater is used to stabilize the temperature in combination with a Eurotherm 3504 proportional-integral-derivative (PID) controller. The time required to stabilize the temperature depends on the temperature change requested, but typically is in the order of 5-10 min. The temperature variation during a typical experiment is less than 0.05°C.

(4) *The spectrometer*. The cell with cryostat is fitted into the sample area of a Bruker IFS 66v or 66v/s Fourier transform spectrometer. For the mid-infrared spectra, a Globar source is used in combination with a Ge/KBr beam splitter and a LN_2-cooled broadband MCT detector. All interferograms were averaged over 500 scans, Blackman-Harris 3-term apodized and Fourier transformed with a zero filling factor of 4 to yield spectra with a resolution of 0.5 cm^{-1}. Figure 2.5 shows a single beam spectrum of the evacuated liquid cell with Si windows by using the described spectrometer parameters.

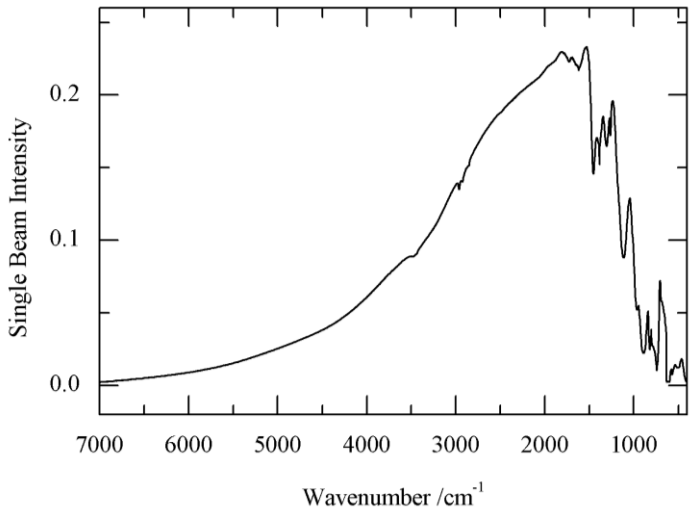

Figure 2.5 The single beam spectrum of the evacuated 10 mm cell with wedged Si windows, suspended in the vacuum shroud with KBr windows recorded using a Globar source and Ge/KBr beam splitter.

2.1.3 General methodology

Before running an experiment, the cell is positioned in the spectrometer and the vacuum shroud, cell and pressure manifold are evacuated. Then the cell is cooled down to the desired temperature left to stabilize for approximately two hours. Subsequently, the solutions are prepared in the following way. An amount of solute gas, monitored by the capacitance manometer, is admitted into an isolated part (with accurately known volume) of the pressure manifold. When opening the valve connecting the actual cell and the pressure manifold, the vapors condense in the cell or on the walls of the filling tube. In case of a binary mixture, this procedure is repeated for the second species. The manifold and the cell are then pressurized with the solvent gas, which immediately starts to condense. This condensation takes place in the cold part of the filling tube and in the actual cell, allowing the deposited compounds to dissolve. The condensation of the rare gas into the liquid cell is quite vigorous: the turbulence created thus suffices to homogenize the solution. After stabilizing the temperature, the solution in most cases is ready for spectroscopic investigation. The exceptions are caused by species with limited solubility which often give rise to small crystalline particles suspended in the solvent. These particles can be dissolved by performing additional temperature cycles in which the temperature is systematically varied between a higher and lower temperature of the temperature range in which the used noble gas is liquid. For all experiments, IR single beam spectra of the evacuated cell recorded at exactly the same temperature as that used for the sample is used as a reference. If necessary, artifacts due to impurities in the solvent gas can be removed by subtracting spectra of liquid noble gas only recorded at exactly the same conditions.

An important characteristic of a solution is the concentration of the solutes. Unfortunately, because it cannot be verified whether the compound deposited into the cell has completely dissolved and because the level of the solvent in the filling tube is not precisely known, an accurate determination of the actual concentrations is very difficult.

2.1.4 Fitting polynomial models with least-squares

For every molecule studied in this work we recorded a data set of infrared spectra of different concentrations dissolved in a liquid noble gas at constant temperature. Subsequently a methodology was developed to separate monomer and complex contributions at each wavenumber by fitting polynomials models mimicking the relations between monomer concentrations and measured absorbances. In this section the least-squares fitting procedure that is used during the fitting is explained by the quadratic model used in Chapter 6. For simplicity the measured absorbance at a given wavenumber for a given concentration is expressed as y and the monomer absorbance at the reference wavenumber is expressed as *x*.

The quadratic polynomials with variables x and x^2 and constant coefficients α1 and α_2 is given by the equation

$$y_i = \alpha_1 x_i + \alpha_2 {x_i}^2 + \varepsilon_i \tag{2.1}$$

in which the ε is the residual error or the difference between the measured absorbance and the fitted absorbance. Given the observed absorbances $\{(x_1, y_1), \cdots, (x_n, y_n)\}$ for n measured concentrations the defined model can be written out for each measured concentration as the following system of equations

$$\begin{array}{c} y_1 = \alpha_1 x_1 + \alpha_2 {x_1}^2 + \varepsilon_1 \\ y_2 = \alpha_1 x_2 + \alpha_2 {x_2}^2 + \varepsilon_2 \\ \vdots \quad\quad \vdots \quad\quad \vdots \quad\quad \vdots \\ y_n = \alpha_1 x_n + \alpha_2 {x_n}^2 + \varepsilon_n. \end{array} \tag{2.2}$$

For purposes of analysis it is convenient to express these equations in matrix form with

$$y = \begin{pmatrix} y_1 \\ \vdots \\ y_n \end{pmatrix}, X = \begin{pmatrix} x_1 & {x_1}^2 \\ \vdots & \vdots \\ x_n & {x_n}^2 \end{pmatrix}, \alpha = \begin{pmatrix} \alpha_1 \\ \alpha_2 \end{pmatrix}, \varepsilon = \begin{pmatrix} \varepsilon_1 \\ \vdots \\ \varepsilon_n \end{pmatrix}. \tag{2.3}$$

Then we can rewrite the system as

$$y = X\alpha + \varepsilon. \tag{2.4}$$

Here α is a 2×1 vector of unknown parameters and ε is a $n \times 1$ vector of unobserved disturbances. If a is the vector of estimates of α, then the estimated model may be written as

$$y = Xa + e. \tag{2.5}$$

Here *e* denotes the $n \times 1$ vector of residuals, which can be computed from the data and the vector of estimates *a* by means of

$$e = y - Xa. \tag{2.6}$$

We denote transposition of matrices by primes ($'$), e.g. the transpose of the residual vector *e* is the $1 \times n$ matrix $e' = (e_1, \cdots, e_n)$. To determine the least squares estimator, we write the sum of squares of the residuals S as function of *a*

$$\begin{aligned} S(a) = \sum_{i=1}^{n} {e_i}^2 = e'e = (y - Xa)'(y - Xa) \\ = y'y - y'Xa - a'X'y + a'X'Xa. \end{aligned} \tag{2.7}$$

"Least squares" means that the overall solution minimizes the sum of the squares of the errors *e* made in the results of every single equation. Therefore, the minimum of $S(a)$is calculated by setting the derivatives of $S(a)$ equal to zero. For the mathematical details about the conversion of Eq. (2.7) derivation we like to refer to literature.[3]

$$\frac{\partial S}{\partial a} = -2X'y + 2X'Xa. \tag{2.8}$$

The least squares estimator is obtained by minimizing $S(a)$. Therefore we set these derivatives equal to zero, which gives the *normal equations*

$$X'Xa = X'y. \tag{2.9}$$

Solving this for *a*, we obtain

$$a = (X'X)^{-1}X'y. \tag{2.10}$$

provided that the inverse of X′X exists, which means that the matrix *X* should have rank 2. As *X* is an n × 2 matrix, this requires in particular that n ≥ 2. In other words the number of observations should be larger than or equal to the number of parameters. In practice we always require more spectra than the number of parameters.

In practice vector y is a part of a n × s matrix *Y* with *s* the number of wavenumbers for which data was recorded in the spectra. Then the quadratic model from Eq. (2.1) is fitted to the data in every column individually by using Eq. (2.10) with a script in Matlab.[4] The resulting coefficients for every wavenumber are then stored as a 2 × s matrix *A*.

The methodology in Chapter 3-5 and 7 is somewhat different as nonnegative constraints are imposed to the fitted coefficients *a*. A comprehensive review of the methods for solving nonnegative least-squares problems has been published by Chen

and Plemmons[5]. The first widely used algorithm, proposed by Lawson and Hanson[6], is the active set method. This algorithm partitions the set of coefficients into the active and passive sets. The active-set contains the variables with values forcibly set to zero and which violate the nonnegative constraint. The passive-set contains the variables that do not violate the constraint. By iteratively updating the feasibility vector with components from the passive set, each iteration is reduced to an unconstrained linear least squares problem that is solvable through QR.[7] The algorithm has a finite convergence.[6] In Chapter 3-5 and 7 Eq. (2.10) was replaced by the Matlab function *lsqnonneg*[8,9] which is based on the active set algorithm as designed by Lawson and Hanson[6]. The results are coefficients that are positive or equal to zero. A more detailed description of the algorithm can be found in Figure S2.1 in the Supporting information.

2.1.5 Determining the relative stability of a homocomplex: Temperature study

A measure for the relative stability is the standard complexation enthalpy $\Delta H°$ which can be derived from a temperature study in which spectra of a solution are recorded at a variety of temperatures. The value of $\Delta H°$ can be obtained by analyzing the resulting band areas of monomer and complex bands of different solutions using the Van't Hoff relation. The key element of the analysis is the approximation that, in a limited temperature interval, the standard complexation enthalpies and the corresponding values for the complexation entropies are independent of temperature.

In this section the Van't Hoff relation is only derived for complexes of self-association molecules, homocomplexes, as this methodology was only used in the case of the dimerization of acetone. The derivation is based on the method used for complexes consisting of different species, heterocomplexes, as earlier described by van der Veken.[10]

The chemical equilibrium for the formation of an oligomer in a solution in which only one compound A is dissolved can be written as

$$nA \rightleftharpoons A_n \qquad (2.11)$$

with n as the number of molecules involved in the cluster. The equilibrium constant K, expressed as a function of mole fractions x

$$K = \frac{x_{A_n}}{x_A^n} \tag{2.12}$$

This equation can be rewritten in function of the molarity C, the average density ρ and the average molare mass M_a of the solution

$$K = \frac{C_{A_n}}{C_A^n}\left(\frac{\rho}{M_a}\right)^{n-1} \tag{2.13}$$

The molarity is in turn related to the integrated intensity $I$of a band in the spectrum by Lambert-Beer's law (2.14) so that Eq. (2.13) is transformed into Eq. (2.15)

$$I_i = \varepsilon_i C_i d \Leftrightarrow C_i = \frac{I_i}{\varepsilon_i d} \tag{2.14}$$

$$K = \frac{I_{A_n}}{I_A^n}\frac{\varepsilon_A^n}{\varepsilon_{A_n}}\left(\frac{\rho d}{M_a}\right)^{n-1} \tag{2.15}$$

in which ε is the molar attenuation coefficient of the band and d the path length of the cell.

The complexation enthalpy $\Delta H°$ is determined from the relation

$$-RT\ln K = \Delta G° = \Delta H° - T\Delta S° \tag{2.16}$$

Combining Eqs. (2.15) and (2.16) leads to

$$-\frac{\Delta H°}{RT} = \ln\frac{I_{A_n}}{I_A^n} + (n-1)\ln\rho + C \tag{2.17}$$

with C as a constant equal to

$$C = \ln\left[\frac{I_{A_n}}{I_A^n}\frac{\varepsilon_A^n}{\varepsilon_{A_n}}\left(\frac{\rho d}{M_a}\right)^{n-1}\right] - \frac{\Delta S°}{R} \tag{2.18}$$

van der Veken[10] showed that the natural logarithm of the density of the cryosolvents is approximately related to the temperature through

$$\ln\rho = a + \frac{b}{T} \tag{2.19}$$

In which a and b are temperature-independent constants. Using this relation, Eq. (2.17) can be written as

$$\ln\frac{I_{A_n}}{I_A^n} = -\frac{\Delta H° + (n-1)Rb}{R}\frac{1}{T} - (C + a) \tag{2.20}$$

This relation shows that the slope of the Van't Hoff plot, multiplied by R, equals

$-(\Delta H° + (n-1)Rb)$. The value of b is the slope of the plot of $\ln \rho$ versus $1/T$. A typical plot, obtained for LKr in the temperature ranges in which vapor pressure is below 15 bar, is shown in Figure 2.6.[2]

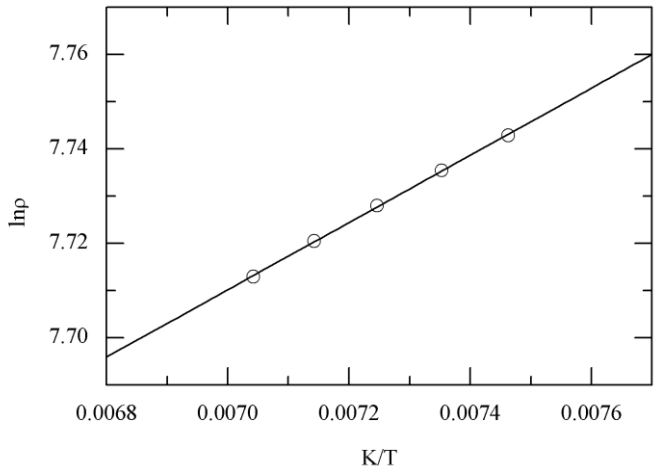

Figure 2.6 Scatter plot and linear regression line for $\ln\rho$ vs the inverse temperature for Kr between 134 and 142 K

The integrated intensities I_A and I_{A_n} are determined by integrating the band areas of the monomer A and the oligomer A_n after separating the overlapping spectra with the polynomial regression explained in Chapter 6.

2.2 Theoretical Calculations

In Chapter 6 and 7 the interpretation of the experimental results is supported by a variety of quantum chemical calculations, in which the structural, spectroscopic, and thermodynamic properties of the species under study are predicted.

2.2.1 Ab initio calculations

Geometries and harmonic vibrational frequencies of monomers and complexes are obtained from *ab initio* calculations using the second order Møller-Plesset perturbation theory (MP2). To account for weak interactions between two molecules the calculations are performed using Dunning's augmented correlation consistent basis set of double

(aug-cc-pVDZ) zeta quality in Gaussian09.[11] The standard aug-cc-pVDZ basis sets were used for hydrogen, carbon, oxygen and fluorine, while aug-cc-pVDZ-PP basis sets including small-core energy-consistent relativistic pseudopotentials (PP) were used for iodine.[12,13] The combination of this method and basis set has led to satisfactory results for halogen bonded complexes before [14-16] and, consequently, a similar approach will be used in the present study.

During all calculations, corrections for Basis Set Superposition Error (BSSE) were accounted for explicitly using the counterpoise technique as proposed by Boys and Bernardi.[17,18]

The *ab initio* complexation energies cannot be compared directly with experimental complexation enthalpies. Firstly, the calculated complexation energy ΔE can transformed into the vapor phase complexation enthalpy ΔH°(vap,calc), by accounting for thermal and zero-point vibrational contributions, ΔH^{T} obtained using statistical thermodynamics

$$\Delta H^{\circ}(\text{vap,calc}) = \Delta E + \Delta H^{T} \tag{2.21}$$

And secondly, a correction for solvent interactions, $\Delta_{sol}H$, yields the complexation enthalpy in noble gas (Ng) solution ΔH°(LNg,calc) which can be compared with the experimental complexation enthalpy ΔH°(LNg). The value of $\Delta_{sol}H$ is calculated using the Monte Carlo Free Energy Perturbation (MC-FEP) approach.

$$\Delta H^{\circ}(\text{LNg, calc}) = \Delta H^{\circ}(\text{vap,calc}) + \Delta_{sol}H \tag{2.22}$$

The corrections will be further discussed in the following sections.

2.2.2 Statistical thermodynamics

As stated above, thermodynamical corrections have to be applied to account for the thermal influences to the interaction energy. These temperature terms are treated in a classical way using statistical thermodynamics.[19]

The enthalpy of a species at temperature *T* can be written as

$$H^T = E^T_{trans} + E^T_{rot} + E^T_{vib} + E^0_{vib} + PV \tag{2.23}$$

The complexation enthalpy is calculated by

$$\Delta H^T = H^T_{complex} - \sum H^T_{monomers} \tag{2.24}$$

Combining Eqs. (2.23) and (2.24) results in

$$\Delta H^T = \Delta E^T_{trans} + \Delta E^T_{rot} + \Delta E^T_{vib} + \Delta E^0_{vib} + \Delta(PV) \tag{2.25}$$

The terms in this equation are calculated using statistical thermodynamics based on the rigid rotor, harmonic oscillator and free internal rotor models and the ideal gas approximation. The classical translational and rotational terms ΔE^T_{trans} and ΔE^T_{rot} equal -1/2RT for each degree of freedom lost in the complexation. Similarly, the pressure-volume work term $\Delta(PV) = \Delta nRT$ accounts for the reduction of the number of free molecules upon complexation. These three terms all have a negative sign and thus have a destabilizing effect on the complexation energy ΔE. The sign of the vibrational terms depends on the frequency shifts upon complexation. The ΔE^0_{vib} term is the zero-point vibrational energy contribution

$$\Delta E^0_{vib} = \frac{1}{2}\sum_{i=1}^{\substack{complex\\modes}} h\nu_i - \frac{1}{2}\sum_{j=1}^{\substack{monomer\\modes}} h\nu_j \tag{2.26}$$

The remaining thermal vibrational term $\Delta E^T_{\mathrm{vib}}$ accounts for the change in vibrational energies, in going from 0 K to *T* K:

$$\Delta E^T_{vib} = N_A h\left(\frac{1}{2}\sum_{i=1}^{\substack{complex\\modes}} \frac{h\nu_i}{e^{\frac{h\nu_i}{k_B T}} - 1} - \frac{1}{2}\sum_{j=1}^{\substack{monomer\\modes}} \frac{h\nu_j}{e^{\frac{h\nu_j}{k_B T}} - 1}\right) \tag{2.27}$$

The frequencies ν are obtained from the *ab initio* calculations and the temperature *T* is set as the midpoints of the temperature interval used in the experimental study.

2.2.3 Solvent effects

Ab initio calculations are performed on a single (super)molecule, isolated from all other molecules in the system. However, when molecules are dissolved in a solvent, the molecule is not isolated and significant solute-solvent interactions can occur. The global effect of a solvent is the result of several contributions, often divided in repulsive (mainly exchange repulsion) and attractive (electrostatic, polarisation, dispersion) effects.[20] To evaluate the influence of the liquid noble gases as solvent, Monte Carlo Free Energy Perturbation simulations are performed.

According to statistical perturbation theory, the Gibbs free energy of solvation $\Delta_{sol}G$ is calculated as the energy difference between a reference system A representing a box containing only solvent molecules and a perturbed system B with a single solute molecule surrounded by the same number of solvent molecules. To avoid numerical instabilities, the introduction of the solute molecule is not carried out in a single step, but involves *k* intermediate (virtual) states between A and B introduced by means of a coupling parameter $\lambda_i (0 \leq \lambda_i \leq 1)$, as illustrated schematically in Figure 2.7.

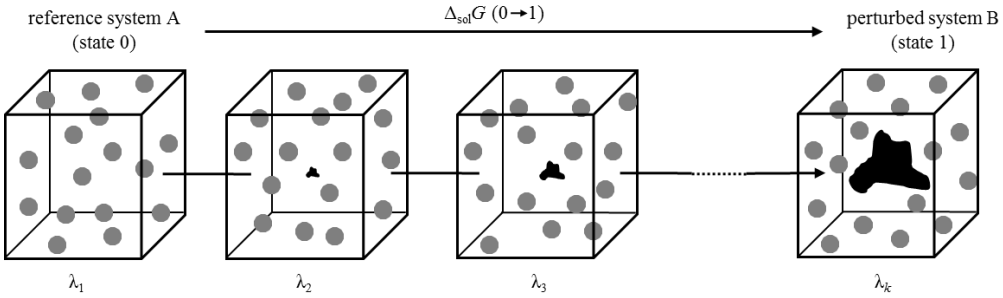

Figure 2.7 Schematic overview for the calculation of $\Delta_{sol}G$ by gradual perturbation of the reference system.

The change in free energy can then be written as the sum of all intermediate energy differences:

$$\Delta_{sol}G(0 \rightarrow 1) = \sum_{i=1}^{k-1} \Delta_{sol}G(\lambda_i \rightarrow \lambda_{i+1}) = -k_B T \sum_{i=1}^{k-1} \ln \left\langle e^{\frac{H_{\lambda_{i+1}} - H_{\lambda_i}}{k_B T}} \right\rangle \qquad (2.28)$$

in which the angle brackets indicate averaging over the ensemble considered and *H* is the Hamiltonian describing the perturbed, λ_{i+1}, and unperturbed, λ_i, systems for each species involved.

In these simulations, the solute-solvent interactions are described using a Lennard-Jones potential, accounting for long-range dispersion attraction and short range exchange repulsion. Solute-solvent interactions are typically described by a sum of two contributions. The first is obtained by using one Lennard-Jones function between each solvent atom j and each atom of the solute molecule i, and an additional term that accounts for the polarization of the solvent atoms by the solute:

$$V = \sum_i \left[4\varepsilon_{ij} \left[\left(\frac{\sigma_{ij}}{r_{ij}} \right)^{12} - \left(\frac{\sigma_{ij}}{r_{ij}} \right)^{6} \right] - \frac{1}{2} \alpha_j E^2 \right] \tag{2.29}$$

in which α_j refers to the polarizability of the noble gas and E is the electric field generated by the solute. The ε and σ parameters for the Lennard-Jones potentials are typically taken from the OPLS (Optimized Potentials for Liquid Simulation) all-atom force field.[21] For an interaction between two different atoms i and j, the following mixing rules are applied:

$$\varepsilon_{ij} = \sqrt{\varepsilon_{ii}\varepsilon_{jj}} \qquad \sigma_{ij} = \frac{1}{2}\left(\sigma_{ii} + \sigma_{jj}\right) \tag{2.30}$$

Each species is calculated at a pressure of 28 bar and at six different temperatures between 88 and 138 K for solutions in liquid argon, between 119 and 179 K for solutions in liquid krypton and between 171 and 231 K for solutions in liquid xenon. Figure 2.8 illustrates the calculation of $\Delta_{sol}G$ for the acetone monomer and dimers in LKr in Chapter 6.

The calculation of the Gibbs energies is then followed by an enthalpy-entropy decomposition involving the expressions

$$\Delta_{sol}H = \Delta_{sol}G + T\Delta_{sol}S \qquad \text{with } \Delta_{sol}S = -\left(\frac{\partial \Delta_{sol}G}{\partial T}\right)_p \tag{2.31}$$

The Monte Carlo Free Energy Perturbation simulations are performed using a locally modified version of BOSS 4.1.[22]

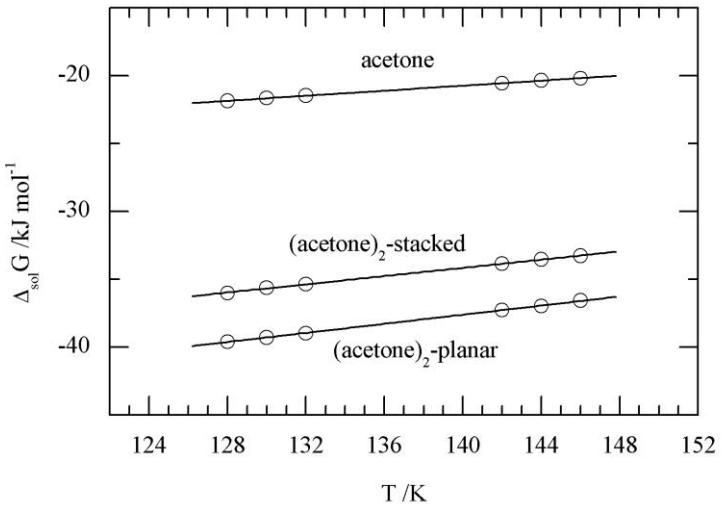

Figure 2.8 Gibbs free energies of solvatation obtained for the acetone monomer and its stacked and planar dimers in LKr

References

[1] W. Herrebout, Top. Curr. Chem., 358 (2015) 79-154.

[2] N. B. Vargaftik, Y. K. Vinogradov and V. S. Yargin, *Handbook of physical properties of liquids and gases - pure substances and mixtures. Third augmented and Revised Edition*, Begell House, Inc., New York, 1996.

[3] C. Heij, P. de Boer, P. H. Franses, T. Kloek and H. K. van Dijk, *Econometric Methods with Applications in Business and Economics*, Oxford University Press, Oxford, 2004.

[4] MATLAB 8.3, The MathWorks Inc., Natick, MA, USA, 2014.

[5] D. Chen and R. J. Plemmons, Nonnegativity Constraints in Numerical Analysis, Proceedings of Symposium on the Birth of Numerical Analysis, Leuven, Belgium, 2007.

[6] C. L. Lawson and R. J. Hanson, *Solving Least Squares Problems*, 1987.

[7] Y. C. Luo and R. Duraiswami, SIAM J. Sci. Comput., 33 (2011) 2848-2863.

[8] L. Shure, in: http://blogs.mathworks.com/loren/2006/12/12/brief-history-of-nonnegative-least-squares-in-matlab/, 2006.

[9] in: http://nl.mathworks.com/help/matlab/ref/lsqnonneg.html.

[10] B. J. van der Veken, J. Phys. Chem., 100 (1996) 17436-17438.

[11] M. J. Frisch, G. W. Trucks, H. B. Schlegel, G. E. Scuseria, M. A. Robb, J. R. Cheeseman, G. Scalmani, V. Barone, B. Mennucci, G. A. Petersson, *et al.*, Gaussian 09, Revision A.02, Gaussian, Inc., Wallingford, CT, USA, 2009.

[12] D. Feller, J. Comput. Chem., 17 (1996) 1571-1586.

[13] K. L. Schuchardt, B. T. Didier, T. Elsethagen, L. Sun, V. Gurumoorthi, J. Chase, J. Li and T. L. Windus, J. Chem. Inf. Model., 47 (2007) 1045-1052.

[14] D. Hauchecorne, A. Moiana, B. J. van der Veken and W. A. Herrebout, Phys. Chem. Chem. Phys., 13 (2011) 10204-10213.
[15] D. Hauchecorne, N. Nagels, B. J. van der Veken and W. A. Herrebout, Phys. Chem. Chem. Phys., 14 (2012) 681-690.
[16] N. Nagels, D. Hauchecorne and W. A. Herrebout, Molecules, 18 (2013) 6829-6851.
[17] S. F. Boys and F. Bernardi, Mol. Phys., 19 (1970) 553-566.
[18] S. l. Simon, M. Duran and J. J. Dannenberg, The Journal of chemical physics, 105 (1996) 11024.
[19] J. H. Knox, *Molecular Thermodynamics: An Introduction to Statistical Thermodynamics for Chemists*, Wiley-Interscience, London, 1971.
[20] B. Mennucci and R. Cammi, *Continuum Solvation Models in Chemical Physics: From Theory to Applications*, 2007.
[21] W. L. Jorgensen, D. S. Maxwell and J. Tirado-Rives, J. Am. Chem. Soc., 118 (1996) 11225-11236.
[22] W. L. Jorgensen, BOSS 4.1., University of Yale, New Haven, 1999.

Supporting information

2. Active-set Method. Given a set of m linear equations in n unknowns which are constrained to be non-negative, let the active-set Z be the subset of variables which violate the non-negativity constraint or are zero and the passive-set P be the variables with positive values. Lawson and Hanson observe that only a small subset of variables remains in the candidate active-set Z at the solution. If the true active-set Z is known, then the NNLS problem is solved by an unconstrained least squares problem using the variables from the passive-set.

Algorithm 1 Active-set method for non-negative least squares [19]

Require: $A \in \mathbb{R}^{m \times n}$, $x = 0 \in \mathbb{R}^n$, $b \in \mathbb{R}^m$, set $Z = \{1, 2, \ldots, n\}$, $P = \emptyset$
Ensure: Solution $\hat{x} \geq 0$ s.t. $\hat{x} = arg\ min \frac{1}{2}\|Ax - b\|^2$

```
1:  while true do
2:    Compute negative gradient w = A^T(b − Ax)
3:    if Z ≠ ∅ and max_{i∈Z}(w_i) > 0 then
4:      Let j = arg max_{i∈Z}(w_i)
5:      Move j from set Z to P
6:      while true do
7:        Let matrix A^P ∈ R^{m×*} s.t. A^P = {columns A_i s.t. i ∈ P}
8:        Compute least squares solution y for A^P y = b
9:        if min(y_i) ≤ 0 then
10:         Let α = −min_{i∈P}(x_i/(x_i − y_j)) s.t. (column j ∈ A^P) = (column i ∈ A)
11:         Update feasibility vector x = x + α(y − x)
12:         Move from P to Z, all i ∈ P s.t. x_i = 0
13:       else
14:         Update x = y
15:         break
16:       end if
17:     end while
18:   else
19:     return x
20:   end if
21: end while
```

In algorithm 1, the candidate active-set Z is updated by first moving the largest positive component variable in the negative gradient w to the passive-set (line 5). This selects the component with the most negative gradient that reduces the residual 2-norm. The variables in the passive-set form a candidate linear least squares system $A^P y = b$ where matrix A^P contain the column vectors in matrix A that correspond to indices in the passive-set (lines 7, 8). At each iteration, the feasibility vector x moves towards the solution vector y while preserving non-negativity (line 11). Convergence to the optimal solution is proven in [19].

The termination condition (line 3) checks if the gradient is strictly positive or if the residual can no longer be minimized. At termination, the following relations satisfy the optimality conditions in (1.3):

1. $w_i \leq 0 \quad i \in Z$ termination condition (line 3).
2. $w_i = 0 \quad i \in P$ solving least squares sub-problem (line 8).
3. $x_i = 0 \quad i \in Z$ updating sets (line 12).
4. $x_i > 0 \quad i \in P$ updating x (lines 10-11).

Chapter 3

The self-associating behavior of HCl in liquid argon: The development and validation of a new methodology

This chapter has been published as

De Beuckeleer, L. I.; Herrebout, W. A., *Exploring the Limits of Cryospectroscopy: Least-Squares Based Approaches for Analyzing the Self-Association of HCl*. Spectrochim. Acta A 2016, 154, 89-97. doi:10.1016/j.saa.2015.10.012

Abstract

To rationalize the concentration dependent behavior observed for a large spectral data set of HCl recorded in liquid argon, least-squares based numerical methods are developed and validated. In these methods, for each wavenumber a polynomial is used to mimic the relation between monomer concentrations and measured absorbances. Least-squares fitting of higher degree polynomials tends to overfit and thus leads to compensation effects where a contribution due to one species is compensated for by a negative contribution of another. The compensation effects are corrected for by carefully analyzing, using *AIC* and *BIC* information criteria, the differences observed between consecutive fittings when the degree of the polynomial model is systematically increased, and by introducing constraints prohibiting negative absorbances to occur for the monomer or for one of the oligomers. The method developed should allow other, more complicated self-associating systems to be analyzed with a much higher accuracy than before.

3.1 Introduction

Hydrogen chloride is a textbook example of a simple hydrogen-bonding molecule. The self-association of HCl into molecular clusters is used as a model in the study of intermolecular interactions. Using different spectroscopic techniques, HCl dimers up to hexamers have been studied in the gas phase through jet-cooled spectroscopy[1-5], in helium nanodroplets[6] and in solid matrices[7,8]. In 1992, van der Veken and De Munck[9] reported a systematic study of HCl dissolved in liquefied noble gases and this work was expanded in 2001 by Herrebout, Van Gils and van der Veken[10]. Inspection of the data available showed that at sufficiently low concentrations, the spectrum is dominated by contributions of the monomeric species, while at higher concentrations, additional bands due to oligomeric species of HCl can be observed at wavenumbers well below that of the monomer.

To be able to rationalize the features observed, in the original paper[9] the phenomenon was firstly analyzed by subjecting it to a factor analysis[11], but because of unsatisfying results this methodology was abandoned and a band profile analysis was performed instead. In this method, the contributions of the monomer and the oligomeric species were approximated by subtracting the spectra of solutions containing larger amounts of HCl and a rescaled spectrum of a highly diluted solution recorded under similar circumstances. Subsequently, the difference spectra were least-squares fitted using a series of Gauss-Lorentz sum profiles. The analysis of the data obtained in isothermal concentration studies allowed assigning the different band features to dimers, trimers, and tetramers. The study of the temperature behavior yielded approximate values for the enthalpies of complexation in the cryosolutions[9,12].

Based on the results obtained during ongoing research projects involving, among others, the studies of more complex systems such as C–H···Y hydrogen[13-21], C–X···Y halogen[13,18,22-28] and lone pair···π[29] interactions, and based on new technological developments made in recent years, we started to realize that the analysis performed[9,12] had several drawbacks and could thus be improved. These ideas originated from the current availability of liquid cells with a smaller optical path allowing more concentrated solutions to be studied without saturating the detector used, and the

integration of new, proportional-integral-derivative (PID) controlled setups allowing spectra to be recorded with a much higher temperature stability than that used in the original studies [9]. Apart from these technological developments, we were also triggered by the observation that results of least-squares band fitting procedures depend strongly on the initial parameters chosen and thus can be severely biased by the end-user.

In this paper, we report on the development of more robust numerical methods in which the concentration dependent behavior observed for a large spectral data set recorded a constant temperature is scrutinized. The new method allows the contributions due to monomers and due to different types of self-association to be separated directly, thereby avoiding the requirement that at the lowest concentrations studied the contribution of complex species should be negligibly small. It will be shown that due to overfitting simpler approaches such as regular least-squares fitting of absorbances versus monomer concentrations fail to accurately determine the different contributions. These drawbacks are corrected for by carefully analyzing, using the statistically acknowledged selection *AIC* and *BIC* criteria, the differences between consecutive fittings when the degree of the polynomial is systematically increased, and by introducing constraints prohibiting negative absorbances to occur for the monomer or for one of the complexes. The models and approaches developed, and the Matlab based software packages used for their implementation should allow other, more complex systems [30,31] to be analyzed with a much higher accuracy than before, thereby avoiding the bias originating from the empirical selection of the initial parameters to be used in traditional least-squares band profile analyses.

3.2 Experimental section

HCl (99%) was purchased from Sigma-Aldrich and was used without further purification. The argon used as a cryosolvent had a stated purity of 99.9995% and was supplied by Air Liquide.

Infrared spectra were recorded on a Bruker IFS 66v Fourier transform spectrometer. For the mid-infrared spectra, a Globar source was used in combination with a Ge/KBr beamsplitter and a LN_2-cooled broad band MCT detector. All interferograms were averaged over 500 scans, Blackman-Harris 3-term apodized and Fourier transformed with a zero filling factor of 4 to yield spectra with a resolution of 0.5 cm^{-1}. The experimental set-up used to investigate the solutions in liquid noble gases has been described before [32]. In the actual cryostat, a liquid cell with 1 cm path length and equipped with wedged Si windows was mounted below a LN_2 dewar. The temperature of the cell body is measured using a Pt-100 thermoresistor. The SunRod electric minicartridge heater is controlled using a Eurotherm 3504 PID controller. The temperature variation during a typical experiment is less than 0.05 K.

Spectra were obtained and preanalyzed using OPUS 6.5. Further calculations were performed using Matlab [33].

3.3 Results and discussion

In the following paragraphs, the general methodology used in this study will be described. Subsequently, results obtained using a fixed-degree polynomial approximation, and results based on the A and B information criteria used to select the appropriate polynomial degree and to avoid overfitting and/or negative absorbances are discussed in detail.

3.3.1 General concept

The general concept of the method used is based on the fact that, with some exceptions [34,35], cryosolutions are known to be in thermodynamical equilibrium. The spectra for cryosolutions of self-associating species therefore are a superposition of monomer spectra and spectra of the different complexes, with the relative absorbances

determined by the equilibrium concentrations *C* and the molar attenuation coefficients ε of the monomeric species and of the associations formed. The latter, are determined by the equilibrium constants *K* involved

$$2 \text{ monomer} \rightleftharpoons \text{dimer} \qquad K_2 = \frac{C_{dimer}}{C_{monomer}{}^2} = \frac{C_{di}}{C_{mono}{}^2} \tag{3.1}$$

$$3 \text{ monomer} \rightleftharpoons \text{trimer} \qquad K_3 = \frac{C_{trimer}}{C_{monomer}{}^3} = \frac{C_{tri}}{C_{mono}{}^3} \tag{3.2}$$

$$4 \text{ monomer} \rightleftharpoons \text{tetramer} \qquad K_4 = \frac{C_{tetramer}}{C_{monomer}{}^4} = \frac{C_{tetra}}{C_{mono}{}^4} \tag{3.3}$$

Starting from these assumptions, each arbitrary wavenumber $\tilde{\nu}_i$ the measured absorbance A_{exp} can be written as a sum of contributions,

$$A_{exp}(\tilde{\nu}_i) = A_{mono}(\tilde{\nu}_i) + A_{di}(\tilde{\nu}_i) + A_{tri}(\tilde{\nu}_i) + A_{tetra}(\tilde{\nu}_i). \tag{3.4}$$

Depending on the wavenumber chosen and on the spectral features of the species present, the actual form of the expression and the number of contributions can differ, typical possibilities being

$$A_{exp}(\tilde{\nu}_i) = A_{mono}(\tilde{\nu}_i) \tag{3.5}$$

for a monomer contribution only,

$$A_{exp}(\tilde{\nu}_i) = A_{mono}(\tilde{\nu}_i) + A_{di}(\tilde{\nu}_i) \tag{3.6}$$

for monomer and dimer contributions,

$$A_{exp}(\tilde{\nu}_i) = A_{mono}(\tilde{\nu}_i) + A_{di}(\tilde{\nu}_i) + A_{tri}(\tilde{\nu}_i) \tag{3.7}$$

for monomer, dimer and trimer contributions, and Eq. (3.4) for monomer, dimer, trimer and tetramer contributions. By choosing an appropriate wavenumber $\tilde{\nu}_m$ for which the absorbance is due to monomers only, i.e.

$$\begin{gathered} A_{exp}(\tilde{\nu}_m) = A_{mono}(\tilde{\nu}_m) \\ \text{and } A_{di}(\tilde{\nu}_m) = A_{tri}(\tilde{\nu}_m) = A_{tetra}(\tilde{\nu}_m) = 0 \end{gathered} \tag{3.8}$$

and by using Lambert-Beer's law

$$A_j(\tilde{\nu}_i) = \varepsilon_j(\tilde{\nu}_i) C_j d \tag{3.9}$$

with ε as the molar attenuation coefficient, C as the concentration in the solution, j as the type of species and d as the path length of the cell used, the different contributions in Eq. (3.4) can be rewritten in terms of the absorbance of the monomer wavenumber $\tilde{\nu}_m$,

$$A_{mono}(\tilde{\nu}_i) = a_1(\tilde{\nu}_i, \tilde{\nu}_m) A_{mono}(\tilde{\nu}_m) \tag{3.10}$$

$$A_{di}(\tilde{\nu}_i) = a_2(\tilde{\nu}_i, \tilde{\nu}_m) A_{mono}(\tilde{\nu}_m)^2 \tag{3.11}$$

$$A_{tri}(\tilde{\nu}_i) = a_3(\tilde{\nu}_i, \tilde{\nu}_m) A_{mono}(\tilde{\nu}_m)^3 \tag{3.12}$$

$$A_{tetra}(\tilde{\nu}_i) = a_4(\tilde{\nu}_i, \tilde{\nu}_m) A_{mono}(\tilde{\nu}_m)^4. \tag{3.13}$$

The coefficients used in these expressions are defined as

$$a_1(\tilde{\nu}_i, \tilde{\nu}_m) = \frac{A_{mono}(\tilde{\nu}_i)}{A_{mono}(\tilde{\nu}_m)} = \frac{\varepsilon_{mono}(\tilde{\nu}_i)}{\varepsilon_{mono}(\tilde{\nu}_m)} \tag{3.14}$$

$$a_2(\tilde{\nu}_i, \tilde{\nu}_m) = \frac{A_{di}(\tilde{\nu}_i)}{A_{mono}(\tilde{\nu}_m)^2} = a_1(\tilde{\nu}_i, \tilde{\nu}_m)^2 \frac{\varepsilon_{di}(\tilde{\nu}_i)}{\varepsilon_{mono}(\tilde{\nu}_m)^2} \frac{1}{d} K_2 \tag{3.15}$$

$$a_3(\tilde{\nu}_i, \tilde{\nu}_m) = \frac{A_{tri}(\tilde{\nu}_i)}{A_{mono}(\tilde{\nu}_m)^3} = a_1(\tilde{\nu}_i, \tilde{\nu}_m)^3 \frac{\varepsilon_{tri}(\tilde{\nu}_i)}{\varepsilon_{mono}(\tilde{\nu}_m)^3} \frac{1}{d^2} K_3 \tag{3.16}$$

$$a_4(\tilde{\nu}_i, \tilde{\nu}_m) = \frac{A_{tetra}(\tilde{\nu}_i)}{A_{mono}(\tilde{\nu}_m)^4} = a_1(\tilde{\nu}_i, \tilde{\nu}_m)^4 \frac{\varepsilon_{tetra}(\tilde{\nu}_i)}{\varepsilon_{mono}(\tilde{\nu}_m)^4} \frac{1}{d^3} K_4 \tag{3.17}$$

Substituting the Eq. (3.12) to (3.15) in Eq. (3.4) results in

$$\begin{aligned} A_{exp}(\tilde{\nu}_i) = {} & a_1(\tilde{\nu}_i, \tilde{\nu}_m) A_{mono}(\tilde{\nu}_m) \\ & + a_2(\tilde{\nu}_i, \tilde{\nu}_m) A_{mono}(\tilde{\nu}_m)^2 \\ & + a_3(\tilde{\nu}_i, \tilde{\nu}_m) A_{mono}(\tilde{\nu}_m)^3 \\ & + a_4(\tilde{\nu}_i, \tilde{\nu}_m) A_{mono}(\tilde{\nu}_m)^4 \end{aligned} \tag{3.18}$$

The above equation shows that for any arbitrary wavenumber, the contributions due to the different species present can in principle be derived by plotting the measured absorbances versus the monomer absorbance at the given reference wavenumber, and using least-squares to fit a polynomial to the resulting data.

It is of interest to note that in Eq. (3.15) to (3.17), the optical path length is introduced. To ensure that changes in the spectra are due to changes in the concentration only, it is therefore necessary that spectra belonging to one data set have

been recorded under identical circumstances using the same liquid cell. Data derived from different liquid cells or obtained using different set-ups should thus not be mixed during numerical analysis, unless corrections for the differences on path length are introduced explicitly.

3.3.2 Measurements and baseline corrections

To assess the general principle of the method described above, and to further optimize the methods used, a data set of 346 spectra of solutions in liquid argon was constructed. The mole fractions of HCl used for the data set are difficult to accurately quantify [9,12], but are estimated to vary between 5.0×10^{-3} and 2.0×10^{-5}. The temperature of the solutions was stabilized at 103 K, the temperature variation during a typical run being less than 0.05 K. These settings were chosen to allow a large fraction of HCl molecules to be involved in self-association and at the same time avoid additional features assigned to solid HCl particles suspended in the solution[36] to appear in the region 2750-2700 cm^{-1}. The concentrations used are chosen so that the region between minimum and maximum absorbance is uniformly covered.

As the outcome of the fitting procedures can largely depend on baseline artifacts, during all experiments, baseline corrections were performed using spectra of pure liquid argon recorded at exactly the same conditions. Moreover, special attention was paid to the removal of remaining water traces caused by small water particles suspended in the solution, or condensation of water vapors onto the cold windows of the cryostat and the detector.

To account for remaining drifts of the baseline, which we believe are caused by small changes in the temperature inside the spectrometer due to the cold cryostat present, an additional straight line baseline correction was applied to all data, the spectral limits used to define the background being 3100 and 2500 cm^{-1}.

3.3.3 Subtraction procedures and least-squares band profile analysis

As the results obtained from the newly developed numerical algorithms will be compared and rationalized with the help of the data reported earlier, it is of interest to summarize the most important data derived from the subtraction and the least-squares band profile analysis. Because the use of factor analysis has proven to be unsatisfying in the original paper[9], this method was not pursued in this study. However, recent insights on the use of factor analysis could lead to complementary results [37,38].

In Figure 3.1A, the infrared spectrum of HCl in liquid argon recorded at 103 K using a solution with mole fraction of 5.0×10^{-3} is compared to the rescaled spectrum of a diluted solution recorded under the same conditions. In addition, the resulting spectrum of the oligomeric species, obtained by subtracting the upper and middle trace, is illustrated in the lower line. The result of the least-squares band profile analysis in which the complex spectrum is fitted using a sum of Gauss/Lorentz sum profiles, and the calculated contributions due to dimer, trimer and tetramer, obtained by summing the respective Gauss/Lorentz sum profiles, are given in Figure 3.1B. As the outcome of the least-squares band profile analysis is often biased by the choice of the initial parameters, in the current study these parameters were optimized to achieve the best agreement with the outcome of the original studies[9,12]. The characteristic wavenumbers derived for the dimer are 2855, 2847 and 2830 cm^{-1}, while those for the trimer and tetramer are 2807 and 2797 cm^{-1}, and 2778 and 2855 cm^{-1}, respectively. Whereas the individual contributions might be seriously affected by the choice of the initial parameters, the summed band profiles for dimer, trimer and tetramer are considered more reliable and can be used to assess the outcome of the newly developed methods.

We would like to explicitly point out that in the spectrum of the highly diluted solution used for the subtraction procedures, a weak feature illustrating the formation of dimers can be observed near 2830 cm^{-1}. The appearance of this feature necessarily leads to an underestimation of the dimer contribution in the subtracted spectrum. The data also illustrates that even for small concentrations, additional features due to oligomeric species are present and the general requirement of a monomer only contribution introduced in the analysis is difficult to achieve.

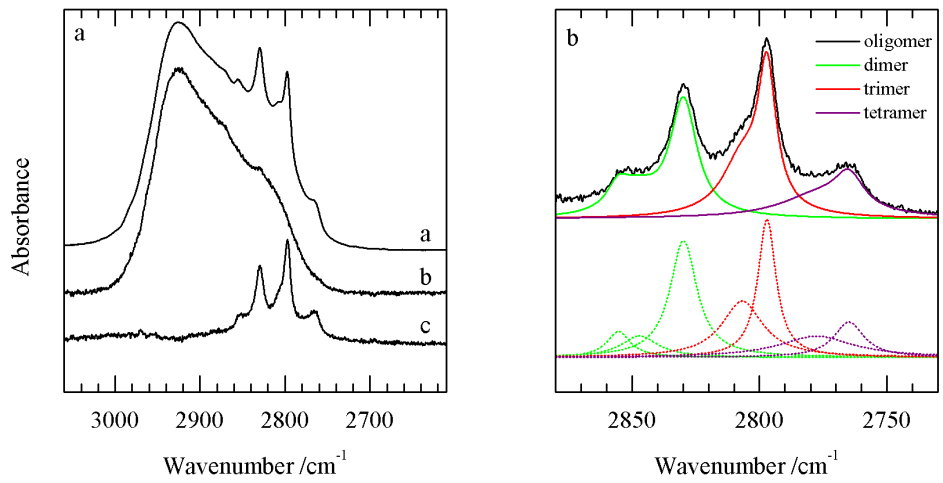

Figure 3.1 (A) Subtraction procedure involving an original spectrum of a concentrated solution of HCl in liquid argon (a) and a rescaled spectrum of a highly diluted solution recorded under the same conditions (b). The result of the subtraction showing the summed contributions of the different oligomers present is given in the bottom trace (c). (B) Results from a least-squares band profile analysis in which the spectrum of the complex species obtained in panel (A) is fitted using Gauss-Lorentz sum profiles (dotted line). The calculated contributions for the dimer, trimer and tetramer, obtained by summing the different Gauss/Lorentz sum profiles involved, are also given (solid line). As the outcome of the least-squares band profile analysis is often biased by the choice of the initial parameters, in the current study these parameters were optimized to achieve the best agreement with the outcome of the original studies[9].

3.3.4 Least-squares fitting of polynomials

In Figure 3.2, typical spectra from the database are shown. Upon increasing the solute concentration, new bands due to self-association can easily be observed to emerge in the 2870-2740 cm^{-1} spectral region, i.e. at wavenumbers red shifted from the monomer wavenumber of 2869 cm^{-1}. The dashed line in Figure 3.2 represents the reference wavenumber $\tilde{\nu}_m$ used to determine the HCl monomer concentration. This wavenumber was chosen as internal standard because no features due to self-association are expected in this region and because its absorbance can be accurately determined for all concentrations studied. The solid lines A to H refer to the wavenumbers for which results obtained from least-squares fitted polynomials will be discussed.

In the following paragraphs the recorded data set will be analyzed by fitting a polynomial through the measured absorbance values for every wavenumber

individually. The data for the different wavenumbers thus are completely independent. In the final step, these contributions for every wavenumber are combined and the isolated spectra of the species present in the solution are obtained without further smoothing. The noise observed therefore is a direct measure for the accuracy of the different contributions determined in the independent least-squares fits.

In Figure 3.3, results obtained by fitting, for each wavenumber, the experimental data with fixed 3rd, 4th and 5th degree polynomials are summarized. Panels a, b, and c refer to the results from a regular polynomial regression in which no constraints are introduced. Panels d, e, and f refer to the solutions from least-squares procedures in which nonnegative constraints are added to avoid negative intensities of the monomer or oligomer species.

The data in panel 3.3a, obtained by using a third polynomial for all wavenumbers to account for dimers and trimers, reveals a strong negative feature for the calculated dimer spectrum near 2765 cm^{-1}. This feature is observed at a wavenumber close to that previously assigned to the tetramer, and is believed to be caused by the underfitting of the data that do not allow contributions due to this species to appear. The artifact due to the underfitting is, at least partially, compensated for by additional intensity for the trimer.

The effect of adding an extra term allowing the contributions of the tetramer to be calculated is shown in panel 3.3b. It can be seen that, apart from some regions where little or no intensity is observed, negative intensities have largely disappeared. The drawback of adding an extra term, is a general increase in noise level. Also, for regions where no or little intensity is observed e.g. for regions with an almost flat baseline, compensation effects are observed where negative contributions calculated for one or more species are balanced by positive contributions in the spectra of the other components.

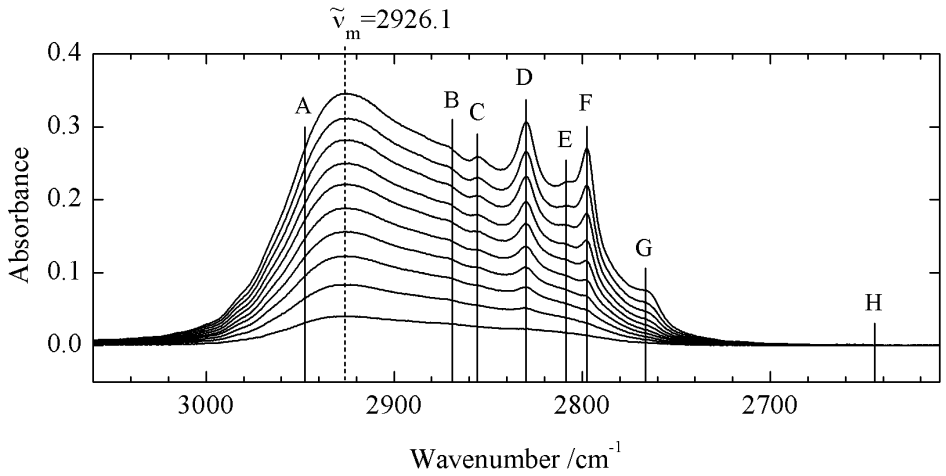

Figure 3.2 Infrared spectra of solutions of HCl in liquid argon, at 103 K. From top to bottom, the mole fraction of HCl decreases from approximately 5.0 x 10^{-3} to 2.0 x 10^{-5}. The 10 spectra shown represent a small fraction of the spectral database used in the fitting procedures.

The effect of increasing noise level and increasing compensation effects is further illustrated in panel 3.3c, where the results of a fitting procedure involving contributions due to dimer, trimer, tetramer and pentamer are shown. It is clear that under these conditions, overfitting of the experimental data leads to severe blurring of the interesting data present. As a result, it becomes more and more difficult to correctly distinguish the different oligomer contributions.

Comparison of the data in panels 3.3a and 3.3d shows that by introducing nonnegative constraints, the signal-to-noise ratio of the calculated spectra is significantly increased. Preventing the spectrum of the dimer to become negative near 2760 cm^{-1}, drastically reduces the overcompensation in the corresponding trimer spectrum. The reduction of the noise level and the underlying compensation effects upon the use of nonnegative constraints is also observed for the 4th and 5th degree polynomial fittings, shown in panels 3.4e and 3.4f, respectively. It can be seen that, in contrast to the results reported for the 3rd degree polynomial fitting, the constrained fitting procedure hardly influences the calculated band profiles of dimer, trimer and tetramer. The result obtained in both approaches also resembles the data derived from the band fitting procedures using Gauss-Lorentz sum profiles, given in Figure 3.1B.

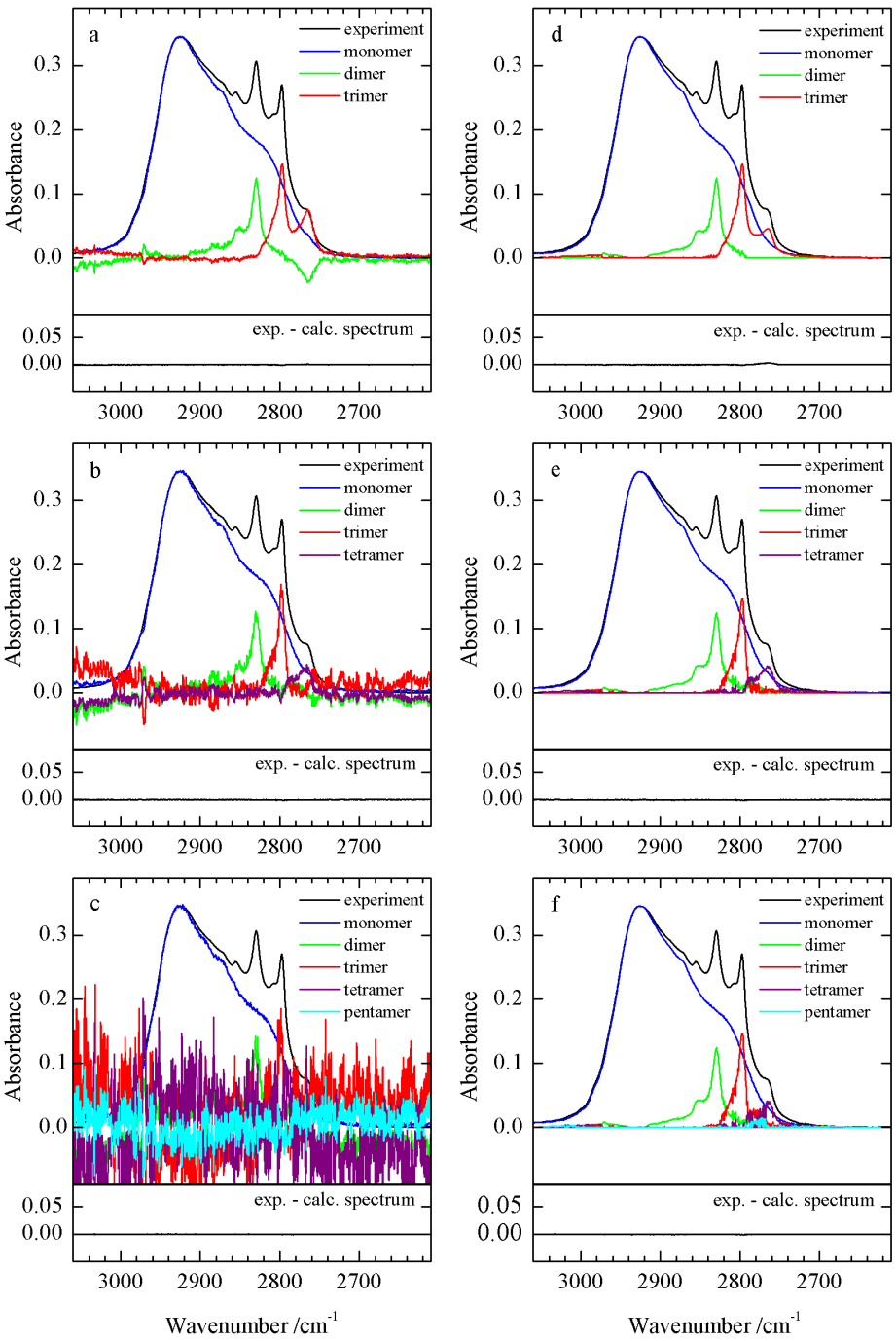

Figure 3.3 The experimental data analyzed using only the 3rd degree polynomial (top), the 4th degree polynomial (middle) and the 5th degree polynomial (bottom) for all wavenumbers with regular least-squares (a,b,c) and adding a nonnegative constraint (d,e,f). The bottom panel shows the difference between the experimental spectrum and the model.

It should be noted that in panel 3.3f some contribution due to pentamer is also predicted to appear near 2780 cm^{-1}. We believe that the appearance of this feature is due to artifacts related to numerical instabilities of the procedures used. Additional evidence for this statement, illustrating that overfitting indeed limits the resolving power required to accurately separate the contributions of trimer and tetramer near 2780 cm^{-1}, will be reported below.

3.3.5 Polynomial selection

Besides using a fixed polynomial degree for all wavenumbers it is also possible to select a model for every wavenumber individually. The panels in Figure 3.4 show the experimental absorbances for A, B, C, D, E, F, G and H obtained from the database. These plots also show least-squares fitted polynomials with different degrees with the intercept equal to zero and with the polynomial degree p equal to 1, 2, 3, 4 or 5.

$$A_{exp}(\tilde{\nu}_i) = \sum_{p=1}^{n} a_{\mathrm{p}}(\tilde{\nu}_i, \tilde{\nu}_m)\,[A_{mon}(\tilde{\nu}_m)]^p \tag{3.19}$$

To facilitate analysis, the lower degree polynomial is always plotted in front of the higher degree polynomials so that changes due to the increase of the degree of the polynomial are readily recognized. This principle allows to visually observe when the addition of a higher-degree term has little or no extra contribution to the quality of the fit.

From the data in Figure 3.4, it can be seen that for case A the experimental data are well reproduced using a linear regression. As expected, the spectral features in this region therefore are fully reproduced using a monomer only approach. For cases B, C and D, a quadratic polynomial model describing monomer and dimer contributions is required, while for cases E and F, a cubic model incorporating monomer, dimer and trimer contributions is needed. For case G, good agreement requires a fourth degree term showing that for this wavenumber a tetramer contribution is needed. Finally, for wavenumber H, located far away from any absorbance, there is no change in the measured absorbance with increasing monomer concentration, therefore a 0^{th} degree polynomial or constant is the best model to mimic this relation. This visual observation

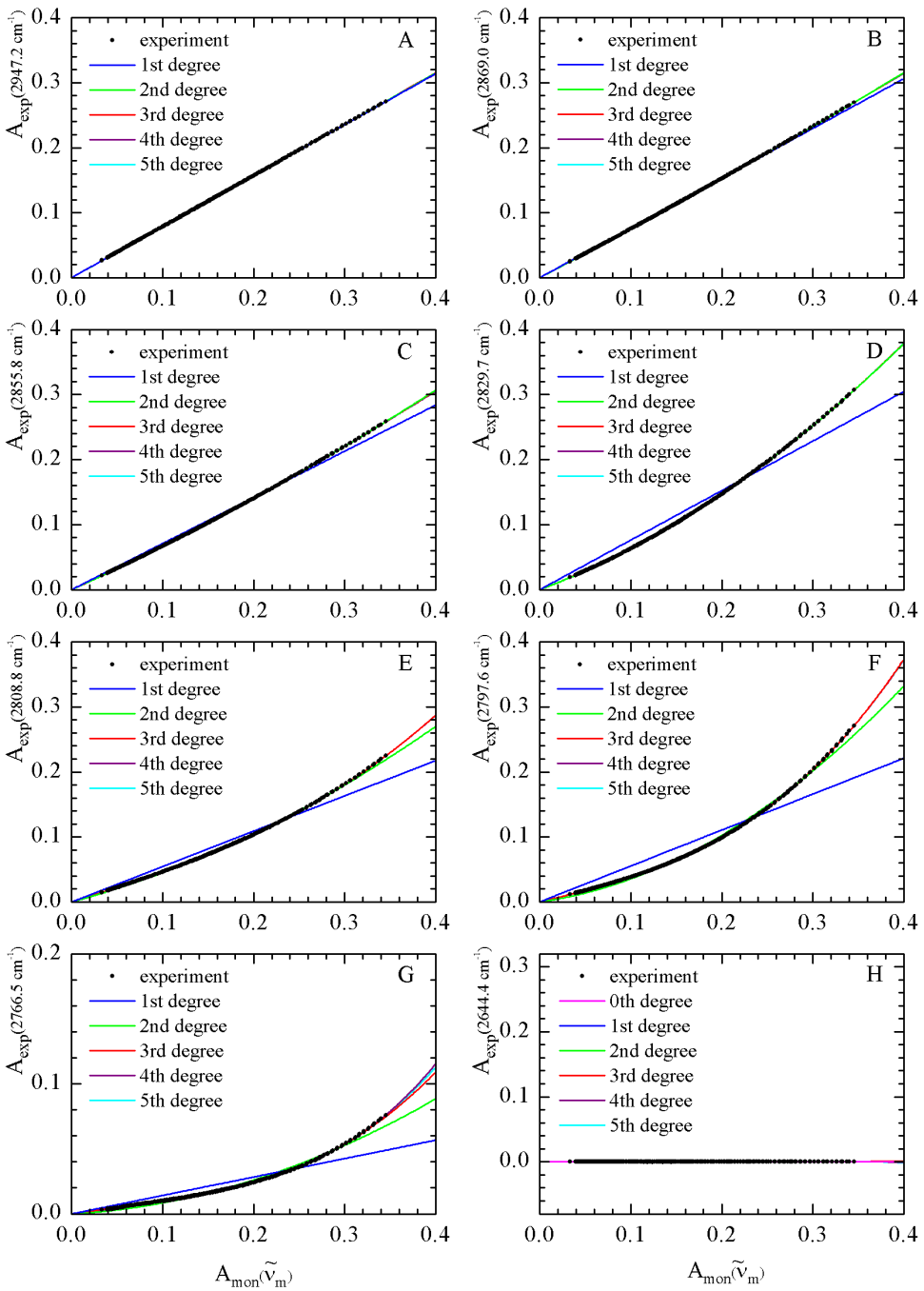

Figure 3.4 Experimental absorbances for the different wavenumbers selected in Figure 3.2 and results from least-squares fitting procedures using different degree polynomials. To facilitate visual comparison, the lower degree polynomials are plotted in front of the higher degree polynomials. For panels A to G where the experimental absorbance versus the monomer absorbance is increasing significantly, the 0^{th} degree polynomial is not shown.

of the appropriate degree can be calculated using statistical selection criteria explained in the following paragraphs.

Apart from the visual comparison, the choice of the optimal polynomial can be guided using several statistical criteria. These criteria are a tool to evaluate whether a certain model performs "better" than another model. Here, we define a "better" model to be one that is parsimonious in the polynomial degree *p* and one that has a smaller residual sum of squares, *RSS*

$$RSS_p(\tilde{\nu}_i) = \sum_{k=1}^{n} [A_{exp,k}(\tilde{\nu}_i) - A_{calc,k}\ (\tilde{\nu}_i)]^2 \tag{3.20}$$

with n as the number of spectra in the data set, i.e. number of measured datapoints for each wavenumber. The top of Table 3.1 indicates the *RSS* values for the polynomials illustrated in Figure 3.4 for the wavenumbers A to H defined in Figure 3.2. Because adding an extra parameter to the polynomial increases the flexibility of the model, the *RSS* values decrease with increasing polynomial degree. If we use the smallest RSS value as a criterion to select the appropriate polynomial degree we would end up with a plot almost identical to Figure 3.3c with a fixed polynomial degree of five. For completeness this plot is shown in Figure S3.1 of the supporting information.

In this paper we compare the polynomial models resulting from two commonly used criteria, the A and B information criteria (*AIC, BIC*) that have a penalty factor for the number of parameters in the model. The *AIC* was published by Akaike [39] in 1973 and is defined as

$$AIC_p(\tilde{\nu}_i) = n \cdot \ln\left(\frac{RSS_p(\tilde{\nu}_i)}{n}\right) + r \cdot 2 \tag{3.21}$$

with *p* as the polynomial degree, *n* as the number of spectra in the data set and *r* as the number of fitted parameters (r=1 for p=0 and r=p-1 for p>0). The 'better' model is then selected as the one with the smallest *AIC* value when comparing with the values for all suggested polynomials. In 1978, Schwarz [40] published a modified information criteria, the *BIC*, which is defined as

$$BIC_p(\tilde{\nu}_i) = n \cdot \ln\left(\frac{RSS_p(\tilde{\nu}_i)}{n}\right) + r \cdot \ln(n) \tag{3.22}$$

As with the *AIC*, the most appropriate model is the one with the minimum *BIC* value. The difference between both criteria is that the *BIC* has a log(*n*) penalty factor, in contrast to the factor 2 in the AIC. This implies that for large data sets, the *BIC* has a heavier penalty for the number of parameters in the model and therefore tends to yield models with fewer parameters, e.g. a lower polynomial degree.

The bottom of Table 3.1 contains the *AIC* and *BIC* values for the polynomials illustrated in Figure 3.4 for the wavenumbers A to H defined in Figure 3.2. It can be seen that the *RSS* values for the higher degree polynomials are all very small, which is expected as these polynomials show good fit with the data in the panels of Figure 3.4. To select the appropriate polynomial, the *AIC* and *BIC* values for 8 wavenumbers were calculated. The smallest *AIC* and *BIC* values are indicated in italic and the accompanying polynomial degree is mentioned. Overall we can conclude that both criteria result in rather large polynomial models. Where we would have expected models 0^{th}, 1^{st} or 2^{nd} degree models for wavenumbers A to D and H, the criteria indicate that 4^{th} or 5^{th} models would be more appropriate. It should also be noted that for wavenumbers C to E a smaller polynomial degree was selected when using the *BIC* then instead of the *AIC*. This is an example of the fact that *BIC* indeed tends to yield in smaller models.

The panels on the left in Figure 3.5 demonstrate the results when applying the *AIC* and the *BIC* to every wavenumber of the recorded data set. Successively, the appropriated polynomial degree is selected according the *AIC* or *BIC* criterion and the monomer and oligomer contributions are plotted in the panels below. Comparison of the spectra obtained with both criteria shows that the *BIC* is tending towards lower polynomial degrees, slightly reducing the noise caused by compensation effects. When comparing the *BIC* result with Figure 3.3c it can be seen that the *BIC* method reduces noise but still a large amount of negative contributions remains. As shown before the noise in the resulting spectrum can be brought down by prohibiting polynomial coefficients to be negative by introducing nonnegative constraints.

Table 3.1 *RSS*, *AIC* and *BIC* values for the least-squares fit of the 0^{th} to 5^{th} degree polynomials at wavenumbers indicated in Figure 3.1. The polynomial regressions of the 1^{st} to 6^{th} degree have an intercept value equal to zero. For both the *AIC* and *BIC* the appropriate polynomial degree is selected as the one with the minimum *AIC* or *BIC* value, which are given in italic.

	p	A	B	C	D	E	F	G	H
		2947.2	2869.0	2855.8	2829.7	2808.8	2797.6	2766.5	2644.4
RSS	0	1.45	1.43	1.31	1.81	0.90	1.22	8.40×10^{-2}	1.32×10^{-5}
	1	2.44×10^{-5}	8.78×10^{-4}	5.49×10^{-3}	5.60×10^{-2}	2.77×10^{-2}	1.32×10^{-1}	1.15×10^{-2}	1.73×10^{-5}
	2	1.62×10^{-5}	1.51×10^{-5}	1.64×10^{-5}	2.11×10^{-5}	6.94×10^{-4}	3.94×10^{-3}	1.00×10^{-3}	1.66×10^{-5}
	3	1.54×10^{-5}	1.50×10^{-5}	1.57×10^{-5}	2.05×10^{-5}	1.044×10^{-5}	1.464×10^{-5}	3.71×10^{-5}	1.26×10^{-5}
	4	1.390×10^{-5}	1.445×10^{-5}	1.48×10^{-5}	2.03×10^{-5}	1.035×10^{-5}	1.458×10^{-5}	1.70×10^{-5}	1.07×10^{-5}
	5	1.398×10^{-5}	1.440×10^{-5}	1.47×10^{-5}	2.01×10^{-5}	1.034×10^{-5}	1.455×10^{-5}	1.63×10^{-5}	1.01×10^{-5}
AIC	0	-1891.8	-1897.4	-1928.4	-1816.4	-2056.9	-1952.3	-2877.7	-5908.0
	1	-5695.2	-4455.8	-3821.9	-3018.0	-3262.2	-2722.6	-3566.7	-5814.4
	2	-5834.5	-5859.0	-5830.7	-5744.1	-4535.1	-3934.1	-4409.0	-5826.8
	3	-5850.3	-5859.6	-5845.0	-5751.8	-5985.4	*-5868.5*	-5546.7	-5921.0
	4	*-5884.4*	*-5871.1*	-5861.9	-5754.0	*-5986.4*	-5867.8	-5815.3	-5974.7
	5	-5882.5	-5870.2	*-5863.4*	*-5754.7*	-5984.8	-5866.6	*-5828.2*	*-5994.6*
Selected degree		4	4	5	5	4	3	5	5
BIC	0	-1887.9	-1893.5	-1924.6	-1812.5	-2053.1	-1948.5	-2873.9	-5904.1
	1	-5691.4	-4451.9	-3818.1	-3014.2	-3258.4	-2718.7	-3562.9	-5810.6
	2	-5826.8	-5851.3	-5823.0	-5736.4	-4527.4	-3926.4	-4401.3	-5819.1
	3	-5838.8	-5848.1	-5833.4	*-5740.3*	*-5973.8*	*-5856.9*	-5535.1	-5909.5
	4	*-5869.0*	*-5855.7*	*-5846.6*	-5738.6	-5971.0	-5852.4	-5799.9	-5959.3
	5	-5863.3	-5851.0	-5844.2	-5735.5	-5965.6	-5847.3	*-5808.9*	*-5975.4*
Selected degree		4	4	4	3	3	3	5	5

Table 3.2 *RSS*, *AIC* and *BIC* values for the least-squares fit with nonnegative constraints of the 0^{th} to 5^{th} degree polynomials at wavenumbers indicated in Figure 3.1. The polynomial regressions of the 1^{st} to 6^{th} degree have an intercept value equal to zero. For both the *AIC* and *BIC* the appropriate polynomial degree is selected as the one with the minimum *AIC* or *BIC* value, which are given in italic.

	p	A	B	C	D	E	F	G	H
		2947.2	2869.0	2855.8	2829.7	2808.8	2797.6	2766.5	2644.4
RSS	0	1.45	1.43	1.31	1.81	0.90	1.22	8.40×10^{-2}	1.32×10^{-5}
	1	2.44×10^{-5}	8.78×10^{-4}	5.49×10^{-3}	5.60×10^{-2}	2.77×10^{-2}	1.32×10^{-1}	1.15×10^{-2}	1.73×10^{-5}
	2	1.62×10^{-5}	1.51×10^{-5}	1.64×10^{-5}	2.11×10^{-5}	6.94×10^{-4}	3.94×10^{-3}	1.00×10^{-3}	1.73×10^{-5}
	3	1.56×10^{-5}	1.51×10^{-5}	1.64×10^{-5}	2.05×10^{-5}	1.04×10^{-5}	1.46×10^{-5}	1.80×10^{-4}	1.73×10^{-5}
	4	1.56×10^{-5}	1.51×10^{-5}	1.64×10^{-5}	2.05×10^{-5}	1.04×10^{-5}	1.46×10^{-5}	1.70×10^{-5}	1.73×10^{-5}
	5	1.56×10^{-5}	1.51×10^{-5}	1.64×10^{-5}	2.05×10^{-5}	1.04×10^{-5}	1.46×10^{-5}	1.70×10^{-5}	1.73×10^{-5}
AIC	0	-1891.8	-1897.4	-1928.4	-1816.4	-2056.9	-1952.3	-2877.7	*-5908.0*
	1	-5695.2	-4455.8	-3821.9	-3018.0	-3262.2	-2722.6	-3566.7	-5814.4
	2	-5834.5	*-5859.0*	*-5830.7*	-5744.1	-4535.1	-3934.1	-4409.0	-5812.4
	3	*-5847.3*	-5857.0	-5828.7	*-5751.8*	*-5985.4*	*-5868.5*	-4999.6	-5810.4
	4	-5845.3	-5855.0	-5826.7	-5749.8	-5983.4	-5866.5	*-5814.9*	-5808.4
	5	-5843.3	-5853.0	-5824.7	-5747.8	-5981.4	-5864.5	-5812.9	-5806.4
Selected degree		3	2	2	3	3	3	4	0
BIC	0	-1887.9	-1893.5	-1924.6	-1812.5	-2053.1	-1948.5	-2873.9	*-5904.1*
	1	-5691.4	-4451.9	-3818.1	-3014.2	-3258.4	-2718.7	-3562.9	-5810.6
	2	-5826.8	*-5851.3*	*-5823.0*	-5736.4	-4527.4	-3926.4	-4401.3	-5804.7
	3	*-5835.7*	-5845.5	-5817.2	*-5740.3*	*-5973.8*	*-5856.9*	-4988.0	-5798.9
	4	-5829.9	-5839.6	-5811.4	-5734.4	-5968.0	-5851.1	*-5799.5*	-5793.0
	5	-5824.0	-5833.8	-5805.5	-5728.6	-5962.1	-5845.2	-5793.7	-5787.2
Selected degree		3	2	2	3	3	3	4	0

Table 3.2 presents the *RSS*, *AIC* and *BIC* values for the polynomial regression with added nonnegative constraints for the wavenumbers A to H defined in Figure 3.2. The polynomial degrees resulting from the A and B information criteria are lower than the ones in Table 3.1 and show a better match with the polynomial degree made by visual inspection of Figure 3.2. It should be noted that the plots of the polynomial models with nonnegative constraints are almost identical with those in Figure 3.2 and can be found in the supporting information as Figure S3.2. Although the degrees selected by both criteria are identical in Table 3.2, this is not the case for all wavenumbers. Inspection of the data in the upper panels of Figure 3.5 shows that for the analysis involving nonnegative constraints, *BIC* generally yields lower values. The predicted contributions for monomer and complexes are almost identical, except for the 2860-2880 red region where the monomer, dimer, trimer and tetramer contributions show substantial overlap. The pentamer contribution observed in Figure 3.3f and in the right (AIC) panel of Figure 3.5 is strongly reduced. This suggests that at least for the systems studied here the *BIC* is able to better separate the different absorbance bands in regions where several contributions overlap.

It can be noted that when looking at the top of Table 3.2 the *RSS* value at every wavenumber stays constant from a certain polynomial degree. This means that when including the nonnegative constraint, the addition of an extra term in the polynomial yields little or no improvement of the fit. Because in this case the *RSS* can be used as another criterion for selection of the polynomial model we added the result in the right picture of Figure S3.1 of the supporting information for completeness.

We like to point out that although we used three different strategies, a fixed polynomial degree or selecting the appropriate polynomial degree with the *AIC* or the *BIC*, at the end the resulting spectra shows high resemblance if the nonnegative constraints are added, Figure 3.3f and the panels on the right of Figure 3.5.

Figure 3.5 The experimental data analyzed with polynomial regression using the minimum value of the *AIC* and the *BIC* to select the appropriate polynomial degree varying between 0 and 5 for every wavenumber. The panels on the left show the different monomer and oligomer contributions using regular least-squares procedures and the results in the right panels are obtained by adding nonnegative constraints for the coefficients. The bottom panel in each figure shows the difference between the experimental spectrum and the model.

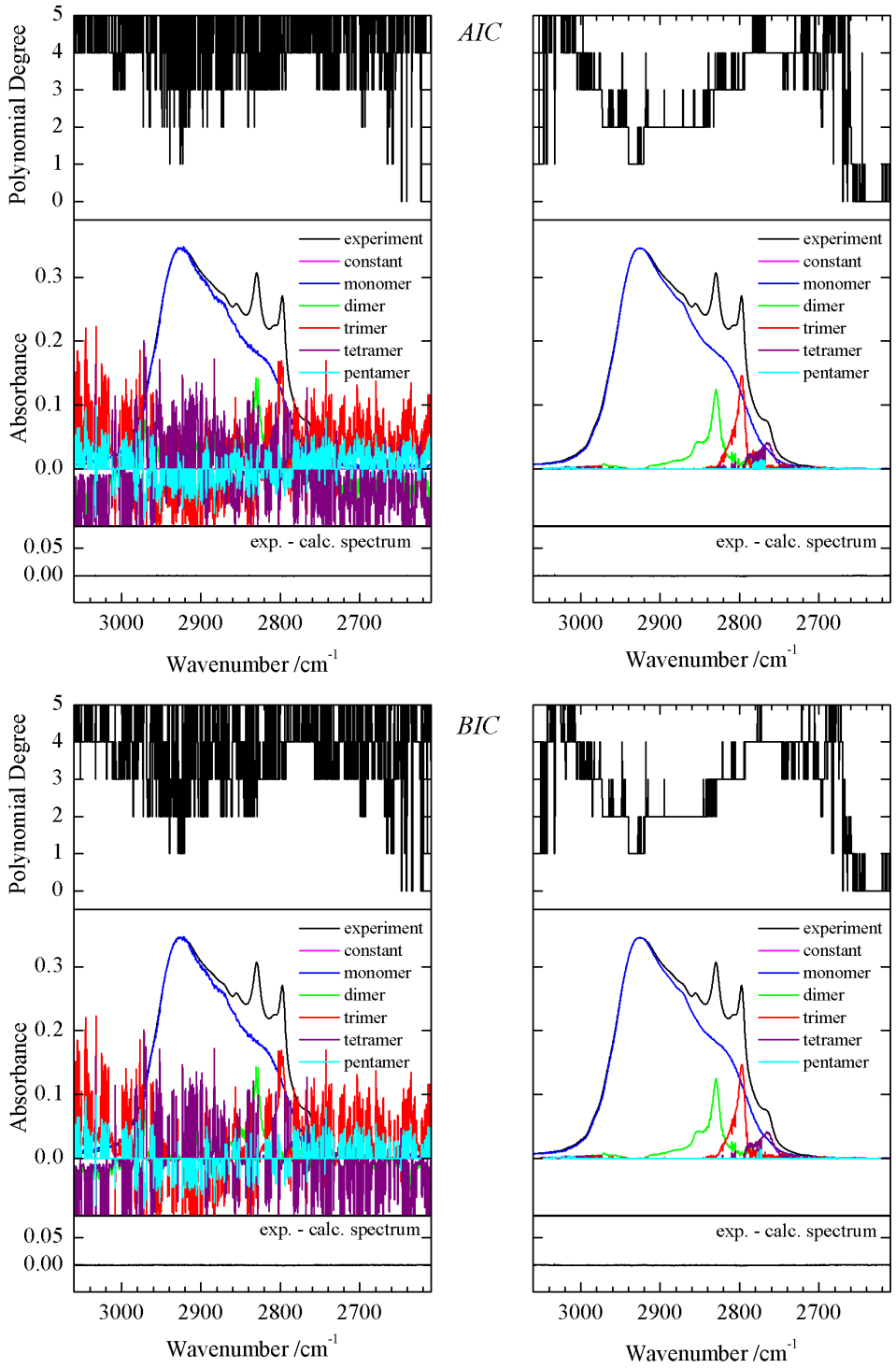
AIC
BIC
Polynomial Degree
Absorbance
experiment
constant
monomer
dimer
trimer
tetramer
pentamer
exp. - calc. spectrum
Wavenumber /cm-1

3.4 Conclusions

In this paper, we report on the development and validation of numerical methods in which the concentration dependent behavior observed for HCl in liquid argon is analyzed by least-squares fitting approaches. In these methods, at each wavenumber a polynomial is used to mimic the relation between monomer concentrations and measured absorbances. It was shown that least-squares fitting of higher degree polynomials tends to overfit and at the same time leads to unphysical compensation effects where a contribution due to one species is compensated for by a negative contribution of another. These issues can be corrected for by carefully analyzing, using AIC or BIC information criteria, the differences between consecutive least-squares fits observed when the degree of the polynomial used is systematically increased, and by introducing additional constraints prohibiting negative absorbances to occur for the monomer or for one of the oligomers. We believe that, the models and approaches developed, and the Matlab based software packages used for their implementation can now be considered robust and thus should allow other systems to be analyzed with a much higher accuracy than before. Results obtained for solutions of ammonia and ammonia-d_3 dissolved in liquid xenon, for which similar but more complicated spectral features due to self-association are known to exist[30,31], are currently investigated, and will be reported in a consecutive study.

References

[1] M. Fárník and D. J. Nesbitt, J. Chem. Phys., 121 (2004) 12386-12395.
[2] M. Fárník, S. Davis and D. J. Nesbitt, Faraday Discuss., 118 (2001) 63-78.
[3] M. D. Schuder, C. M. Lovejoy, R. Lascola and D. J. Nesbitt, J. Chem. Phys., 99 (1993) 4346-4362.
[4] A. Furlan, S. Wülfert and S. Leutwyler, Chem. Phys. Lett., 153 (1988) 291-295.
[5] T. Häber, U. Schmitt and M. A. Suhm, Phys. Chem. Chem. Phys., 1 (1999) 5573-5582.
[6] D. Skvortsov, M. Y. Choi and A. F. Vilesov, J. Phys. Chem. A, 111 (2007) 12711-12716.
[7] A. J. Barnes, K. Szczepaniak and W. J. Orville-Thomas, J. Mol. Struct., 59 (1980) 39-53.
[8] A. Engdahl and B. Nelander, J. Chem. Phys., 94 (1990) 8777-8780.
[9] B. J. van der Veken and F. R. De Munck, J. Chem. Phys., 97 (1992) 3060-3071.
[10] W. A. Herrebout, J. Van Gils and B. J. van der Veken, J. Mol. Struct., 563-564 (2001) 249-255.
[11] E. R. Malinowski, *Factor Analysis in Chemistry*, 3rd ed., John Wiley & Sons, Inc., New York, 2002.
[12] B. J. van der Veken, J. Phys. Chem., 100 (1996) 17436-17438.
[13] N. Nagels, Y. Geboes, B. Pinter, F. De Proft and W. A. Herrebout, Chem. Eur. J., 20 (2014) 8433-8443.
[14] B. Michielsen, C. Verlackt, B. J. van der Veken and W. A. Herrebout, J. Mol. Struct., 1023 (2012) 90-95.
[15] B. Michielsen, J. J. J. Dom, B. J. van der Veken, S. Hesse, M. A. Suhm and W. A. Herrebout, Phys. Chem. Chem. Phys., 14 (2012) 6469-6478.
[16] J. J. J. Dom, B. J. van der Veken, B. Michielsen, S. Jacobs, Z. F. Xue, S. Hesse, H. M. Loritz, M. A. Suhm and W. A. Herrebout, Phys. Chem. Chem. Phys., 13 (2011) 14142-14152.
[17] J. J. J. Dom, B. Michielsen, B. U. W. Maes, W. A. Herrebout and B. J. van der Veken, Chem. Phys. Lett., 469 (2009) 85-89.
[18] D. Hauchecorne, N. Nagels, B. J. van der Veken and W. A. Herrebout, Phys. Chem. Chem. Phys., 14 (2012) 681-690.
[19] B. Michielsen, W. A. Herrebout and B. J. van der Veken, ChemPhysChem, 8 (2007) 1188-1198.
[20] B. Michielsen, J. J. J. Dom, B. J. van der Veken, S. Hesse, Z. F. Xue, M. A. Suhm and W. A. Herrebout, Phys. Chem. Chem. Phys., 12 (2010) 14034-14044.
[21] B. Michielsen, W. A. Herrebout and B. J. van der Veken, ChemPhysChem, 9 (2008) 1693-1701.
[22] D. Hauchecorne, R. Szostak, W. A. Herrebout and B. J. van der Veken, ChemPhysChem, 10 (2009) 2105-2115.
[23] D. Hauchecorne, B. J. van der Veken, A. Moiana and W. A. Herrebout, Chem. Phys., 374 (2010) 30-36.
[24] D. Hauchecorne, A. Moiana, B. J. van der Veken and W. A. Herrebout, Phys. Chem. Chem. Phys., 13 (2011) 10204-10213.

[25] D. Hauchecorne, B. J. van der Veken, W. A. Herrebout and P. E. Hansen, Chem. Phys., 381 (2011) 5-10.
[26] D. Hauchecorne and W. A. Herrebout, J. Phys. Chem. A., 117 (2013) 11548-11557.
[27] N. Nagels, D. Hauchecorne and W. A. Herrebout, Molecules, 18 (2013) 6829-6851.
[28] N. Nagels and W. A. Herrebout, Spectrochim. Acta A, 136 (2015) 16-26.
[29] Y. Geboes, N. Nagels, B. Pinter, F. De Proft and W. A. Herrebout, J. Phys. Chem. A, 119 (2015) 2502-2516.
[30] W. A. Herrebout, S. M. Melikova, S. N. Delanoye, K. S. Rutkowski, D. N. Shchepkin and B. J. van der Veken, J. Phys. Chem. A, 109 (2005) 3038-3044.
[31] K. S. Rutkowski, W. A. Herrebout, S. M. Melikova, P. Rodziewicz, B. J. van der Veken and A. Koll, Spectrochim. Acta A, 61 (2005) 1595-1602.
[32] W. Herrebout, Top. Curr. Chem., 358 (2015) 79-154.
[33] in MATLAB 8.3, The MathWorks Inc., Natick, MA, USA, 2014.
[34] B. J. van der Veken and W. A. Herrebout, J. Phys. Chem. A, 105 (2001) 7198-7204.
[35] A. I. Fishman, W. A. Herrebout and B. J. van der Veken, J. Phys. Chem. A, 106 (2002) 4536-4542.
[36] M. O. Bulanin and G. Y. Zelikina, Phase Equilibria and Spectral Analysis of Cryosystems., in: R. J. H. Clark and R. E. Hester (Eds.) Molecular Cryospectroscopy. Advances in Spectroscopy., Wiley, Chichester, 1995, pp. 22-34.
[37] A. I. Fishman, A. I. Noskov, R. M. Aminova and R. A. Skochilov, Spectrochim. Acta A, 136 (2015) 100-106.
[38] A. B. Remizov and R. A. Skochilov, Proc. SPIE 5507, 2004, pp. 195-202.
[39] H. Akaike, IEEE Transactions on Automatic Control, 19 (1974) 716-723.
[40] G. Schwarz, The Annals of Statistics, 6 (1978) 461-464.

Supporting information

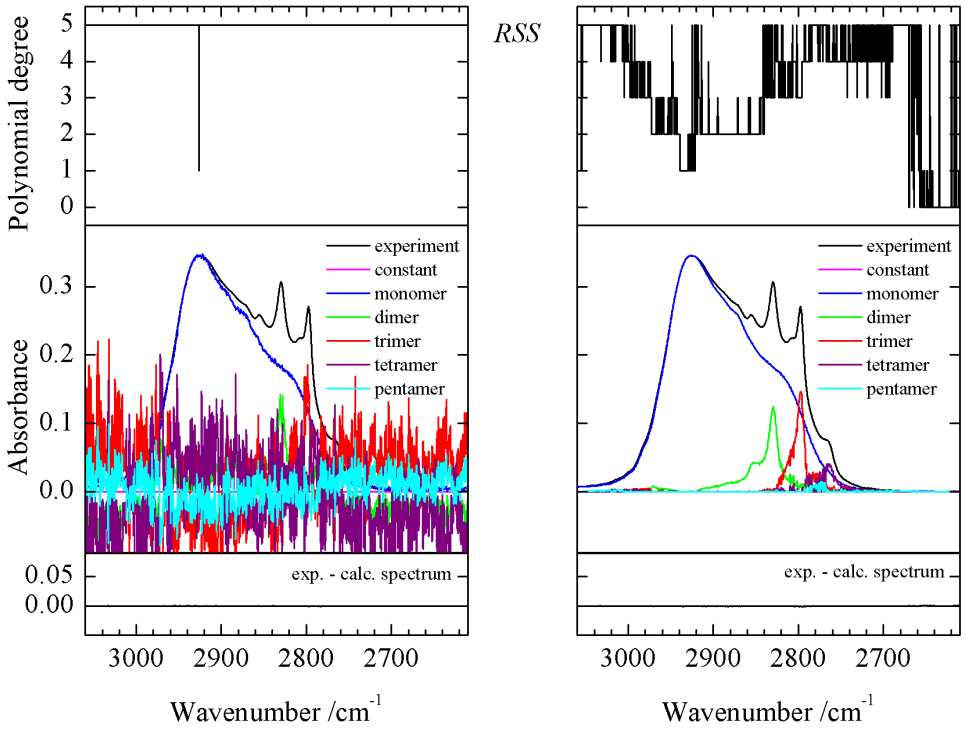

Figure S3.1 The experimental data analyzed with polynomial regression using the minimum value of the RSS to select the appropriate polynomial degree varying between 0 and 5 for every wavenumber. The left panels show the different monomer and oligomer contributions using regular least-squares procedures and the results in the right panels are obtained by adding nonnegative constraints for the coefficients.

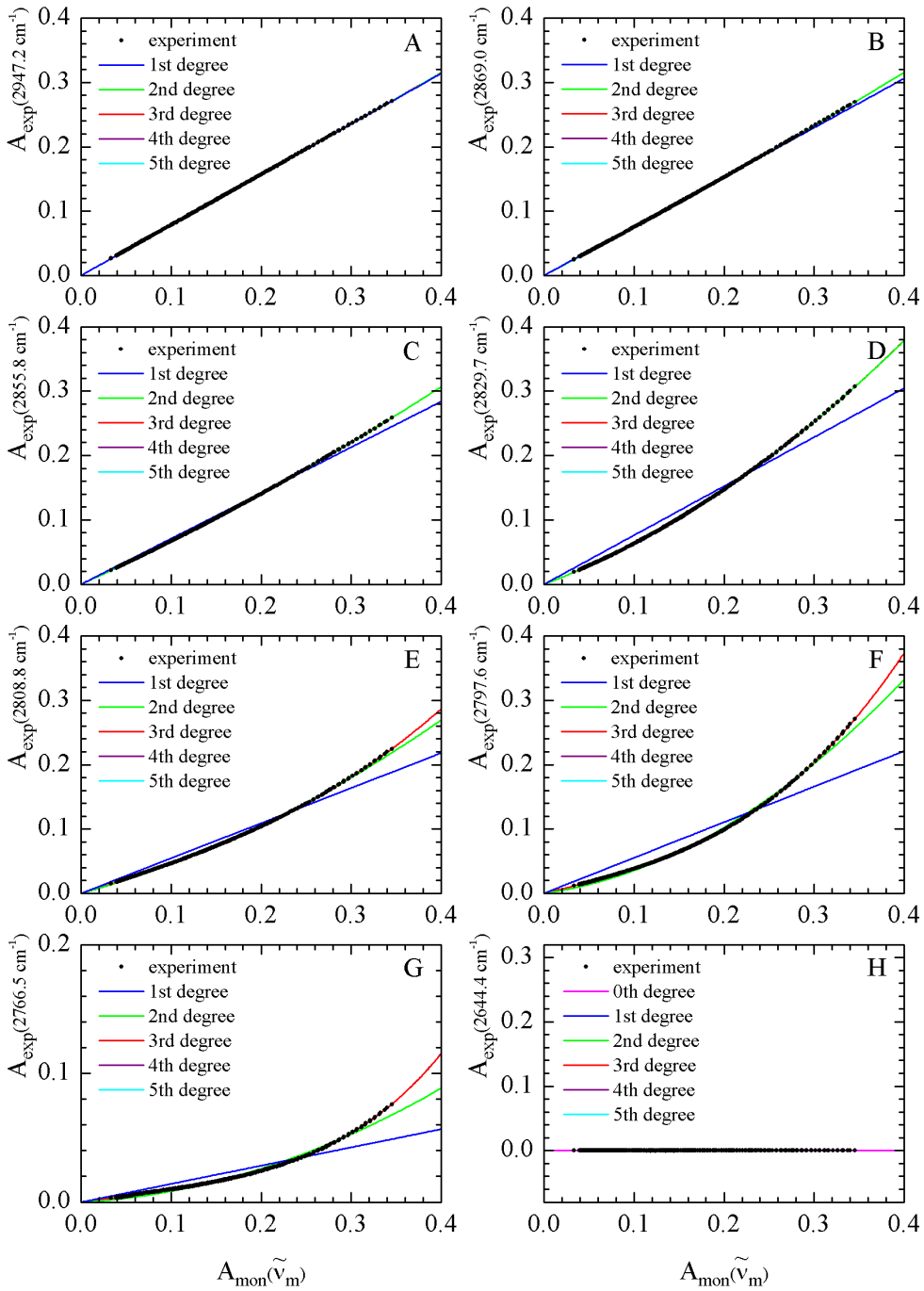

Figure S3.2 Experimental absorbances for the different wavenumbers selected in Figure 1.2 and results from least-squares fitting procedures with nonnegative constraints using different degree polynomials. To facilitate visual comparison, the lower degree polynomials are plotted in front of the higher degree polynomials. For panels A to G where the experimental absorbance versus the monomer absorbance is increasing significantly, the 0^{th} degree polynomial is not shown.

Chapter 4

The self-associating behavior of NH_3 and ND_3 in liquid xenon

This chapter has been submitted as

De Beuckeleer, L. I.; Herrebout, W. A., *The self-associating behavior of NH_3 and ND_3 in liquid xenon* to J. Mol. Struct. on 07/12/2015

Abstract

In this study we report on the analysis of isothermal spectra of NH_3 and ND_3 solutions in liquid xenon at 203 K using newly developed and validated least-squares approaches to investigate the its self-associating behavior. For both species we observe clear dimer bands in the spectral area of the $\nu_1+\nu_4$, $\nu_3+\nu_4$ and $\nu_1+\nu_2$, $\nu_3+\nu_2$ combination bands. The analysis of the N–D stretching area, allows us to characterize clear contributions of dimers and trimers. The analysis of the N–H stretching area is hampered by the occurrence of a time dependent band due to solid water traces during the experiments. For NH_3 we also performed an investigation of the N–H bending region, ν_2, which demonstrated a small dimer absorption band. These obtained results compare well with literature data.

4.1 Introduction

Solutions in liquefied inert gases have proven to be an ideal medium to study molecular complexes held together by weak and medium-strong interactions.[1] They create a weakly interacting environment that, combined with the low temperatures used, leads to small bandwidths and thus facilitates the detection of complex bands only slightly shifted from the monomer modes. Although most experiments reported are focusing on heterocomplexes involving an electron rich Lewis base and an electron deficient region related to a hydrogen bond[2-4], a halogen bond[4-7] or a lone pair-π acceptor[8], these solutions also form an ideal medium to investigate self-association through hydrogen bonding between two, three or more identical molecules.

Information on the appearance of self-association in the cryosolutions studies is typically obtained from isothermal experiments, in which spectra of solutions containing different concentrations of the solute are recorded. In many cases, the contributions of the monomer and the oligomeric species are approximated by subtracting the spectra of solutions containing larger amounts of the solute and a rescaled spectrum of a highly diluted solution recorded under similar circumstances. Subsequently, information on the origin of the different features observed in the difference spectra is obtained by determining their integrated intensities and their dependence upon the monomer intensity. This subtraction approach is somewhat limited as it requires that at the lowest concentrations studied the contribution of complex species in the spectra is negligibly small. Moreover, because the outcome of least-squares band fitting procedures used to determine the integrated intensities of the different spectral features often depends strongly on the initial parameters chosen and thus can be biased by the end-user, integrated intensities obtained for the different species often are less reliable than required.

To overcome these problems, we have recently reported on the development and validation of numerical methods in which the concentration dependent behavior observed for HCl in liquid argon is analyzed by least-squares fitting approaches.[9] In these methods, for each wavenumber a polynomial is used to mimic the relation between monomer concentrations and measured absorbances. It was shown that by

selecting the appropriate polynomial degree by using the *BIC* selection criterion, and by introducing additional constraints prohibiting negative absorbances to occur for the monomer and oligomers, the contributions due to monomers and self-associated species can be determined with a much higher accuracy than before. To further validate the models developed, in this study, results obtained for solutions of ammonia (NH_3) dissolved in liquid xenon (LXe), for which similar but more complicated spectral features due to self-association are known to exist[10,11], are reported. It is important to stress that, although spectral features due to self-association have been observed for ammonia in LXe, the data obtained for NH_3[10,11] did not allow a detailed assignment of the features observed. Moreover, for ND_3, no studies in cryosolvents were yet reported.

By combining new experimental data and the recently developed methodologies we aim to i) further expand and analyze the available data for ammonia, and ii) complement the data available with data derived for ND_3. The results will also be compared with literature data focusing on the earlier observations of different types of clusters in solid matrices.

4.2 Experimental section

NH_3 (stated purity of 99,99%) and ND_3 (stated purity of 99%) were purchased from Sigma-Aldrich and Cambridge Isotope Laboratories respectively and were used without further purification. The xenon used as a cryosolvent had a stated purity of 99.999% and was supplied by Linde.

A dataset of 328 infrared spectra for NH_3 and 246 spectra for ND_3 solutions in LXe was recorded on a Bruker IFS 66v Fourier transform spectrometer. A Globar source was used in combination with a Ge/KBr beamsplitter and a LN_2-cooled broad band MCT detector. The interferograms were averaged over 500 scans at an unapodized resolution of 0.5 cm^{-1}, averaged over 500 scans, and Blackman–Harris three-term apodized before Fourier transformation. The experimental set-up used to investigate the solutions in liquid noble gases has been described before.[1] In the actual cryostat, a liquid cell with 1 cm path length, equipped with wedged Si windows, was mounted below a LN_2 dewar. The temperature of the cell body is measured using a Pt-100

thermoresistor. The SunRod electric minicartridge heater is controlled using a Eurotherm 3504 PID controller. The temperature of the solutions was stabilized at 203 K, the temperature variation during a typical run being less than 0.05 K. Spectra were obtained and preanalyzed using OPUS 6.5. Further analyses were performed using Matlab.[12]

The mole fractions of NH_3 and ND_3 used for the datasets are difficult to accurately quantify[13,14], but are estimated to vary between 1.5×10^{-2} and 9.4×10^{-4} for NH_3 and 9.4×10^{-3} and 9.4×10^{-4} for ND_3. The concentrations used are chosen so that the region between minimum and maximum absorbance is uniformly covered.

As the outcome of the used fitting procedures can be strongly influenced by baseline artefacts, it was found necessary to perform baseline corrections on the complete dataset using spectra of pure LXe recorded at exactly the same conditions. Another critical parameter often hampering the numerical analyses to be performed is related to small traces of solid, amorphous or crystalline water suspended in the solution or condensed onto the cold elements present in the cryostat and/or detector. As is clear from the bottom panel in Figure 4.1, these water traces manifest themselves as a broad band in the 3650-3050 cm^{-1} region which fully overlaps with the N–H stretching region of NH_3 and with a combination band of ND_3. The traces are observed to slightly increase during experiments, and, due to changes in relative intensities, are extremely difficult to subtract. Therefore, to avoid further numerical instabilities, no such corrections were introduced. To account for remaining baseline drifts, which we believe are due to small temperature changes inside the spectrometer due to the colder parts present, additional straight line baseline corrections was applied to all data. For NH_3 these straight lines were generated from 6850 to 6210, from 6210 to 5620, from 5620 to 3990, from 3990 to 2205, and from 2205 to and 665 cm^{-1}. For ND_3 these lines were generated from 5365 to 5023, from 5023 to 4362, from 4362 to 3390, from 3390 to 3005, from 3005 to 1820, and from 1820 to 535 cm^{-1}.

4.3 Results and discussion

4.3.1 Least-squares fitting method: general concept

Recently, a least-squares based methodology to isolate overlapping absorption bands of monomeric and oligomeric species observed in the spectra of cryosolutions was developed and validated.[9] The method is based on the assumption that the measured absorbance at a wavenumber $\tilde{\nu}_i$, $A_{exp}(\tilde{\nu}_i)$ is the sum of individual contributions related to the monomer, A_{mono}or to one of the oligomers, e.g. dimer A_{di}, trimer A_{tri}, tetramer A_{tetra}, etc., i.e.

$$A_{exp}(\tilde{\nu}_i) = A_{mono}(\tilde{\nu}_i) + A_{di}(\tilde{\nu}_i) + A_{tri}(\tilde{\nu}_i) + A_{tetra}(\tilde{\nu}_i) + \cdots \quad (4.1)$$

The experimental absorbances for each wavenumber $\tilde{\nu}_i$ of all contributing species in the solution are then expressed as a function of the absorbance of a chosen monomer wavenumber $\tilde{\nu}_m$ with the polynomial degree p equal to 1, 2, 3, 4 or 5 with intercept equal to zero

$$A_{exp}(\tilde{\nu}_i) = \sum_{p=1}^{n} a_{\mathrm{p}}(\tilde{\nu}_i, \tilde{\nu}_m)\,[A_{mono}(\tilde{\nu}_m)]^p. \quad (4.2)$$

with the coefficient $a_{\mathrm{p}}(\tilde{\nu}_i, \tilde{\nu}_m)$ being a constant related to the equilibrium constant of the oligomerization reaction.[9] The monomer wavenumber $\tilde{\nu}_m$ is used as an internal standard and is chosen based on the fact that no features due to self-association are observed or expected to appear in the region considered. Moreover, special attention is paid to the fact that for all concentrations studied the absorbance can be accurately determined. When there is no change in the measured absorbance with increasing monomer concentration, a 0^{th} degree polynomial or constant is the best model to mimic this relation.

In the applied model selection procedure, the experimental data for a given wavenumber are least-squares fitted using a series of polynomials of 1^{st}, 2^{nd}, 3^{rd}, 4^{th} and 5^{th} degree. Subsequently, the 'better' polynomial model is selected with the B information criterion, *BIC*, published by Schwarz[15] and defined as

$$BIC_p(\tilde{\nu}_i) = \mathrm{n} \cdot \ln\left(\frac{RSS_p(\tilde{\nu}_i)}{n}\right) + r \cdot \ln(n) \quad (4.3)$$

with n as the number of spectra in the dataset which is equal to the number of measured datapoints for each wavenumber and *r* as the number of fitted parameters (r=1 for p=0 and r=p-1 for p>0) and with sum of squares *RSS*, defined as

$$RSS_p(\tilde{\nu}_i) = \sum_{k=1}^{n} [A_{exp,k}(\tilde{\nu}_i) - A_{calc,k}\,(\tilde{\nu}_i)]^2 \tag{4.4}$$

Here, we define the "better" model as the model that is parsimonious in the polynomial degree *p* and one that has a smaller residual sum of squares, *RSS*

Despite the model selection strategy, higher degree polynomials lead to compensation effects in which a large positive contribution is calculated for one of the species, and another strongly negative compensating feature is predicted for another. To avoid this kind of noise, nonnegative constraints were added, prohibiting the coefficients to become negative during the polynomial regression.

In the following paragraph the recorded dataset will be analyzed by fitting a series polynomials with nonnegative constraints through the measured absorbance values for every wavenumber individually. The data for the different wavenumbers thus are completely independent. After selection of the appropriate polynomial degree using the *BIC*, the contributions for every wavenumber are calculated and combined and the isolated spectra of the species present in the solution are obtained without further smoothing.

It should also be noted that when showing the results a value will be shown for the constant until pentamer contribution. If the selected degree does not allow a certain contribution the coefficient will be set to be zero resulting in a contribution equal to zero.

4.3.2 The NH_3 and ND_3 spectra and subtraction procedures

Figure 4.1 shows typical infrared spectra from the database of NH_3 and ND_3 recorded at 203 K with liquefied xenon as solvent. The broad absorptions with substantial PQR structure observed in the N–H stretching region, 3950-3000 cm^{-1}, and the N–D stretching region, 2800-2200 cm^{-1}, are caused by the overlapping ν_3 (degenerate asymmetric stretching vibration), ν_1 (symmetric stretching vibration) and $2\nu_4$ (overtone

of asymmetric bending vibration) monomer bands, of which the band centers and relative intensities are difficult to determine.[3,11] The inserts given in Figure 4.1 illustrate that with increasing concentration of NH_3 or ND_3, new bands due to self-associated species emerge.

The fundamental vibrations ν_4 (degenerate asymmetric bending vibration) and ν_2 (symmetric bending or umbrella vibration) are observed near 1618 and 960 cm^{-1} for NH_3 and 1183 and 770 cm^{-1} for ND_3. As before, rotational PQR structure due to hindered internal rotation of ammonia in the cryosolutions is observed for all modes. It is clear from Figure 4.1 that, whereas features due to self-associating are easily observed for the stretching regions, no such features can be deduced for the other modes. The different behavior is explained by the fact that upon complexation, an extreme increase in infrared intensity, by a factor up to 80 times [16] is observed for the N–H and N–D stretching modes, whereas the intensity of the other modes is hardly influenced. From this, it must be concluded that, although features due to self-association are clearly visible in some regions of the spectra, their equilibrium concentration in the solutions studied should still be remarkably low. Apart from the band ascribed above, in the spectra of NH_3 and ND_3, additional bands are observed near 5026 and 4415 cm^{-1} and 3724 and 3321 cm^{-1}, respectively. These bands are assigned to the combination $\nu_1+\nu_4$, $\nu_3+\nu_4$ and $\nu_1+\nu_2$, $\nu_3+\nu_2$ respectively.[11] The feature at 4865 cm^{-1} observed in the spectra of ND_3 originates from the $\nu_1+\nu_3$ combination. The absorption near 1455 cm^{-1} observed in the spectra of ND_3 is assigned to a trace of ND_2H present in the ND_3 sample used. Based on calculated infrared intensities for both samples, and on existing literature data[17], the relative abundance of this species in the solution is estimated to be close to 6 %. It may be noted that, due to severe overlap with modes of the parent molecule, no features due to ND_2H were observed for other spectral regions. Also, no features due to NDH_2 were detected.

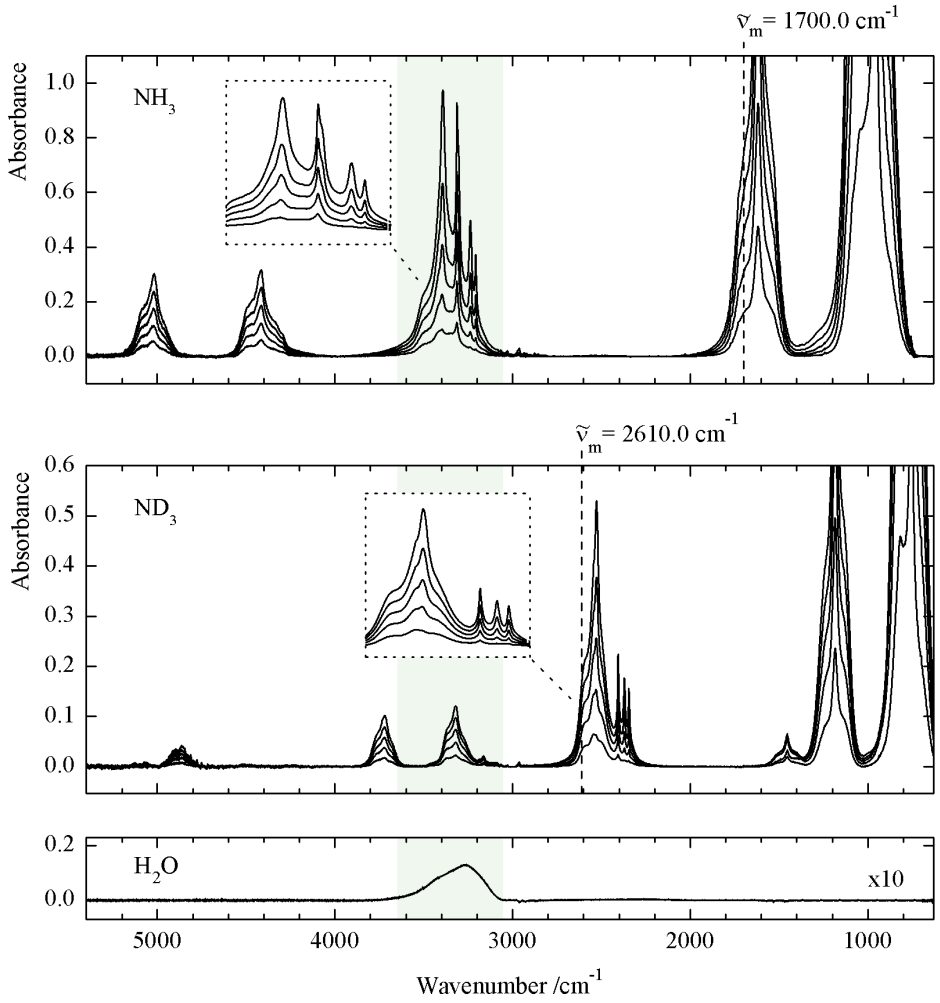

Figure 4.1 Infrared spectra of solutions in LXe at 203 K, with at the top 5 spectra of NH_3 and at the middle 5 spectra of ND_3. The spectra shown for each of the species represent only a small fraction of the spectral database used in the fitting procedures. The N–H and N–D stretching areas are magnified in the inserts. The bottom spectrum is an example of a spectrum of solid water that builds up during the measurements. Its spectral region is illustrated by the shaded area.

As a benchmark for least-squares polynomial fitting approaches, it is helpful to analyze the results that can be obtained using standard subtraction procedures. As mentioned before, these approaches are based on the assumption that at the lowest concentrations studied, only absorptions due to monomeric species are present. Moreover, it is assumed that in the concentration range studied the monomer spectrum

does not change. The subtraction procedure also requires the scaling factor of the diluted spectrum to be optimized. To this end, we have chosen to compare the absorbances at the reference wavenumbers $\tilde{\nu}_m$ = 1700.0 cm^{-1} for NH_3 and $\tilde{\nu}_m$ = 2610.0 cm^{-1} for ND_3. For completeness, the used reference wavenumbers $\tilde{\nu}_m$ are denoted with a dashed line in Figure 4.1.

The resulting spectra for $(NH_3)_x$ and $(ND_3)_x$ obtained from the subtraction procedures based on the reference wavenumbers given and based on the spectra given in Figure 4.1 are shown in the top panels of Figure 4.2. The spectral analysis for the 2330-500 cm^{-1} spectral region, obtained for solutions that, due to the strong infrared intensity of the monomer band, are diluted by a factor of approximately 5 are given in the lower panel. In agreement with the above observations, intense oligomer features, shown in trace c, are observed in the N–H and N–D stretching areas. In addition, weaker features not immediately obvious from Figure 4.2 are also present in the regions of the combination bands and of the NH_3 bending mode ν_2.

It should be stressed that because of the underlying nature, the subtraction procedures described above allow estimating the total spectrum of the self-associated species, but do not allow the accurate determination of the individual contributions due to the different species present. A more thorough analysis of the spectral data available therefore requires more rigorous approaches including, e.g. the least-squares fitting methodology recently developed.

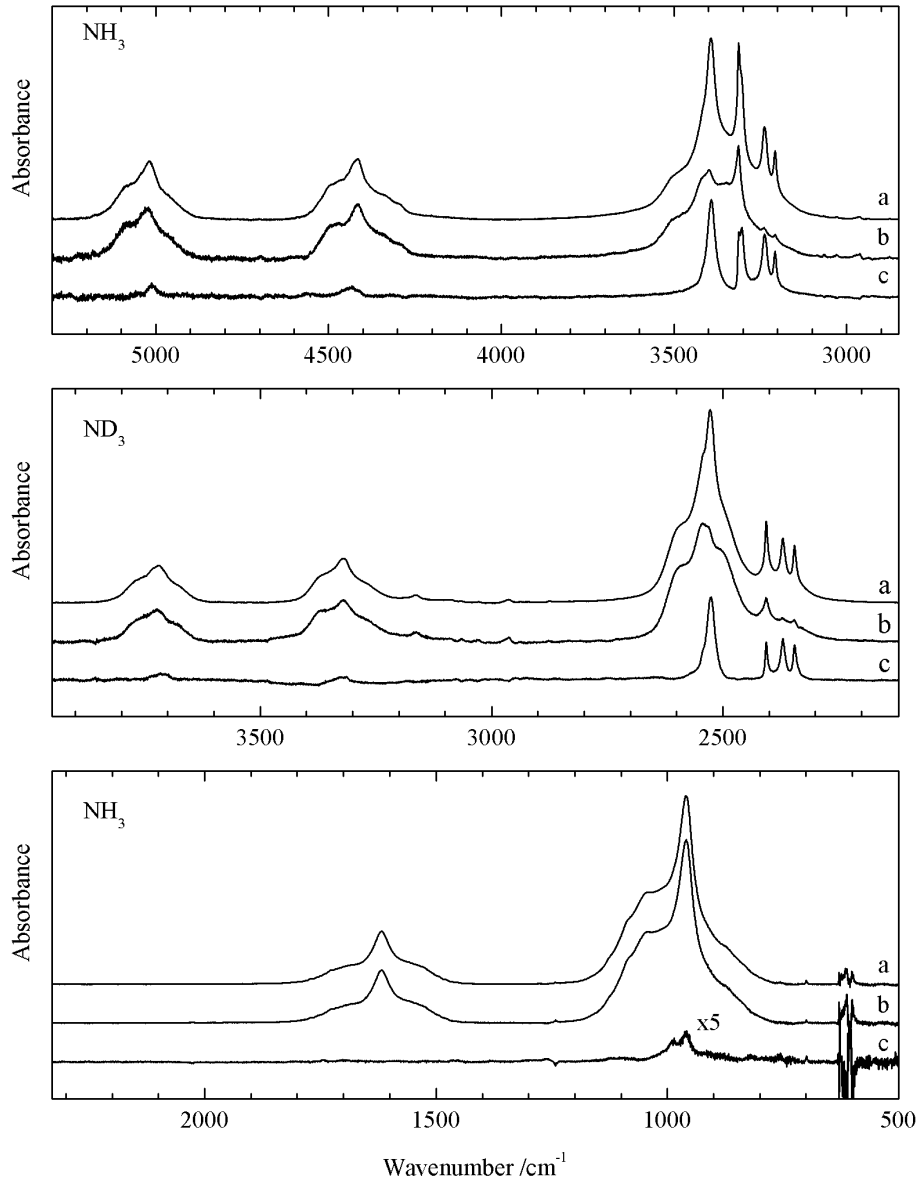

Figure 4.2 Subtraction procedure involving an original spectrum of a concentrated solution of NH_3 and ND_3 in LXe, trace a, and a rescaled spectrum of a highly diluted solution recorded under the same conditions, trace b. The result of the subtraction showing the summed contributions of the different oligomers present is given in trace c.

4.3.3 Separating monomer and oligomer contributions

Figure 4.3A and 4.3B show the results obtained by using polynomial regression with added nonnegative constraints, using the minimum value of the *BIC* to select the appropriate polynomial degree for every wavenumber. The selection is made between polynomials of 0^{th} to 5^{th} degrees, allowing all contributions up to pentamer to be included. Comparison of the results based on the least-squares fitting procedure and those derived from the subtraction procedures shows that, in general results are comparable. However, more detailed information about the origin of the oligomeric features can be obtained with the numerical methods.

The N–H stretch has been shown to be most sensitive to the formation of N–H···N hydrogen bonded clusters and this region was studied.[16] The presence of the changing water band around 3500-3100 cm^{-1} prevents a reliable fitting of the polynomials in the N–H stretching region. The results shown in Figure 4.3A assign the found oligomer features only to dimers and pentamers and not to trimers and tetramers. This seems very unlikely and does not compare with the results from earlier observations in solid matrices[18-20] and liquid helium droplets[16], illustrated in Table 4.1. Furthermore, these features are also not compatible with the results for ND_3, which are discussed in the next paragraph.

As the water band does not overlap with the ND_3 stretching regions and analysis allows contributions due to dimer and trimer species to be reliably characterized. The absorption bands are resolved in dimer contributions at 2529, 2406, 2370 and 2346 cm^{-1} and trimer features at 2541, 2519, 2369 and 2343 cm^{-1}. Moreover, a feature due to a tetramer is calculated to appear near 2507 cm^{-1}. Inspection of the data obtained with limited literature data summarized in Table 4.2 shows that for both the dimer and the trimer, good agreement is observed between the wavenumbers derived from the cryosolutions and those derived from the solid argon matrices by Süzer and Andrews[18].

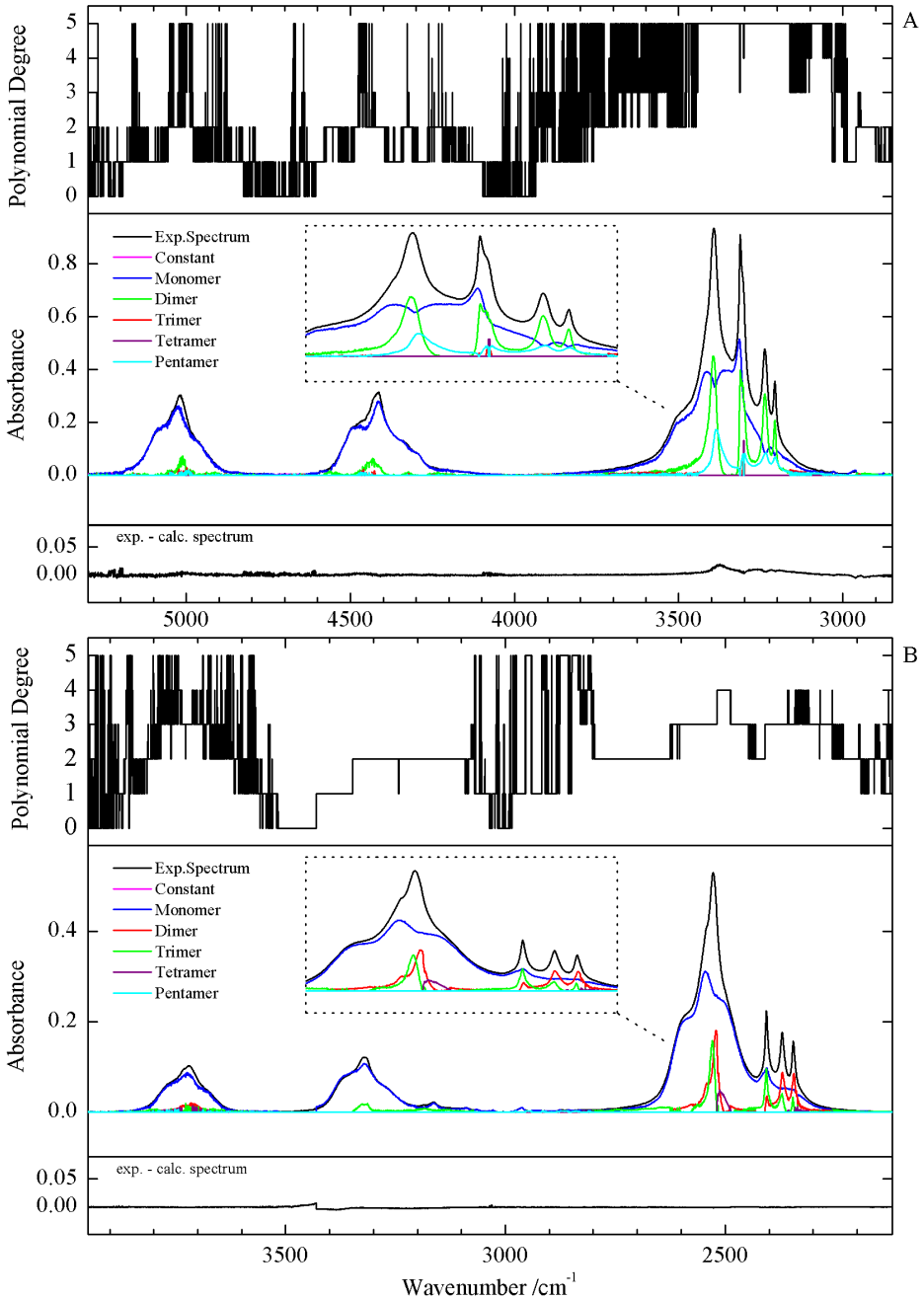

Figure 4.3 The results for the 5300-2850 cm^{-1} region of NH_3 (A) and the 3950-2100 cm^{-1} region of ND_3 (B) obtained by analyzing the experimental data with polynomial regression with added nonnegative constraints, using the minimum value the *BIC* to select the appropriate polynomial degree varying between 0 and 5 for every wavenumber. The bottom panel shows the difference between the experimental and calculated spectrum. The N–H and N–D stretching areas are magnified in the insert.

As illustrated in Figure 4.3A and 3B, for the combination bands $\nu_1+\nu_4$, $\nu_3+\nu_4$ and $\nu_1+\nu_2$, $\nu_3+\nu_2$ for NH_3 and for ND_3 absorption bands can be assigned to dimers. Apart from these features, additional, weaker traces due to a trimer are also present in three of the regions. Unfortunately, the limited signal-to-noise ratio due to low intensities and, consequently, low absorbances, make an unambiguous assignment of these trimer bands impossible.

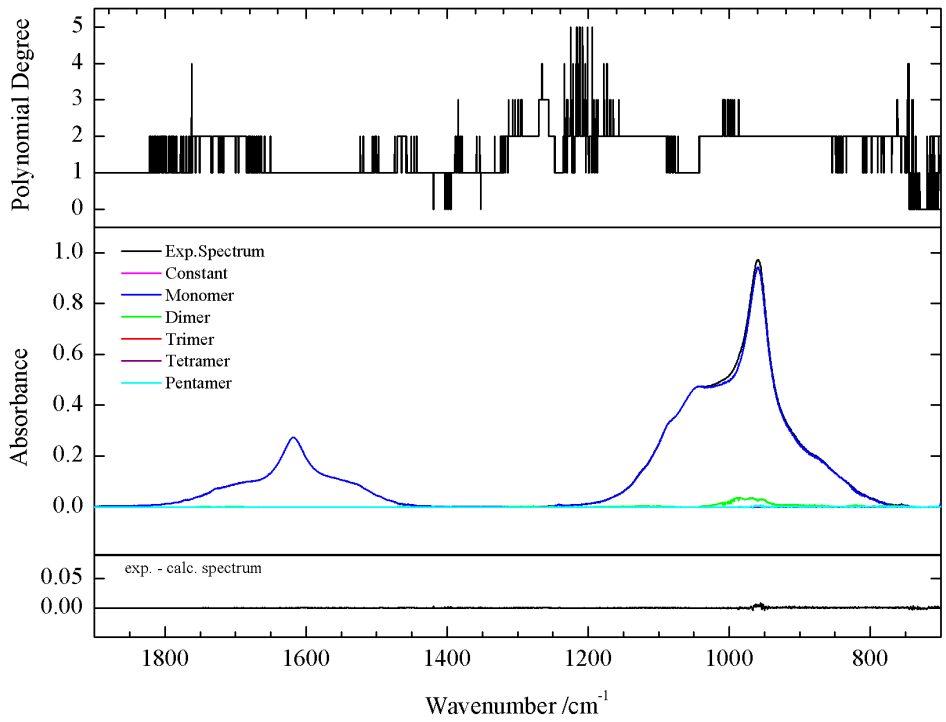

Figure 4.4 The results for the 1900-775 cm^{-1} region of NH_3 obtained by analyzing the experimental data with polynomial regression with added nonnegative constraints, using the minimum value the *BIC* to select the appropriate polynomial degree varying between 0 and 5 for every wavenumber. The bottom panel shows the difference between the experimental and calculated spectrum.

Figure 4.4 summarizes the results for the NH_3 bending vibration ν_2. The indicated results were obtained using a spectral database of only 85 spectra, i.e. using a database significantly smaller than that used for the other regions. The reason for this is related to the strong infrared intensity which, in combination with the characteristics of the MCT detector and the optical path length of 10 mm used does not allow accurate intensities to be measured for larger concentrations. Inspection of the data in Figure 4.4

clearly shows that in this spectral region, the measured spectra are largely dominated by the monomer contributions with origins at 1618 and 960 cm^{-1} for ν_4 and ν_2, the only feature illustrating the presence of higher associations being a weak dimer band around 970 cm^{-1}. The observed complex band derived from the polynomial regression using *BIC* selection matches quite well with that derived from the subtraction procedures. As illustrated in Table 4.1 the observed complexation shift is in line with the shifts reported by Suzer and Andrews.[18]

4.4 Conclusions

In this study we report on the analysis of isothermal spectra of NH_3 and ND_3 solutions in LXe using the newly developed and validated least-squares fitting of polynomials methodology. For both species we observe clear dimer bands in the spectral area of the $\nu_1+\nu_4$, $\nu_3+\nu_4$ and $\nu_1+\nu_2$, $\nu_3+\nu_2$ combination bands. There are also some weaker trimer signals but because of the limited signal-to-noise ratio due to low intensities and, consequently, low absorbances, it is impossible to make an unambiguous assignment. The analysis of N–D stretching area allowed us to characterize clear contributions of dimers and trimers. For NH_3 we also performed an investigation of the N–H bending region which demonstrated a small dimer absorption band.

In general the analyses are hampered by the occurrence of a time dependent band of solid water traces which was impossible to subtract as it overlaps with the N–H stretching region for NH_3 and the $\nu_1+\nu_2$, $\nu_3+\nu_2$ for ND_3. Therefore it was not possible to determine a reliable assignment for the oligomer signals in the N–H stretching region. The obtained results are in good comparison with literature data on ammonia clusters in solid matrices.

Table 4.1 Assignment of the monomer and resulting oligomer absorption bands of NH_3 in LXe at 203 K and a comparison with previous literature investigations.

Assignment	Experiment	Literature							
	Liquid Xe 203 K	Liquid Xe [11] 178K	Ar matrix[18]	Ar matrix [19]	Ar matrix[20]	Ne matrix	N_2 matrix[18]	N_2 matrix[19]	Liquid He droplets[16]
Monomer									
$\nu_1 + \nu_4(E)$, $\nu_3 + \nu_4(E)$	5026	5019	5047.5			5074.0, 5059.6	5043		
$\nu_1 + \nu_2(A_1)$, $\nu_3 + \nu_2(E)$	4415	4416	4450.1,4324.4			4466.7,4448.5*	4441,4319		
						4339.7,4319.2*			
$\nu_3(E)$		/	3447.3	/		3465.4, 3453.1*	3440.7	/	3443.1
$\nu_1(A_1)$		3312	3345.4	3329		3364.2, 3350.1*	3330.6	3330	3335.8
$2\nu_4(E)$		3236	3238.8	3239			3234.8	3235	3238.7
$2\nu_4(A_1)$		3206		/			3234.8		3216.1
$\nu_4(E)$	1618	1618	1638.9	1620		1644.7, 1643.1	1631	/	
$\nu_2(A_1)$	960	961	974.3	/		968.5, 960.9*	969.7	970	
Dimer									
$\nu_1 + \nu_4(E)$, $\nu_3 + \nu_4(E)$	5012								
$\nu_1 + \nu_2(A_1)$, $\nu_3 + \nu_2(E)$	4432		4423,4306				4416		
$\nu_3(E)$			3400.7	3421, 3400	3422.3, 3400.7, 3393	3418.8	3402.4	3427?, 3402	3441.5, 3431.2 3423.1, 3420.4
$\nu_1(A_1)$			3310.8	3325, 3310	3325.3, 3310.8	3320.2	3312.1	3312	3326.2, 3328.2, 3331.8, 3334.7
			3242.4	3242	3242.4, 3212.6	3253.3	3244.7	3244	
$2\nu_4(E)$									

$2\nu_4(A_1)$							3251
ν_4(E)		1631	1632	1631			
$\nu_2(A_1)$	970	999.8	1000	999.8	1003.6	1004 986	
Trimer							
$\nu_1 + \nu_4$(E), $\nu_3 + \nu_4$(E) $\nu_1 + \nu_2(A_1)$, $\nu_3 + \nu_2$(E)							
ν_3(E)		3391	3391	3413,3386		3391	3444.6,3433.3, 3403.0,3399.2
$\nu_1(A_1)$		3306	3304	3315, 3246	3310	3308	3316.5
		3236, 3212	3236, 3212	3242, 3219	3216,3240	~3230, ~3215	
$2\nu_4$(E)							3321.0
$2\nu_4(A_1)$							3256.5
ν_4(E)		1645	1645	1636	1013		
$\nu_2(A_1)$		1018	1018	1038		1014	
Multimer							
			3378 3296 3228 3202			3384	

*site splitting

Table 4.2 Assignment of the monomer and resulting oligomer absorption bands of ND_3 in LXe at 203 K and a comparison with previous literature investigations.

Assignment	Experiment	Literature	
	Liquid Xe 203 K	Ar matrix [18]	Ar matrix [20]
Monomer			
$\nu_1 + \nu_3$	4865		
$\nu_1 + \nu_4$(E), $\nu_3 + \nu_4$(E)	3724		
$\nu_1 + \nu_2(A_1)$, $\nu_3 + \nu_2$(E)	3321		
ν_3(E)	2545	2553	2548.5, 2543.8, 2527
$\nu_1(A_1)$	2406	2414	2410, 2373
$2\nu_4$(E)	/		2346.4
$2\nu_4(A_1)$	/		2340
ν_4(E)	1183	1190	1185
$\nu_2(A_1)$	770	760	781
Dimer			
$\nu_1 + \nu_4$(E), $\nu_3 + \nu_4$(E)			
$\nu_1 + \nu_2(A_1)$, $\nu_3 + \nu_2$(E)	3321		
ν_3(E)	2529	2527	
$\nu_1(A_1)$	2406	2410	
		2373	
$2\nu_4$(E)	2371		
$2\nu_4(A_1)$	2346		
ν_4(E)		1185	
$\nu_2(A_1)$		781	
Trimer			
$\nu_1 + \nu_4$(E), $\nu_3 + \nu_4$(E)			
$\nu_1 + \nu_2(A_1)$, $\nu_3 + \nu_2$(E)			
ν_3(E)	2541, 2519	2519	
$\nu_1(A_1)$	2405	2410(D+T)	
		2318, 2336	
$2\nu_4$(E)	2370		
$2\nu_4(A_1)$	2343		
ν_4(E)		1206	
$\nu_2(A_1)$		792	
Tetramer			
ν_3(E)	2505		

References

[1] W. Herrebout, Top. Curr. Chem., 358 (2015) 79-154.
[2] J. J. J. Dom, B. J. van der Veken, B. Michielsen, S. Jacobs, Z. F. Xue, S. Hesse, H. M. Loritz, M. A. Suhm and W. A. Herrebout, Phys. Chem. Chem. Phys., 13 (2011) 14142-14152.
[3] B. Michielsen, J. J. J. Dom, B. J. van der Veken, S. Hesse, M. A. Suhm and W. A. Herrebout, Phys. Chem. Chem. Phys., 14 (2012) 6469-6478.
[4] N. Nagels, Y. Geboes, B. Pinter, F. De Proft and W. A. Herrebout, Chem. Eur. J., 20 (2014) 8433-8443.
[5] D. Hauchecorne, R. Szostak, W. A. Herrebout and B. J. van der Veken, ChemPhysChem, 10 (2009) 2105-2115.
[6] D. Hauchecorne, B. J. van der Veken, A. Moiana and W. A. Herrebout, Chem. Phys., 374 (2010) 30-36.
[7] D. Hauchecorne, A. Moiana, B. J. van der Veken and W. A. Herrebout, Phys. Chem. Chem. Phys., 13 (2011) 10204-10213.
[8] Y. Geboes, N. Nagels, B. Pinter, F. De Proft and W. A. Herrebout, J. Phys. Chem. A, 119 (2015) 2502-2516.
[9] L. I. De Beuckeleer and W. A. Herrebout, Spectrochim. Acta A, 154 (2016) 89-97.
[10] W. A. Herrebout, S. M. Melikova, S. N. Delanoye, K. S. Rutkowski, D. N. Shchepkin and B. J. van der Veken, J. Phys. Chem. A, 109 (2005) 3038-3044.
[11] K. S. Rutkowski, W. A. Herrebout, S. M. Melikova, P. Rodziewicz, B. J. van der Veken and A. Koll, Spectrochim. Acta A, 61 (2005) 1595-1602.
[12] in MATLAB 8.3, The MathWorks Inc., Natick, MA, USA, 2014.
[13] B. J. van der Veken and F. R. De Munck, J. Chem. Phys., 97 (1992) 3060-3071.
[14] B. J. van der Veken, J. Phys. Chem., 100 (1996) 17436-17438.
[15] G. Schwarz, The Annals of Statistics, 6 (1978) 461-464.
[16] M. N. Slipchenko, B. G. Sartakov, A. F. Vilesov and S. S. Xantheas, J. Phys. Chem. A, 111 (2007) 7460-7471.
[17] F. P. Reding and D. F. Hornig, J. Chem. Phys., 19 (1951) 594.
[18] S. Suzer and L. Andrews, J. Chem. Phys., 87 (1987) 5131-5140.
[19] A. J. Barnes, J. Mol. Struct., 237 (1990) 19-32.
[20] J. P. Perchard, R. B. Bohn and L. Andrews, J. Phys. Chem., 95 (1991) 2707-2712.

Chapter 5

The self-associating behavior of pyrrole in liquid xenon

This chapter has been published as
De Beuckeleer, L. I.; Herrebout, W. A., *The self-associating behavior of pyrrole in liquid xenon*. J. Mol. Struct. 2016, 1108, 71-79.
doi:10.1016/j.molstruc.2015.11.067

Abstract

The self-associating behavior of pyrrole in liquid xenon was investigated by analyzing a data set of 185-113 infrared spectra obtained for different concentrations recorded at a constant temperature of 203 K. Analysis of the data using a recently developed least-squares approach allows the vibrational spectra of the monomer and of the different oligomers to be isolated. Apart from the monomer transitions, intense absorption bands originating from pyrrole trimers are observed in almost every spectral region including regions for which no data have yet been reported. Apart from these bands, weak features proving the presence of pyrrole dimer and pyrrole tetramer in the solutions are also reported. The weak character of the dimer bands observed and the low concentrations of these species deduced are explained by the fact that the cryosolutions studied are in chemical equilibrium and by the fact that due to strong cooperative effect present in the trimer, the complexation equilibria are strongly shifted towards the latter species, thereby strongly reducing the equilibrium concentrations of dimer and tetramer.

5.1 Introduction

Solutions in liquefied inert gases have become an ideal medium to investigate weakly bound molecular complexes. They create a weakly interacting environment which, combined with the low temperatures used, leads to small bandwidths and thus facilitates the detection of complex bands only slightly shifted from the monomer modes. The complexes studied so far mainly involve heterocomplexes involving, among others, a hydrogen or halogen bond interaction.[1-10] In addition, it has been possible to observe aggregates due to self-associating of molecules that simultaneously provide a hydrogen bond donor and acceptor group within their structure.

Whereas the analysis of spectra obtained for mixed solutions can be based on robust subtraction procedures in which spectra of the mixed solution are compared with spectra of the non-interacting monomers, the analysis of spectra of solutions containing self-associating species is more complicated. The reason for this is due to the fact that even for much diluted solutions, the spectra obtained often are determined by non-interacting monomers and by homocomplexes, thereby limiting the possibilities to accurately determine the spectra caused by the monomers only.

To overcome the limitation of the standard subtraction procedures used for heterodimers, we have recently developed least-squares fitting based methods in which, for each wavenumber studied, contributions due to monomers and the homocomplexes are isolated by analyzing the observed absorbances in an isothermal concentration series, and by fitting the data with a higher-degree polynomial mimicking the relations between monomer concentrations and measured absorbances. Validation experiments involving solutions of HCl in liquid argon [12] showed that by analyzing the differences between consecutive fittings and by introducing nonnegative constraints, the contributions due to monomers and self-associated species could be accurately resolved with a much higher accuracy than before. To further rationalize the possibilities and, eventually, limitations, of the methods developed, more testing involving other self-associating species is required. Therefore, in the current study, we expand the data set towards the self-associating model system, pyrrole (C_4H_4NH). The structure thus provides a compact donor N-H group and acceptor π-system in one molecule which can

lead to self-association trough one or more N-H···π hydrogen bonds. The choice of pyrrole as a third model systems is ideal because i) the pyrrole molecule is often considered a basic building block for a large family of important biomolecules [13-15] and references therein and ii) the self-association of the pyrrole monomers is well documented experimentally, in the gas phase [16-19], in traditional or less-traditional solvents including, *e.g.* CCl_4 and CCl_3F [20-22], and in solid matrices [11]. The different homocomplexes also have been thoroughly studied by density function theory calculations. [11,20]

It is worth noting that in most of the studies reported, the study of the vibrational spectra of pyrrole and its oligomers strongly focusses on the N-H stretch and the N-H out-of-plane bend [16,20-23], thereby limiting the analysis of data available in other spectral regions. An exception to these studies is the work of Gómez-Zavaglia *et al*. [11] These authors reported on the complete mid infrared spectrum of pyrrole trapped in solid argon and xenon matrices. Besides the assignment of the absorption bands of the pyrrole monomer, they successfully assigned a large number of absorption features related to pyrrole clusters up to tetramer. In the following paragraphs, experimental details on the self-associating behavior of pyrrole in solutions in liquid xenon at 183 K are reported. Inspection of the data shows that by using the recently developed polynomial regression based methods, spectral data due to monomer pyrrole and due to dimer and trimer species can be accurately resolved. The results support and expand the data on the solid matrices reported by Gómez-Zavaglia *et al*.[11] Apart from further validating the least-squares fitting approach, the analysis therefore also leads to a more complete characterization of the self-association in pyrrole and their effects on the vibrational spectra obtained.

5.2 Experimental section

Pyrrole (99,99%) was purchased from TCI Europe and was purified with a cold vacuum bulb to bulb distillation. The solvent gas, xenon, had a stated purity of 99.999% and was supplied by Linde.

A data set of 212 mid-infrared spectra of pyrrole in liquid xenon was recorded on a Bruker IFS 66v Fourier transform spectrometer. A Globar source was used in combination with a Ge/KBr beamsplitter and a LN_2-cooled broad band MCT detector. All interferograms were averaged over 500 scans, Blackman-Harris 3-term apodized and Fourier transformed with a zero filling factor of 4 to yield spectra with a resolution of 0.5 cm^{-1}. The experimental set-up used to investigate the solutions in liquid noble gases has been described before.[24] For all experiments, a liquid cell with 1 cm path length and equipped with wedged Si windows was mounted below a LN_2 dewar. The temperature of the cell body is measured using a Pt-100 thermoresistor. The SunRod electric minicartridge heater is controlled using a Eurotherm 3504 PID controller. The temperature of the solutions was stabilized at 203 K, the temperature variation during a typical run being less than 0.05 K. Spectra were obtained and preanalyzed using OPUS 6.5. Further calculations were performed using Matlab.[25]

The mole fractions of pyrrole used for the data sets are difficult to accurately quantify [26,27], but are estimated to vary between approximately 9.4×10^{-5} and 2.8×10^{-4}. The concentrations used are chosen so that the region between minimum and maximum absorbance is uniformly covered. Figure 5.2 shows different spectra of the gathered data set for the five spectra regions that were investigated. As the outcome of the used fitting procedures can largely depend on baseline artifacts, during all experiments, baseline corrections were performed using spectra of pure liquid xenon recorded at exactly the same conditions. Moreover, special attention was paid to remove spectral features by small water particles suspended in the solution, or condensation of water vapors onto the cold windows of the cryostat and the detector.

5.3 Results and discussion

5.3.1 Vibrational spectra

The pyrrole molecule has a C_{2v} symmetry point group that spans 24 fundamental vibrations. In the C_{2v} symmetry the *z*-axis is the axis of symmetry, but the choice of the *x*- and *y*-axis, hence the identification of the two planes in Table 5.1, is somewhat arbitrary. The lack of solid guidelines has manifested itself in literature two different

numbering schemes and different use of symmetry labels B_1 and B_2.[11,17,28-31] To avoid confusion, we followed the recommendations of Mulliken[32] and defined the *x*- and *y*-axis as stated in Figure 5.1. Using these conventions, also used by Herman and co-workers[30], the fundamental modes span the $9A_1 + 3A_2 + 4B_1 + 8B_2$ symmetries with all but three A_2 modes being active in the infrared. The modes are numbered according to descending degree of wavenumber in each symmetry block.

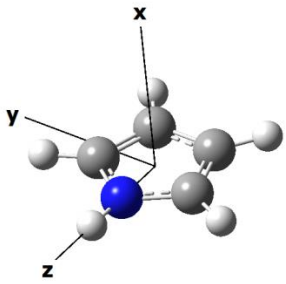

Figure 5.1 Illustration of the *xyz*-frame used to characterize the symmetry elements and irreducible representations of the pyrrole structure.

Table 5.1 Character Table of the C_{2v} symmetry point group with the defined planes of symmetry (the *xyz*-frame is defined in Figure 5.1).

C_{2v}	E	$C_2(z)$	$\sigma_v(xz)$	$\sigma_v(yz)$
A_1	1	1	1	1
A_2	1	1	-1	-1
B_1	1	-1	1	-1
B_2	1	-1	-1	1

Since all fundamental bands occur at wavenumbers above 450 cm^{-1} [11], all 21 infrared active modes could be observed under the experimental conditions used in this study. The typical spectral regions of the recorded data set of pyrrole, for which the assignments of monomer and oligomer absorption bands will be discussed in the following paragraphs, are given in Figure 5.2. In this figure it can easily be observed that upon increasing the solute concentration, new bands due to self-association emerge in every spectral region of the vibrational spectrum. The complete assignment, largely

based on the results reported for the gas phase and solid state[11,28,30], can be found in Table 5.2.

5.3.2 Least-squares fitting method

Recently, a polynomial regression approach to isolate overlapping absorption bands of monomeric and oligomeric species observed in the spectra of cryosolutions was developed and validated.[12] The method is based on the assumptions that the measured absorbance at a wavenumber $\tilde{\nu}_i$, $A_{exp}(\tilde{\nu}_i)$ is the sum of individual contributions related to the monomer, A_{mono} or to one of the oligomers, e.g. dimer A_{di}, trimer A_{tri}, tetramer A_{tetra}, etc., i.e.

$$A_{exp}(\tilde{\nu}_i) = A_{mono}(\tilde{\nu}_i) + A_{di}(\tilde{\nu}_i) + A_{tri}(\tilde{\nu}_i) + A_{tetra}(\tilde{\nu}_i) + \cdots \tag{5.1}$$

The experimental absorbances for each wavenumber $\tilde{\nu}_i$ originating from all contributing species in the solution are then expressed [12] as a function of the absorbance of a chosen monomer wavenumber $\tilde{\nu}_m$ with the polynomial degree p equal to 1, 2, 3, 4 or 5 with intercept equal to zero.

$$A_{exp}(\tilde{\nu}_i) = \sum_{p=1}^{n} a_{\mathrm{p}}(\tilde{\nu}_i, \tilde{\nu}_m)\,[A_{mono}(\tilde{\nu}_m)]^p \tag{5.2}$$

with the coefficient $a_{\mathrm{p}}(\tilde{\nu}_i, \tilde{\nu}_m)$ being a constant related to the equilibrium constant of the oligomerization reaction.[12] The monomer wavenumber $\tilde{\nu}_m$ is used as an internal standard and is chosen based on the fact that no features due to self-association are observed or expected to appear in the region considered. Moreover, special attention is paid to the fact that for all concentrations studied the absorbance can be accurately determined. In the case of pyrrole $\tilde{\nu}_m$ has been set at 3504.0 cm^{-1} as in this region the oligomer bands are well separated from the monomer transition.

To select the appropriate model at wavenumber $\tilde{\nu}_i$, the experimental data for a given wavenumber are least-squares fitted using a series of polynomials of 0^{th}, 1^{st}, 2^{nd}, 3^{rd}, 4^{th} and 5^{th} degree. Subsequently, the 'better' polynomial model is selected with the *BIC* information criterion, published by Schwarz [33] and defined as

$$BIC_p(\tilde{\nu}_i) = \mathrm{n} \cdot \ln\left(\frac{RSS_p(\tilde{\nu}_i)}{n}\right) + k \cdot \ln(n) \tag{5.3}$$

with n as the number of spectra in the data set which is equal to the number of measured data points for each wavenumber and k as the number of fitted parameters and with sum of squares *RSS*, defined as

$$RSS_p(\tilde{\nu}_i) = \sum_{k=1}^{n} [A_{exp,k}(\tilde{\nu}_i) - A_{calc,k}\,(\tilde{\nu}_i)]^2 \tag{5.4}$$

Here, we define the "better" model as the model that is parsimonious in the polynomial degree *p* and one that has a smaller residual sum of squares, *RSS*

Despite the model selection strategy, higher degree polynomials lead to compensation effects in which a large positive contribution is calculated for one of the species, and another strongly negative compensating feature is predicted for another. To avoid this kind of noise, nonnegative constraints were added, prohibiting the coefficients to become negative during the polynomial regression.

In the following paragraph the recorded data set will be analyzed by fitting a series polynomials with nonnegative constraints through the measured absorbance values for every wavenumber individually. The data for the different wavenumbers thus are completely independent. After selection of the appropriate polynomial degree using the *BIC*, the contributions for every wavenumber are calculated and combined and the isolated spectra of the species present in the solution are obtained without further smoothing. It should also be noted that when showing the results a value will be shown for the constant until pentamer contribution. If the selected degree does not allow a certain contribution the coefficient will be set to be zero resulting in a contribution equal to zero.

To get reliable results a spectral data set was put together for each spectral region individually, illustrated in Figure 5.2. This implies that for regions with higher intensities the data set will be smaller as the spectral data for the concentrated solutions is more likely to be influenced by the non-linearity of the detector, so that fitting of these data will yield unreliable results. In Figure 5.3-5.7 the experimental spectrum depicted always refers to the highest concentration used for the specific data set.

Because of the varying sizes of the data set, the spectra shown thus do not always belong to the same experimental spectrum.

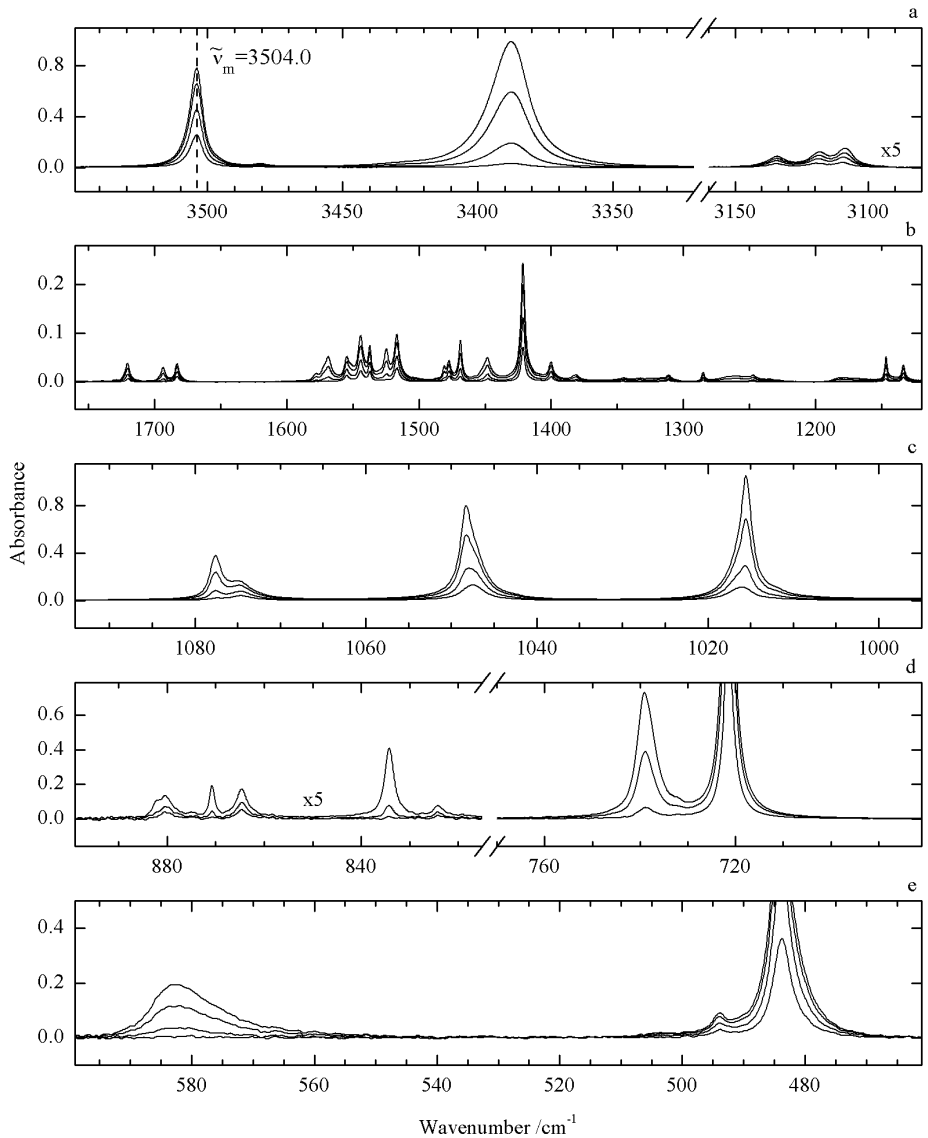

Figure 5.2 Infrared spectra of pyrrole in solutions with liquid xenon, at 183 K. The spectra shown represent only a small fraction of the spectral database used in the different fitting procedures. The spectra depicted in the different panels do not necessarily belong to the same spectra but are selected from the data sets put together for each region individually.

5.3.3 Monomer, dimer, trimer and tetramer spectra

Because the N-H stretch in pyrrole is quite sensitive to hydrogen bonding, its spectral region has already been well documented through jet [16], solution [20-22] and matrix-isolated studies [11]. Based on these experiments we expect the presence of signals related to monomers, dimers, trimers and possibly tetramers.[16,21] Figure 5.3 shows the results using the nonnegative constrained polynomial regression method with the *BIC* as selection criterion for the N-H stretching region using a data set of 174 spectra and the C-H stretching region using a data set of 185 spectra.

The data shows a narrow absorption band at 3504.0 cm^{-1} that can be assigned to the N-H stretching mode ν_1 of the pyrrole monomer. The wavenumber for this band is in excellent agreement with the data for solid xenon matrix studies which showed monomer features between 3504.6 and 3499.1 cm^{-1}. The data also compares relatively with the wavenumbers of 3523.0 and 3520.8 cm^{-1} derived from argon matrices.[11] The small monomer feature observed at 3480.5 cm^{-1} corresponds to the hot transition $\nu_1 + \nu_{16} - \nu_{16}$ originating in the low-wavenumber out-of-plane bending vibration ν_{16} at 483.9 cm^{-1}.[17]

The most striking band emerging due to self-associating of the compound is the intense broad band observed at 3387.5 cm^{-1}. This band is redshifted from the monomer by 116.5 cm^{-1}, and according to the least-squares fitting approach is largely due to the trimer. The redshift observed is in good agreement with the shift of -138 cm^{-1} observed for this species in jet experiments using helium or argon as carrier gasses [16] and with the shift of approximately -125 cm^{-1} reported for the argon matrices [11]. The most stable pyrrole trimer is predicted to have a C_{3h} symmetry in which every molecule acts simultaneously as a hydrogen bond donor and acceptor.[11] This structure leads to two degenerate (E') infrared-active stretching vibrations, which corresponds to out-of-phase or asymmetrical motions of the N-H bonds, and an in-phase or symmetrical (A') stretch that is symmetry forbidden in infrared, but noticeable in Raman experiments.[16] The appearance of a single absorption band with a wavenumber close to that observed in the gas phase and in the matrices, obviously, leads to the conclusion that also in the cryosolutions studied, the pyrrole trimer is characterized by a similar structure.

Inspection of the data in Figure 5.3 shows that apart from the band assigned to pyrrole trimer, a weak broad spectral feature between 3280 and 3470 cm^{-1} due to pyrrole tetramer is calculated to appear with its origin near 3375 cm^{-1}, i.e. at spectral region strongly overlapping with but slightly redshifted from the band assigned to pyrrole trimer. The appearance of weak spectral intensity due to the tetramer at the low wavenumber side of the pyrrole trimer band is in line with the data by Dauster *et al.*, showing that in the jet spectra obtained using argon as a carrier gas, the tetramer band is observed redshifted relative to the trimer [16] by 10 cm^{-1}.

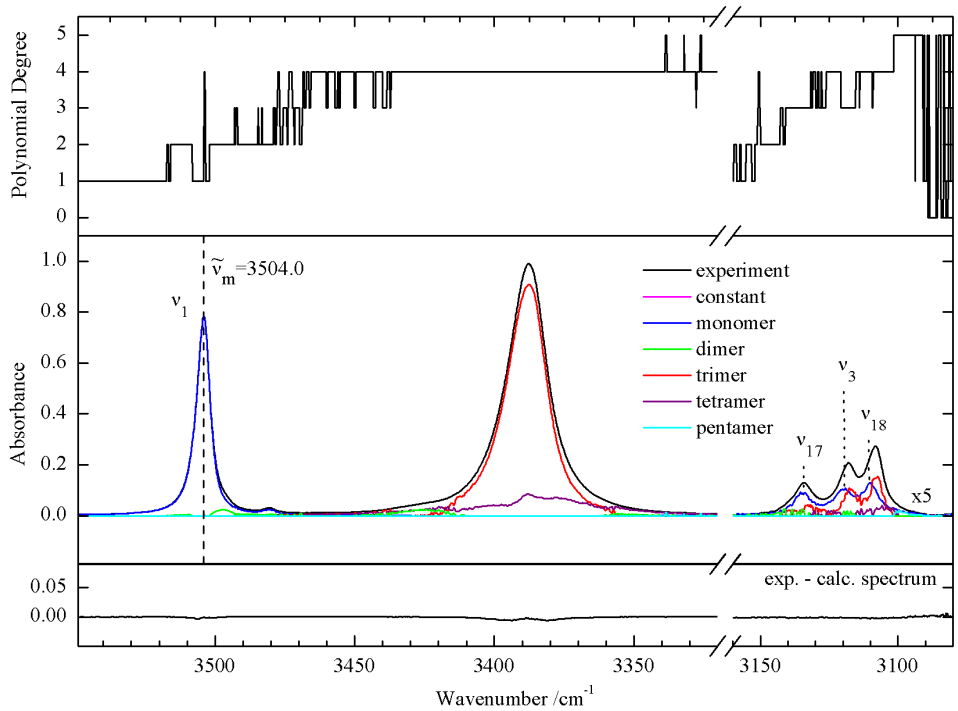

Figure 5.3 Results for the N-H and C-H stretching (absorbance x5) regions of pyrrole, obtained by analyzing the experimental data with polynomial regression with added nonnegative constraints, using the minimum *BIC* value to select the appropriate polynomial degree varying between 0 and 5 for every wavenumber. The reference wavenumber $\tilde{\nu}_m$ used as an internal standard for the pyrrole monomer concentration is indicated in with a dashed line. The bottom panel shows the difference between the experimental and calculated spectrum. Only the fundamental monomer transitions are named, the remaining transitions can be found in Table 5.2.

Except for the monomer, trimer and possible tetramer features, the analysis also identifies two weak dimer features at 3497.0 and ~3425 cm^{-1}, i.e. redshifted from the

monomer band by 7.0 and 79 cm^{-1}. The observed wavenumber shift of 7.0 cm^{-1} compares favorably with the data obtained in the gas phase jet expansion (7-5 cm^{-1}) [16] and solid matrix experiments (11-13 cm^{-1}) [11] for the acceptor N-H stretching mode and thus we assigned the 3497 cm^{-1} band to the non-interacting N-H stretch in the proton acceptor. In the gas phase and matrix-isolation experiments, the wavenumber of the donor N-H stretch is observed to show a downshift of 87, 96 [16] and 103-112 cm^{-1} [11], which is comparable with the observed wavenumber shift of 79 cm^{-1} observed above. As a consequence, this band was assigned to the donor N-H stretch in the pyrrole dimer. Further evidence for the assignment of the 3497.0 and ~3425 cm^{-1} bands was obtained by comparing the integrated band areas of the bands calculated with predicted infrared intensities, the main results obtained for the B3LYP/6-311++G(d,p) level[11] being 3588.0 cm^{-1} and 76.0 km mol^{-1} for the mode in the acceptor molecule and 3523.3 cm^{-1} and 329.6 km mol^{-1} for that in the donor molecule. Numerical integration of the bands at 3497.0 and 3425 cm^{-1} yield an experimental intensity ratio of approximately 0.36. Although the accuracy of this number might be somewhat doubted due to the weak nature of the bands involved, and although the calculated values do not allow to correct for effects due to anharmonicity or due to nearby solvent atoms, we consider this value to be in agreement with the value of 0.28 derived by comparing the calculated infrared intensities.

It is of interest to note that for all spectra obtained, the observed dimers bands have an intensity that is considerably smaller than that observed for the trimers. The weak character of the dimer bands observed is explained by the fact that, in contrast to the other techniques used before [11,16-18], the cryosolutions studied are in chemical equilibrium. Taking into account the large cooperative effects present in the trimer, it indeed is not surprising in solution the complexation equilibria are strongly shifted towards the trimer species thereby strongly reducing the equilibrium concentrations of dimer and tetramer.

In Figure 5.3 also the results for the C-H stretching region are presented. The plot shows that apart from the transitions near 3134.2, 3119.9 and 3110.2 cm^{-1} assigned to the C-H asymmetrical stretches ν_{17}, ν_3 and ν_{18}, of monomer pyrrole, new features due to the corresponding modes in the pyrrole trimer are present at 3132.3, 3117.0 and

3108.0 cm^{-1}, i.e. at a wavenumber slightly redshifted from the monomer modes. The observation of well-defined features due to monomer and trimer clearly shows that by using the least-squares fitting procedures new spectral features can be identified that, because of large overlap with the monomer transitions, largely escaped detection in previous studies [11]. The data for the C-H stretching mode, therefore clearly illustrates the added value and complementarity of the least-squares fitting method towards the other method often used. It might be noted that apart from the features assigned to ν_{17}, ν_3 and $\nu_{18,}$ spectral feature are also expected to appear for the fourth symmetrical C-H stretch $\nu_{2.}$ In agreement with the gas phase and the matrix-isolation data [11,28,30] and with the results from DFT calculations [11] showing that these modes are extremely weak both in the monomer and in the clusters, no features due to this mode were observed.

Figure 5.4 shows the results for the 1760-1120 cm^{-1} spectral region obtained by using a data set of 185 spectra. In this interval the monomer gives rise to 7 fundamental transitions [11], the C=C asymmetric and symmetric stretches, ν_{19} and ν_4, the C-N asymmetric stretch ν_{20}, the C-C stretch ν_5, the in-plane C-H asymmetric bend ν_{21}, the N-H in-plane bending vibration ν_6, and the breathing mode ν_{18}. These modes appear at 1537.1, 1468.8, 1421.3, 1400.1, 1285.0, 1147.4 and 1133.6 cm^{-1}, respectively. The remaining monomer features are assigned to combination bands and can be found in Table 5.2.

Least-squares fitting based analysis of the spectra shows that also for these modes, features due to dimer and trimer are calculated. It is of interest to note that in the studies reported earlier discussions of the changes in these spectral regions were kept concise, and that it was even concluded that in general the self-associating behavior hardly had an effect on the vibrational spectra of pyrrole.[20] The results reported in Figure 5.4, clearly show that this is not the case and confirms the above statement that least-squares fitting methods can lead to much more detailed information, and thus has a strong added value to the results presented in literature before. It must be noted that because multiple overlapping absorption bands and the low overall intensity some caution must be expressed while analyzing the data in the 1600-1500 cm^{-1} spectral region. For this reason we consider the appearance of the dimer bands in this region as somewhat tentative.

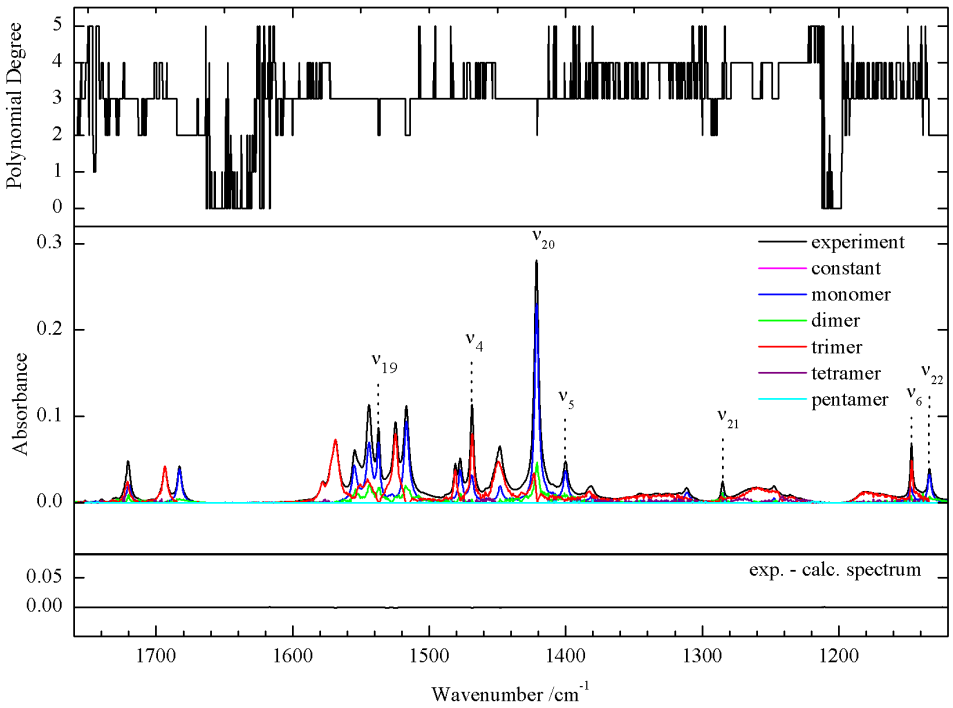

Figure 5.4 Results for the 1760-1120 cm^{-1} region of pyrrole, obtained by analyzing the experimental data with polynomial regression with added nonnegative constraints, using the minimum *BIC* value to select the appropriate polynomial degree varying between 0 and 5 for every wavenumber. The bottom panel shows the difference between the experimental and calculated spectrum. Only the fundamental monomer transitions are named, the remaining transitions can be found in Table 5.2.

In the 1100-1000 cm^{-1} spectral range, illustrated in Figure 5.5, we could assign two symmetric and one asymmetric in-plane C-H bending modes; ν_7, ν_8 and ν_{23}, respectively. With increasing concentration, as demonstrated in Figure 5.2 panel c, different features arise for each of these fundamental transitions. For the ν_{23} and ν_8 modes near 1047 and 1016 cm^{-1}, the emerging oligomer bands show complete overlap with the monomer absorption bands, causing a visual change of the band shape. For the ν_7 mode at 1074.6 cm^{-1} the oligomer band shows a larger wavenumber shift. Using the developed least-squares method and a data set of 113 spectra we can resolve the overlapping monomer and oligomer bands and perform a correct assignment. In Figure 5.5, all the overlapping bands are resolved and it can be seen clearly that ν_{23} and ν_8 both consist of a monomer and a trimer band that have only shifted for

approximately 1 cm^{-1}. Besides the magnitude of the shift, the behavior of the trimer bands also differs in the direction of the shift: ν_7 and ν_{23} are blue shifted, while the ν_8 mode experiences a small redshift. These observations are all in full agreement with matrix isolations experiments and calculations presented in previous literature studies.[11]

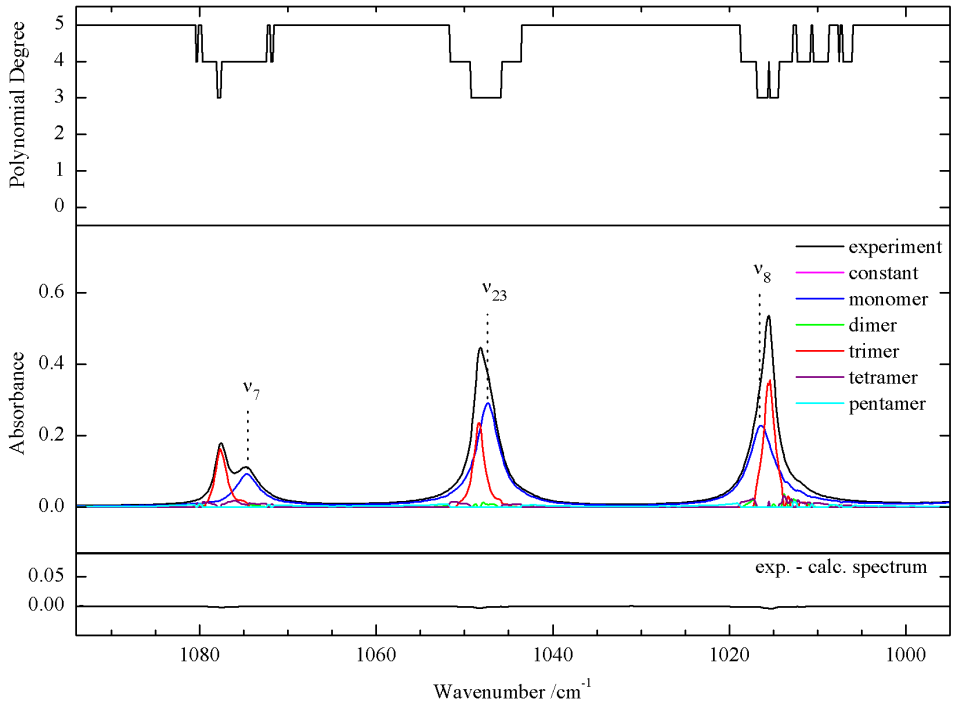

Figure 5.5 The results for the C-H in-plane bending region of pyrrole, obtained by analyzing the experimental data with polynomial regression with added nonnegative constraints, using the minimum *BIC* value to select the appropriate polynomial degree varying between 0 and 5 for every wavenumber. The bottom panel shows the difference between the experimental and calculated spectrum. Only the fundamental monomer transitions are named, the remaining transitions can be found in Table 5.2.

An interesting observation shown in the upper panel of Figure 5.5 is the high polynomial degree selected by the analysis for the low intensity wavenumbers. We assume that this is related to but very low intensity, but nonzero, nature observed at these wavenumbers, making it rather impossible to fit the data with the correct polynomial model. To improve fitting, it might be of interest to record additional spectra at higher or lower concentrations. However, adding such data would require the use of different liquid cells with different, larger or smaller, optical path lengths.[24]

Such approach, unfortunately, is strongly hampered by the requirement that in order to reliably predict the contributions of the different species present with the numerical procedures used, all spectra must be recorded using exactly the same optical path length and at exactly the same temperature. Such conditions, obviously, are not possible if data obtained using different liquid cells are combined.

The results from the least squares fitting procedures for the 890-680 and 600-460 cm^{-1} regions, analyzed with data sets of 185 and 124 spectra respectively, shown in Figure 5.2d-e are summarized in Figure 5.6 and 5.7. For monomer pyrrole, bands due to the C-N-C in-plane bending mode ν_9, the C-C-C in-plane asymmetric bending mode ν_{24}, the asymmetric and symmetric out-of-plane C-H bending modes ν_{13} and ν_{14}, and the out-of-plane N-H bending ν_{16}, were assigned at 880.6, 864.6, 824.2, 721.6 and 484.0 cm^{-1} respectively. Although the mode has B_1 symmetry and should in principle be infrared active, the asymmetric ring torsion ν_{15} was not observed. The absence of this vibration mode agrees with literature data [11,28,30].

The results of polynomial regression using the *BIC* for the full data set of 185 spectra are presented in Figure 5.6. For both ν_{24} and ν_{13} a trimer band appears strongly blue shifted and isolated from the monomer band. In the case of $\nu_{9,}$ oligomeric band with a blue shift of only 2 cm^{-1} and strongly overlapping with the monomer band is predicted for the pyrrole dimer

The most intense fundamental mode in the pyrrole vibrational spectrum in Figure 5.6 is the symmetric out-of-plane C-H bending mode ν_{14}. The presence of oligomers in the solution causes the appearance of an intense absorption band blue shifted from the 721.6 cm^{-1} monomer band. Because the database of pyrrole was developed by focusing on a good coverage of the ν_1 absorption band, which has a lower intensity, and because the detector in the 800-400 cm^{-1} has found to behave linearly below an absorbance of 0.6, only spectra showing an absorbance smaller than 0.6 for the complex bands were used. The selection gave a set of 124 spectra in which the absorbances of the complex bands were below the set limit. For all spectra used, the absorbance of the more intense monomer band near 721.6 cm^{-1} was noted to exceed the limit between from approximately 723.2 to 719.9 cm^{-1}. Although results for this region were obtained during the fitting procedures, these data were omitted from the data presented. The most

striking oligomer feature in Figure 5.6 is the intense blue shifted trimer band at 738.9 cm^{-1}. Its wavenumber shift of 17.3 cm^{-1} compares well with the 11.7-12.7 cm^{-1} shift of the Xe matrix experiments. In addition, the appearance of weak band was noticed between the monomer and trimer band, near ~732cm^{-1} with a wavenumber blue shift of ~10.4 cm^{-1}. Based on the results of a matrix isolation study [11] this band can be assigned to the symmetric out-of-plane C-H bending mode of the dimer, as the blue shift in the solid matrix being close to 9 cm^{-1}. However, this assignment is not clearly confirmed in Figure 5.6.

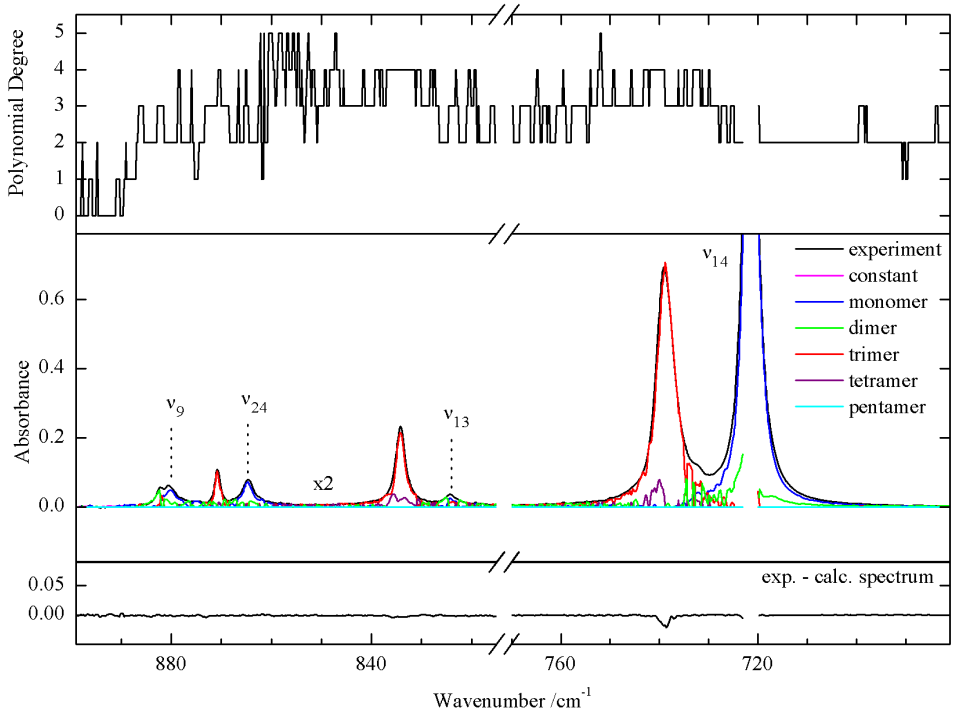

Figure 5.6 The results for the 810-900 and 770-680 cm^{-1} regions of pyrrole, obtained by analyzing the experimental data with polynomial regression with added nonnegative constraints, using the minimum *BIC* value to select the appropriate polynomial degree varying between 0 and 5 for every wavenumber. The bottom panel shows the difference between the experimental and calculated spectrum. Only the fundamental monomer transitions are named, the remaining transitions can be found in Table 5.2.

Apart from the 732.4 cm^{-1}, band tentatively assigned to the symmetric out-of-plane C-H bending mode of the dimer, it should in principle be possible to also characterize the corresponding asymmetric out-of-plane C-H bending mode of the dimer. This band has been observed in solid xenon to appear at a wavenumber approximately 2 cm^{-1} blue

shifted from the monomer transition. The analysis shows the start of a dimer feature close to the origin of the monomer band that indeed can be caused by a dimer acceptor band. Due to the restrictions noted above, this assignment cannot be fully confirmed with the current model.

Finally the suggestion of the tetramer contribution to appear at 740.8 cm^{-1} is also an interesting feature, as this observation shows resemblance with the matrix results by Gómez-Zavaglia [11].

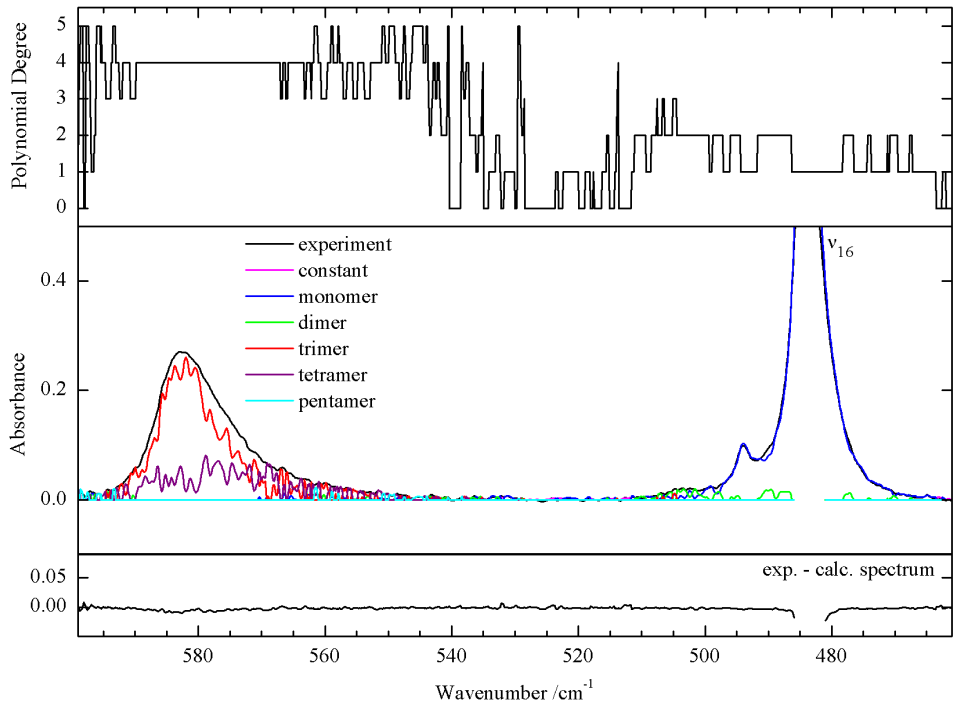

Figure 5.7 Results for the out-of-plane N-H bending region of pyrrole, obtained by analyzing the experimental data with polynomial regression with added nonnegative constraints, using the minimum *BIC* value to select the appropriate polynomial degree varying between 0 and 5 for every wavenumber. The bottom panel shows the difference between the experimental and calculated spectrum. Only the fundamental monomer transitions are named, the remaining transitions can be found in Table 5.2.

Because the participation of the N-H bond in the N-H···π interaction, the N-H out-of-plane bending mode, ν_{16}, like the N-H stretching mode, is also expected to be quite sensitive to the formation of hydrogen bonding in the pyrrole oligomers, causing a large wavenumber shift for oligomer bands. For the analysis the full data set of 185 spectra was used but because of the limitation of the detector in the 800-400 cm^{-1} region the

result between 485-482 cm^{-1}, where the absorbance is higher than 0.6, is left out. The wavenumber of this mode in the monomer was found to be 484.0 cm^{-1}. On the shoulder of this absorption band there is a second monomer feature at 493.9 cm^{-1} that can be assigned the $3\nu_{16}$-$2\nu_{16}$ exited state of the ν_{16} transition. Figure 5.2e shows that with increasing concentration a broad band arises at 583.0 cm^{-1}, with a large blue shift of 99.0 cm^{-1}. According to the results of the least-squares fitting with nonnegative constraints, illustrated in Figure 5.7, this band is originating from trimers in the solution. This observation is in agreement with matrix isolation studies that resulted in a trimer band with a blue shift at around 100 cm^{-1}.[11] In the latter study the "free" N-H group of the hydrogen bond acceptor molecule of the dimer gives rise to an out-of-plane vibration blue shifted by approximately 30 cm^{-1}. The analysis of the data set in Figure 5.7 indicates the presence of a dimer transition at 504.0 cm^{-1}, with a blue shift of 20.0 cm^{-1}. Taking into account the difference in surrounding between the use of xenon as a solid and as a liquid solvent in our experiment, we assigned the 504.0 cm^{-1} absorption band to the acceptor molecule. The second dimer transition for this region, originating from N-H out-of-plane bending vibration, was not be observed in the matrix experiments and was not assigned in the cryosolution spectra .

Inspection of the data in Figure 5.7 shows that apart from the band assigned to pyrrole trimer, a weak broad spectral feature due to pyrrole tetramer is also calculated to appear in approximately the same region. The appearance of weak spectral intensity due to the tetramer at the low wavenumber side of the pyrrole trimer band is in line with the data by Gómez-Zavaglia *et al*., showing that for solid matrices, the tetramer band is observed blue shifted relative to the trimer [16] by approximately 10 to 15 cm^{-1}.

Table 5.2 Assignment of the monomer and resulting oligomer absorption bands of pyrrole in solution with xenon at 183 K and a comparison with previous literature investigations.[a]

Assignment	Experiment						
	Monomer			Oligomer			
Based on [11,28,30]	Liquid Xe 183 K	Xe matrix[11] 9 K	Ar matrix[11] 9 K		Liquid Xe 183 K	Xe matrix[11] 9 K	Ar matrix[11] 9 K
$\nu_1(A_1)$	**3504.0**	3504.6/3500.6/3499.1	3523.0/3520.8	D	**3497.0**		3510
				D	**~3425**		3418/3409
				T	**3387.5**		3396
				Te	**~3375**		3378
$\nu_1 + \nu_{16} - \nu_{16}$ hb	**3480.5**						
$\nu_2(A_1)$	**n.o.**		n.o.	T	**n.o.**		
$\nu_{17}(B_2)$	**3134.2**		~3134.8	T	**3132.3**		
$\nu_3(A_1)$	**3119.9**		~3119.4	T	**3117.0**		
$\nu_{18}(B_2)$	**3110.2**		3109.8	T	**3108.0**		
$2\nu_{10}(A_1)$	**1720.0**	1719.1	1721.9	T	**1720.9**		
$\nu_{10} + \nu_{13}(B_2)$	**1682.9**	1681.8	1684.8	T	**1693.5**		
$\nu_{10} + \nu_{11}(A_1)$	**1554.8**	1555.9	1556.8				
$\nu_{13} + \nu_{14}(A_1)$	**1544.0**	1545.7/1543.3	1545.6				
$\nu_{19}(B_2)$	**1537.1**	1537.8/1536.1	1539.1	T	**1524.6**		1520
$\nu_{11} + \nu_{13}(B_2)$	**1516.6**	1517.3	1521.0/1518.8/1517.6				
$\nu_{10} + \nu_{12}(A_1)/\nu_4(A_1)$ FR	**1477.2**	1477.3	1479.5	T	**1480.9**		
$\nu_4(A_1)/\nu_{10} + \nu_{12}(A_1)$ FR	**1468.8**	1471.1/1468.8	1472.7/1471.0/1469.8	T	**1468.5**		
$2\nu_{14}(A_1)$	**1448.2**	~1448.7	1450.2	T	**1449.2**		
$\nu_{20}(B_2)$	**1421.3**	1425.0/1421.3	1425.8/1423.5				
$\nu_5(A_1)/2\nu_{11}(A_1)$ FR	**1400.1**	1400.8	1401.9				

$2\nu_{11}(A_1)/\nu_5(A_1)$ FR	**1381.0**	1381.1	1382.6				
$\nu_{11}+\nu_{12}(A_1)$	**1311.4**	1312.7	1312.3				
$\nu_{21}(B_2)$	**1285.0**	1286.0/1284.4	1285.6	T	**1260.7**		1267
$\nu_6(A_1)$	**1147.4**	1146.6	1149.0	T	**1146.7**		1146.6
$\nu_{22}(B_2)$	**1133.6**	1133.9	1136.7				
$\nu_7(A_1)$	**1074.6**	1074.6	1076.2	T	**1077.6**	1083/1081 Agr	1079
$\nu_{23}(B_2)$	**1047.4**	1047.7/1046.7	1048.5	T	**1048.3**	1050/1051 Agr	1049
$\nu_8(A_1)$ [b]	**1016.4**	1023.5/1018.9/1016.4	1017.2	T	**1015.5**	1015/986 Agr	1016
$3\nu_{16}-\nu_{16}(A_1)$	**990.0**	993.0/980.7	995.9/997.9				
$2\nu_{16}(A_1)$ [b]	**977.5**		976.0/974.3				
$\nu_9(A_1)$	**880.6**	880.2	881.0	T	**882.3**	882 Agr	883 Agr
$\nu_{24}(B_2)$	**864.6**	864.4	865.3	T	**870.7**	867	869
$\nu_{10}(A_2)$	**n.o.**	n.o.	n.o.	T			
$\nu_{13}(B_1)$	**824.2**	824.9	826.6/825.0	T	**834.2**	832	835/838
$\nu_{14}(B_1)$	**721.6**	722.3/721.3	725.4/721.9	Te	**740.8**	738	752
				T	**738.9**	734	744
				D	**~732**	731	738
				D	**n.o.**	723	725
$\nu_{11}(A_2)$	**n.o.**	n.o.	n.o.				
$\nu_{15}(B_1)$	**n.o.**	n.o.	n.o.				
$\nu_{12}(A_2)$	**n.o.**	n.o.	n.o.				
$3\nu_{16}$-$2\nu_{16}(B_1)$	**493.9**						
$\nu_{16}(B_1)$	**484.0**	493.6/491.6/488.5/ 485.6/483.4	483.7/483.0/481.9	Te		593/589	590
				T	**583.0**	583	570
				D	**n.o.**	n.o.	560
				D	**504.0**	514	509

[a] n.o., not observed; hb, hotband, FR, Fermi resonance; M=monomer; D=dimer; T=trimer; Te=Tetramer; H=higher order aggregates; Agr= M,T,Te,H.

[b] the ν_8 transition is described as a FR with $2\nu_{16}$ by Fausto *et al.* [11]

5.4 Conclusions

The self-associating behavior of pyrrole is observed through the complete mid infrared spectrum of a solution in liquid xenon. The assignments of the monomer vibrational modes closely follow those reported previously for the pyrrole in the gas and solid phase.[11,28]. Clear intense absorption bands originating from pyrrole trimers are present in every spectral region, but bands indicating the presence of dimers and tetramers are scarce and weak. The absence of dimer signals is surprising, as they have been observed in the gas phase and solid phase in previous literature investigations, but it suggest that at chemical equilibrium the strong cooperative effects in the trimer cause dimers to pick up an extra pyrrole unit to create the more stable trimer and consequently keep the dimer concentration low. In jet or in matrices dimer signals are more intense as the nonequilibrium state allows a higher dimer concentration then in solution. The assignment of tetramer bands is tentative given that comparable literature data is rather scarce [11,16]. All in all, the current results obtained with the newly developed least-squares method are consistent with matrix isolation experiments in liquid argon and xenon and density functional theory calculations [11] but also add many oligomer signals that have not yet been reported before. Analyzing the pyrrole data showed the added valued of least-squares approaches in the resolving data of larger and more complicated self-associating systems.

References

[1] Y. Geboes, F. Proft and W. A. Herrebout, J. Phys. Chem. A, 119 (2015) 5597-5606.
[2] Y. Geboes, N. Nagels, B. Pinter, F. De Proft and W. A. Herrebout, J. Phys. Chem. A, 119 (2015) 2502-2516.
[3] D. Hauchecorne, R. Szostak, W. A. Herrebout and B. J. van der Veken, ChemPhysChem, 10 (2009) 2105-2115.
[4] B. Michielsen, W. A. Herrebout and B. J. van der Veken, ChemPhysChem, 8 (2007) 1188-1198.
[5] D. Hauchecorne, A. Moiana, B. J. van der Veken and W. A. Herrebout, Phys. Chem. Chem. Phys., 13 (2011) 10204-10213.
[6] D. Hauchecorne, B. J. van der Veken, A. Moiana and W. A. Herrebout, Chem. Phys., 374 (2010) 30-36.

[7] B. Michielsen, J. J. J. Dom, B. J. van der Veken, S. Hesse, Z. F. Xue, M. A. Suhm and W. A. Herrebout, Phys. Chem. Chem. Phys., 12 (2010) 14034-14044.
[8] B. Michielsen, W. A. Herrebout and B. J. van der Veken, ChemPhysChem, 9 (2008) 1693-1701.
[9] J. J. J. Dom, B. Michielsen, B. U. W. Maes, W. A. Herrebout and B. J. van der Veken, Chem. Phys. Lett., 469 (2009) 85-89.
[10] S. N. Delanoye, W. A. Herrebout and B. J. van der Veken, J. Phys. Chem. A, 109 (2005) 9836-9843.
[11] A. Gómez-Zavaglia and R. Fausto, J. Phys. Chem. A, 108 (2004) 6953-6967.
[12] L. I. De Beuckeleer and W. A. Herrebout, Spectrochim. Acta A, 154 (2016) 89-97.
[13] H. Fischer, *Akademische Verlag: Die Chemie Des Pyrrols*, Leipzig, 1934, 1937, 1940, Vol. I.
[14] K. Kushwaha, C. C. Malakar, S. Stas, F. Lemière and K. Abbaspour Tehrani, RSC Adv., 5 (2015) 10139-10151.
[15] T. Tsuchimoto, Chemistry, 17 (2011) 4064-4075.
[16] I. Dauster, C. A. Rice, P. Zielke and M. A. Suhm, Phys. Chem. Chem. Phys., 10 (2008) 2827-2835.
[17] A. Mellouki, R. Georges, M. Herman, D. L. Snavely and S. Leytner, Chem. Phys., 220 (1997) 311-322.
[18] Y. Matsumoto and K. Honma, J. Chem. Phys., 127 (2007) 184310.
[19] G. Columberg and A. Bauder, J. Chem. Phys., 106 (1997) 504.
[20] V. Stefov, L. Pejov and B. Šoptrajanov, J. Mol. Struct., 649 (2003) 231-243.
[21] M.-C. Bernard-Houplain and C. Sandorfy, Can. J. Chem., 51 (1973) 1075-1082.
[22] W. T. Grubbs, T. P. Dougherty and E. J. Heilweil, J. Phys. Chem., 99 (1995) 10716-10722.
[23] S. Sun, H. Tang and P. Wu, Phys. Chem. Chem. Phys., 11 (2009) 7611.
[24] W. Herrebout, Top. Curr. Chem., 358 (2015) 79-154.
[25] MATLAB 8.3, The MathWorks Inc., Natick, MA, USA, 2014.
[26] B. J. van der Veken and F. R. De Munck, J. Chem. Phys., 97 (1992) 3060-3071.
[27] B. J. van der Veken, J. Phys. Chem., 100 (1996) 17436-17438.
[28] T. D. Klots, R. D. Chirico and W. V. Steele, Spectrochim. Acta A, 50 (1994) 765-795.
[29] V. Barone, Chem. Phys. Lett., 383 (2004) 528-532.
[30] A. Mellouki, J. Liévin and M. Herman, Chem. Phys., 271 (2001) 239-266.
[31] M. Epshtein, A. Portnov, N. Mayorkas, S. Rosenwaks, B. Brauer and I. Bar, J. Phys. Chem. A, 117 (2013) 11618-11623.
[32] R. S. Mulliken, J. Chem. Phys., 23 (1955) 1997.
[33] G. Schwarz, The Annals of Statistics, 6 (1978) 461-464.

Chapter 6

The Self-Associating Behavior of Acetone in Liquid Krypton

This chapter has been published as

De Beuckeleer, L. I.; Herrebout, W. A., *The Self-Associating Behavior of Acetone in Liquid Krypton*, J. Phys. Chem. A, 2016, doi: 10.1021/acs.jpca.5b10405

Abstract

Acetone molecules are inclined to self-associate through dipole-dipole interactions because of their large dipole moment. Infrared spectroscopy of compounds dissolved in liquid noble gases supported by high level *ab initio* calculations allows investigating the self-associating behavior and determining the thermodynamical properties. In this study, infrared spectra of various concentrations of acetone dissolved in liquid krypton are recorded at constant temperature. Overlapping monomer and dimer spectra are separated by analyzing the obtained data set with numerical methods based on least-squares fitting. Although acetone is known to self-associate, only a few spectral features have been presented in literature before. In this study, the application of new numerical approaches succeeds in resolving overlapping spectra and allows observing isolated acetone dimer absorption bands for the complete mid infrared spectrum. By use data set of spectra recorded at temperatures between 134 and 142 K, the experimental standard dimerization enthalpy was determined to be -10.8 kJ mol^{-1}. MP2/aug-cc-pVDZ calculations predicted a stacked and planar dimer geometry of which the stacked geometry is more stable. Combining MP2 energies and single point corrections involving CCSD(T) calculations and Complete Basis Set extrapolations based on the MP2/aug-cc-pVDZ equilibrium geometry lead to complexation energy of -28.4 kJ mol^{-1} for the stacked geometry and -15.1 kJ mol^{-1} for the planar geometry. The corresponding values for the complexation enthalpies in solution, obtained by combining these values with corrections for thermal and solvent influences are -13.7 and 5.8 kJ mol^{-1}.

6.1 Introduction

Because of their large dipole moment[1], acetone molecules are inclined to interact with each other through long range dipole-dipole interactions and short-range C-H···O hydrogen bonding interactions. As a result, the properties of acetone dimers have been the subject of various studies. Early evidence for the self-association of acetone and other ketones was reported by Lin and co-workers.[2] These authors investigated the self-association of acetone, 2,3-butanedione and acetylacetone in carbon tetrachloride and hexadecane solutions by partition, solubility and isopiestic techniques, and estimated the equilibrium constants for the dimerization reaction at 15 and 25°C. The complexation enthalpy for dimerization of acetone in hexadecane was derived to be -11.7 kJ mol^{-1}. Additional evidence supporting the idea of self-association of acetone in the liquid and in the vapor phase was reported by Frurip *et al.*[3] These authors measured the thermal conductivity of acetone vapor at temperatures between 341 and 378 K over the pressure range of 200-1200 Torr, and estimated the standard enthalpy for acetone dimer formation to be -13.5 ± 1.4 kJ mol^{-1}. The authors supported their experimental studies with *ab initio* molecular orbital calculations, and concluded that the dimer had a cyclic structure stabilized by two C-H···O hydrogen bonds.

Early spectroscopic evidence for acetone self-association was reported by Tiffon *et al.*[4], Schindler *et al.*[5] and Knözinger *et al.*[6] The first authors studied ^{17}O NMR chemical shifts and line widths at variable temperature. The chemical shift data were found to be consistent with a monomer-dimer equilibrium with a standard association enthalpy and entropy of -4.6 kJ mol^{-1} and -35.6 J mol^{-1} K^{-1}. Analysis of the line width measurements suggested that the dimer does not reorient in the liquid as a rigid unit, but must rather be considered as a short-lived electrostatic-collided complex. W. Schindler and co-workers used Raman spectroscopy to study the effect of pressure on the C=O stretching wavenumber and the isotropic line shape of this mode in liquid acetone.[5] Knözinger *et al.* focused on the far-infrared spectra of acetone trapped in argon matrices, and concentrated on the changes observed while annealing the matrices.[6] More recent spectroscopic studies on acetone self-association involve, among others, the combination of molecular beam experiments with photoionization

detection with tunable coherent vacuum-ultraviolet spectroscopy[7,8] and near edge-X-ray absorption spectroscopy [9].

Continuing on experimental studies by Jalilian[10] describing the infrared and NMR spectra of binary azeotropes formed by mixing acetone and cyclohexane, Arivazhagan *et al*.[11] recently reported on a combined experimental and theoretical study on the behavior of acetone in cyclohexane solutions. The spectroscopic studies were performed using traditional FTIR, ^{13}C NMR and UV-vis spectroscopic methods and mainly focused on changes in wavenumbers and chemical shifts observed when passing from the pure liquids to a binary solution. Among other changes, blue shifts observed for the C=O stretching mode, the C–C=O bending modes and the C–H stretching modes were explained as the result of molecular complexes. From the limited data available it was concluded that in its pure form, acetone exists as molecular entities self-associated through blue-shifting C–H···O hydrogen bonds, while in the mixture with cyclohexane the dimers are dissociated so that only monomers remain.

It must be noted explicitly that in the latter studies, evidence for the occurrence of acetone dimers in solutions was derived from changes in wavenumbers or chemical shifts, and that for none of the solutions studied, separate bands due to monomers and complexes were reported. This observation is in line with the earlier observations suggesting that in the liquid phase, interactions between acetone molecules mainly give rise to short-lived species formed during the collision of two molecules. Taking into account that individual spectral features proving the simultaneous occurrence of monomers and binary complexes have been observed for a variety of complexes involving acetone as a Lewis base, and considering that these complexes often had a complexation enthalpy similar to or even smaller[12,13] than the numbers reported above for the acetone dimers, however, there seems no reason why such features should not be present for acetone dimers. We therefore believe that the observations and the conclusions derived from the above studies should be questioned.

Building on experimental evidence showing the applicability to characterize homo and heterodimers[14-19], infrared spectroscopy of solutions in liquefied noble gases can shed light on the nature of acetone dimers and, eventually, also higher associations. The advantage of the approach is based on the fact that the inert gases used as a solvent

create a weakly interacting environment that, combined with the low temperatures used, lead to small bandwidths and thus facilitates the detection of complex bands only slightly shifted from the monomer modes. In addition, the cryosolutions can be used to determine thermodynamical properties of the species studied as the solutions are in chemical equilibrium. Therefore, cryospectroscopy also allows the determination of the standard enthalpy of formation in an independent way, of which the resulting values can be used to assess the scattered literature data summarized above.

For heterodimers, analysis of the spectra obtained for mixed cryosolutions typically involves subtraction procedures in which the spectra of the monomers and of the complexes are separated by recording monomer spectra at exactly the same temperature, and by rescaling and subtracting these spectra from those obtained for the mixed solution. Similar to gas-phase studies including among others hydrogen bonded complexes with dimethylamine[20] and halothane[21-23], the rescaled monomer spectra represent the contributions of the respective monomers studied, while the difference spectra obtained show the spectral features due to the complexes present. For studies involving homodimers, including the case of acetone dimer studied here, subtraction based procedures often are hampered by the fact that even for lowest concentrations studied spectra typically contains spectral features due to monomers and homodimers. Hence, for such systems, no monomer only spectra required for reliable subtraction processes are available. To overcome the limitations of the subtraction procedures, we have recently reported on more sophisticated approaches based on constrained least-squares fitting algorithms.

To be able to rationalize the spectral features related to the weak molecular complexes formed between acetone molecules, in this study, infrared spectra of solutions in liquid krypton (LKr) containing mole fractions of acetone varying between 4.2×10^{-4} and 5.6×10^{-5} are recorded, at temperatures between 134 and 142 K. The resulting spectra are analyzed using a least-squares fitting based method similar to that used for the studies of HCl and pyrrole oligomers.[17,18] The spectroscopic studies are supported by MP2 and single point CCSD(T) *ab initio* calculations to predict the structural, energetical and spectroscopic properties of the different complexes that can be formed, and by Monte Carlo Free Energy Perturbation (MC-FEP) and statistical

thermodynamical calculations to rationalize the effects of temperature and of solvatation on the complexation enthalpies measured. The results show that, in contrast to earlier studies, separate bands due to acetone monomer and acetone dimer can be identified. Analysis of the temperature dependence also allows the complexation enthalpy for the dimer in cryosolutions and in the gas phase to be reliably determined. The results for the first time show that cryosolutions can yield interesting information on complexes largely determined by long-range dipole-dipole interactions and that applications should thus not be limited to typical Lewis base - Lewis acid interactions involving, among others, hydrogen and boron halides, C–H hydrogen and C–X halogen bond donors and electron deficient molecules such as CO_2, OCS and N_2O.[15,24,25]

6.2 Experimental details

The sample of acetone ($(CH_3)_2CO$, 99,5%) was purchased from Acros and was used without further purification. The krypton used as a cryosolvent had a stated purity of 99.9995% and was supplied by Air Liquide.

Infrared spectra of acetone in LKr were recorded on a Bruker IFS 66v Fourier transform spectrometer. A Globar source was used in combination with a Ge/KBr beamsplitter and a LN_2-cooled broad band MCT detector. All interferograms were averaged over 500 scans, Blackman-Harris 3-term apodized and Fourier transformed with a zero filling factor of 4 to yield spectra with a resolution of 0.5 cm^{-1}. The experimental set-ups used to investigate the solutions in liquid noble gases have been described before.[26] In the actual cryostat, a liquid cell with 1 cm path length and equipped with wedged Si windows was mounted below a LN_2 dewar. The temperature of the cell body is measured using a Pt-100 thermoresistor. The SunRod electric minicartridge heater is controlled using a Eurotherm 3504 PID controller. The temperature of the solutions were stabilized at 134, 135, 136, 137, 138, 139, 140, 141 or 142 K, the temperature variation during a typical run being less than 0.05 K. Spectra were obtained and preanalyzed using OPUS 6.5. The data sets consisted of 117 till 153 spectra. Further calculations were performed using Matlab.[27]

The mole fractions of acetone used for the data sets are difficult to accurately quantify[28,29], but are estimated to vary between 4.2×10^{-4} and 5.6×10^{-5}. As acetone has a limited solubility in LKr[12,13,30,31], the amount of acetone dissolved in the cryosolvent was increased by increasing the temperature to 160 K after filling the cell at 123 K and then lowering it back to the wanted temperature. The concentrations used are chosen so that the region between minimum and maximum absorbance is uniformly covered and all measured regions have absorbances below 1. Figure 6.3 shows five spectra of the data set of 138 K for the relevant regions of the spectrum.

As the outcome of the used fitting procedures are perturbed by baseline artifacts, baseline corrections on the complete data set were performed using spectra of pure LKr recorded under exactly the same conditions. Another critical parameter often hampering the numerical analyses to be performed is related to small traces of solid, amorphous or crystalline, water suspended in the solution or condensed onto the cold elements present in the cryostat and/or detector. The traces are observed to slightly increase during experiment, and, due to changes in relative intensities, are difficult to subtract. To account for remaining baseline drifts, which we believe are due to small temperature changes inside the spectrometer due to the colder parts present, an additional straight line baseline correction was applied to all data. These lines are drawn connecting points where the absorbance is known to be zero. In the case of acetone these straight lines were generated from 3752 to 3057, from 3057 to 2876, from 2876 to 2812, from 2812 to 2667, from 2667 to 1935, from 1935 to 1615, from 1615 to 1286, from 1286 to 1140, and from 1140 to 960 cm^{-1}.

6.3 Computational details

To support our experimental measurements, geometries and harmonic vibrational frequencies were obtained from *ab initio* MP2 calculations performed using Dunning's augmented correlation consistent basis set of double zeta quality (aug-cc-pVDZ) in Gaussian09.[32] The geometry optimizations were performed using default optimization settings. The counterpoise technique as proposed by Boys and Bernardi was used during all *ab initio* calculations to account for basis set superposition error.[33] More

reliable energies at the basis set limit were calculated with Molpro[34] using the extrapolation scheme of Truhlar, in which the effect of electron correlation is obtained from MP2 calculations[35].

$$E_{CBS}^{HF} = \frac{3^{\alpha}}{3^{\alpha} - 2^{\alpha}} E_3^{HF} - \frac{2^{\alpha}}{3^{\alpha} - 2^{\alpha}} E_2^{HF} \tag{6.1}$$

$$E_{CBS}^{cor,MP2} = \frac{3^{\beta}}{3^{\beta} - 2^{\beta}} E_3^{cor,MP2} - \frac{2^{\beta}}{3^{\beta} - 2^{\beta}} E_2^{cor,MP2} \tag{6.2}$$

In these calculations α = 3.4 and β=2.2,[35] while energies with subscript 2 and 3 are calculated using the aug-cc-pVDZ and aug-cc-pVTZ basis sets respectively.

Furthermore, a correction for higher degree correlation effects is made using Hobza's method,[36,37] yielding results of $E_{CBS}^{CCSD(T)}$ quality.

$$\Delta E^{CCSD(T)} = \left| E^{CCSD(T)} - E^{MP2} \right|_{aug-cc-pVDZ} \tag{6.3}$$

$$E_{CBS}^{CCSD(T)} = E_{CBS}^{HF} + E_{CBS}^{cor,MP2} + \Delta E^{CCSD(T)} \tag{6.4}$$

A calculated complexation energy ΔE(CCSD(T)) is transformed into vapor phase complexation enthalpy ΔH°(vap,calc), by accounting for thermal and zero-point vibrational contributions. Correction of this calculated enthalpy value with solvent effects yields a complexation enthalpy in solution ΔH°(LKr,calc) which can be compared with the experimental complexation enthalpy ΔH°(LKr). Corrections for thermal effects and zero-point vibrational contributions were obtained using statistical thermodynamics [38], whereas the effects of solvation were accounted for using the Monte Carlo Free Energy Perturbation (MC-FEP) approach in an in-house modified version of BOSS 4.0.[39]

6.4 Results and discussion

6.4.1 Vibrational modes of acetone monomer

The acetone molecule has a C_{2v} symmetry point group that spans 24 fundamental vibrations. In the C_{2v} symmetry the z-axis is the axis of symmetry, but the choice of the x- and y-axis, hence the identification of the two planes in Table 6.1, is arbitrary. To resolve this ambiguity we followed the recommendations of Mulliken.[40] Therefore we

defined the x- and y-axis as stated in Figure 6.1. This way the fundamental modes span the $8A_1 + 4A_2 + 5B_1 + 7B_2$ symmetries with all but four A_2 modes being active in the infrared. The modes are numbered according to descending wavenumber in each symmetry block. Because the x- and y-axis are interchanged compared to the several previous literature investigations, also the numbering of the vibrational modes disagrees with most [7,41-44] and agrees with only a few previous vibrational studies on acetone [45,46]. The correspondence between previous and present numbering and symmetry labels is as follows:

modes 1-7 (A_1) and 9-11 (A_2) are unchanged,

modes 13-17 (B_1) in most of the literature are now modes 20-24 (B_2),

modes 18-24 (B_2) in most of the literature are now modes 13-19 (B_1).

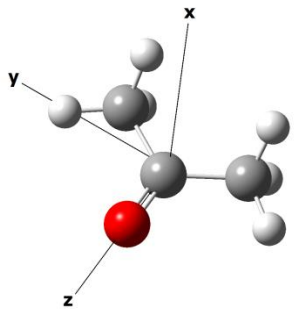

Figure 6.1 MP2/aug-cc-pVDZ equilibrium structure with the defined x-,y-,z-axes of the acetone monomer with C2v symmetry

Table 6.1 Character Table of the C_{2v} symmetry point group (the x-, y- and z-axis are defined in Figure 6.1)

C_{2v}	E	$C_2(z)$	$\sigma_v(xz)$	$\sigma_v(yz)$
A_1	1	1	1	1
A_2	1	1	-1	-1
B_1	1	-1	1	-1
B_2	1	-1	-1	1

Figure 6.2 shows the spectrum of the recorded data set with the highest concentration of acetone dissolved in LKr at 138 K. The mid infrared vibrational spectrum is characterized by an intense absorption band assigned to the carbonyl stretching vibration, ν_3, around 1725 cm^{-1}. This band has been one of the most popular features to study the clustering interactions involving acetone.[5,8,43,44,47] Other signals that have been used involve the C–H stretches[7,8] near the 3009-2926 cm^{-1} region, the CH_3 deformation modes ν_{21} and ν_5 near 1361-1355 cm^{-1}, and the asymmetric C–C stretching, ν_{22} near 1217 cm^{-1} [44]. In the next paragraphs we will report on the self-associating behavior of acetone by studying the effect of varying the concentration in all spectral regions, i.e. in the region often used to study heterocomplexes and in the neglected regions.

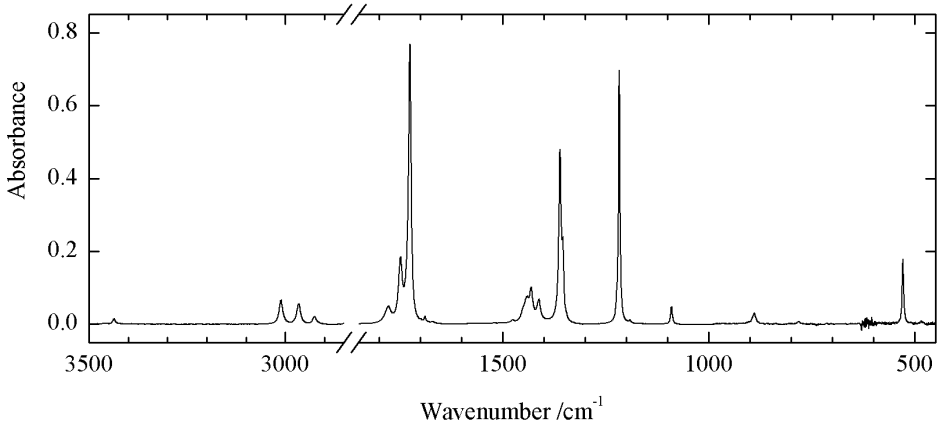

Figure 6.2 Infrared spectrum of acetone dissolved LKr recorded at 138 K

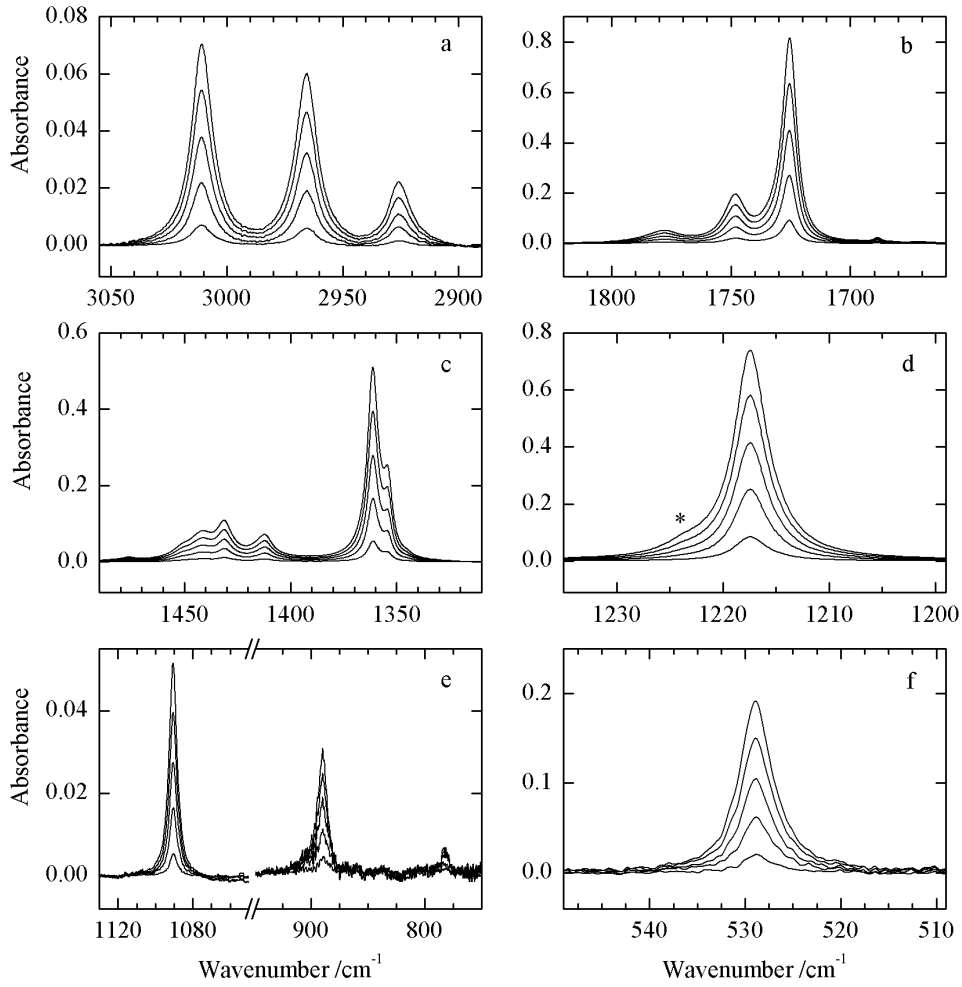

Figure 6.3 Infrared spectra of solutions of acetone in LKr, at 138 K. The spectra shown for each of the species represent only a small fraction of the spectral database used in the fitting procedures. * indicates a new absorption band emerging when increasing the acetone concentration.

6.4.2 Least-squares fitting of quadratic polynomials

When self-association occurs, an increase in concentration should yield new bands, due to oligomers, becoming noticeable in the spectra. Figure 6.3 shows the dependence with the concentration of the acetone cryosolutions of the most relevant spectral regions, illustrated with a selection of 5 spectra from the 138 K data set. New visual features arise with increasing concentration except for one new band, indicated with * in panel 6.3d, appearing as a shoulder to the ν_{22} transition.

To determine if other dimer features are present in the remaining spectral regions, the data set was analyzed using the newly developed least-squares based approach, with the purpose of isolating overlapping absorption bands of monomeric and oligomeric species. It has already been validated with the self-associating molecules HCl and pyrrole.[17,18]

The general concept of the method used is based on the fact that, with some exceptions[48,49], cryosolutions are known to be in thermodynamical equilibrium. The spectra for cryosolutions of self-associating species therefore are a superposition of monomer spectra and spectra of the different complexes, with the relative absorbances determined by the equilibrium concentrations *C* and the molar attenuation coefficients ε of the monomeric species and of the associations formed. The latter are determined by the equilibrium constant *K* involved.

$$2\ \text{monomer} \rightleftharpoons \text{dimer} \qquad K_2 = \frac{C_{dimer}}{C_{monomer}{}^2} = \frac{C_{di}}{C_{mono}{}^2} \tag{6.5}$$

Starting from these assumptions, for each arbitrary wavenumber $\tilde{\nu}_i$ the measured absorbance A_{exp} can be written as a sum of absorbance contributions related to the monomer A_{mono} or to one of the oligomers, in this case only dimer A_{di}, i.e.

$$A_{exp}(\tilde{\nu}_i) = A_{mono}(\tilde{\nu}_i) + A_{di}(\tilde{\nu}_i) \tag{6.6}$$

By choosing an appropriate wavenumber $\tilde{\nu}_m$ for which the absorbance is due to monomer only, i.e.

$$A_{exp}(\tilde{\nu}_m) = A_{mono}(\tilde{\nu}_m) \text{ and } A_{di}(\tilde{\nu}_m) = 0 \tag{6.7}$$

and by using the Lambert-Beer law

$$A_j(\tilde{\nu}_i) = \varepsilon_j(\tilde{\nu}_i) C_j d \tag{6.8}$$

with ε as the molar attenuation coefficient, C as the concentration in the solution, j as the type of species and d as the path length of the cell used, the different contributions in Eq. (6.6) can be rewritten in terms of the absorbance of the monomer wavenumber $\tilde{\nu}_m$;

$$A_{mono}(\tilde{\nu}_i) = a_1(\tilde{\nu}_i, \tilde{\nu}_m) A_{mono}(\tilde{\nu}_m) \tag{6.9}$$

$$A_{di}(\tilde{\nu}_i) = a_2(\tilde{\nu}_i, \tilde{\nu}_m) A_{mono}(\tilde{\nu}_m)^2 \tag{6.10}$$

The coefficients $a_{\mathrm{p}}(\tilde{\nu}_i, \tilde{\nu}_m)$,with p representing the polynomial degree, used in these expressions are defined as

$$a_1(\tilde{\nu}_i, \tilde{\nu}_m) = \frac{A_{mono}(\tilde{\nu}_i)}{A_{mono}(\tilde{\nu}_m)} = \frac{\varepsilon_{mono}(\tilde{\nu}_i)}{\varepsilon_{mono}(\tilde{\nu}_m)} \tag{6.11}$$

$$a_2(\tilde{\nu}_i, \tilde{\nu}_m) = \frac{A_{di}(\tilde{\nu}_i)}{A_{mono}(\tilde{\nu}_m)^2} = a_1(\tilde{\nu}_i, \tilde{\nu}_m)^2 \frac{\varepsilon_{di}(\tilde{\nu}_i)}{\varepsilon_{mono}(\tilde{\nu}_m)^2} \frac{1}{d} K_2 \tag{6.12}$$

Substituting the Eq.(6.9) and (6.10) in Eq. (6.6) results in

$$A_{exp}(\tilde{\nu}_i) = a_1(\tilde{\nu}_i, \tilde{\nu}_m) A_{mono}(\tilde{\nu}_m) + a_2(\tilde{\nu}_i, \tilde{\nu}_m) A_{mono}(\tilde{\nu}_m)^2 \tag{6.13}$$

The above equation shows that for any arbitrary wavenumber $\tilde{\nu}_i$, the contributions due to the different species present can in principle be derived by plotting, for all solutions and concentrations studied, the measured absorbances at $\tilde{\nu}_i$ versus the corresponding monomer absorbances measured at the given reference wavenumber $\tilde{\nu}_m$, and using least-squares to fit a polynomial to the resulting data. Examples of typical fits are presented in Figure 6.4.

The chosen reference wavenumber $\tilde{\nu}_m$ is used as an internal standard and is chosen based on the fact that no features due to self-association are observed or expected to appear in the region considered. In the case of acetone, $\tilde{\nu}_m$ was chosen in the spectral region of the ν_{22} transition. As described before this band shows a dimer feature blue-shifted from the monomer band center, for this reason the absorbance at a wavenumber on the lower wavenumber side is more likely to only have a monomer contribution. $\tilde{\nu}_m$ was set to be 1216.5 cm^{-1}. In order to check if the choice of this wavenumber is suitable we compare the results of the analysis with the outcome of a subtraction routine. In the

case of the self-associating species the subtraction routine can be performed by scaling a low concentration spectrum to a high concentration spectrum, resulting in a spectrum that contains only signals of oligomeric species. As observed in the earlier HCl study[18], low concentration spectra often already contain traces of oligomers, leading to an underestimation of the presence of the oligomers in the oligomers spectrum. The results obtained using subtraction procedures therefore must always be treated with caution. Although a subtraction routine underestimates the presence of the dimer and in principle cannot be used for quantitative measurements, it can still be used to give us an idea of the shape and width of the dimer band. The dimer contribution resulting from the subtraction routine is illustrated with the red trace in Figure 6.5.

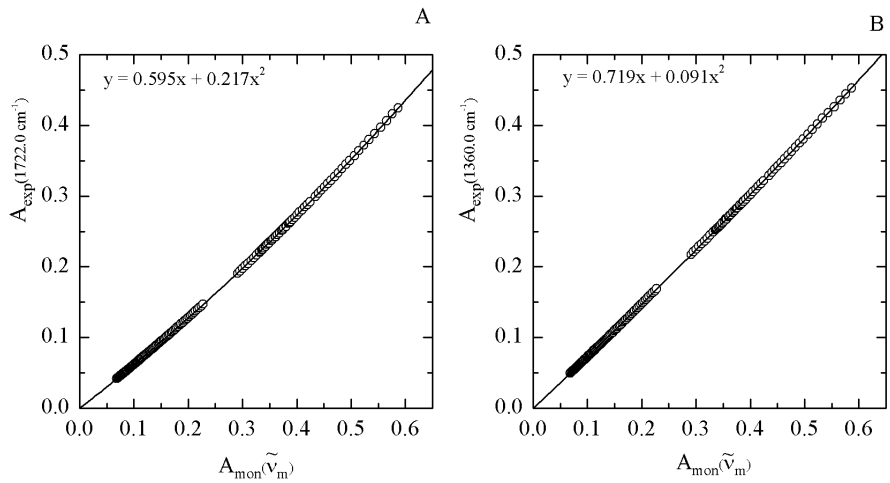

Figure 6.4: Two examples of a quadratic polynomial fitted through the measured absorbances for different concentrations at a certain wavenumber versus the monomer absorbances for different concentrations at the reference wavenumber $\tilde{\nu}_m$ set at 1216.5 cm^{-1}. Panel A illustrates the fit at 1722.0 cm^{-1} and Panel B for 1360.0 cm^{-1}.

Figure 6.5, parts a1 and a2, shows the monomer and dimer contribution, for the cryosolution containing an approximate mole fraction of 4.2 x 10^{-4} and recorded at 138 K. The results shown are derived by analyzing the data set using the second degree polynomial as described in Eq. (6.13). In Figure 6.5a2, it can be seen that the dimer contribution at $\tilde{\nu}_m$, at 1216.5 cm^{-1}, is zero. This result is determined by the general assumption suggesting that for all solutions studied, the measured absorbance at the reference wavenumber is solely determined by monomer species. Comparing the results in Figure 6.5a2 with the dimer contribution derived from an approximate subtraction

procedure, illustrated with the red trace, it is obvious that this assumption is not completely valid. Indeed, the absorbance at 1216.5 cm^{-1} should not be zero but should be approximately 0.02.

The conclusion that the absorbance at $\tilde{\nu}_m$, $A_{exp}(\tilde{\nu}_m)$, not only consists of a monomer contribution, but actually consists of a monomer and dimer contribution, $A_{mono}(\tilde{\nu}_m)$ and $A_{di}(\tilde{\nu}_m)$, somewhat weakens the choice for the reference wavenumber made. However, as all other modes are expected to show similar dimer bands largely or completely overlapping with the monomer bands, apart from data in the immediate vicinity of 1216.5 cm^{-1}, no other options for reliable reference wavenumbers are available. To overcome the problem, a somewhat arbitrary correction was introduced, in which the value of $A_{mono}(\tilde{\nu}_m)$ was corrected, by (i) estimating the dimer contribution and (ii) subtracting this value from $A_{exp}(\tilde{\nu}_m)$.

$$A_{mono}(\tilde{\nu}_m) \approx A_{exp}(\tilde{\nu}_m) - A_{di}(\tilde{\nu}_m) \tag{6.14}$$

To estimate the value of the dimer contribution, the band derived from the fitting procedure was symmetrized over an axis of symmetry originating from the maximum of the band. The axis of symmetry chosen is indicated with the dash dot line in panel 4b. The $A_{mono}(\tilde{\nu}_m)$ values obtained by correcting the absorbance of the symmetrized dimer band at $\tilde{\nu}_m$ from $A_{exp}(\tilde{\nu}_m)$ leads to the results shown in Figure 6.5b.

Comparison of data in Figure 6.5b show that, although the agreement is already significantly improved, the resulting dimer band obtained by using the corrected monomer intensities, and that obtained from the approximate subtraction is far from excellent. Realizing that the monomer intensities required for the determination of the dimer band are directly influenced by the outcome, i.e the dimer contribution itself, we attempted to improve the agreement using a self-consistent procedure, in which the correction is repeated until only minor changes in the calculated spectra of monomer and dimer are observed. In order to improve the resemblance of fitted dimer band with the subtracted one, it was chosen to shift the axis of symmetry for 1.5 cm^{-1} to the lower wavenumber side, as illustrated in Figure 6.5c. This resulted in a larger correction for $A_{exp}(\tilde{\nu}_m)$ indicated with the arrow in Figure 6.5c. As the fitted result indeed showed

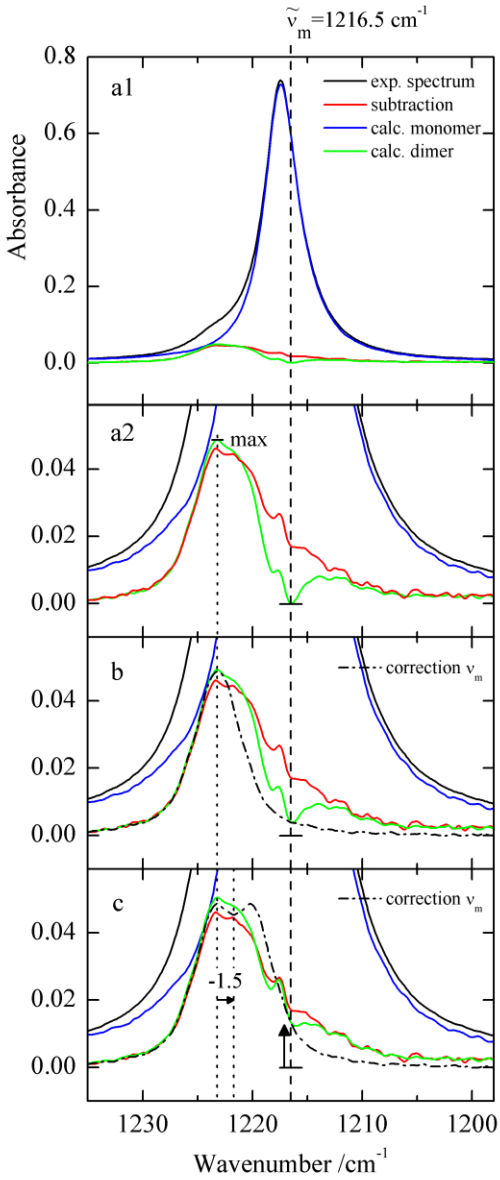

Figure 6.5. Results from least-squares procedures using a 2nd degree polynomial. The monomer wavenumber at 1216.5 cm^{-1} is indicated with the vertical dashed line. The upper panel shows the calculated monomer and dimer contributions without corrections of $\tilde{\nu}_m$ with a blue and green trace. The red trace illustrates the dimer contribution obtained from a subtraction procedure. In panel a2 the dimer contribution is magnified. The absorbance at $\tilde{\nu}_m$ is corrected by reflecting the higher wavenumber half of the calculated dimer band at the wavenumber with maximum absorbance indicated with the dotted line. This correction and the resulting monomer and dimer contributions of the first iteration are shown in panel b with a dash dot trace. In order to get a better resemblance with the subtraction trace the axis of symmetry was moved for 1.5 cm^{-1} to the lower wavenumber side. The new correction and the results of the first iteration using this correction are shown in panel c.

more resemblance with the subtraction it was decided to use this method to analyze vibrational spectrum of acetone. Also in this case multiple iterations were introduced, but again no major changes of the dimer contributions were observed. The result shows that also for the other modes, spectral features illustrating self-association can be identified. As these features typically escape detection in classical subtraction procedures or visual comparisons, the results therefore clearly illustrate the added value of the least-squares based method.

6.4.3 Vibrational spectra of the acetone monomer and dimer

By using the corrected monomer intensity obtained for the reference wavenumber 1216.5 cm^{-1}, reliable data can also be derived for the other spectral regions for which, at first sight, no dimer contributions are to be expected. Figure 6.6 shows the fitted monomer and dimer contributions for the most important regions of the acetone spectrum applying the method illustrated in Figure 6.5c to the data set of 138 K. The results show that apart from the dimer band at 1222.7 cm^{-1} other dimer features can be reliably predicted, at wavenumbers close to or almost identical to those of the monomer species. The assignment of the experimental spectra is presented in Table 6.2. The approximate description of vibrational modes adopted is similar to those previously used by Dellepiane *et al.*[41] and Consani *et al.*[47] The assignments of the monomer closely follow those reported for the compound in the gaseous phase[41] and in the solid argon matrix[43,47]. For the dimer, only few results are available in previous literature studies and these will be mentioned further down the text.

In the C–H stretching region (Figure 6.6a), three main monomer bands assigned to respectively the degenerate stretches, ν_1 and ν_{18}, the stretch ν_{13} and the degenerate stretches, ν_2 and ν_{19} are observed at 3011.1, 2965.7 and 2926.1 cm^{-1}. For these monomer bands, dimer features shifted by -2.0, 0.0 and 0.1 cm^{-1} respectively, are predicted at 3009.1, 2965.7 and 2926.2 cm^{-1}. These values differ from the gas phase IR/VUV spectroscopy values reported by Guan *et al.*[8] who reported red and blue shifts of -8, 4 and 0 cm^{-1} respectively. The reason for the discrepancies is not fully understood but most probably is related to solute-solvent interactions in the cryosolutions slightly

perturbing both the fundamental wavenumbers of the modes present and the Fermi resonances with overtones and combinations bands present. It is interesting to note that the C–H stretching region was also studied by Matsuda *et al.*[7] The data reported by these authors were also based on the combination of infrared spectroscopy and VUV photoionization detection, but did not lead to any observation of dimer bands in this region.

Although perturbed by Fermi resonance involving the $\nu_{22} + \nu_{24}$ transition[50,51], the intense C=O stretching mode has been the most popular transition to study the intermolecular interactions with acetone.[8,43,44,47] The results of the fitting procedures of this spectral region are displayed in Figure 6.6b. The monomer band in LKr was found to appear near 1725.6 cm^{-1}. The fitting procedure revealed a dimer band, slightly red-shifted from the monomer by -2.2 cm^{-1}, at 1723.4 cm^{-1}. Combination of the small shift observed and the strong infrared intensity observed for the monomer, most probably, is the reason why no comparable dimer signal has been reported in literature before.

In the 1500-1300 cm^{-1} spectral region (Figure 6.6c), the monomer gives rise to five fundamental transitions due to CH_3 deformation modes: the weaker bands due to ν_{14}, ν_4, ν_{20} appear at 1451.0, 1431.3 and 1412.3. The more intense modes ν_{21}, ν_5 modes are observed at, 1361.1 and 1354.6 cm^{-1}. Apart from these bands, in the spectra of the cryosolutions, additional bands related to dimer formation are observed for every mode, except for ν_{14}. These dimer signals all show complete overlap with the monomer bands and escaped detection in earlier studies.

Panel 5d shows the results for the C–C asymmetric stretching region discussed in detail above. The dimer band at 1222.7 cm^{-1} is blue-shifted from the monomer at 1217.4 cm^{-1}. The shift of 5.3 cm^{-1} is the largest observed complexation shift in the recent experimental study. No spectral features related to this band have been reported before.

Panels e and f of Figure 6.5 illustrate the appearance of complex bands for four much weaker fundamentals. The monomer bands at 1090.2 and 530.2 cm^{-1} are assigned to the out-of-plane CH_3 rock and the C=O in-plane bending vibration, and are accompanied by a dimer signal emerging 2.0 and 1.3 cm^{-1} blue-shifted from the monomer,

respectively. The presence of traces of solid water in the solution perturbs the analysis in the 1000-700 cm^{-1} region and limits the signal-to-noise. Consequently, a reliable analysis of the features in this region due to the in-plane CH_3 rocking and the symmetric C–C stretching modes at ~889 and ~782 cm^{-1} is not possible.

The weak feature at ~893 cm^{-1} can tentatively be assigned to the dimer. Because of the limited signal-to-noise ratio, we decided to remain cautious about its nature and to not include this feature in the list of observed wavenumbers. The predictions for the ~782 cm^{-1} band suggests an unrealistically compensation effect in which the monomer spectrum is largely overestimated and is compensated by a negative dimer contribution. This band, again, is not included in Table 6.2.

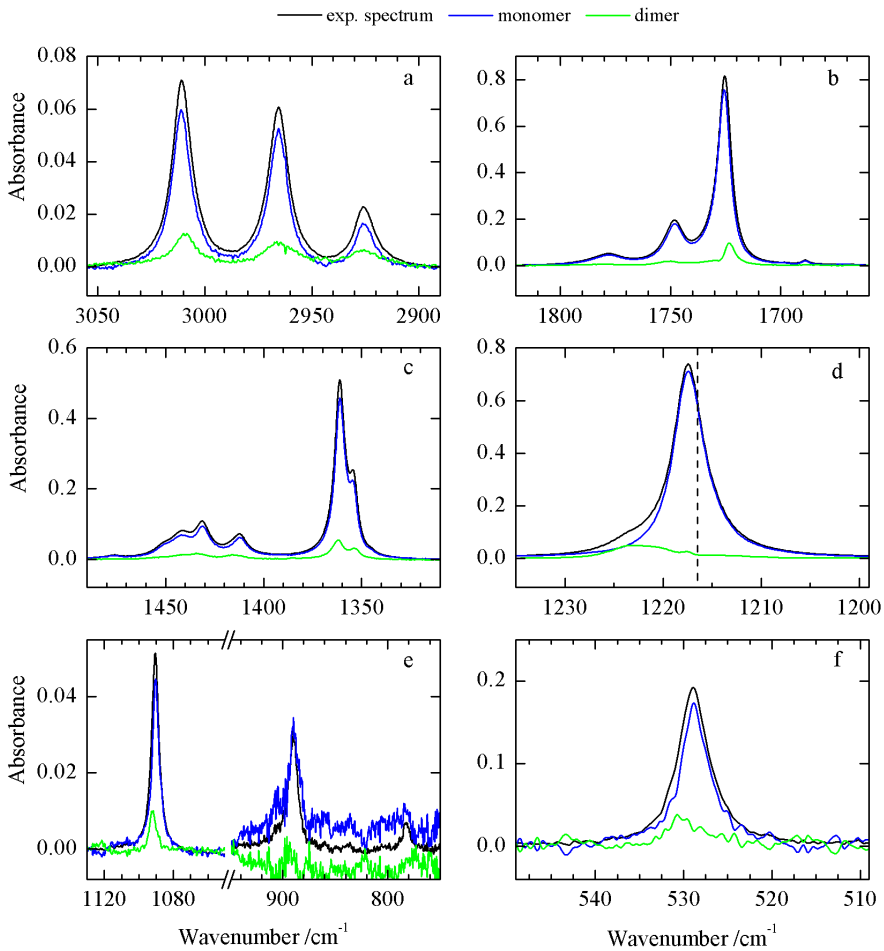

Figure 6.6 Results from least-squares procedures using a 2nd degree polynomial with a corrected absorbance at the monomer wavenumber at 1216.5 cm^{-1} (dashed line in panel d).

Table 6.2 Assignment of experimental monomer and dimer absorption bands of acetone in solution with krypton at 138 K and a comparison with previous literature investigations [a]

Monomer						Dimer			
			experimental			experimental		calculated MP2/aug-cc-pVDZ	
Number	approximate description [c] [45,47]	symm	gas phase[41]	solid Ar matrix 9 K [43,47]	LKr 138 K	LKr 138 K	$\Delta\nu$	stacked $\Delta\nu$	planar $\Delta\nu$
$2\nu_3$		A_1	3453		3436.7				
ν_1	νC–H $_{as}$	A_1	3018.5	3018.6	3011.1	3009.1	-2.0	-5.7	-2.7
ν_{18}	νC–H $_{as}$	B_2						-5.6	-5.3
ν_{13}	νC–H	B_1	2972	2972.6	2965.7	2965.7	0.0	3.0	-1.5
ν_2	νC–H $_{sym}$	A_1	2937	2932.2	2926.1	2926.2	0.1	-1.5	-2.2
ν_{19}	νC–H $_{sym}$	B_2						-1.4	-5.1
					2843.0				
					2787.2				
$\nu_{22}+\nu_5$			2576		2569.0				
$\nu_{21}+\nu_{23}$			2256		2247.7				
$\nu_{21}+\nu_7$			2140		2139.7				
					2105.2				
$2\nu_{23}$				1768.3	1778.0	1780.2	2.2		
$\nu_{22}+\nu_{24}$ FR[b]				1747.2	1748.1	1750.5	2.4		
ν_3 FR[b]	νC=O	A_1	1731	1721.4	1725.6	1723.4	-2.2	-1.0	0.5
					1476.2				
ν_{14}	$\delta CH_{3\,as}$	B_1	1454	1451.7	1451.0			3.0	6.5

				1444.3	1441.4	1441.5	0.1		
ν_4	$\delta CH_{3\ as}$	A_1	1435	1429.4	1431.3	1434.1	2.8	0.9	3.4
ν_{20}	δCH_3	B_2	1410	1406.9	1412.3	1415.2	2.9	-2.7	0.9
ν_{21}	$\delta CH_{3\ sym}$	B_2	1363.5	1361.6	1361.1	1361.9	0.8	1.2	2.9
ν_5	$\delta CH_{3\ sym}$	A_1		1354.1	1354.6	1353.3	-1.3	-2.4	1.8
ν_{22}	νC-C $_{as}$	B_2	1215.5	1216.6	1217.4	1222.7	5.3	6.1	3.7
					1191.4				
ν_{15}	rock $CH_{3\ oop}$	B_1	1090.5	1091.7	1090.2	1092.2	2.0	1.7	2.2
ν_{23}	rock $CH_{3\ ip}$	B_2	891	882.4	889			8.0	8.2
ν_7	νC–C $_{sym}$	A_1	777	780.9	782			0.0	2.2
ν_{24}	δC=O $_{ip}$	B_2	530	528.9	528.9	530.2	1.3	1.7	3.1

[a] Wavenumbers in cm^{-1}.
[b] FR, Fermi resonance
[c] ν, stretching; δ, deformation or bend; rock, rocking; sym, symmetric; as, antisymmetric; ip, in-plane; oop, out-of-plane;

6.4.4 Experimental dimerization enthalpy

The experimental dimerization enthalpy was measured using a van't Hoff plot, illustrated in Figure 6.7. The underlying equation establishes a linear relation between the inverse temperature and the logarithm of the intensity product $I_{di}/{I_{mon}}^2$, with a slope equal to $-[\Delta H°(LKr) + Rb]/R$ and b being a correction factor to account for the changes in solvent density upon temperature variation.[29] Data sets of acetone solutions in LKr were recorded at temperatures between 134 and 142 K. After resolving the spectra with the least-squares approaches, it was possible to integrate the intensity of a monomer band, I_{mono}, and of the related dimer feature, I_{di}. Figure 6.7 shows the van't Hoff plots for two spectral regions, 1860-1640 and 1260-1148 cm^{-1}, that respectively result in complexation enthalpies of -10.3 ± 1.6 and -11.4 ± 1.6 kJ mol^{-1} with error margins equal to twice the standard deviation. The average value, -10.8 ± 1.1 kJ mol^{-1}, compares well with the earlier values of -13.5 ± 1.4 kJ mol^{-1} and -11.7 kJ mol^{-1} reported by Frurip *et al.* [3] and Lin *et al.* [2], respectively, and is line with typical values obtained for other hydrogen and or halogen bonded complexes observed in cryosolutions.[14,19,22,26,52,53] The value is significantly larger than the value of -4.6 kJ mol^{-1} derived from ^{17}O NMR chemical shifts and line widths.[54]

6.4.5 ***Ab initio calculated geometries, energies and wavenumber shifts of the acetone dimer***

Although a good agreement is found between the experimental complexation enthalpy derived in this study, and the values reported in literature, some remarks must certainly be made. For example, the experiments reported were conducted at temperatures well below room temperature, while all literature values were derived using data obtained at room temperature or at elevated temperatures. In addition, no corrections for solvent effects discriminating between the gas phase experiments and the experiments in LKr and discriminating between the cryosolutions and the more traditional solvents were introduced.

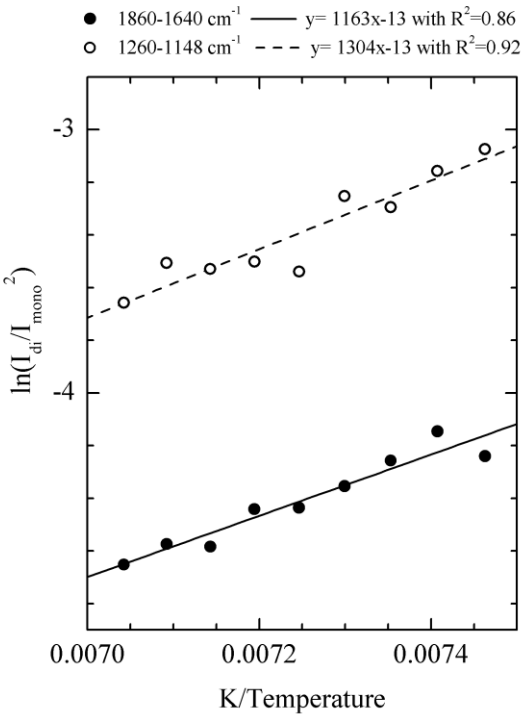

Figure 6.7 Van't Hoff plots for the acetone dimer observed in LKr for the spectral region of 1860-1640 (full circles) and 1260-1148 cm^{-1} (open circles) region in the temperature interval 134-142 K.

Recent studies involving a variety of hydrogen and halogen bonded complexes have shown that, after taking into account the necessary corrections for solvent effects and thermal contributions, good agreement can be achieved between experimental complexation energies derived from cryosolutions and theoretical data for the isolated complexes using Complete Basis Set extrapolations and single point CCSD(T) corrections[37]. To further rationalize the data derived from the cryosolutions, also in this study such calculations were initiated.

In Figure 6.8 the MP2/aug-cc-pVDZ equilibrium geometries for both geometries are shown. The Cartesian coordinates of the monomers and of the complexes are also given in the Supporting Information. Both structures are characterized by a side-by-side configuration, with the carbonyl being aligned in opposite directions. In agreement with literature data, the most stable geometry has a stacked structure in which the planes of the molecules parallel to each other and perpendicular to the plane through both

carbonyl groups.[3,7,55,56] The second, less stable, geometry has a planar structure in which both planes are almost coplanar.

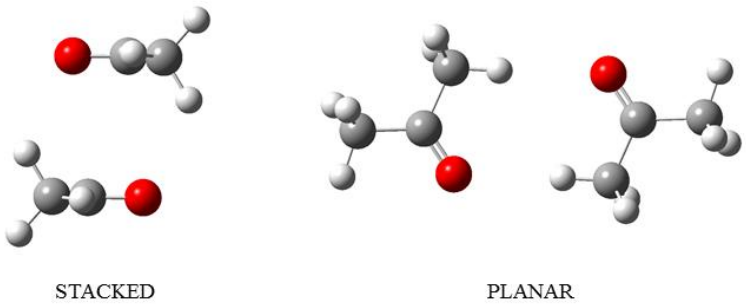

Figure 6.8 MP2/aug-cc-pVDZ equilibrium geometries and symmetries for the planar and stacked acetone dimer

It can be noted that the nature of the interaction in the acetone dimers is not always subscribed to dipole-dipole interactions. Hermida-Ramón *et al*.[56] suggested that dimer formation is due to the origination of four C=O···H–C hydrogen bonds, while Frurip *et al* [3] suggested that there are only two of such interactions present. Tamenori *et al*.[9] on the other hand noted that the interaction probably is a combination of dipole-dipole and C=O···H–C hydrogen bonding interactions. Regarding the nature of the interactions between the two acetone units we assume that long the distance (range) dipole-dipole interaction is the driving force for the clustering. But as the distance between the two dipoles shortens a number of C=O···H–C hydrogen bonds arise, creating an extra stabilization to keep the units in the stacked geometry. It should also be mentioned that the actual geometry in the liquid state will not be a rigid antiparallel arrangement of the two dipoles as it will constantly collide with solvent atoms.

Table 6.3 presents the calculated interaction energies derived from the MP2/aug-cc-pVDZ equilibrium geometries and derived from the and CBS and CCSD(T) single point corrections. To allow comparison with the experimental complexation enthalpies derived from the cryosolutions measurements, the CCSD(T)/CBS based complexation energies ΔE(CCSD(T)) were transformed into vapor phase complexation enthalpies ΔH°(vap,calc), by accounting for thermal and zero-point vibrational contributions. In addition, to estimate the complexation enthalpies in solutions, further noted as ΔH°(LKr,calc), corrections related to the solute-solvent interactions in the solutions

were accounted for. The corrections for zero-point vibrational and thermal influences were based on the standard rigid rotor/harmonic oscillator model regularly used in statistical thermodynamics.[38] The calculations were performed at 138 K for Kr, i.e. at the midpoint of the temperature interval used during the experimental study. The structural parameters and harmonic vibrational frequencies used were obtained by MP2/aug-cc-pVDZ calculations.

The solvent influences on the complexation enthalpies were derived from the solvation Gibbs energies in LKr, obtained by simulating the immersion of monomers and complexes from the gas phase into the solution, using a Monte Carlo Free Energy Perturbation (MC-FEP) approach. To this end, solvation Gibbs energies of monomers and complexes were estimated at 6 different temperatures varying from 127 to 145 K for LKr at a pressure of 28 bar. The enthalpy of solvation $\Delta_{sol}H$ was then extracted using the expressions $\Delta_{sol}H = \Delta_{sol}G + T\Delta_{sol}S$ and $\Delta_{sol}S = -(\partial\, \Delta_{sol}G/\partial T)_p$. Also for these calculations, the MP2/aug-cc-pVDZ equilibrium geometry was used.

Table 6.3 shows that in agreement with the rather large difference in stability derived for the complexation energies, a significant difference in stability is predicted for the vapor phase complexation enthalpy, the value for the stacked geometry being approximately 8 kJ mol^{-1} more stable than that of the planar geometry.

Table 6.3 MP2/aug-cc-pVDZ, ΔE(DZ), and the CCSD(T)/CBS,ΔE(CCSD(T)), interaction energies including BSSE corrections, calculated vapor phase interaction enthalpies (vap,calc), calculated interaction enthalpies in liquid krypton (LKr,calc) and corresponding experimentally obtained interaction enthalpies for the planar and stacked acetone dimer (LKr,exp) in kJ mol^{-1}.

	Stacked Dimer	Planar Dimer
ΔE (DZ)	-25.7	-13.0
Δ*E* (CCSD(T))	-28.4	-15.1
ΔH°(vap,calc)	-25.5	-12.1
ΔH°(LKr,calc)	-13.7	-5.8
ΔH° (LKr,exp)	-10.8 ± 1.1	

The large difference in complexation energy suggests that in the cryosolutions studied, the chemical equilibrium is shifted towards complexes with a stacked geometry. Addition information supporting this idea was derived by comparing the calculated harmonic vibrational wavenumbers for monomers and dimers and by comparing the calculated complexation shifts for planar and stacked geometries with the wavenumber shifts observed experimentally. The calculated wavenumbers shifts of the fundamental modes of the both dimer structures can be found in Table S6.4 (MP2/aug-cc-pVDZ), Table S6.8 (MP2/ cc-pVTZ), Table S6.12 (MP2/aug-cc-pVTZ). The wavenumber shifts are being compared with the experimental shifts by plotting the values and calculating the linear regressing line, presented in Figure 6.9.

Although the vibrational spectra of both dimers show only small differences and hence only give rise to small changes in complexation shifts, the linear regression lines give rise to small differences in correlation coefficients, the values being 0.54 for of the stacked dimer and 0.43 for the planar dimer. These results support the idea stated that the experimental result compares better with the stacked dimer. However, taking into consideration the rather low values for the correlation coefficients obtained, this statement remains somewhat tentative.

To account for possible effects of basis sets used and to obtain information on the error margins to be expected for the calculated complexation shifts, calculations were repeated for the cc-pVTZ, and the aug-cc-pVTZ basis sets. The results are included in Figure 6.9. The results show that for most of the modes considered, the sign of the complexation shifts remains largely unaffected by the choice of the basis set. In contrast, significant changes for the absolute values can be observed for some of the modes. The results further illustrate that for all used basis sets, the correlation coefficients for the linear regression lines are somewhat larger for the stacked geometry. The calculated correlation coefficients for the stacked and planar geometries are 0.54 and 0.43 for the aug-cc-pVDZ basis set, 0.60 and 0.39 for the cc-pVTZ basis set and 0.64 and 0.45 for the aug-cc-pVTZ basis set. The large similarity observed supports the idea that in the cryosolutions, and maybe also in other solutions, the more compact stacked geometry is stabilized. Unfortunately, taking into consideration that for some of the modes the absolute values of the calculated complexation shifts vary

significantly, and taking into account that experimental values reported can be influenced for anharmonic effects, solvent effects and thermal effects[21,22], no solid conclusion can be drawn.

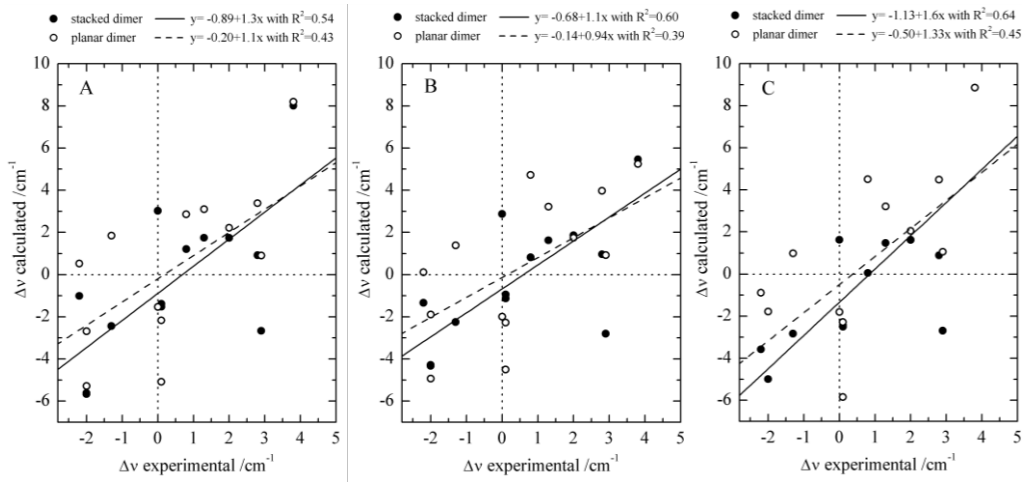

Figure 6.9 Linear fit of the experimental and calculated (A: MP2/aug-cc-pVDZ, B: MP2/cc-pVTZ, C: MP2/aug-cc-pVTZ) complexation shifts for the stacked (full circles) and the planar (open circles) acetone dimer with corresponding linear regression lines.

6.5 Conclusions

Using a data set of spectra of different concentrations at constant temperature, the vibrational spectrum of acetone in liquid Kr was resolved in a monomer and dimer contribution using a newly developed least-squares approach. The assignment of the monomer spectrum fully supports the assignments of the gas-phase spectrum of the compound made by Dellepiane[41]. It was observed that all spectral regions show dimer bands that overlap completely with the related monomer bands except for the dimer band assigned to the $\nu_{\mathrm{C-C\,as}}$ mode at 1222.7 cm^{-1} for which a complex band blue-shifted from the monomer band by 5.3 $cm^{-1}$is observed. For the first time a complete assignment of the experimental mid infrared spectrum of the acetone dimer was made. Using spectra recorded at different temperatures between 134 and 142 K, the experimental dimerization enthalpy was measured to be 10.8 ± 0.8 kJ mol^{-1}. *Ab initio* calculations predicted a stacked and planar dimer geometry of which the stacked geometry is more stable.

Complexation energies were obtained by combining the MP2 energies and single point corrections involving CCSD(T) calculations and Complete Basis Set extrapolations based on the MP2/aug-cc-pVDZ equilibrium geometry. These calculations lead to complexation energies of -28.4 kJ mol^{-1} for the stacked and -15.1 kJ mol^{-1} for the planar dimer. The corresponding values for the complexation enthalpies in solution, obtained by combining the energies with corrections for thermal and solvent influences are -13.7 and -5.8 kJ mol^{-1}. Additional data supporting the idea that the stacked geometry is strongly preferred in the cryosolutions was attempted by carefully comparing the experimental with theoretical complexation shifts obtained at the MP/aug-cc-pVDZ, MP2/cc-pVTZ and MP2/aug-cc-pVTZ levels. Unfortunately, because of the deviations observed between the values obtained from the different basis sets, and because the experimental values are often influenced by anharmonic, solvent and thermal effects, no unambiguous assignment or a specific geometry could be deduced.

References

[1] R. Peter and H. Dreizler, Z. Naturforsch., A: Phys. Sci., 20 (1965) 301-312.
[2] T. F. Lin, S. D. Christian and H. E. Affsprung, J. Phys. Chem., 71 (1967) 968-973.
[3] D. J. Frurip, L. A. Curtiss and M. Blander, J. Phys. Chem., 82 (1978) 2555-2561.
[4] B. Tiffon, B. Ancian and J.-E. Dubois, Chem. Phys. Lett., 73 (1980) 89-93.
[5] W. Schindler, P. T. Sharko and J. Jonas, J. Chem. Phys., 76 (1982) 3493-3496.
[6] E. Knözinger and R. Wittenbeck, J. Mol. Spectrosc., 105 (1984) 314-323.
[7] Y. Matsuda, K. Ohta, N. Mikami and A. Fujii, Chem. Phys. Lett., 471 (2009) 50-53.
[8] J. Guan, Y. Hu, M. Xie and E. R. Bernstein, Chem. Phys., 405 (2012) 117-123.
[9] Y. Tamenori, O. Takahashi, K. Yamashita, T. Yamaguchi, K. Okada, K. Tabayashi, T. Gejo and K. Honma, J. Chem. Phys., 131 (2009) 174311.
[10] M. R. Jalilian, Spectrochim. Acta A, 69 (2008) 812-815.
[11] G. Arivazhagan, A. Elangovan, R. Shanmugam, R. Vijayalakshmi and P. P. Kannan, Chem. Phys. Lett., 627 (2015) 101-106.
[12] B. J. van der Veken, S. N. Delanoye, B. Michielsen and W. A. Herrebout, J. Mol. Struct., 976 (2010) 97-104.
[13] S. N. Delanoye, W. A. Herrebout and B. J. van der Veken, J. Phys. Chem. A, 109 (2005) 9836-9843.

[14] D. Hauchecorne, N. Nagels, B. J. van der Veken and W. A. Herrebout, Phys. Chem. Chem. Phys., 14 (2012) 681-690.
[15] W. A. Herrebout, N. Nagels and B. J. van der Veken, ChemPhysChem, 10 (2009) 3054-3060.
[16] Y. Geboes, F. Proft and W. A. Herrebout, J. Phys. Chem. A, 119 (2015) 5597-5606.
[17] L. I. De Beuckeleer and W. A. Herrebout, J. Mol. Struct., 1108 (2016) 71-79.
[18] L. I. De Beuckeleer and W. A. Herrebout, Spectrochim. Acta A, 154 (2016) 89-97.
[19] D. Hauchecorne and W. A. Herrebout, J. Phys. Chem. A., 117 (2013) 11548-11557.
[20] L. Du and H. G. Kjaergaard, J. Phys. Chem. A, 115 (2011) 12097-12104.
[21] B. Michielsen, J. J. J. Dom, B. J. van der Veken, S. Hesse, Z. F. Xue, M. A. Suhm and W. A. Herrebout, Phys. Chem. Chem. Phys., 12 (2010) 14034-14044.
[22] B. Michielsen, J. J. J. Dom, B. J. van der Veken, S. Hesse, M. A. Suhm and W. A. Herrebout, Phys. Chem. Chem. Phys., 14 (2012) 6469-6478.
[23] B. Michielsen, C. Verlackt, B. J. van der Veken and W. A. Herrebout, J. Mol. Struct., 1023 (2012) 90-95.
[24] P. Van Ginderen, W. A. Herrebout and B. J. van der Veken, J. Phys. Chem. A, 107 (2003) 5391-5396.
[25] E. J. Sluyts and B. J. van der Veken, J. Am. Chem. Soc., 118 (1996) 440-445.
[26] W. Herrebout, Top. Curr. Chem., 358 (2015) 79-154.
[27] MATLAB 8.3, The MathWorks Inc., Natick, MA, USA, 2014.
[28] B. J. van der Veken and F. R. De Munck, J. Chem. Phys., 97 (1992) 3060-3071.
[29] B. J. van der Veken, J. Phys. Chem., 100 (1996) 17436-17438.
[30] S. N. Delanoye, W. A. Herrebout and B. J. van der Veken, J. Am. Chem. Soc., 124 (2002) 11854-11855.
[31] W. A. Herrebout, S. N. Delanoye, B. U. Maes and B. J. van der Veken, J. Phys. Chem. A, 110 (2006) 13759-13768.
[32] M. J. Frisch, G. W. Trucks, H. B. Schlegel, G. E. Scuseria, M. A. Robb, J. R. Cheeseman, G. Scalmani, V. Barone, B. Mennucci, G. A. Petersson, *et al.*, Gaussian 09, Revision A.02, Gaussian, Inc., Wallingford, CT, USA, 2009.
[33] S. F. Boys and F. Bernardi, Mol. Phys., 19 (1970) 553-566.
[34] H.-J. Werner, P. J. Knowles, G. Knizia, F. R. Manby, M. Schütz, P. Celani, T. Korona, R. Lindh, A. Mitrushenkov, G. Rauhut, *et al.*, MOLPRO, version 2012.1, A Package of *ab Initio* Programs, 2012.
[35] D. G. Truhlar, Chem. Phys. Lett., 294 (1998) 45-48.
[36] P. Jurečka and P. Hobza, J. Am. Chem. Soc., 125 (2003) 15608-15613.
[37] J. Řezáč, K. E. Riley and P. Hobza, J. Chem. Theory Comput., 8 (2012) 4285-4292.
[38] J. H. Knox, *Molecular Thermodynamics*, John Wiley & Sons Ltd, New York, 1971.
[39] W. L. Jorgensen, BOSS - Biochemical and Organic Simulation System, in: P. v. R. Schleyer (Ed.) Encyclopedia of Computational Chemistry, John Wiley & Sons Ltd, New York, 1998, pp. 3281-3285.

[40] R. S. Mulliken, J. Chem. Phys., 23 (1955) 1997.
[41] G. Dellepiane and J. Overend, Spectrochim. Acta, 22 (1966) 593-614.
[42] J. D. Rogers, B. Rub, S. Goldman and W. B. Person, J. Phys. Chem., 85 (1981) 3727-3729.
[43] S. W. Han and K. Kim, J. Phys. Chem., 100 (1996) 17124-17132.
[44] K. Sundararajan and N. Ramanathan, J. Mol. Struct., 833 (2007) 150-160.
[45] P. Cossee, J. Chem. Phys., 44 (1966) 97-111.
[46] Y. G. Smeyers, M. L. Senent, V. Botella and D. C. Moule, J. Chem. Phys., 98 (1993) 2754-2767.
[47] K. Consani, J. Phys. Chem., 91 (1987) 5586-5588.
[48] B. J. van der Veken and W. A. Herrebout, J. Phys. Chem. A, 105 (2001) 7198-7204.
[49] A. I. Fishman, W. A. Herrebout and B. J. van der Veken, J. Phys. Chem. A, 106 (2002) 4536-4542.
[50] M. T. Forel and M. Fouassier, Spectrochim. Acta A, 23 (1967) 1977-1980.
[51] M. Mailloux, J. Weinman and S. Weinman, C. R. Acad. Sci. C Chim., 276 (1973) 379-382.
[52] Y. Geboes, N. Nagels, B. Pinter, F. De Proft and W. A. Herrebout, J. Phys. Chem. A, 119 (2015) 2502-2516.
[53] N. Nagels, Y. Geboes, B. Pinter, F. De Proft and W. A. Herrebout, Chem. Eur. J., 20 (2014) 8433-8443.
[54] B. Ancian, B. Tiffon and J.-E. Dubois, Chem. Phys., 74 (1983) 171-177.
[55] F. Kollipost, A. V. Domanskaya and M. A. Suhm, J. Phys. Chem. A, 119 (2015) 2225-2232.
[56] J. M. Hermida-Ramón and M. A. Ríos, J. Phys. Chem. A, 102 (1998) 2594-2602.

Supporting information

Table S6.1 Cartesian coordinates of the optimized geometry of the acetone monomer at MP2/aug-cc-pVDZ level.

	X	Y	Z
Acetone			
C	0.000000	0.000000	0.180083
O	0.000000	0.000000	1.411068
C	0.000000	1.291622	-0.617403
H	0.887011	1.328841	-1.271370
H	-0.887011	1.328841	-1.271370
H	0.000000	2.152710	0.062635
C	0.000000	-1.291622	-0.617403
H	-0.887011	-1.328841	-1.271370
H	0.887011	-1.328841	-1.271370
H	0.000000	-2.152710	0.062635

Table S6.2 Cartesian coordinates of the optimized geometry of the stacked acetone dimer at MP2/aug-cc-pVDZ level.

	X	Y	Z
Stacked dimer			
C	1.589042	0.000000	0.347958
O	1.006342	0.000000	1.435801
C	1.946459	-1.289217	-0.362706
H	1.380152	-1.337897	-1.307965
H	3.019721	-1.304485	-0.613366
H	1.693918	-2.151162	0.268573
C	1.946459	1.289217	-0.362706
H	3.019721	1.304486	-0.613365
H	1.380152	1.337897	-1.307965
H	1.693918	2.151162	0.268574
C	-1.589090	0.000000	-0.347984
O	-1.006333	0.000000	-1.435797
C	-1.946450	1.289217	0.362711
H	-3.019715	1.304528	0.613349
H	-1.380164	1.337853	1.307985
H	-1.693858	2.151166	-0.268543
C	-1.946450	-1.289217	0.362711
H	-1.380164	-1.337853	1.307985
H	-3.019715	-1.304528	0.613349
H	-1.693858	-2.151166	-0.268543

Table S6.3 Cartesian coordinates of the optimized geometry of the planar acetone dimer at MP2/aug-cc-pVDZ level.

	X	Y	Z
Planar dimer			
C	-2.425872	-0.099238	-0.005140
O	-1.749819	-1.129280	-0.045976
C	3.923226	0.148672	0.240727
H	4.147580	-0.321474	1.213014
H	4.457149	-0.430643	-0.530117
H	4.271922	1.189297	0.244859
C	1.812038	-1.272376	-0.200073
H	2.173984	-1.690826	-1.155199
H	2.148311	-1.956501	0.59641
H	0.715546	-1.212528	-0.214214
C	2.425873	0.099238	-0.005145
O	1.749819	1.129281	-0.045980
C	-1.812038	1.272376	-0.200072
H	-2.14831	1.956502	0.596411
H	-0.715546	1.212528	-0.214214
H	-2.173986	1.690824	-1.155198
C	-3.923227	-0.148673	0.240727
H	-4.147583	0.321473	1.213013
H	-4.457147	0.430643	-0.530119
H	-4.271922	-1.189297	0.244857

Table S6.4 Calculated symmetries, wavenumbers (in cm^{-1}), infrared intensities (in km mol^{-1}) and complexation shifts (in cm^{-1}) at MP2/aug-cc-pVDZ level for the fundamental vibrational modes of the acetone monomer, and with counterpoise correction for the stacked dimer and planar dimer.

	monomer C_{2v}			stacked dimer			planar dimer		
	symmetry	$\tilde{\nu}$	intensity	$\tilde{\nu}$	intensity	$\Delta\tilde{\nu}$	$\tilde{\nu}$	intensity	$\Delta\tilde{\nu}$
ν_1	A_1	3199.6	4.6	3194.3	0.0	-5.3	3196.9	16.1	-2.7
				3194.0	10.9	-5.7	3196.9	0.1	-2.7
ν_{18}	B_2	3198.8	9.8	3193.2	21.4	-5.6	3193.5	10.3	-5.3
				3192.6	0.0	-6.1	3192.6	0.3	-6.2
ν_{13}	B_1	3149.9	14.9	3153.5	0.0	3.6	3148.4	22.3	-1.5
				3152.9	19.6	3.0	3148.3	1.1	-1.6
ν_9	A_2	3144.0	0.0	3147.4	0.0	3.4	3139.9	5.1	-4.1
				3147.4	0.5	3.4	3139.8	2.4	-4.2
ν_2	A_1	3065.4	7.2	3064.1	0.0	-1.3	3063.4	0.1	-2.1
				3063.9	11.8	-1.5	3063.3	20.4	-2.2
ν_{19}	B_2	3061.0	1.5	3060.1	0.0	-0.9	3055.9	0.3	-5.1
				3059.6	3.9	-1.4	3055.9	22.5	-5.1
ν_3	A_1	1731.5	125.3	1730.5	219.0	-1.0	1732.0	272.3	0.5
				1723.2	0.0	-8.3	1726.4	0.3	-5.1
ν_{14}	B_1	1480.3	18.4	1483.4	0.0	3.1	1486.8	25.5	6.5
				1478.1	35.4	-2.2	1484.0	2.9	3.7
ν_4	A_1	1457.4	29.0	1458.3	78.9	0.9	1462.8	1.8	5.4
				1457.6	2.0	0.2	1460.8	17.7	3.4
ν_{10}	A_2	1454.2	0.0	1457.5	0.0	3.2	1456.7	0.8	2.4
				1452.8	0.0	-1.5	1455.0	35.4	0.8
ν_{20}	B_2	1448.8	0.1	1448.6	0.0	-0.3	1451.3	0.3	2.5
				1446.1	0.4	-2.7	1449.7	0.6	0.9
ν_{21}	B_2	1385.1	70.8	1386.3	145.9	1.2	1388.5	6.8	3.4
				1385.8	0.0	0.7	1387.9	114.1	2.9
ν_5	A_1	1368.6	12.6	1366.2	47.1	-2.4	1371.7	0.9	3.1
				1364.9	0.0	-3.8	1370.5	37.4	1.8
ν_{22}	B_2	1248.1	42.5	1254.2	53.9	6.1	1255.2	2.9	7.1
				1248.5	0.0	0.4	1251.8	90.1	3.7
ν_{15}	B_1	1097.3	1.2	1100.1	0.0	2.8	1099.5	2.0	2.2
				1099.0	9.6	1.7	1099.0	0.0	1.7
ν_6	A_1	1071.4	0.0	1075.5	0.0	4.0	1074.6	0.7	3.2
				1074.7	0.0	3.2	1073.1	0.0	1.7
ν_{23}	B_2	893.6	4.2	901.7	6.5	8.0	902.1	0.7	8.5
				901.4	0.0	7.7	901.8	8.4	8.2

ν_{11}	A_2	873.2	0.0	873.2	0.2	0.0	875.6	0.0	2.4
				871.7	0.0	-1.4	874.1	0.2	0.9
ν_7	A_1	807.2	1.3	812.0	1.2	4.8	809.3	0.0	2.2
				811.5	0.0	4.3	807.8	4.1	0.7
ν_{24}	B_2	527.1	14.8	528.8	26.8	1.7	530.2	33.1	3.1
				527.6	0.0	0.5	529.6	0.6	2.5
ν_{16}	B_1	479.9	0.5	486.7	0.0	6.8	482.3	0.1	2.4
				479.4	1.4	-0.5	481.2	1.2	1.3
ν_8	A_1	376.4	1.3	381.1	0.0	4.8	383.2	5.0	6.9
				379.6	2.0	3.2	381.0	0.0	4.6
ν_{17}	B_1	145.7	0.1	155.3	0.0	9.6	156.6	0.2	10.9
				151.9	0.7	6.1	150.1	0.1	4.4
ν_{12}	A_2	20.6	0.0	101.3	28.1		98.5	0.0	
				94.3	0.0		95.1	0.0	
				72.6	0.0		74.3	0.0	
				66.7	0.4		67.8	13.8	
				64.1	0.0		55.0	0.1	
				52.1	0.0		24.7	11.2	
				50.3	0.4		24.6	0.3	
				20.7	5.0		12.3	1.4	

Table S6.5 Cartesian coordinates of the optimized geometry of the acetone monomer at MP2/ cc-pVTZ level.

	X	Y	Z
Acetone			
C	0.00000000	0.00000000	0.18355300
O	0.00000000	0.00000000	1.40092500
C	0.00000000	1.28098500	-0.61455700
H	0.87651500	1.31731400	-1.26132100
H	-0.87651500	1.31731400	-1.26132100
H	0.00000000	2.13424700	0.05562700
C	0.00000000	-1.28098500	-0.61455700
H	-0.87651500	-1.317314 -	1.26132100
H	0.87651500	-1.31731400	-1.26132100
H	0.00000000	-2.13424700	0.05562700

Table S6.6 Cartesian coordinates of the optimized geometry of the stacked acetone dimer at MP2/cc-pVTZ level.

	X	Y	Z
Stacked dimer			
C	1.58286500	0.00000000	-0.34469100
O	1.03282600	0.00000400	-1.43407100
C	1.92459200	1.27856400	0.37423200
H	1.34541400	1.32671100	1.29674500
H	2.97970000	1.29280800	0.64532400
H	1.68955300	2.13265300	-0.25305500
C	1.92457700	-1.27856900	0.37422900
H	2.97968600	-1.29282800	0.64531800
H	1.34540200	-1.32671200	1.29674500
H	1.68952500	-2.13265400	-0.25305900
C	-1.58286600	0.00000100	0.34469200
O	-1.03283000	0.00000300	1.43407400
C	-1.92457900	-1.27856600	-0.37423200
H	-2.97968800	-1.29282500	-0.64531800
H	-1.34540600	-1.32670300	-1.29674900
H	-1.68952500	-2.13265400	0.25305200
C	-1.92458700	1.27856500	-0.37423200
H	-1.34540300	1.32671300	-1.29674200
H	-2.97969300	1.29281100	-0.64533100
H	-1.68955100	2.13265400	0.25305700

Table S6.7 Cartesian coordinates of the optimized geometry of the planar acetone dimer at MP2/cc-pVTZ level.

	X	Y	Z
Planar dimer			
C	2.422333	0.103791	-0.004474
O	1.759708	1.126503	-0.040647
C	3.913235	0.138096	0.22933
H	4.138856	-0.325373	1.190158
H	4.431995	-0.440651	-0.534143
H	4.26696	1.163961	0.228456
C	1.807763	-1.258621	-0.193213
H	2.15306	-1.6733	-1.14149
H	2.144704	-1.937886	0.589381
H	0.723658	-1.196362	-0.196634
C	-2.422343	-0.103795	-0.004563
O	-1.75971	-1.126504	-0.040679
C	-1.807762	1.258622	-0.193231
H	-2.144718	1.937864	0.589379
H	-0.723658	1.196363	-0.19663
H	-2.15304	1.673331	-1.141501
C	-3.91323	-0.138095	0.229332
H	-4.138803	0.325389	1.190165
H	-4.432028	0.440641	-0.534123
H	-4.266956	-1.163959	0.228492

Table S6.8 Calculated symmetries, wavenumbers (in cm^{-1}), infrared intensities (in km mol^{-1}) and complexation shifts (in cm^{-1}) at MP2/cc-pVTZ level for the fundamental vibrational modes of the acetone monomer, and with counterpoise correction for the stacked dimer and planar dimer.

	monomer C_{2v}			stacked dimer			planar dimer		
	symmetry	$\tilde{\nu}$	intensity	$\tilde{\nu}$	intensity	$\Delta\tilde{\nu}$	$\tilde{\nu}$	intensity	$\Delta\tilde{\nu}$
ν_1	A_1	3206.7	3.6	3202.7	0.0	-4.0	3204.8	13.1	-1.9
				3202.4	8.8	-4.3	3204.8	0.1	-1.9
ν_{18}	B_2	3205.7	7.7	3201.4	17.5	-4.3	3200.7	10.0	-4.9
				3200.9	0.0	-4.8	3199.7	0.3	-5.9
ν_{13}	B_1	3161.5	11.9	3164.9	0.0	3.4	3159.5	18.6	-2.0
				3164.4	15.2	2.9	3159.5	0.8	-2.0
ν_9	A_2	3155.6	0.0	3158.9	0.0	3.3	3151.8	3.7	-3.8
				3158.8	0.6	3.2	3151.7	2.4	-3.9
ν_2	A_1	3080.6	5.1	3079.7	0.0	-0.9	3078.5	0.0	-2.2
				3079.5	8.8	-1.1	3078.4	17.0	-2.3
ν_{19}	B_2	3076.0	1.2	3075.5	0.0	-0.5	3071.5	3.8	-4.5
				3075.0	3.1	-0.9	3071.5	13.6	-4.5
ν_3	A_1	1774.7	113.1	1773.3	193.0	-1.3	1774.8	244.7	0.1
				1766.1	0.0	-8.6	1769.1	0.2	-5.6
ν_{14}	B_1	1504.9	19.6	1507.9	0.0	3.0	1512.0	29.2	7.2
				1502.4	37.8	-2.5	1508.8	2.6	3.9
ν_4	A_1	1483.3	27.7	1484.2	76.6	1.0	1489.0	2.4	5.7
				1484.9	1.2	1.7	1487.2	9.9	4.0
ν_{10}	A_2	1481.6	0.0	1483.3	0.0	1.7	1483.5	0.7	1.9
				1479.7	0.0	-1.9	1481.4	39.4	-0.2
ν_{20}	B_2	1475.1	0.2	1474.9	0.0	-0.2	1477.5	0.2	2.3
				1472.3	0.5	-2.8	1476.1	1.3	0.9
ν_{21}	B_2	1397.0	71.4	1397.9	151.7	0.8	1402.8	5.4	5.8
				1397.3	0.0	0.3	1401.8	107.9	4.7
ν_5	A_1	1386.7	14.8	1384.4	52.2	-2.3	1389.0	1.6	2.3
				1383.5	0.0	-3.2	1388.1	51.0	1.4
ν_{22}	B_2	1253.2	53.8	1260.3	74.0	7.2	1259.8	3.5	6.6
				1253.9	0.0	0.7	1256.5	113.1	3.3
ν_{15}	B_1	1118.8	1.6	1121.9	0.0	3.0	1120.6	3.0	1.7
				1120.7	11.4	1.9	1119.9	0.0	1.1
ν_6	A_1	1084.1	0.0	1088.0	0.0	3.9	1087.3	0.5	3.1
				1087.1	0.1	3.0	1085.9	0.0	1.8

				Acetone					
ν_{23}	B_2	901.8	5.4	907.2	7.9	5.5	907.2	0.8	5.4
				906.8	0.0	5.1	907.0	10.9	5.3
ν_{11}	A_2	887.5	0.0	887.6	0.7	0.1	891.0	0.0	3.5
				885.8	0.0	-1.7	889.5	0.2	2.0
ν_7	A_1	805.7	1.7	810.7	1.6	5.0	808.0	0.0	2.3
				810.1	0.0	4.4	806.6	4.7	0.9
ν_{24}	B_2	530.3	14.8	531.9	27.1	1.6	533.5	33.0	3.2
				530.7	0.0	0.4	532.7	0.6	2.4
ν_{16}	B_1	484.7	0.3	491.5	0.0	6.8	487.5	0.2	2.8
				485.8	0.8	1.1	486.4	0.8	1.7
ν_8	A_1	376.1	1.0	380.7	0.0	4.6	382.7	4.2	6.6
				379.0	1.6	2.9	380.7	0.0	4.6
ν_{17}	B_1	143.2	0.0	152.8	0.0	9.6	153.6	0.1	10.3
				152.1	0.3	8.9	147.3	0.1	4.1
ν_{12}	A_2	15.7	0.0	101.0	25.2		100.6	0.0	
				90.7	0.0		97.5	0.0	
				73.9	0.0		69.6	0.0	
				66.5	0.5		64.7	12.1	
				63.0	0.0		53.8	0.1	
				54.3	0.0		27.0	0.2	
				46.7	0.7		23.2	9.5	
				22.5	4.1		13.6	1.7	

Table S6.9 Cartesian coordinates of the optimized geometry of the acetone monomer at MP2/aug-cc-pVTZ level.

	X	Y	Z
Acetone			
C	0.00000000	0.00000000	0.18196800
O	0.00000000	0.00000000	1.40168000
C	0.00000000	1.28144200	-0.61420700
H	0.87724600	1.31559200	-1.26145600
H	-0.87724600	1.31559200	-1.26145600
H	0.00000000	2.13592600	0.05552900
C	0.00000000	-1.28144200	-0.61420700
H	-0.87724600	-1.315592 -	1.26145600
H	0.87724600	-1.31559200	-1.26145600
H	0.00000000	-2.13592600	0.05552900

Table S6.10 Cartesian coordinates of the optimized geometry of the stacked acetone dimer at MP2/aug-cc-pVTZ level.

	X	Y	Z
Stacked dimer			
C	1.55841200	-0.00000100	0.34916800
O	0.98874100	-0.00000900	1.43182700
C	1.90864100	-1.27904700	-0.36274300
H	1.33325700	-1.32710000	-1.28898400
H	2.96591500	-1.28888800	-0.62849800
H	1.67197200	-2.13408900	0.26392100
C	1.90861800	1.27905800	-0.36273000
H	2.96589800	1.28894000	-0.62845700
H	1.33325500	1.32708700	-1.28898400
H	1.67190000	2.13409300	0.26392600
C	-1.55841600	-0.00000200	-0.34917000
O	-0.98874200	-0.00000400	-1.43183000
C	-1.90862200	1.27905200	0.36273600
H	-2.96590100	1.28892000	0.62847500
H	-1.33325000	1.32709600	1.28898400
H	-1.67192300	2.13408500	-0.26392800
C	-1.90863400	-1.27905100	0.36274100
H	-1.33326000	-1.32708800	1.28899000
H	-2.96591200	-1.28891700	0.62848100
H	-1.67193500	-2.13408900	-0.26391500

Table S6.11 Cartesian coordinates of the optimized geometry of the planar acetone dimer at MP2/cc-pVTZ level.

	X	Y	Z
Planar dimer			
C	2.396806	0.101712	-0.005143
O	1.72939	1.124278	-0.046492
C	3.884874	0.143293	0.240836
H	4.102881	-0.326818	1.201103
H	4.410481	-0.43028	-0.522987
H	4.235594	1.170872	0.248846
C	1.787523	-1.261401	-0.199606
H	2.145473	-1.673229	-1.14549
H	2.121821	-1.938899	0.586782
H	0.702223	-1.20391	-0.212863
C	-2.396807	-0.101712	-0.00514
O	-1.729391	-1.124279	-0.046493
C	-1.787521	1.261401	-0.199601
H	-2.121822	1.938901	0.586784
H	-0.702221	1.20391	-0.212855
H	-2.145468	1.673225	-1.145487
C	-3.884874	-0.143292	0.240835
H	-4.102883	0.326826	1.201099
H	-4.410481	0.430275	-0.522992
H	-4.235594	-1.170871	0.248853

Table S6.12 Calculated symmetries, wavenumbers (in cm^{-1}), infrared intensities (in km mol^{-1}) and complexation shifts (in cm^{-1}) at MP2/aug-cc-pVTZ level for the fundamental vibrational modes of the acetone monomer, and with counterpoise correction for the stacked dimer and planar dimer.

	monomer C_{2v}			stacked dimer			planar dimer		
	symmetry	$\tilde{\nu}$	intensity	$\tilde{\nu}$	intensity	$\Delta\tilde{\nu}$	$\tilde{\nu}$	intensity	$\Delta\tilde{\nu}$
ν_1	A_1	3200.9	2.9	3196.3	0.0	-4.6	3199.1	12.0	-1.8
				3195.9	8.3	-5.0	3199.1	0.1	-1.8
ν_{18}	B_2	3199.9	7.6	3194.9	16.7	-5.0	3192.0	15.8	-7.9
				3194.5	0.0	-5.5	3190.8	0.4	-9.2
ν_{13}	B_1	3154.7	10.1	3156.9	0.0	2.2	3152.9	14.8	-1.8
				3156.3	11.8	1.6	3152.9	0.7	-1.8
ν_9	A_2	3148.9	0.0	3151.0	0.0	2.0	3144.7	3.5	-4.3
				3150.8	0.7	1.9	3144.6	2.5	-4.4
ν_2	A_1	3074.4	5.3	3072.2	0.0	-2.3	3072.2	0.0	-2.2
				3071.9	9.9	-2.5	3072.2	15.5	-2.3
ν_{19}	B_2	3070.0	0.8	3068.2	0.0	-1.8	3064.1	24.9	-5.8
				3067.6	2.5	-2.4	3064.0	0.2	-5.9
ν_3	A_1	1756.2	130.2	1752.7	222.7	-3.6	1755.3	281.8	-0.9
				1743.9	0.0	-12.4	1749.2	0.3	-7.1
ν_{14}	B_1	1509.0	19.5	1512.1	0.0	3.1	1515.9	27.0	6.9
				1506.3	37.1	-2.7	1512.9	2.6	3.9
ν_4	A_1	1486.5	31.4	1487.4	84.2	0.9	1492.7	2.7	6.2
				1488.3	1.5	1.9	1491.0	14.2	4.5
ν_{10}	A_2	1485.1	0.0	1486.6	0.0	1.5	1485.9	0.6	0.8
				1482.8	0.0	-2.3	1483.9	43.6	-1.1
ν_{20}	B_2	1478.3	0.3	1478.4	0.0	0.1	1480.8	0.1	2.6
				1475.6	0.7	-2.7	1479.3	1.0	1.1
ν_{21}	B_2	1400.5	64.4	1400.5	136.6	0.1	1406.3	4.9	5.8
				1400.2	0.0	-0.3	1405.0	91.6	4.5
ν_5	A_1	1392.2	14.9	1389.4	54.0	-2.8	1394.0	2.0	1.8
				1388.3	0.0	-3.9	1393.2	52.5	1.0
ν_{22}	B_2	1254.5	52.9	1262.2	70.6	7.6	1261.6	3.7	7.0
				1255.9	0.0	1.3	1258.3	110.9	3.8
ν_{15}	B_1	1121.2	1.6	1123.9	0.0	2.7	1123.2	2.8	2.0
				1122.8	12.2	1.6	1122.6	0.0	1.4
ν_6	A_1	1087.0	0.0	1091.0	0.0	3.9	1090.4	0.6	3.4
				1090.1	0.0	3.1	1089.1	0.0	2.0

ν_{23}	B_2	901.8	5.4	912.0	7.5	10.3	910.8	0.9	9.1
				911.6	0.0	9.9	910.6	10.6	8.9
ν_{11}	A_2	892.0	0.0	890.5	1.0	-1.4	894.6	0.0	2.6
				889.2	0.0	-2.8	893.1	0.2	1.1
ν_7	A_1	806.4	1.6	811.7	1.6	5.3	809.0	0.0	2.5
				811.1	0.0	4.7	807.4	4.8	1.0
ν_{24}	B_2	531.3	14.4	533.2	25.9	1.9	534.5	32.4	3.2
				531.8	0.0	0.5	533.9	0.6	2.6
ν_{16}	B_1	484.4	0.5	492.1	0.0	7.6	487.5	0.2	3.1
				484.2	1.3	-0.2	486.4	1.1	2.0
ν_8	A_1	377.3	1.3	382.3	0.0	5.0	384.7	5.1	7.5
				380.4	2.0	3.1	382.2	0.0	4.9
ν_{17}	B_1	140.8	0.1	153.7	0.0	12.9	153.4	0.2	12.6
				150.0	0.7	9.2	146.7	0.1	5.9
ν_{12}	A_2	24.5	0.0	109.8	28.9		98.9	0.0	
				98.3	0.0		95.5	0.0	
				80.6	0.0		76.1	0.0	
				72.8	0.5		70.2	14.2	
				66.8	0.0		54.8	0.1	
				57.7	0.0		24.5	11.1	
				55.9	0.4		23.8	0.3	
				21.3	5.1		12.1	1.6	

Chapter 7

A characterization of the halogen bonded complexes of CF_3X (X = I or Br) with dimethyl ether and acetone in cryosolutions

This chapter will be submitted as
De Beuckeleer, L. I.; Herrebout, W. A., *Dimers or higher associations? A characterization of the halogen bonded complexes of CF_3X (X = I or Br) with dimethyl ether and acetone in cryosolutions.*

Abstract

Acetone molecules dissolved in liquid krypton are inclined to self-associate into dimers. This behavior affects its use as a prototype Lewis base in studies of weak intermolecular interactions. In this study infrared spectra of mixed solutions of dimethyl ether and CF_3X and of acetone and CF_3X (with X = I or Br) dissolved in liquid argon and liquid krypton are recorded at constant temperature. The dataset for dimethyl ether is used to validate a numerical method based on least-squares fitting of a model including contributions of both monomers and a heterodimer with 1:1 stoichiometry. The resulting monomer and dimer spectra show excellent agreement with previous studies found in literature. The analysis of the dataset for acetone requires an extension of the model with contributions for the acetone homodimer and for the $(acetone)_2 \cdot CF_3X$ and $acetone \cdot (CF_3X)_2$ trimers. The results show that many signals for $(acetone)_2 \cdot CF_3I$ are observed, while only a few bands due to $acetone \cdot (CF_3I)_2$ occur. The use of numerical approaches adjusted to the specificities of a mixture of two compounds allows to reliably resolve overlapping spectra of monomers and heterocomplexes and characterizing heterocomplex features that could not be deduced using earlier methods. To support the assignments made, *ab initio* calculations predicting geometries, relative stabilities and harmonic vibrational frequencies for the species envisaged are performed.

7.1 Introduction

Solutions in liquefied inert gases have proven to be an ideal medium to study molecular complexes held together by weak and medium-strong interactions.[1] They create a weakly interacting environment that, combined with the low temperatures used, leads to small bandwidths and thus facilitates the detection of complex bands only slightly shifted from the monomer modes. This advantage makes it possible to thoroughly investigate heterocomplexes involving an electron rich Lewis base and an electron deficient region related to a hydrogen bond[2-4], a halogen bond[4-7] or a lone pair-π acceptor[8] under equilibrium conditions. In addition, experimental data can be derived for homocomplexes where two or more identical molecules associate.[9-11]

For heterocomplexes, experimental evidence for the formation on complexes is typically obtained by carefully comparing spectra of monomers and mixtures and by the observation of new bands appearing upon mixing. Moreover, more accurate data is obtained using so-called subtraction procedures in which spectra of the monomers recorded under identical circumstances are multiplied by a scaling factor and subsequently subtracted from the spectrum of the mixture. The value of this scaling factor is such that, after subtraction, no features due to the monomers are withheld and that the remaining spectrum thus solely contains bands assigned to the complexes formed.[1] For homocomplexes, experimental evidence is typically found by carefully analyzing spectral changes occurring while changing temperature and/or concentration of the solute. Because in many cases, including much diluted solutions, both monomers and homocomplexes are present simultaneously, the traditional subtraction procedure discussed above cannot be used, and thus more sophisticated numerical methods must be applied. A typical example of such a method involves the fitting of measured absorbances, for each wavenumber, to monomer absorbances determined at one or more reference wavenumbers. This method was successfully validated and applied to prototypes of hydrogen bonding such as HCl and pyrrole clusters.[9,10] A similar approach was recently used to analyze the spectra of solutions of acetone in liquid krypton.[11] The results lead to the conclusion that at the temperature studied a large

fraction of the acetone molecules present are involved in dimer formation, and yield a spectrum that is quite similar to and only slightly shifted from that of the monomers.

The observation of a large fraction of acetone molecules being involved in dimer formation obviously affects its use as a prototype Lewis base in studies of heterocomplexes. Results obtained from mixed solutions containing acetone and typical hydrogen and halogen bonding donors therefore should not be tackled using the routine approaches but require a dedicated approach in which the contributions of monomer acetone, dimer acetone and their complexes with the acceptor molecule are separated using more sophisticated numerical approaches. In the following paragraphs we report on the development and validation of an extended least-squares based model, based on the experience gathered while studying the prototypes for hydrogen bonding and the acetone dimer formation in solutions, allowing such analysis to be performed on a routine basis.

The first part of the study involves the development of the model and the applications towards the study of halogen bonded complexes formed between dimethyl ether and the trifluoromethyl halides CF_3Br and CF_3I. The spectral properties of these complexes have been described in detail before[12] and are considered to be excellent test cases involving two monomers and a single complex with a 1:1 stoichiometry. The second part of the study involves the application of the model towards the complexes formed between acetone and the same halogen bond donors. Such complexes have not been reported before but are considered ideal test cases for more complex solutions contain possibly six different species, i.e. acetone, CF_3X, $(acetone)_2$, acetone$\cdot CF_3X$, $(acetone)_2\cdot CF_3X$ and. acetone$\cdot(CF_3X)_2$. To support the rationalization of the results obtained, and to support the idea of different complexes species present, the experimental studies are supported by standard *ab initio* methods in which the spectroscopic properties of the species studied are predicted.

7.2 Experimental section

The samples of trifluoromethyliodide (CF_3I, 99%) and dimethyl ether (DME, 99%) were purchased from Sigma Aldrich. The samples of trifluorobromide (CF_3Br, 99%) and acetone ($(CH_3)_2CO$, 99,5%) were purchased from Pfaltz & Bauer and Acros respectively. All samples were used without further purification. The cryosolvents argon and krypton had stated purities of 99.9999% and 99.9995% respectively and were supplied by Air Liquide.

Infrared spectra were recorded on a Bruker IFS 66v Fourier transform spectrometer. A Globar source was used in combination with a Ge/KBr beamsplitter and a LN_2-cooled broad band MCT detector. All interferograms were averaged over 500 scans, Blackman-Harris 3-term apodized and Fourier transformed with a zero filling factor of 4 to yield spectra with a resolution of 0.5 cm^{-1}. The experimental set-up used to investigate the solutions in liquid noble gases has been described before [1]. In the actual cryostat, a liquid cell with 1 cm path length and equipped with wedged Si windows was mounted below a LN_2 dewar. The temperature of the cell body is measured using a Pt-100 thermoresistor. The SunRod electric minicartridge heater is controlled using a Eurotherm 3504 PID controller. The temperatures of the argon and krypton solutions were stabilized at 103 K and 138 K respectively. The temperature variation during a typical run is less than 0.05 K. Spectra were obtained and preanalyzed using OPUS 6.5. Further calculations were performed using Matlab.[13]

The data sets recorded consist of 328 spectra for mixtures of CF_3I and DME in liquid argon (LAr), 200 spectra for mixtures of CF_3Br and DME in LAr and, 274 spectra for mixtures of CF_3I and acetone in liquid krypton (LKr). For each set, spectra were measured for a series of different concentrations and concentration ratios. The mole fractions of the species used are difficult to accurately quantify[14,15], but are estimated to vary between 1.1×10^{-4} to 2.9×10^{-3} for CF_3X, between 9.6×10^{-5} for 3.1×10^{-3} for DME and between 1.1×10^{-4} for 4.3×10^{-4} for acetone. To maximize the amount of species dissolved, the temperature of the solution in LAr was increased to 111 K after filling the cell at 103 K and was subsequently stabilized at 103 K. For the solutions in LKr, solutions were prepared at 123 K, heated to 160 K, and stabilized at 138 K. The

concentrations and concentration ratios used are chosen so that the region between minimum and maximum absorbance for both monomers is uniformly covered.

A critical parameter often hampering numerical analyses is related to small traces of solid, amorphous or crystalline, water particles suspended in the solution or condensed onto the cold elements present in the cryostat and/or detector. These traces are observed to slightly vary during experiments, and, due to changes in relative absorbances, are difficult to subtract. Therefore, no additional corrections were introduced. To account for baseline drifts, which we believe are due to small temperature changes inside the spectrometer due to the colder parts present, straight line baseline corrections were applied to all data. These lines are defined by connecting points where the absorbance is expected to be zero. For the mixtures of DME and CF_3I, a single straight line was used from 2670 to 1955 cm^{-1}, while for the mixtures of DME and CF_3Br, two straight lines were defined, from 2470 to 1790 and from 1790 to 495 cm^{-1}, respectively. For the solutions of acetone and CF_3I in LKr, a series of straight lines was defined, the limits for the intervals used being 3752, 3057, 2876, 2812, 2667, 1940, 1645, and 960 cm^{-1}.

7.3 Results and discussion

7.3.1 General methodology

Recently we developed and validated a robust numerical approach that enables the investigation of spectra in which spectral features due to monomers and homocomplexes are present simultaneously, and in which monomer absorbances cannot be accurately determined using traditional subtraction procedures.[9] In this method the monomeric and different oligomeric contributions are obtained by fitting the measured absorbances, for each wavenumber, to monomer absorbances using a higher order polynomial. The new approach is based on the fact that, with some exceptions[16,17], cryosolutions are known to be in thermodynamical equilibrium. For the formation of homocomplexes the equilibrium reaction and the equilibrium constant K_p can be written as

$$pA \rightleftharpoons A_p \qquad K_p = \frac{C_{A_p}}{C_A^p} \tag{7.1}$$

with the equilibrium concentrations *C* and *p* the number of molecules in the complex. The spectra of the mixtures of species in cryosolutions can be seen as a superposition of monomer spectra and spectra of possible complexes, so that the measured absorbance at a wavenumber $\tilde{\nu}_i$, $A_{exp}(\tilde{\nu}_i)$ equals the sum of individual contributions related to the monomer, A_1 or to one of the oligomers, e.g. dimer A_2, trimer A_3, tetramer A_4, etc., i.e.

$$A_{exp}(\tilde{\nu}_i) = A_1(\tilde{\nu}_i) + A_2(\tilde{\nu}_i) + A_3(\tilde{\nu}_i) + A_4(\tilde{\nu}_i) + \cdots \tag{7.2}$$

The experimental absorbances for each wavenumber $\tilde{\nu}_i$ originating from all contributing species in the solution are then expressed as a function of the absorbance of a chosen monomer wavenumber $\tilde{\nu}_m$ with the polynomial degree p equal to 1, 2, 3, 4 or 5 with intercept equal to zero.

$$A_{exp}(\tilde{\nu}_i) = \sum_{p=1}^{n} a_{\mathrm{p}}(\tilde{\nu}_i, \tilde{\nu}_m)\,[A_{mon}(\tilde{\nu}_m)]^p \tag{7.3}$$

The coefficient $a_{\mathrm{p}}(\tilde{\nu}_i, \tilde{\nu}_m)$ being a constant related to the equilibrium constant K_p of the oligomerization reaction

$$p = 1\text{: } a_1(\tilde{\nu}_i, \tilde{\nu}_m) = \frac{A_1(\tilde{\nu}_i)}{A_1(\tilde{\nu}_m)} = \frac{\varepsilon_1(\tilde{\nu}_i)}{\varepsilon_1(\tilde{\nu}_m)} \tag{7.4}$$

$$p > 1\text{: } a_{\mathrm{p}}(\tilde{\nu}_i, \tilde{\nu}_m) = a_1(\tilde{\nu}_i, \tilde{\nu}_m)^p \frac{\varepsilon_p(\tilde{\nu}_i)}{\varepsilon_1(\tilde{\nu}_m)^p} \frac{1}{d^{p-1}} K_p \tag{7.5}$$

with ε as the molar attenuation coefficients of the monomeric species and of the associations formed, *d* as the path length of the cell.

These equations can be adjusted so they can also be used to analyze spectra of two or more species to investigate the formation of heterocomplexes. For a mixed solution in which two species A and B are in equilibrium with a complex with 1:1 stoichiometry,

$$\mathrm{A} + \mathrm{B} \rightleftharpoons \mathrm{AB} \qquad K_{AB} = \frac{C_{AB}}{C_A \cdot C_B} \tag{7.6}$$

A similar expression can be easily derived in which, for each arbitrary wavenumber $\tilde{\nu}_i$ the measured absorbance A_{exp} can be written as a sum of absorbance contributions

related to the monomers A and B A_A and A_B and to the heterocomplexes, e.g. the dimer A_{AB},

$$A_{exp}(\tilde{\nu}_i) = A_A(\tilde{\nu}_i) + A_B(\tilde{\nu}_i) + A_{AB}(\tilde{\nu}_i) \tag{7.7}$$

Hence, by choosing appropriate reference wavenumbers $\tilde{\nu}_m$ (A) and $\tilde{\nu}_m$ (A) for which the measured absorbances are due to monomer A or monomer B only, i.e.

$$A_{exp}(\tilde{\nu}_{mA}) = A_A(\tilde{\nu}_{mA}) \text{ and } A_{AB}(\tilde{\nu}_{mA}) = A_B(\tilde{\nu}_{mB}) = 0 \tag{7.8}$$

$$A_{exp}(\tilde{\nu}_{mB}) = A_B(\tilde{\nu}_{mB}) \text{ and } A_{AB}(\tilde{\nu}_{mB}) = A_A(\tilde{\nu}_{mB}) = 0$$

and by using Lambert-Beer's law

$$A_j(\tilde{\nu}_i) = \varepsilon_j(\tilde{\nu}_i) C_j d \tag{7.9}$$

It can be assumed that the different contributions in Eq. (7.7) can be rewritten in terms of the absorbance of the monomer wavenumbers $\tilde{\nu}_{mA}$ and $\tilde{\nu}_{mB}$;

$$A_A(\tilde{\nu}_i) = a_{\mathrm{A}}(\tilde{\nu}_i, \tilde{\nu}_{mA,}\tilde{\nu}_{mB}) A_A(\tilde{\nu}_{mA}) \tag{7.10}$$

$$A_B(\tilde{\nu}_i) = a_{\mathrm{B}}(\tilde{\nu}_i, \tilde{\nu}_{mA,}\tilde{\nu}_{mB}) A_B(\tilde{\nu}_{mB}) \tag{7.11}$$

$$A_{AB}(\tilde{\nu}_i) = a_{\mathrm{AB}}(\tilde{\nu}_i, \tilde{\nu}_{mA,}\tilde{\nu}_{mB}) A_A(\tilde{\nu}_{mA}) A_B(\tilde{\nu}_{mB}) \tag{7.12}$$

The coefficients $\mathrm{a}(\tilde{\nu}_i, \tilde{\nu}_{mA,}\tilde{\nu}_{mB,})$ used in these expressions are defined as

$$a_{\mathrm{A}}(\tilde{\nu}_i, \tilde{\nu}_{mA,}\tilde{\nu}_{mB,}) = \frac{A_A(\tilde{\nu}_i)}{A_A(\tilde{\nu}_{mA})} = \frac{\varepsilon_A(\tilde{\nu}_i)}{\varepsilon_A(\tilde{\nu}_{mA})} \tag{7.13}$$

$$a_{\mathrm{B}}(\tilde{\nu}_i, \tilde{\nu}_{mA,}\tilde{\nu}_{mB,}) = \frac{A_B(\tilde{\nu}_i)}{A_B(\tilde{\nu}_{mB})} = \frac{\varepsilon_B(\tilde{\nu}_i)}{\varepsilon_B(\tilde{\nu}_{mB})} \tag{7.14}$$

$$\begin{aligned} a_{\mathrm{AB}}(\tilde{\nu}_i, \tilde{\nu}_{mA,}\tilde{\nu}_{mB,}) &= \frac{A_{AB}(\tilde{\nu}_i)}{A_A(\tilde{\nu}_{mA}) A_B(\tilde{\nu}_{mB})} \\ &= a_{\mathrm{A}}(\tilde{\nu}_i, \tilde{\nu}_{mA,}\tilde{\nu}_{mB}) a_{\mathrm{B}}(\tilde{\nu}_i, \tilde{\nu}_{mA,}\tilde{\nu}_{mB,}) \frac{\varepsilon_{AB}(\tilde{\nu}_i)}{\varepsilon_A(\tilde{\nu}_{mA})\varepsilon_B(\tilde{\nu}_{mB})} \frac{1}{d} K_{AB} \end{aligned} \tag{7.15}$$

Substituting the above Eqs (7.10), (7.11) and (7.12) in equation (7.7) results in

$$\begin{aligned} A_{exp}(\tilde{\nu}_i) = {} & a_{\mathrm{A}}(\tilde{\nu}_i, \tilde{\nu}_{mA,}\tilde{\nu}_{mB}) A_A(\tilde{\nu}_{mA}) \\ & + a_{\mathrm{B}}(\tilde{\nu}_i, \tilde{\nu}_{mA,}\tilde{\nu}_{mB}) A_B(\tilde{\nu}_{mB}) \\ & + a_{\mathrm{AB}}(\tilde{\nu}_i, \tilde{\nu}_{mA,}\tilde{\nu}_{mB}) A_A(\tilde{\nu}_{mA}) A_B(\tilde{\nu}_{mB}) \end{aligned} \tag{7.16}$$

Besides dimers, it also occurs that a mixture of two monomers results in the formation of higher complexes with 2:1 and/or 1:2 stoichiometry.[18-20] In this case Eq. (7.16) can be expanded with extra terms

$$\begin{aligned} A_{exp}(\tilde{\nu}_i) = {} & a_{\mathrm{A}}(\tilde{\nu}_i, \tilde{\nu}_{mA,}\tilde{\nu}_{mB})A_A(\tilde{\nu}_{mA}) \\ & + a_{\mathrm{B}}(\tilde{\nu}_i, \tilde{\nu}_{mA,}\tilde{\nu}_{mB})A_B(\tilde{\nu}_{mB}) \\ & + a_{\mathrm{AB}}(\tilde{\nu}_i, \tilde{\nu}_{mA,}\tilde{\nu}_{mB})A_A(\tilde{\nu}_{mA})A_B(\tilde{\nu}_{mB}) \\ & + a_{A_2B}(\tilde{\nu}_i, \tilde{\nu}_{mA,}\tilde{\nu}_{mB})A_A(\tilde{\nu}_{mA})^2A_B(\tilde{\nu}_{mB}) \\ & + a_{AB_2}(\tilde{\nu}_i, \tilde{\nu}_{mA,}\tilde{\nu}_{mB})A_A(\tilde{\nu}_{mA})A_B(\tilde{\nu}_{mB})^2 \end{aligned} \tag{7.17}$$

with coefficients

$$\begin{aligned} & a_{A_2B}(\tilde{\nu}_i, \tilde{\nu}_{mA,}\tilde{\nu}_{mB,}) = \frac{A_{A_2B}(\tilde{\nu}_i)}{A_A(\tilde{\nu}_{mA})^2A_B(\tilde{\nu}_{mB})} \\ & = a_{\mathrm{A}}(\tilde{\nu}_i, \tilde{\nu}_{mA,}\tilde{\nu}_{mB,})^2 a_{\mathrm{B}}(\tilde{\nu}_i, \tilde{\nu}_{mA,}\tilde{\nu}_{mB,}) \frac{\varepsilon_{A_2B}(\tilde{\nu}_i)}{\varepsilon_A(\tilde{\nu}_{mA})^2\varepsilon_B(\tilde{\nu}_{mB})} \frac{1}{d^2} K_{A_2B} \end{aligned} \tag{7.18}$$

$$\begin{aligned} & a_{AB_2}(\tilde{\nu}_i, \tilde{\nu}_{mA,}\tilde{\nu}_{mB,}) = \frac{A_{AB_2}(\tilde{\nu}_i)}{A_A(\tilde{\nu}_{mA})A_B(\tilde{\nu}_{mB})^2} \\ & = a_{\mathrm{A}}(\tilde{\nu}_i, \tilde{\nu}_{mA,}\tilde{\nu}_{mB,})a_{\mathrm{B}}(\tilde{\nu}_i, \tilde{\nu}_{mA,}\tilde{\nu}_{mB,})^2 \frac{\varepsilon_{AB_2}(\tilde{\nu}_i)}{\varepsilon_A(\tilde{\nu}_{mA})\varepsilon_B(\tilde{\nu}_{mB})^2} \frac{1}{d^2} K_{AB_2} \end{aligned} \tag{7.19}$$

and with equilibrium constants

$$2\mathrm{A} + \mathrm{B} \rightleftharpoons A_2B \qquad K_{A_2B} = \frac{C_{A_2B}}{C_A{}^2 \cdot C_B} \tag{7.20}$$

$$\mathrm{A} + 2\mathrm{B} \rightleftharpoons AB_2 \qquad K_{AB_2} = \frac{C_{AB_2}}{C_A \cdot C_B{}^2} \tag{7.21}$$

The above Eqs. (7.16) and (7.17) show that for any arbitrary wavenumber $\tilde{\nu}_i$, the contributions due to the different species present can in principle be determined by plotting the measured absorbances versus the monomer absorbances at the given reference wavenumbers $\tilde{\nu}_{mA}$ and $\tilde{\nu}_{mB}$, and using multiple regression to fit a 3D polynomial to the resulting data.

7.3.2 CF_3X and dimethyl ether

The vibrational spectra of solutions in LAr containing mixtures of DME and the trifluoromethyl halides CF_3X with X = Br or I have been described in detail before by Hauchecorne *et al.*[5] Apart from the bands assigned to the monomers, new bands due to 1:1 complexes were observed for a variety of modes localized in the DME or CF_3X moiety. In addition, for the solutions containing a large excess of CF_3Br, weak spectral

features assigned to 1:2 complexes in which two different CF_3X molecules binds to single DME moiety were observed to emerge at temperatures below 96 K. The observation of a variety of complex bands showing a significant complexation shift with respect to the monomer wavenumbers, and the lack of complexes with a higher stoichiometry at temperatures above 96 K, makes the solutions an excellent test case for systems in which, apart from the monomer, only a single binary complex is present. The solutions, therefore, are considered as an ideal test case to validate the methods put forward for such cases.

Figure 7.1 shows the comparison of vibrational spectra of mixtures of the trifluoromethyl halides CF_3Br and CF_3I with dimethyl ether dissolved in LAr from the recorded data set with spectra of solutions containing only monomoners. The appearance of new bands that cannot be found in the monomer spectra proves the formation of 1:1 complexes.

The reliability of the models discussed above strongly depends on the reference wavenumbers $\tilde{\nu}_m$ used as an internal standard. This value is typically determined by carefully analyzing the spectra of the mixed solutions to find regions in which no features due dimerization are observed or can be expected to appear.

Although for both DME and CF_3X, a variety of complex bands were observed at wavenumbers significantly shifted from those of the monomers, for all spectral regions studied, the bands of monomer and complex were observed to substantially overlap. As a consequence, no regions in which the measured absorbances are caused by monomer DME or monomer CF_3X only could be identified. These results, obviously, led to the conclusion that for none of the monomers, reliable values for reference wavenumbers $\tilde{\nu}_{mA}$ or $\tilde{\nu}_{mB}$ to be used as internal standards could be identified. Hence, more sophisticated approaches are required.

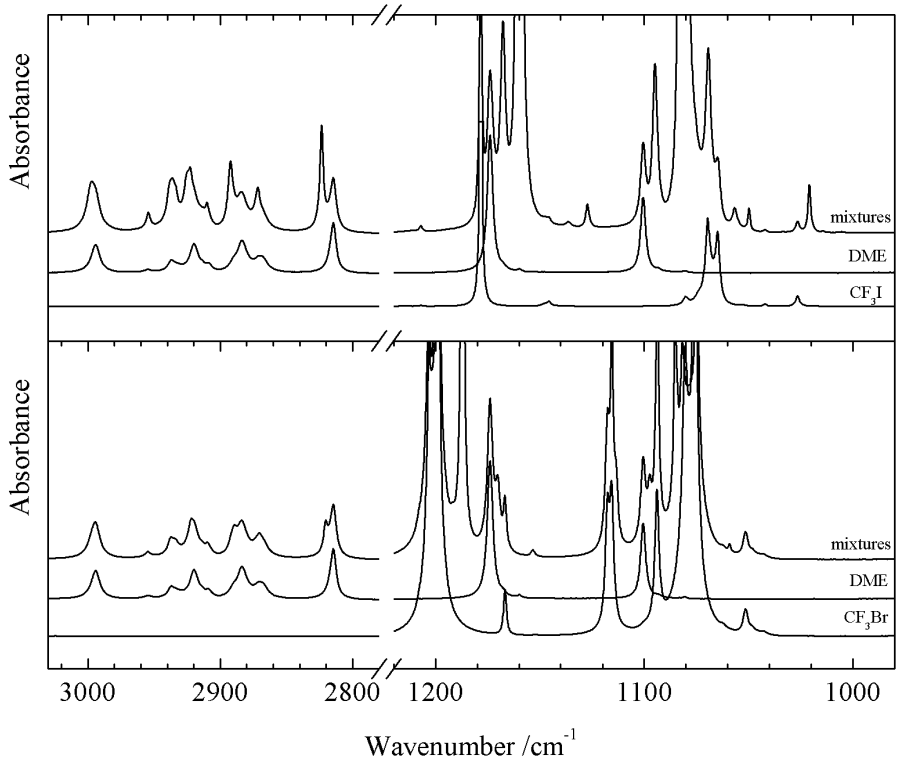

Figure 7.1. Infrared spectra of the 3030-2780 and 1220-980 cm^{-1} regions for solutions in LAr of mixtures of DME with CF_3I (upper panel) and CF_3Br (bottom panel) at 103 K. In each panel a spectrum of a mixed solution is as the upper trace, and those of the solutions containing only DME and CF_3X are shown as the middle and lower traces respectively. The spectra shown for the mixture solutions is obtained from the spectral database used in the least-squares fitting procedures.

To correct for the lack of reliable reference wavenumbers $\tilde{\nu}_{mA}$ or $\tilde{\nu}_{mB}$ in this study, we opted to develop numerical methods that can be used to estimate the monomer and dimer contributions to the measured absorbance at a specific wavenumber. The calculated monomer absorbances $A_A(\tilde{\nu}_{mA})$ and $A_B(\tilde{\nu}_{mB})$ at the reference wavenumber $\tilde{\nu}_{mA}$ and $\tilde{\nu}_{mB}$ could then be used in further analyses.

$$A_{exp}(\tilde{\nu}_{mA}) \approx A_A(\tilde{\nu}_{mA}) + A_{AB}(\tilde{\nu}_{mA}) \text{ and } A_B(\tilde{\nu}_{mA}) = 0 \qquad (7.22)$$

$$A_{exp}(\tilde{\nu}_{mB}) \approx A_B(\tilde{\nu}_{mB}) + A_{AB}(\tilde{\nu}_{mB}) \text{ and } A_A(\tilde{\nu}_{mB}) = 0 \qquad (7.23)$$

The idea of estimating the monomer and dimer contribution in a special region largely determined by overlapping bands was based on earlier observations in a study on the self-associating behavior of acetone, showing that similar approaches were proven successful.[9]

In Figures 7.2 and 7.3 results are summarized obtained by applying the different procedures used to estimate the monomer absorbances of DME and CF_3I and of DME and CF_3Br and to calculate the absorbances for the complexes. The absorbance for the DME monomer was obtained from the ν_2 asymmetric C-H stretching mode at 2814.6 cm^{-1}. The absorbances for monomer CF_3I and monomer CF_3Br were derived from the measured absorbances at 1026.4 and 1051.4 cm^{-1} respectively. The former value is assigned to the $\nu_2+\nu_3$ combination in monomer CF_3I, and is complemented by a complex band red shifted from the monomer by -6.4 cm^{-1}. The latter value originates from the $\nu_1(^{13}C)$ CF_3 asymmetric stretching mode in $^{13}CF_3Br$ with the corresponding complex band being observed at 1059.1 cm^{-1}. In Figure 7.2 and 7.3 the used reference wavenumbers are indicated with a dashed line.

In the panels a1 and a2 of Figure 7.2 and 7.3, band profiles derived from a standard fitting procedure and obtained from subtraction procedures similar to those reported by Hauchecorne et al.[5] are compared. The standard fitting procedure involves the fitting of the spectral data using the monomer absorbances measured at 2814.6 and 1026.4 cm^{-1} for DME and CF_3I (Figure 7.2) and at 2814.6 and 1051.4 cm^{-1} for DME and CF_3Br (Figure 7.3). For all plots, the data obtained for the subtraction procedures are given in red, while the data derived for the fitting procedure are plotted in cyan (DME), blue (CF_3X) and green ($DME{\cdot}CF_3X$). The panels a1 show the results for the complete spectrum. The panels a2 focus on the lower absorbances and are obtained by expanding the absorbance scale used in the top panels.

Inspection of the data in panels 7.2a1, 7.2a2, 7.3a1 and 7.3a2 shows that in general the results derived from both procedures are in excellent agreement, while minor differences between the calculated profiles are observed near 1026.4 cm^{-1} and 1051.4 cm^{-1} only, i.e. at wavenumbers close to the reference wavenumbers used to estimate the monomer absorbances. The deviations are related to the assumption that the dimer contributions at the reference wavenumbers chosen are close zero and thus

can be neglected, while it is clear from Figures 7.2 and 7.3 that this is not always the case.

To correct for the additional absorbance of the complex bands, an iterative procedure was initiated in which the outcome of the obtained results were refined until no further improvement was observed. The refinement is based on the assumptions that at the reference wavenumbers used, the measured absorbances are not only due to monomer, but must be assigned to monomer and dimer simultaneously, as illustrated before in Eq. (7.22) and (7.23). A first method to correct the absorbances involves a symmetry operation in which the absorbances at wavenumbers further away from the reference wavenumber are folded back with respect to a specific symmetry axis. The latter typically is set at the maximum of the calculated band profile. A second method is applied in cases where only a small dip is observed in the overlapping spectrum. This method involves the use of a straight line to bridge the dip. Because the calculated dimer contributions are determined by the monomer absorbances of both interacting molecules, and because similar problems arise for both the halogen donor and the acceptor, each iteration introduces corrections for both DME and CF_3X monomer absorbances simultaneously.

Panels b of Figure 7.2 demonstrate the results after correction of the monomer absorbances of DME and CF_3I. The dotted lines added at 2823.4 cm^{-1} and 1020.8 cm^{-1} refer to the symmetry axis used to estimate the dimer contribution close to the reference wavenumbers and the mirrored band is represented by the dash-dotted line. Inspection of the data obtained showed that a significant correction is introduced in the first iteration, but that changes in the subsequent iterations are negligible. The results shown in Figure 7.2 therefore refer to the data obtained after a single iteration. Correcting for the dimer contributions, at the respective reference wavenumbers, yields monomer and complex contributions that are in excellent agreement with those obtained using standard subtraction procedures. It can be noted that the small feature at 1018.2 cm^{-1} can be assigned to the $\nu_2+\nu_3(^{13}C)$ vibrational mode of CF_3I.

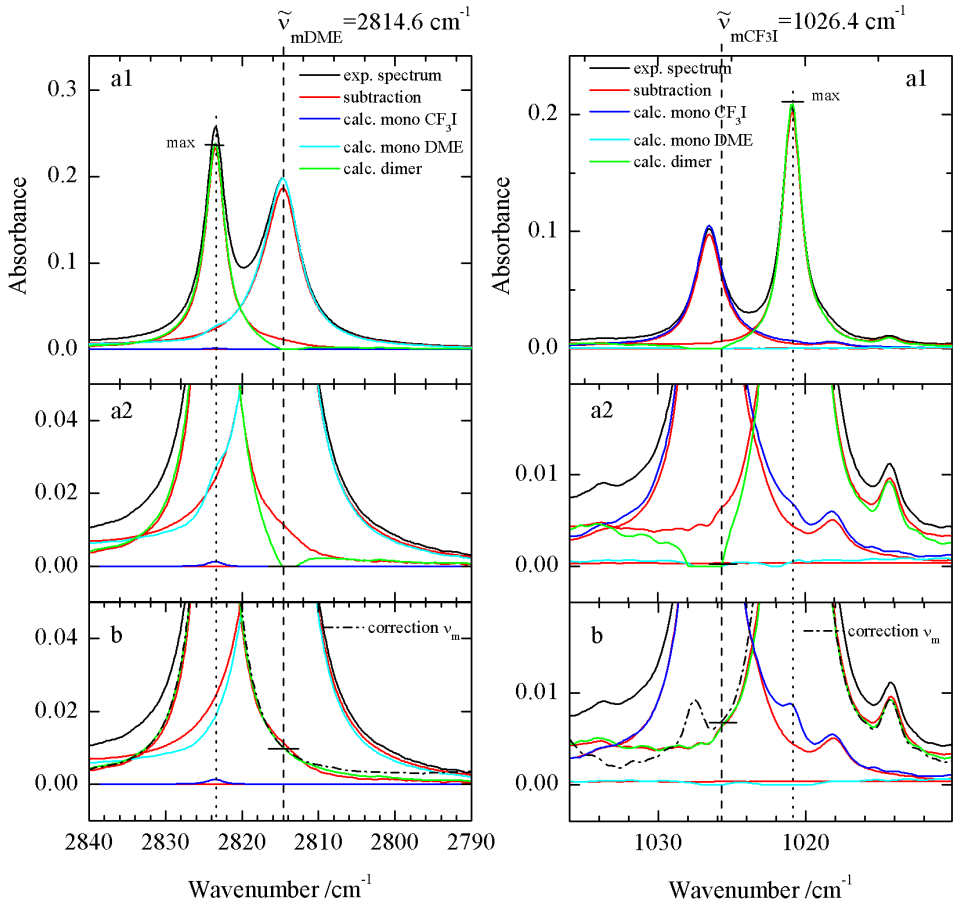

Figure 7.2. The correction procedures of the absorbances at $\tilde{\nu}_m$ for DME and CF_3I with the results from least-squares procedures using Eq. (7.16). The monomer wavenumbers at 2814.6 cm^{-1} for DME and 1216.5 cm^{-1} for CF_3I are indicated with vertical dashed lines. The upper panel shows the calculated monomer and dimer contributions without corrections of $A(\tilde{\nu}_m)$. The red traces illustrate the monomer and dimer contributions obtained from a subtraction procedure. In panels a2 the dimer contributions at $\tilde{\nu}_m$ are magnified. The absorbance at $\tilde{\nu}_m$ is corrected by reflecting the higher wavenumber half (in case of DME) or the lower wavenumber half (in case of CF_3I) of the calculated dimer band at the wavenumber with maximum absorbance. These corrections (dash dot trace) and the resulting monomer and dimer contributions of the first iteration are shown in panels b.

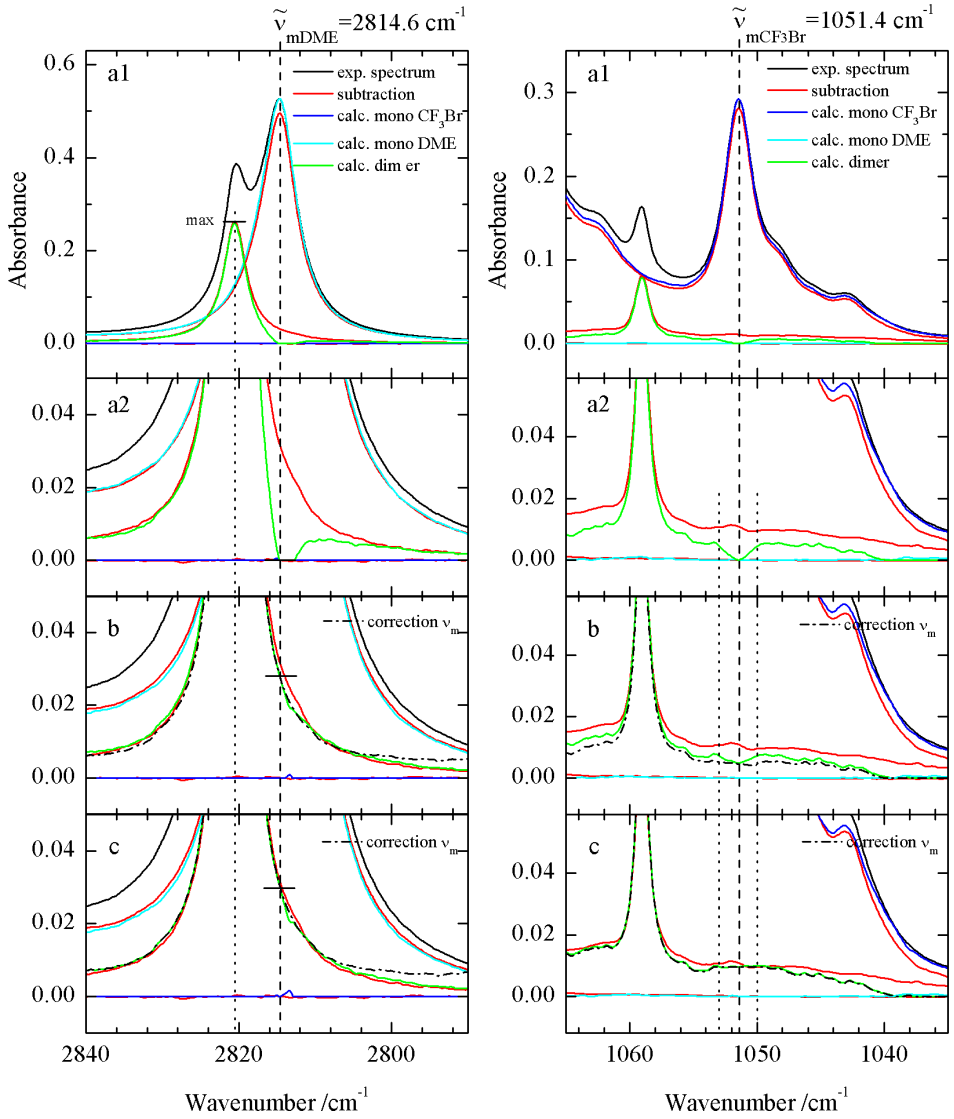

Figure 7.3 The correction procedures of the absorbances at $\tilde{\nu}_m$ for DME and CF_3Br with the results from least-squares procedures using Eq. (7.16). The monomer wavenumbers at 2814.6 cm^{-1} for DME and 1051.4 cm^{-1} for CF_3Br are indicated with vertical dashed lines. The upper panel shows the calculated monomer and dimer contributions without corrections of $A(\tilde{\nu}_m)$. The red traces illustrate the monomer and dimer contributions obtained from a subtraction procedure. In panels a2 the dimer contributions at $\tilde{\nu}_m$ are magnified. For DME, the absorbance at $\tilde{\nu}_m$ is corrected by reflecting the higher wavenumber half of the calculated dimer band at the wavenumber with maximum absorbance. For CF_3I, the dip in the dimer spectrum around $\tilde{\nu}_m$ can be eliminated by drawing a straight line between the calculated values of the dimer contribution at 1050.0 and 1053.0 cm^{-1} (dotted lines). These corrections (dash dot trace) and the resulting monomer and dimer contributions of the first iteration are shown in b panels. This method of correcting was repeated four times and c panels show the results of the fourth iteration.

The results obtained by introducing a correction for the monomer absorbances of DME and CF_3Br are shown in the lower panels of Figure 7.3. As for the case above, a symmetry axis was defined at the center of the dimer band at 2820.5 cm^{-1}, to estimate the dimer contribution at the reference wavenumber $\tilde{\nu}_{m\mathrm{DME}}$. In contrast, corrections for the dimer contribution at $\tilde{\nu}_{m\mathrm{CF_3Br}}$ were introduced by generating a straight line from 1053.0 and 1050.0 cm^{-1} to bridge the dip caused by neglecting the dimer contribution in the first calculation. Inspection of the data obtained showed that a significant correction is introduced in the first iteration, and that further changes can be noted during the second, third and fourth iteration cycle. Therefore, in Figure 7.3, both the results after the first and the fourth cycle are given.

Using the corrected monomer absorbances for DME, CF_3I and CF_3Br obtained at the fourth iteration, a final fit was performed for the whole spectral region. The results of these fits are given in Figure 7.4. It can be seen that in general, spectra of the monomer and of the complexes can be reliably separated. The results yield spectra very similar to those obtained by Hauchecorne *et al.*[5] using standard subtraction procedures. This shows that besides its use to study self-associating molecules, the least-squares fitting approach developed can also be used to accurately isolate monomer and heterocomplex spectra. It should be noted that in some spectral regions shown in Figure 7.4, data for the monomer and/or the complex contributions are deselected. The reason for this is related to the fact that the recorded data was obtained for a solution giving rise to full or almost full absorbance and, consequently, giving problems with the non-linearity of the detector, at the wavenumbers omitted.

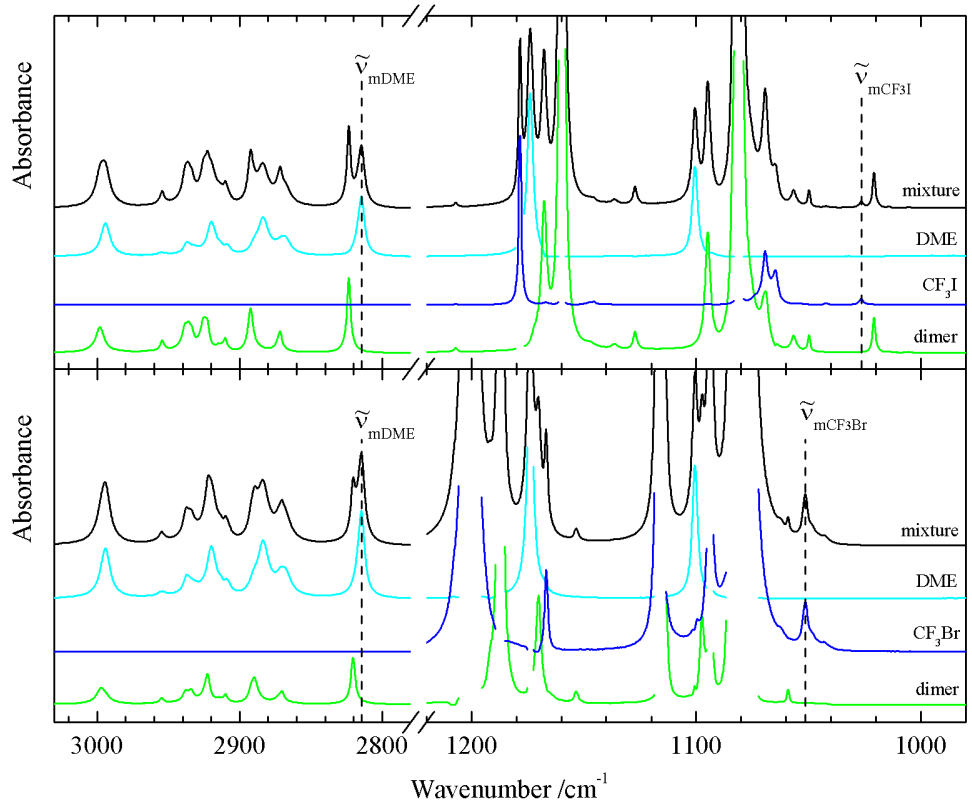

Figure 7.4 Results for the 3030-2780 and 1220-980 cm^{-1} spectral regions from least-squares fitting procedures using Eq. (7.16) with corrected absorbances at the monomer wavenumbers of DME at 2814.6 cm^{-1} and CF_3I and CF_3Br, at 1026.4 and 1051.4 cm^{-1} respectively (dashed lines).

7.3.3 CF_3X and acetone

Vibrational spectra of the mixtures of CF_3Br and CF_3I with acetone dissolved in LKr were investigated at 138 K. Typical spectra obtained for the data set of 274 spectra of CF_3I and acetone obtained by changing concentrations and concentration ratios of both compounds are given in Figure 7.5. Panels a to d show regions related to modes localized in acetone, while panels e and f illustrate absorption bands due to CF_3I. Inspection of the data shows that with changing ratios and concentrations new bands appear in all panels of Figure 7.5. In the acetone C–H stretching region, panel 7.5a, emerging complex bands are not easily observed as they only show a limited wavenumber shift and therefore completely overlap with the three monomer bands. A

similar case is the 1500-1300 cm^{-1} spectral region in panel 7.5c where the new features overlap with the bands assigned to five CH_3 deformation modes. But in this panel it can be observed that the shape of the overlapping bands gradually changes due to growing complex features. On the other hand some new signals however show larger wavenumber shifts, which results in more separated bands that are more easily identified. This is the case for among other modes, the C=O stretching region in panel 5b that shows an extra red shifted band around 1730 cm^{-1}, the CF_3 stretching region in panel 5e shows a red and blue-shifted feature at respectively 1157 and 1178 cm^{-1} and the $\nu_2+\nu_3$ combination band in panel f for which a small feature appears on the lower wavenumber side.

Surprisingly, when inspecting panel 5d, two new features appear blue shifted from the ν_{22} transition at 1217.4 cm^{-1} (indicated with *). These signals show a different concentration behavior and should thus be assigned to two different species with a different stoichiometry. Based on the observed concentration dependencies and the predicted complexation shifts (*vide infra*), it is tentative to assign the first feature at 1224.6 cm^{-1} to the dimer and the second around 1229 cm^{-1} to a complex with higher stoichiometry, e.g. a $(acetone)_2 \cdot CF_3I$ or $acetone \cdot (CF_3I)_2$ trimer. As earlier research demonstrated, acetone is inclined to self-associate in LKr and therefore acetone dimer bands should also be expected.[11] As the spectral features due to such species were observed to largely overlap with those of the monomer, no specific bands due to this species can be identified. To determine which clusters are present in the solution, and to determine their relative contributions in the spectra recorded, the data set was analyzed using the least-squares fitting approach.

Inspection of the data of mixtures of acetone and CF_3Br curiously enough showed no features due to dimers or trimers. Due to the low solubility of acetone we were obliged to work with solutions of LKr instead of the solutions of LAr as with the CF_3Br and DME mixtures. As the change to LKr includes that the solutions are recorded at higher temperatures, only the stronger bonded complexes, e.g. complexes with CF_3I, have equilibrium concentrations well above the detection limit.

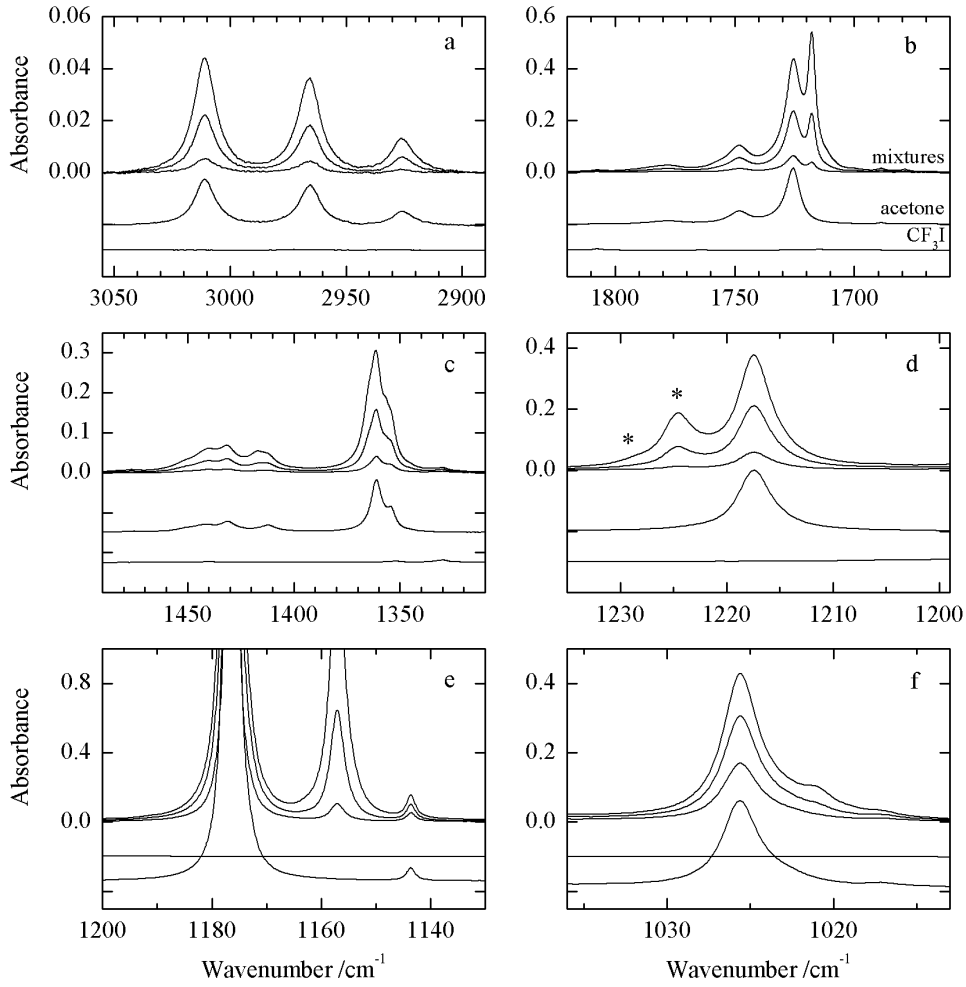

Figure.7.5 Infrared spectra of the 3055-2890, 1820-1660, 1490-1310, 1235-1199, 1200-1130, and 1110-1005 cm^{-1} regions for solutions in LAr of mixtures of acetone with CF_3I at 138 K. In each panel three spectra of mixed solutions are given as stacked traces, while those of the solutions containing only acetone and CF_3I are shown as the middle and lower traces respectively. The spectra shown for the mixture solutions represent only a small fraction of the spectral database used in the fitting procedures.

For the CF_3X-acetone mixture the appropriate model thus needs to account for the presence of complex species with higher stoichiometry and to account for the formation of acetone dimers. Therefore the model described by Eq. (7.17), which already includes contribution for the heterodimers AB and heterotrimers A_2B and AB_2, needs to be extended with an extra term for the acetone dimer A_2. The equilibrium describing the acetone dimerization is illustrated in Eq. (7.1) with p equal to 2 and according to Eq. (7.3) the corresponding contribution, using Lambert-Beer's law, Eq. (7.9), can be written as

$$A_{A_2}(\tilde{\nu}_i) = a_{A_2}(\tilde{\nu}_i, \tilde{\nu}_{mA}) A_A(\tilde{\nu}_{mA})^2 \tag{7.24}$$

in which the coefficients $a(\tilde{\nu}_i, \tilde{\nu}_{mA})$ are defined as

$$a_{A_2}(\tilde{\nu}_i, \tilde{\nu}_{mA,}) = \frac{A_{A_2}(\tilde{\nu}_i)}{A_A(\tilde{\nu}_{mA})^2} = a_{A_2}(\tilde{\nu}_i, \tilde{\nu}_{mA,})^2 \frac{\varepsilon_{A_2}(\tilde{\nu}_i)}{\varepsilon_A(\tilde{\nu}_{mA})^2} \frac{1}{d} K_{A_2} \tag{7.25}$$

Extending Eq. (7.17) with Eq. (7.23) finally gives

$$\begin{aligned} A_{exp}(\tilde{\nu}_i) = {} & a_{\mathrm{A}}(\tilde{\nu}_i, \tilde{\nu}_{mA,} \tilde{\nu}_{mB}) A_A(\tilde{\nu}_{mA}) \\ & + a_{\mathrm{B}}(\tilde{\nu}_i, \tilde{\nu}_{mA,} \tilde{\nu}_{mB}) A_B(\tilde{\nu}_{mB}) \\ & + a_{\mathrm{AB}}(\tilde{\nu}_i, \tilde{\nu}_{mA,} \tilde{\nu}_{mB}) A_A(\tilde{\nu}_{mA}) A_B(\tilde{\nu}_{mB}) \\ & + a_{A_2B}(\tilde{\nu}_i, \tilde{\nu}_{mA,} \tilde{\nu}_{mB}) A_A(\tilde{\nu}_{mA})^2 A_B(\tilde{\nu}_{mB}) \\ & + a_{AB_2}(\tilde{\nu}_i, \tilde{\nu}_{mA,} \tilde{\nu}_{mB}) A_A(\tilde{\nu}_{mA}) A_B(\tilde{\nu}_{mB})^2 \\ & + a_{A_2}(\tilde{\nu}_i, \tilde{\nu}_{mA}) A_A(\tilde{\nu}_{mA})^2 \end{aligned} \tag{7.26}$$

The choice of $\tilde{\nu}_{mA}$ and $\tilde{\nu}_{mB}$, or $\tilde{\nu}_{mACE}$ and $\tilde{\nu}_{mCF_3I}$, is based on previous studies. The study on the self-association of acetone in LKr showed that the most suitable reference wavenumber $\tilde{\nu}_{mACE}$ is situated on the lower wavenumber side of the ν_{22} transition. As before, this value was set to 1216.5 cm^{-1}.[11] The reference wavenumber for CF_3I, $\tilde{\nu}_{mCF_3I}$, was based on the analysis of the spectra given in Figure 7.5, and was chosen to be 1026.4 cm^{-1}. As can be seen in Figure 7.5, the acetone dimer overlaps with other appearing complex bands. To improve the detection of the acetone dimer band we performed the analysis with Eq. (7.26) on a dataset consisting of the spectra of the mixture of acetone and CF_3I, and the acetone spectra gathered in a previous acetone dimerization study[11]. Panels a1 and a2 of Figure 7.6 show the fitted contributions of the acetone and CF_3I monomers, acetone and acetone·CF_3I dimers, and, $(acetone)_2$·CF_3I and acetone·$(CF_3I)_2$ trimers for the cryosolutions containing an approximate mole

fraction of 4.3 x 10^{-4} and 3.9 x 10^{-4} and recorded at 138 K. In the ν_{22} spectral region the major blue-shifting features observed are originating from acetone·CF_3I, acetone dimer and (acetone)$_2$·CF_3I. The relative intensity of the acetone dimer band observed in the $\tilde{\nu}_{mACE}$ spectral region resembles the previous results[11], which proves the validity of the numerical approach. For the $\nu_2+\nu_3$, combination in CF_3I the analysis yields features assigned to the presence of acetone, acetone·CF_3I and acetone·$(CF_3I)_2$.

As described before these results are determined by the general assumption that for all solutions studied the measured absorbances at the reference wavenumbers are solely determined by monomer species. In the acetone and DME-CF_3I investigations the first results were compared with the dimer contribution obtained from an approximate subtraction procedure and it was decided that the general assumption was not completely valid and corrections of both $A_{ACE}(\tilde{\nu}_{mACE})$ and $A_{CF_3I}(\tilde{\nu}_{mCF_3I})$ were introduced. In the mixtures of acetone and CF_3I the comparison with subtraction traces is not obvious as the dimer and trimer features overlap and cannot be separated with the subtraction technique. In the $\tilde{\nu}_{mCF_3I}$ spectral region the acetone·CF_3I dimer band does not show any overlap with the band center, therefore the introduction of a correction for $A_{CF_3I}(\tilde{\nu}_{mCF_3I})$ was deemed unnecessary. On the other hand we do need to introduce a correction at $\tilde{\nu}_{mACE}$. Because it is assumed that at $\tilde{\nu}_{mACE}$ all contributions besides the acetone monomer are zero, there is a dip in the CF_3I monomer, the acetone dimer and the (acetone)$_2$·CF_3I trimer spectrum at $\tilde{\nu}_{mACE}$, which overlaps with the ν_{22} absorbance band. The correction procedure of the acetone dimer band is identical to the one used in an earlier investigation[11] and will not be discussed in this article. As for the CF_3I and (acetone)$_2$·CF_3I traces the dips can be removed, as before, by simply bridging them with a straight line between the resulting CF_3I and (acetone)$_2$·CF_3I absorbances at 1220.3 and 1215 cm^{-1} (illustrated with the dotted lines) and subtracting the found CF_3I absorbances at $\tilde{\nu}_{mACE}$ from $A_{ACE}(\tilde{\nu}_{mACE})$. These corrections were repeated four times and improvement was followed up visually. Only minimal changes were observed. After the fourth iteration the corrected value for the acetone monomer absorbance in Eq. (7.26) leads to the results illustrated in Figure 7.6b.

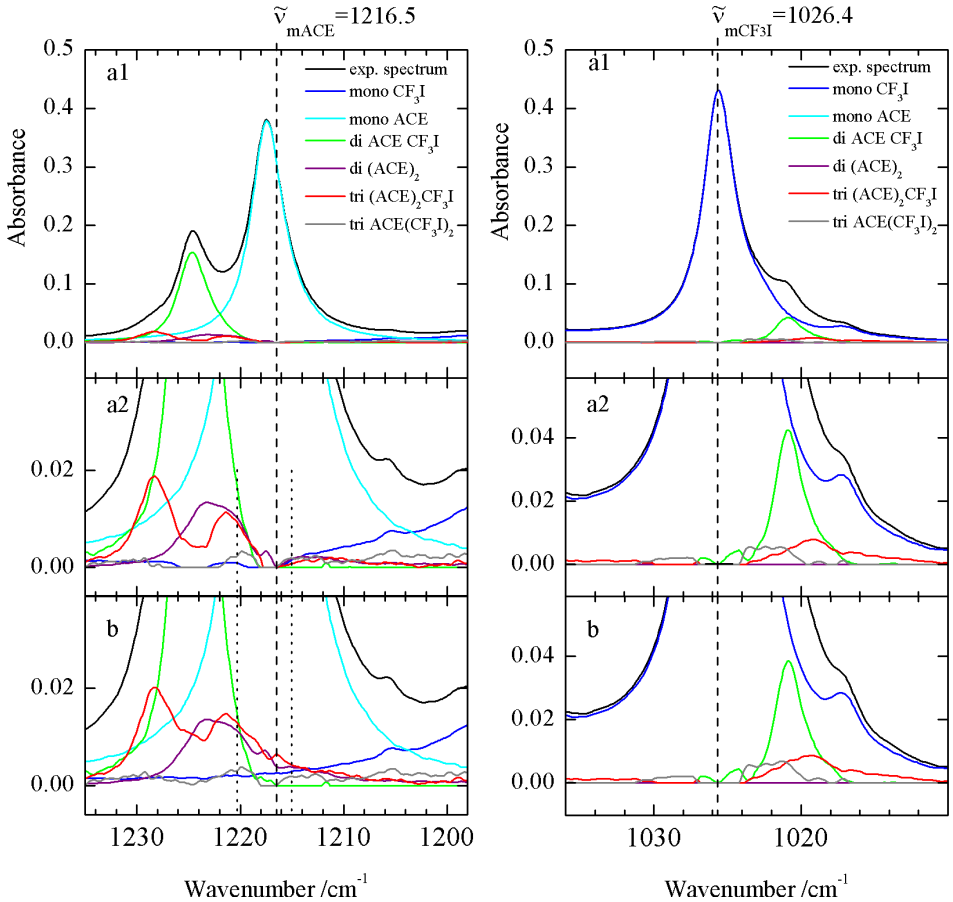

Figure 7.6. The correction procedure of the absorbances at $\tilde{\nu}_m$ for acetone (ACE) with the results from least-squares procedures using Eq.(7.26). The monomer wavenumbers at 1216.5 cm^{-1} for acetone and 1216.5 cm^{-1} for CF_3I are indicated with vertical dashed lines. The upper panel shows the calculated monomer, dimer and trimer contributions without corrections of $A(\tilde{\nu}_{mACE})$. In panels a2 the dimer and trimer contributions at $\tilde{\nu}_m$ are magnified. The absorbance at $\tilde{\nu}_{mACE}$ is corrected for by correcting the shape of the acetone dimer band according to a previous investigation[11], shown in panels b and by eliminating the dips in the CF_3I and the $(acetone)_2{\cdot}CF_3I$ spectrum around $\tilde{\nu}_{mACE}$ by drawing a straight line between the calculated values of the dimer contribution at 1015.0 and 1020.3 cm^{-1} (dotted lines). The resulting contributions from the fourth iteration are shown.

Figure 7.7 and 7.8 shows the fitted monomer, dimer and trimer contributions for six important regions of the acetone-CF_3I spectrum obtained by applying the above method to the complete data set. The results show that apart from the dimer and trimer bands around $\tilde{\nu}_{mACE}$ and $\tilde{\nu}_{mCF_3I}$ other dimer and trimer features are predicted. The assignment of the experimental spectra is presented in Table 7.1. The assignments of the acetone monomer and dimer in LKr at 138 K and that for the CF_3I monomer closely follow the

values reported earlier.[5,11] For acetone·CF_3I, (acetone)$_2$·CF_3I and acetone·$(CF_3I)_2$, no results are available in literature.

It should be noted that for panel e a limited dataset of 179 spectra was used in which the dimer band had an absorbance well below 1. The small features assigned as trimer bands close to the center of the dimer are believed to be caused by artifacts introduced in the numerical procedure and will not be discussed in detail.

Inspection of the data in Figure 7.7 and 7.8 shows that in every panel intense dimer bands and weaker bands due to (acetone)$_2$·CF_3I trimer are present, but that only few very weak features due to acetone·$(CF_3I)_2$ features appear. For the three main bands in the acetone C–H stretching region (Figure 7.7a and 7.8a), two features due to acetone·CF_3I dimer are calculated to appear blue-shifted from the monomer wavenumber at 3011.4 and 2970.6 cm^{-1}. In addition, three features due to (acetone)$_2$·CF_3I trimer are observed near 3011, 2962.4 and 2926 cm^{-1}. No bands due to acetone·$(CF_3I)_2$ were observed

The formation of heterocomplexes gives rise to intense absorption bands with large shifts from the fundamental C=O stretching mode, illustrated in panels 7.7b and 7.8b. The dimer can be observed red shifted for the monomer transition by 7.9 cm^{-1}, at 1717.7 cm^{-1}. The bands of (acetone)$_2$·CF_3I and acetone·$(CF_3I)_2$ are observed to show substantial overlap with the dimer band and are predicted at 1721.4 and 1711.8 cm^{-1} and at 1724.4 and 1708.1 cm^{-1}, respectively.

In the 1500-1300 cm^{-1} spectral region (Figure 7.5c) with transitions assigned to CH_3 deformation modes, features due to complex formation are observed to appear red shifted from the monomer vibrations. In total, five, four and one feature due to dimer, (acetone)$_2$·CF_3I and acetone·$(CF_3I)_2$ are obtained.

Panels 7.7d and 7.8d show the results for the C–C asymmetric stretching region (Figure 7.5d). Apart from the monomer bands at 1217.4 cm^{-1}, bands blue-shifted with respect to the monomer and assigned to acetone·CF_3I dimer and (acetone)$_2$·CF_3I bands appear at 1224.7 cm^{-1} and at 1228.3 and 1221.3 cm^{-1}, respectively. Panels 7.7e and 7.8e and f illustrate the appearance of complex bands for vibrational modes CF_3I. For both regions, complexation gives rise to an intense dimer band and weaker trimer bands.

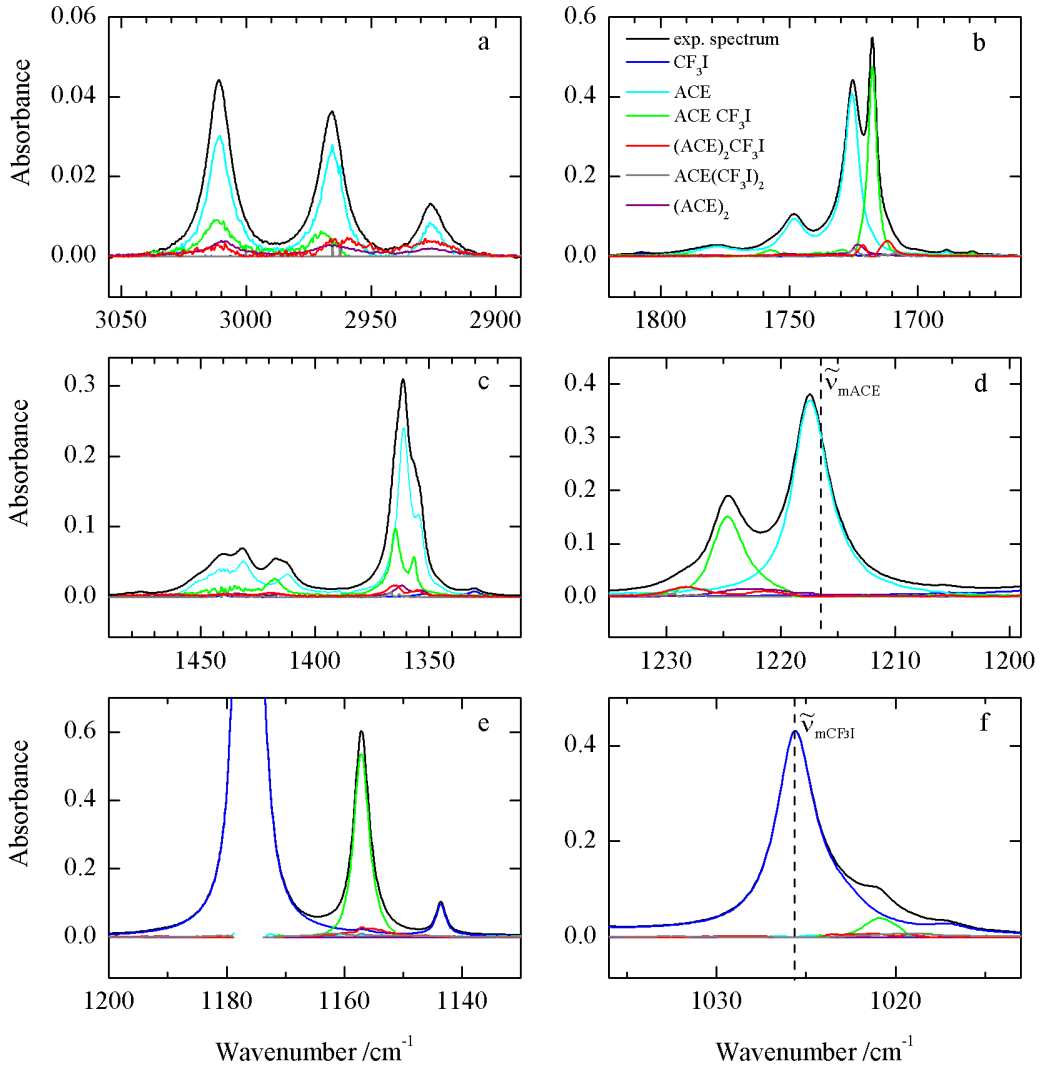

Figure 7.7 Results from least-squares procedures using Eq.(26) including corrections of the $(acetone)_2$, CF_3I, and $(acetone)_2 \cdot CF_3I$ contributions at the monomer wavenumber at 1216.5 cm^{-1} (dashed line in panel d). The CF_3I reference wavenumber was set to be 1026.4 cm^{-1} (dashed line in panel f).

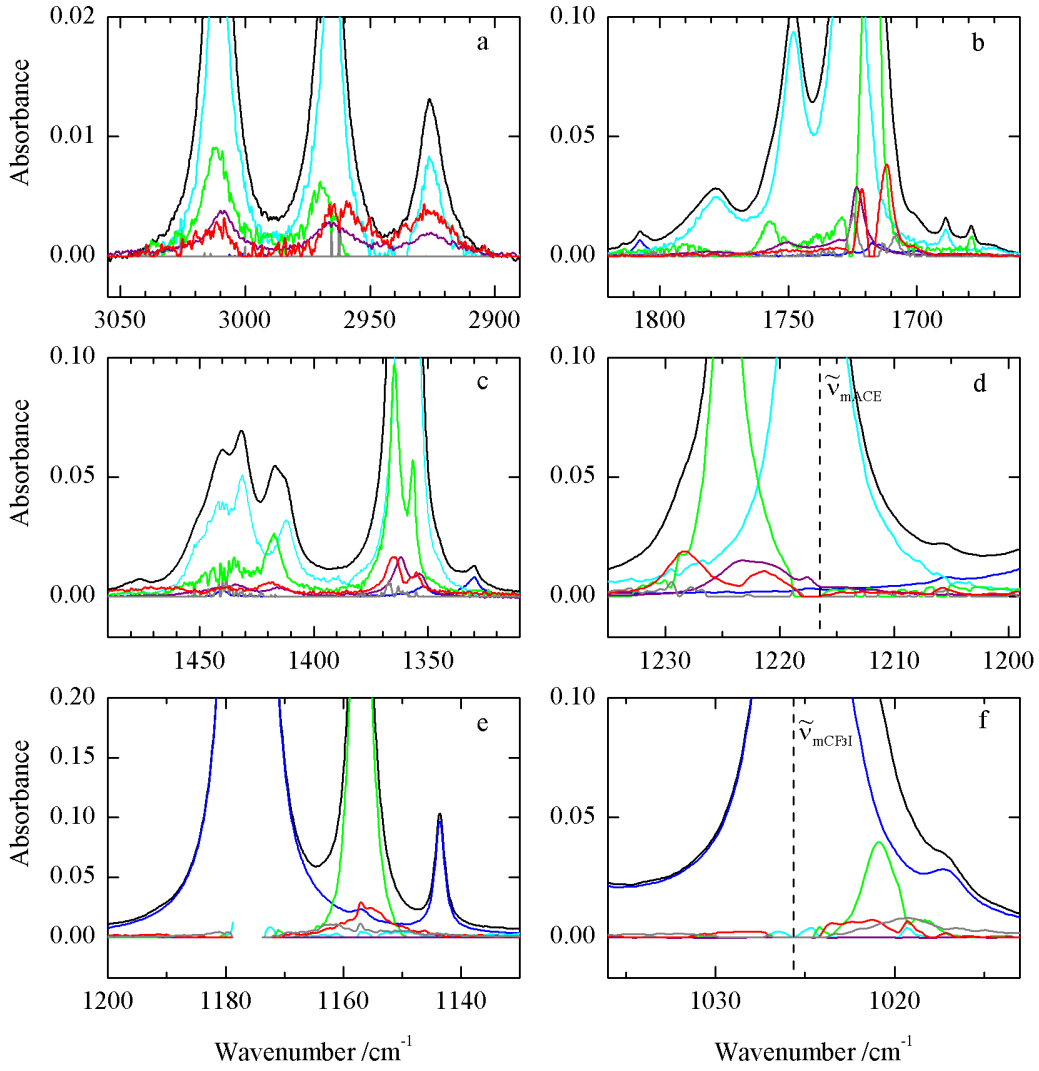

Figure 7.8 Results from least-squares procedures using Eq.(26) including corrections of the $(acetone)_2$, CF_3I, and $(acetone)_2 \cdot CF_3I$ contributions at the monomer wavenumber at 1216.5 cm^{-1} (dashed line in panel d). The CF_3I reference wavenumber was set to be 1026.4 cm^{-1} (dashed line in panel f).The legend is identical to that of Figure 7.7.

Table 7.1. Assignment of experimental monomer, dimer and trimer absorption bands of acetone and CF_3I in solution with krypton at 138 K[a]

Monomer			Dimer				
	Assignment	LKr 138K [11]	$(ACE)_2$ [11]		$ACE{\cdot}CF_3I$		
			$\tilde{\nu}$	$\Delta\nu$	$\tilde{\nu}$	$\Delta\nu$	$\Delta\nu$ calc[c]
Acetone	$2\nu_3$	3436.7					
	ν_1	3011.1	3009.1	-2.0	3011.4	0.3	7.7
	ν_{18}						5.2
	ν_{13}	2965.7	2965.7	0.0	2970.6	4.9	8.0
	ν_2	2926.1	2926.2	0.1			6.1
	ν_{19}						6.3
	$2\nu_{23}$	1778.0	1780.2	2.2	~1792	~14	
	$\nu_{22} + \nu_{24}$ FR[b]	1748.1	1750.5	2.4	1757.4	9.3	
	ν_3 FR[b]	1725.6	1723.4	-2.2	1717.7	-7.9	-2.0
		1441.4	1441.5	0.1	~1444	~2.6	
	ν_4	1431.3	1434.1	2.8	~1435	~3.7	1.9
	ν_{20}	1412.3	1415.2	2.9	1417.8	5.5	1.0
	ν_{21}	1361.1	1361.9	0.8	1364.8	3.7	6.7
	ν_5	1354.6	1353.3	-1.3	1356.8	2.2	4.6
	ν_{22}	1217.4	1222.7	5.3	1224.7	7.3	9.9
	ν_{24}	528.9	530.2	1.3	~534	~5.1	8.3
CF_3I	$\nu_1 + \nu_2$	1807.6			1815	7.4	
	$\nu_2 + \nu_5$	1280.4			1277.6	-2.8	
	$\nu_2 + 2\nu_6$	1266.0			1262.5	-3.5	
	ν_4	1176.2			1157.1	-19.1	-18.2
							-20.4
	$\nu_1(^{13}C)$	1040.4			1047.6	7.2	
	$\nu_2 + \nu_3$	1025.6			1020.9	-4.7	
	$\nu_2 + \nu_3(^{13}C)$	1017.3					
	ν_2	741.0			737.2	-3.8	-4.8
	$\nu_2(^{13}C)$	735.2			731.3	-3.9	

[a] Wavenumbers in cm^{-1}.
[b] FR, Fermi resonance
[c] from harmonical frequencies calculated with MP2/aug-cc-pVDZ(-PP),
[d] in both trimers the presence of two identical molecules gives rise to two complexation shifts for the frequencies of that molecule

Trimer							
$(ACE)_2 \cdot CF_3I$				$ACE \cdot (CF_3I)_2$			
$\tilde{\nu}$	$\Delta\nu$	$\Delta\nu$ calc[c, d]		$\tilde{\nu}$	$\Delta\nu$	$\Delta\nu$ calc[c, d]	
~3011	~-0.1	3.6 2.6	2.7 2.4				
2962.4	-3.3	13.8	6.8				
~2926	~0.1	6.7 7.2	3.4 4.4				
1721.4	4.2	0.1		1724.4	-1.2	-8.6	
1711.8	-13.8		-6.1	1708.1	-17.5	-8.6	
~1439	~7.7	2.3	1.8				
1419.5	7.2	0.0	-1.8				
1365.3	4.2	6.7	3.8	1367.2	6.1	9.3	
1355.2	0.6	0.7	-1.1				
1228.3	10.9	11.3					
1221.3	3.9		5.9				
1156.0	-20.2	-16.8		1162.2	-14	-14.8	-16.4
1019.2	-6.4	-25.7		~1021	~-4.6		

To support our experimental measurements**,** geometry optimizations and harmonic vibrational frequency calculations were performed at the MP2/aug-cc-pVDZ(-PP) using Gaussian09.[21] As before[4], the standard aug-cc-pVDZ basis set was used for hydrogen, carbon, oxygen and fluorine, while aug-cc-pVDZ-PP basis set including small-core energy-consistent relativistic pseudopotentials (PP) were used for iodine.[22,23] The combination of this method and basis set has led to satisfactory results for halogen bonded complexes before[7,12,24] and, consequently, a similar approach was used in the present study. The counterpoise technique as proposed by Boys and Bernardi was used during all *ab initio* calculations to account for basis set superposition error.[25] The equilibrium geometries and complexation energies for the different complexes are summarized in Figure 7.9. The Cartesian coordinates of the calculated monomer, dimer and trimer geometries are given in Table S7.1-S7.5 in the Supporting Information.

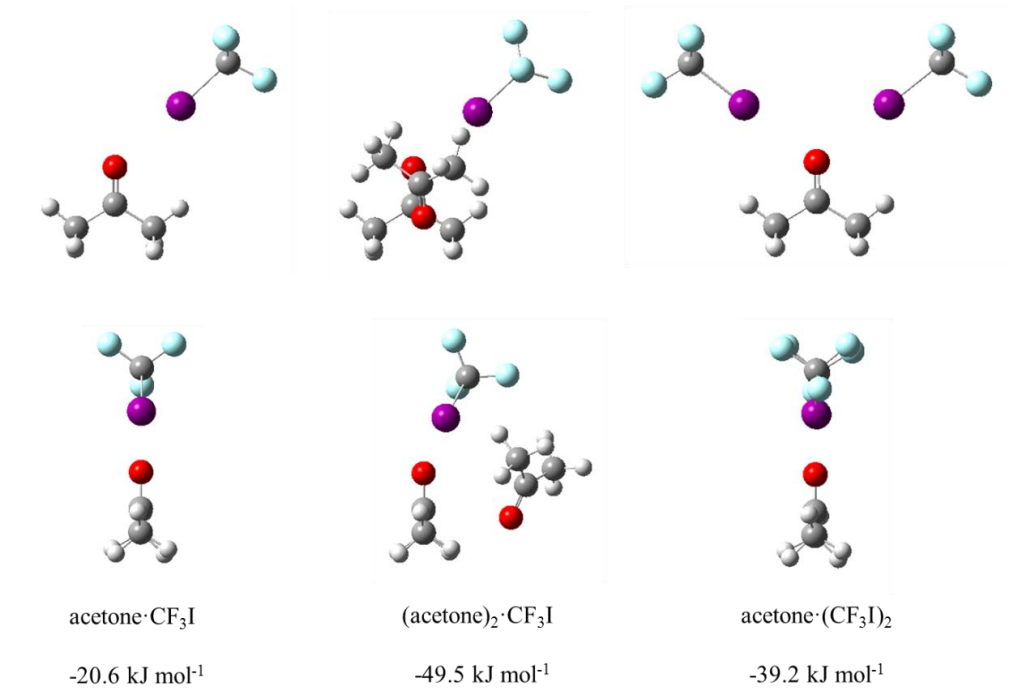

Figure 7.9 MP2/aug-cc-pVDZ-PP equilibrium geometries and complexation energies ΔE for the acetone·CF_3I dimer and for the $(acetone)_2$·CF_3I and acetone·$(CF_3I)_2$ trimers

For the 1:1 and 1:2 complexes acetone·CF_3I and acetone·$(CF_3I)_2$ the calculations result in typical C–I···O halogen bonded complexes, in which the CF_3I molecules are oriented towards one or both of the oxygen lone pairs.[26] The complexation energy of -20.6 kJ mol^{-1} for the 1:1 complex compares favorably with the values reported for dimethyl ether-CF_3I and suggests that both type of oxygen donors lead to halogen bonds with a similar strength. The value for the bifurcated complex in which two CF_3I molecules bind towards to oxygen lone pairs is only slightly smaller than twice the value obtained for the 1:1 complex. This suggests that in the trimer only small anti-cooperative effects are present in which the first halogen bond weakens the second one and vice versa. The complexation energy for the 2:1 complex formed by binding an additional CF_3I molecule towards the acetone dimer equals -49.4 kJ mol^{-1}. This value is significantly larger than the value of -39.2 kJ mol^{-1} obtained for the complexes with 1:2 stoichiometry. The differences in relative stability are in line with the experimental observations suggesting that in the cryosolutions both types of trimers are formed, and that the equilibrium concentration of the $(acetone)_2$·CF_3I complex is significantly larger than that of the acetone·$(CF_3I)_2$ complex.

In Figure 7.10, the complexation shifts for the 1:2 and 2:1 complexes obtained from the cryosolutions and those deduced from the MP2/aug-cc-pVDZ-PP harmonic vibrational frequencies (Table S7.6) are compared. Taking into account that the harmonic vibrational frequencies were derived for isolated complexes in the gas phase at 0 K and thus does not conclude corrections for thermal or solvent contribution fairly good agreement between experiment and theory is found. Important deviations between experiment and theory are observed for the C=O stretching[27] and C-H stretching modes[28]. The exact reason for these discrepancies is not fully understood, but most probably is due to the fact that in the monomer and in the complexes, these modes are heavily perturbed by Fermi resonances, while such effects are completely neglected while calculating the harmonic vibrational frequencies.

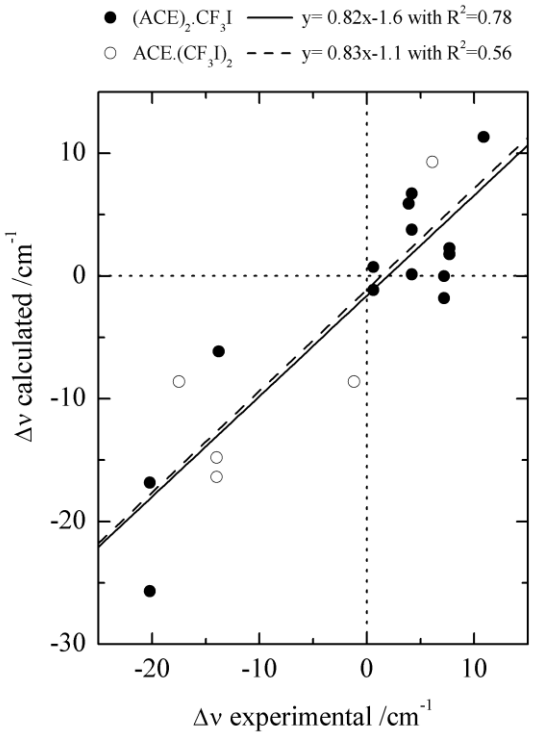

Figure 7.10 Linear fit of the experimental and calculated complexation shifts for the (acetone)$_2$·CF_3I (full circles) and the acetone·$(CF_3I)_2$ (open circles) trimer in Table 7.1 with corresponding linear regression lines.

7.4 Conclusions

The existing methodology of analyzing spectra of self-associating species in liquid noble gases was extended to allow spectra of mixtures of two compounds to be analyzed. Because of the presence of two monomers, mimicking the relation between monomer concentrations and measured absorbances requires a 3D instead of a 2D polynomial. The new model was validated by analyzing a data set of mixtures containing DME and CF_3X (with X = I or Br) in liquid argon. Apart from the bands assigned to the monomers, bands due to 1:1 complexes were observed for a variety of modes localized in the DME or CF_3X moiety. The results yield monomer and dimer spectra similar to those in earlier studies.[5] To analyze the data set of the acetone and CF_3I in liquid krypton the model needed to be further extended with terms to account for 1:2 and 2:1 trimers and acetone dimers. The analysis showed that clear heterodimer signals are present in all studied regions. It also showed many signals for $(acetone)_2 \cdot CF_3I$ but only a few for $acetone \cdot (CF_3I)_2$. Standard *ab initio* calculations predicted the optimized geometries of the $(acetone)_2 \cdot CF_3I$ and $acetone \cdot (CF_3I)_2$ trimers and determined that the former has a complexation energy that is 10 kJ mol^{-1} larger than the latter, stating that the $(acetone)_2 \cdot CF_3I$ is more likely to be formed in the solution in comparison to the $acetone \cdot (CF_3I)_2$. It can safely be concluded that the least-squares fitting approach can also be used to accurately isolate monomer and homo and heterocomplex spectra.

References

[1] W. Herrebout, Top. Curr. Chem., 358 (2015) 79-154.
[2] J. J. J. Dom, B. J. van der Veken, B. Michielsen, S. Jacobs, Z. F. Xue, S. Hesse, H. M. Loritz, M. A. Suhm and W. A. Herrebout, Phys. Chem. Chem. Phys., 13 (2011) 14142-14152.
[3] B. Michielsen, J. J. J. Dom, B. J. van der Veken, S. Hesse, M. A. Suhm and W. A. Herrebout, Phys. Chem. Chem. Phys., 14 (2012) 6469-6478.
[4] N. Nagels, Y. Geboes, B. Pinter, F. De Proft and W. A. Herrebout, Chem. Eur. J., 20 (2014) 8433-8443.
[5] D. Hauchecorne, R. Szostak, W. A. Herrebout and B. J. van der Veken, ChemPhysChem, 10 (2009) 2105-2115.

[6] D. Hauchecorne, B. J. van der Veken, A. Moiana and W. A. Herrebout, Chem. Phys., 374 (2010) 30-36.
[7] D. Hauchecorne, A. Moiana, B. J. van der Veken and W. A. Herrebout, Phys. Chem. Chem. Phys., 13 (2011) 10204-10213.
[8] Y. Geboes, N. Nagels, B. Pinter, F. De Proft and W. A. Herrebout, J. Phys. Chem. A, 119 (2015) 2502-2516.
[9] L. I. De Beuckeleer and W. A. Herrebout, Spectrochim. Acta A, 154 (2016) 89-97.
[10] L. I. De Beuckeleer and W. A. Herrebout, J. Mol. Struct., 1108 (2016) 71-79.
[11] L. I. De Beuckeleer and W. A. Herrebout, J. Phys. Chem. A, (2016).
[12] D. Hauchecorne, N. Nagels, B. J. van der Veken and W. A. Herrebout, Phys. Chem. Chem. Phys., 14 (2012) 681-690.
[13] MATLAB 8.3, The MathWorks Inc., Natick, MA, USA, 2014.
[14] B. J. van der Veken and F. R. De Munck, J. Chem. Phys., 97 (1992) 3060-3071.
[15] B. J. van der Veken, J. Phys. Chem., 100 (1996) 17436-17438.
[16] B. J. van der Veken and W. A. Herrebout, J. Phys. Chem. A, 105 (2001) 7198-7204.
[17] A. I. Fishman, W. A. Herrebout and B. J. van der Veken, J. Phys. Chem. A, 106 (2002) 4536-4542.
[18] B. Michielsen, J. J. J. Dom, B. J. van der Veken, S. Hesse, Z. F. Xue, M. A. Suhm and W. A. Herrebout, Phys. Chem. Chem. Phys., 12 (2010) 14034-14044.
[19] G. P. Everaert, W. A. Herrebout, B. J. van der Veken, J. Lundell and M. Rasanen, Chem-Eur J, 4 (1998) 321-327.
[20] R. Szostak, W. A. Herrebout and B. J. van der Veken, Physical Chemistry Chemical Physics, 2 (2000) 3983-3991.
[21] M. J. Frisch, G. W. Trucks, H. B. Schlegel, G. E. Scuseria, M. A. Robb, J. R. Cheeseman, G. Scalmani, V. Barone, B. Mennucci, G. A. Petersson, *et al.*, Gaussian 09, Revision A.02, Gaussian, Inc., Wallingford, CT, USA, 2009.
[22] D. Feller, J. Comput. Chem., 17 (1996) 1571-1586.
[23] K. L. Schuchardt, B. T. Didier, T. Elsethagen, L. Sun, V. Gurumoorthi, J. Chase, J. Li and T. L. Windus, J. Chem. Inf. Model., 47 (2007) 1045-1052.
[24] N. Nagels, D. Hauchecorne and W. A. Herrebout, Molecules, 18 (2013) 6829-6851.
[25] S. F. Boys and F. Bernardi, Mol. Phys., 19 (1970) 553-566.
[26] W. Zierkiewicz, D. C. Bieńko, D. Michalska and T. Zeegers-Huyskens, Theoretical Chemistry Accounts, 134 (2015) 103.
[27] B. J. van der Veken, S. N. Delanoye, B. Michielsen and W. A. Herrebout, J. Mol. Struct., 976 (2010) 97-104.
[28] W. A. Herrebout, S. M. Melikova, S. N. Delanoye, K. S. Rutkowski, D. N. Shchepkin and B. J. van der Veken, J. Phys. Chem. A, 109 (2005) 3038-3044.

Supporting information

Table S7.1: Cartesian coordinates of the optimized geometry of the acetone monomer at MP2/aug-cc-pVDZ level.

	X	Y	Z
Acetone			
C	0.000000	0.000000	0.180083
O	0.000000	0.000000	1.411068
C	0.000000	1.291622	-0.617403
H	0.887011	1.328841	-1.271370
H	-0.887011	1.328841	-1.271370
H	0.000000	2.152710	0.062635
C	0.000000	-1.291622	-0.617403
H	-0.887011	-1.328841	-1.271370
H	0.887011	-1.328841	-1.271370
H	0.000000	-2.152710	0.062635

Table S7.2: Cartesian coordinates of the optimized geometry of the CF_3I monomer at MP2/aug-cc-pVDZ-PP level.

	X	Y	Z
CF_3I			
C	0.000000	0.000000	-1.170751
F	0.000000	1.259768	-1.647066
F	-1.090991	-0.629884	-1.647066
F	1.090991	-0.629884	-1.647066
I	0.000000	0.000000	0.971609

Table S7.3: Cartesian coordinates of the optimized geometry of the acetone·CF_3I dimer at MP2/aug-cc-pVDZ-PP level.

	X	Y	Z
Acetone·CF_3I			
C	-3.524337	0.036249	-0.000281
O	-2.547938	-0.717230	0.000946
C	-4.935273	-0.510092	0.000532
H	-5.513950	-0.065881	0.825356
H	-5.436799	-0.224777	-0.938191
H	-4.917361	-1.602132	0.093890
C	-3.372793	1.541895	-0.001341
H	-3.962608	1.981608	-0.820643
H	-3.774792	1.947220	0.941256
H	-2.317896	1.823502	-0.102123
C	2.512930	0.142443	-0.000231
F	2.784526	1.467499	-0.017778
F	3.099429	-0.380847	1.099594
F	3.104153	-0.410707	-1.082766
I	0.402467	-0.216381	0.000177

Table S7.4: Cartesian coordinates of the optimized geometry of the $(acetone)_2 \cdot CF_3I$ trimer at MP2/aug-cc-pVDZ-PP level.

	X	Y	Z
$(Acetone)_2 \cdot CF_3I$			
C	-2.810637	-1.43202	0.03866
O	-1.859726	-1.310956	-0.741123
C	-2.103354	2.103862	0.115874
O	-2.883613	1.470816	0.830862
C	-2.611297	-1.646455	1.520214
H	-3.105177	-0.830069	2.069011
H	-3.085076	-2.593787	1.823618
H	-1.543279	-1.668423	1.768388
C	-4.237075	-1.360872	-0.453801
H	-4.804592	-2.241209	-0.114086
H	-4.707846	-0.466829	-0.015404
H	-4.257202	-1.296616	-1.548474
C	-2.184092	2.044024	-1.393842
H	-2.121697	3.055219	-1.825054
H	-1.32263	1.468576	-1.770409
H	-3.110902	1.54897	-1.707855
C	-1.016153	2.97553	0.706246
H	-0.04924	2.759571	0.226402
H	-1.255053	4.032623	0.503669
H	-0.948186	2.815287	1.788934
C	2.920588	0.112376	0.124848
F	2.933133	1.462367	0.242503
F	3.445117	-0.400338	1.260111
F	3.745914	-0.21548	-0.893722
I	0.931929	-0.608675	-0.214073

Table S7.5: Cartesian coordinates of the optimized geometry of the acetone·$(CF_3I)_2$ trimer at MP2/aug-cc-pVDZ-PP level.

	X	Y	Z
Acetone·$(CF_3I)_2$			
C	-0.000072	3.256456	-0.000044
O	-0.000099	2.020294	0.000615
C	-1.288750	4.044849	0.012411
H	-1.254386	4.817378	0.795958
H	-1.396742	4.566180	-0.952705
H	-2.147643	3.381535	0.168283
C	1.288574	4.044864	-0.013387
H	1.254257	4.816248	-0.798071
H	1.396355	4.567641	0.950969
H	2.147579	3.381442	-0.168179
C	-3.891590	-1.410688	-0.001629
I	-2.285126	0.006214	0.001128
F	-5.086289	-0.790368	-0.122794
F	-3.772345	-2.279459	-1.028281
F	-3.912588	-2.124827	1.144198
C	3.891662	-1.410606	0.001159
F	3.896503	-2.142309	-1.133696
F	5.087874	-0.788590	0.095817
F	3.787110	-2.263449	1.042675
I	2.285127	0.006219	-0.000628

Table S7.6: Calculated symmetries, wavenumbers (in cm^{-1}), infrared intensities (in km mol^{-1}) and complexation shifts (in cm^{-1}) at MP2/aug-cc-pVDZ-(PP) level for the fundamental vibrational modes of the acetone and CF_3I monomers and with counterpoise correction for acetone·CF_3I, (acetone)$_2$·CF_3I and acetone·$(CF_3I)_2$.

Monomers				Dimers			Trimers					
Assignment and Symm.		Freq.	IR-int.	Acetone·CF_3I			(Acetone)$_2$·CF_3I			Acetone·$(CF_3I)_2$		
				Freq.	IR-int.	Δν	Freq.	IR-int.	Δν	Freq.	IR-int.	Δν
	Acetone											
ν_1	A_1	3199.6	4.6	3207.3	4.6	7.7	3203.2	4.6	3.6	3206.3	1.8	6.7
							3202.3	4.5	2.7			
ν_{18}	B_2	3198.8	9.8	3204.0	5.8	5.2	3201.4	13.3	2.6	3205.9	6.1	7.1
							3201.2	4.2	2.4			
ν_{13}	B_1	3149.9	14.	3157.9	8.6	8.0	3163.7	7.5	13.8	3158.4	5.1	8.5
							3156.7	10.6	6.8			
ν_9	A_2	3144.0	0.0	3152.1	0.4	8.1	3158.0	0.3	14.0	3152.9	1.1	8.9
							3152.4	1.6	8.4			
ν_2	A_1	3065.4	7.2	3071.5	6.2	6.1	3072.2	8.0	6.7	3071.6	5.1	6.1
							3068.9	4.2	3.4			
ν_{19}	B_2	3061.0	1.5	3067.3	0.4	6.3	3068.2	1.9	7.2	3067.7	0.0	6.7
							3065.4	1.2	4.4			
ν_3	A_1	1731.5	125	1729.5	202.4	-2.0	1731.6	215.3	0.1	1722.9	245.3	-8.6
							1725.3	95.7	-6.1			
ν_{14}	B_1	1480.3	18.	1480.8	15.7	0.5	1482.0	12.6	1.7	1479.3	13.1	-1.0
							1476.9	18.2	-3.4			
ν_4	A_1	1457.4	29.	1459.3	22.9	1.9	1459.7	9.0	2.3	1459.4	16.8	2.1
							1459.2	44.7	1.8			
ν_{10}	A_2	1454.2	0.0	1453.5	7.6	-0.8	1455.2	2.1	1.0	1450.8	14.5	-3.5
							1449.8	9.8	-4.5			
ν_{20}	B_2	1448.8	0.1	1449.8	0.8	1.0	1448.8	3.5	0.0	1449.2	0.9	0.4
							1447.0	6.8	-1.8			
ν_{21}	B_2	1385.1	70.	1391.8	68.3	6.7	1391.8	68.3	6.7	1394.4	63.5	9.3
							1388.9	71.0	3.8			
ν_5	A_1	1368.6	12.	1373.2	16.0	4.6	1369.4	23.6	0.7	1374.9	19.7	6.3
							1367.5	19.4	-1.1			

Monomers				Dimers			Trimers					
Assignment and Symm.		Freq.	IR-int.	Freq.	IR-int.	Δν	Freq.	IR-int.	Δν	Freq.	IR-int.	Δν
Acetone				Acetone·CF_3I			$(Acetone)_2$·CF_3I			Acetone·$(CF_3I)_2$		
ν_{22}	B_2	1248.1	42.	1258.0	33.7	9.9	1259.5	31.0	11.3	1263.6	28.4	15.5
							1254.0	18.8	5.9			
ν_{15}	B_1	1097.3	1.2	1099.5	1.2	2.2	1099.9	5.5	2.6	1099.7	1.2	2.4
							1096.5	8.9	-0.8			
ν_6	A_1	1071.4	0.0	1075.5	24.7	4.1	1078.7	1.5	7.3	1076.9	34.3	5.4
							1072.5	105.9	1.1			
ν_{23}	B_2	893.6	4.2	902.1	2.7	8.4	905.7	2.8	12.1	908.1	1.8	14.4
							905.2	2.8	11.6			
ν_{11}	A_2	873.2	0.0	874.8	0.1	1.6	875.1	0.3	2.0	875.3	0.2	2.1
							873.2	0.1	0.1			
ν_7	A_1	807.2	1.3	814.4	0.6	7.2	819.2	0.3	12.0	817.4	0.2	10.2
							810.6	1.0	3.5			
ν_{24}	B_2	527.1	14.	535.4	19.1	8.3	537.5	20.4	10.4	540.4	22.7	13.3
							529.7	10.7	2.6			
ν_{16}	B_1	479.9	0.5	483.6	0.4	3.7	484.1	0.2	4.2	484.8	0.4	4.9
							480.1	1.1	0.2			
ν_8	A_1	376.4	1.3	382.2	3.8	5.8	386.3	2.9	9.9	386.1	5.2	9.8
							378.3	1.7	1.9			
ν_{17}	B_1	145.7	0.1	142.5	0.1	-3.3	153.9	0.6	8.2	159.8	2.1	14.1
							137.5	0.9	-8.2			
ν_{12}	A_2	20.6	0.0	46.3	0.0	25.8	32.3	0.1	11.7			

CF_3I				Acetone·CF_3I			$(Acetone)_2$·CF_3I			Acetone·$(CF_3I)_2$		
ν_4	E	1162.4	455	1144.2	225.5	-18.2	1145.6	214.5	-16.8	1150.9	440.4	-11.5
										1149.5	13.1	-12.9
				1142.0	222.0	-20.4	1136.7	234.7	-25.7	1147.6	246.0	-14.8
										1146.1	185.3	-16.4
ν_1	A_1	1060.0	547	1072.3	578.3	12.3	1071.6	457.2	11.6	1073.6	485.9	13.6
										1063.8	743.8	3.8
ν_2	A_1	722.4	34.	717.7	22.8	-4.8	716.6	21.3	-5.8	719.0	22.9	-3.4
										718.5	32.6	-3.9
ν_5	E	518.9	1.1	517.4	0.4	-1.5	517.3	0.2	-1.6	518.0	0.3	-0.9
							516.4	0.7	-2.5	517.9	1.0	-1.0
				517.4	0.7	-1.5				517.7	0.0	-1.2
										517.6	0.8	-1.3
ν_3	A_1	295.0	0.3	292.6	5.5	-2.4	291.3	6.4	-3.8	293.1	3.5	-2.0
										292.5	4.4	-2.5
ν_6	E	269.1	0.1	271.6	0.1	2.6	272.5	0.1	3.5	271.6	0.1	2.6
										271.4	0.1	2.4
				88.2	8.9		109.4	12.7		138.0	0.3	
				65.0	3.2		104.9	1.8		109.3	12.0	
				58.1	0.4		97.3	9.0		75.8	2.9	
				27.6	0.9		87.6	1.2		75.1	0.9	
				16.9	0.6		78.4	2.8		67.4	0.6	
				2.1	1.0		73.3	3.1		42.6	0.2	
							64.7	1.3		38.3	0.0	
							52.6	1.0		36.3	0.0	
							40.6	1.0		27.4	0.2	
							35.3	2.5		15.4	0.0	
							32.3	0.1		14.0	1.0	
							25.4	0.4		11.9	0.2	
							13.1	0.1		0.9	0.1	
							7.5	0.0		0.4	0.0	

Chapter 8

Summary and conclusions

In this work new numerical methods have been developed to separate monomer and complex contributions in overlapping spectra recorded with infrared spectroscopy of cryosolutions in liquid noble gases. The introduction of a PID-controller in the experimental set-up constructed by J. Dom[1] allowed to record data sets of spectra of different concentrations at constant temperature. This last chapter will summarize our findings and is divided into two main parts. In the first part the advances made in analyzing spectra of self-associating molecules are discussed. These molecules are inclined to interact with each other and thus form oligomers or homocomplexes. In the second part these advances are used to interpret complicated spectra of mixtures of two molecules that form heterocomplexes.

8.1 Homocomplexes

In Chapter 3 to 6 we develop a new numerical approach that enables the investigation of spectra in which spectral features due to monomers and homocomplexes are present simultaneously, and in which monomer contribution cannot be accurately determined using traditional subtraction procedures. In this method the monomeric and different oligomeric contributions at each wavenumber are obtained by fitting the measured absorbances to monomer absorbances using a higher degree polynomial. The new approach is based on the fact that cryosolutions are in therrmodynamical equilibrium. The equilibrium constant K_p of the formation of homocomplexes and can be written as

$$pA \rightleftharpoons A_p \qquad\qquad K_p = \frac{C_{A_p}}{C_A^p} \tag{8.1}$$

with the equilibrium concentrations *C* and *p* as the number of molecules in the complex. The spectra of the mixtures of species in cryosolutions can be seen as a superposition of monomer spectra and spectra of possible homocomplexes, so that the measured absorbance at a wavenumber $\tilde{\nu}_i$, $A_{exp}(\tilde{\nu}_i)$ equals the sum of individual contributions related to monomers, A_1 or to one of the oligomers, e.g. dimers A_2, trimers A_3, tetramers A_4, etc., i.e.

$$A_{exp}(\tilde{\nu}_i) = A_1(\tilde{\nu}_i) + A_2(\tilde{\nu}_i) + A_3(\tilde{\nu}_i) + A_4(\tilde{\nu}_i) + \cdots \tag{8.2}$$

The experimental absorbance at a wavenumber $\tilde{\nu}_i$ originating from all contributing species in the solution can then be expressed as polynomial in function of the monomer absorbance at a chosen reference wavenumber $\tilde{\nu}_m$ with the polynomial degree p equal to 1, 2, 3, 4 or 5 with the intercept equal to zero.

$$A_{exp}(\tilde{\nu}_i) = \sum_{p=1}^{n} a_{\mathrm{p}}(\tilde{\nu}_i, \tilde{\nu}_m)\,[A_{mon}(\tilde{\nu}_m)]^p \tag{8.3}$$

The coefficient $a_{\mathrm{p}}(\tilde{\nu}_i, \tilde{\nu}_m)$ is a constant related to the equilibrium constant K_p of the oligomerization reaction that can be fitted by using the method of least-squares.

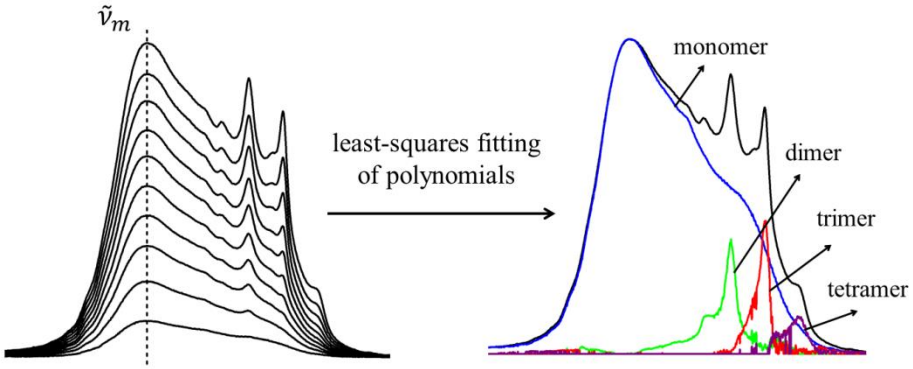

Figure 8.1 Summary of the analysis of the HCl dissolved in liquid argon. The result shows the monomer, dimer, trimer and tetramer contributions.

The spectra of four self-associating molecules were analyzed with the new methodology incorporated in a Matlab script.[2] The first molecule to validate the method was hydrogen chloride (HCl). Its spectra were recorded in liquid argon solutions at 103 K. It showed that the least-squares fitting of higher degree polynomials tends to overfit and at the same time leads to unphysical compensation effects where a positive contribution due to one species is compensated for by a negative contribution of another. These issues can be corrected for by on the one hand implementing a procedure to select the appropriate polynomial at each wavenumber with the B information criterion (*BIC*)[3]. In this criterion the selection is based on the differences between consecutive fits when systematically increasing the degree of the polynomial model. On the other hand additional constraints are introduced prohibiting negative absorbances to occur for the monomer and oligomers. Finally each term of the fitted

polynomial can be plotted for every wavenumber to obtain the oligomer bands. This procedure is illustrated in Figure 8.1. The results showed well separated oligomeric bands originating from dimers, trimers, tetramers present in the solutions. The observed complexbands compared well with previous literature.[4]

The second data set subjected to the new methodology was a set of spectra of ammonia (NH_3) dissolved in liquid xenon. The self-associating behavior of this molecule was already been observed before but the data did not allow to make a detailed assignment of the emerging features. As no such features have yet been reported for ammonia-d_3 (ND_3) also data sets of ND_3 dissolved in liquid xenon were analyzed. When increasing the concentration, for both species oligomer bands appeared in the spectra. But unfortunately, time dependent artifacts due to the presence of solid water hampered the analysis as it overlapped completely with the N–H stretching area and therefore, making an unambiguous assignment impossible. As the artefacts did not show overlap with the N–D stretching region it was possible to analyze the spectra of ND_3. In this case oligomer bands originating from dimers, trimers and tetramers were observed.

In the third investigation the self-associating behavior of pyrrole in solutions in liquid xenon was reported. Analysis of the data showed that by using the least-squares polynomial regression based methodology, spectral data due to pyrrole monomers, dimers, trimers and tetramers could be resolved. The assignments of the monomer vibrational modes closely follow those reported previously for the pyrrole in the gas- and solid-phase.[5,6] Clear intense absorption bands originating from pyrrole trimers are present in every spectral region, but bands indicating the presence of dimers and tetramers are rather scarce and weak. The absence of clear dimer signals is surprising, as they have been observed in the gas- and solid- phase in previous literature investigations. But it suggest that at chemical equilibrium the strong cooperative effects in trimers cause a dimer to pick up an extra pyrrole unit to create the more stable trimer and consequently keep the dimer concentration low. The assignment of tetramer bands is tentative given that comparable literature data is rather scarce. All in all, the current results obtained with the newly developed method are consistent with results from literature but also add many oligomer signals that have not yet been reported before.

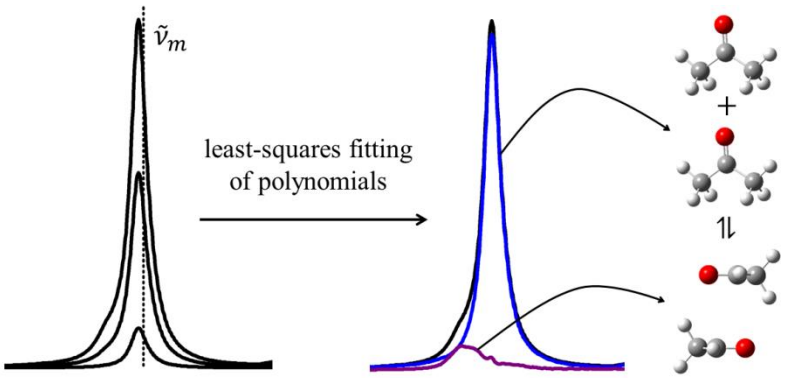

Figure 8.2 Summary of the analysis of the acetone dissolved in liquid krypton. The result shows the dimer (purple trace) contribution in the experimental spectra.

The fourth self-associating molecule studied was acetone. Infrared spectra of acetone dissolved in liquid krypton were recorded at constant temperature. By fitting a quadratic polynomial model to the data, the vibrational spectrum was resolved in a monomer and dimer contribution. The assignment of the monomer spectrum fully supports the assignments of the gas-phase spectrum found in literature[7]. It was observed that all spectral regions show dimer bands that overlap completely with the related monomer bands except for the dimer band assigned to the $\nu_{\mathrm{C-C\ as}}$ mode at 1222.7 cm^{-1} for which a complex band blue-shifted from the monomer band by 5.3 cm^{-1} is observed, as illustrated in Figure 8.2. For the first time a complete assignment of the experimental mid infrared spectrum of the acetone dimer was made. Using spectra recorded at different temperatures between 134 and 142 K, the experimental dimerization enthalpy was measured to be -10.8 ± 1.1 kJ mol^{-1}. *Ab initio* calculations predicted a stacked and a planar dimer geometry of which the stacked geometry is 13.3 kJ mol^{-1} more stable with a CCSD(T) dimerization energy of -28.4 kJ mol^{-1}. The theoretical standard dimerization enthalpy was determined to be -13.7 kJ mol^{-1}, by Monte Carlo Free Energy Perturbation (MC-FEP) simulation and statistical thermodynamical calculations to rationalize the effects of temperature and of solvatation.

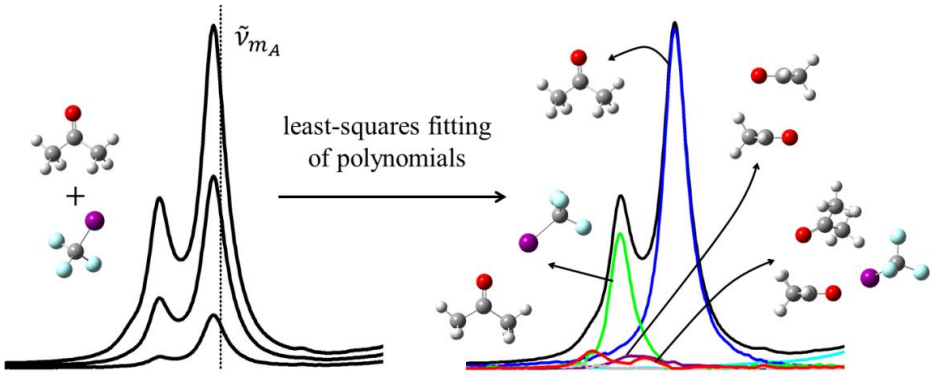

Figure 8.3 Summary of the analysis of mixtures of acetone and CF_3I dissolved in liquid krypton. The result shows the presence of the acetone (blue) and CF_3I (cyan) monomers and the $(acetone)_2$, acetone·CF_3I, $(acetone)_2$·CF_3I, complexes by respectively a purple, green and red trace, in the presented region of the experimental spectra.

8.2 Heterocomplexes

The observation of acetone molecules being involved in dimer formation obviously affects its use as a carbonyl prototype Lewis base in studies of heterocomplexes. To analyze the spectra of mixed solutions containing acetone and hydrogen and halogen bonding donors, routine subtraction procedures are not sufficient but a dedicated approach based on the methodology developed for homocomplexes is required. In Chapter 7 the existing equations were adjusted so they can also be used to analyze spectra for mixed solutions in which two species A and B are in equilibrium with a complex with 1:1 stoichiometry:

$$A + B \rightleftharpoons AB \qquad K_{AB} = \frac{C_{AB}}{C_A \cdot C_B} \tag{8.4}$$

Based on this equilibrium an expression was derived in which, for each arbitrary wavenumber $\tilde{\nu}_i$ the measured absorbance A_{exp} could be written as a sum of absorbance contributions related to the monomers A and B, respectively A_A and A_B and to the heterocomplexes, e.g. the dimer AB, A_{AB}:

$$A_{exp}(\tilde{\nu}_i) = A_A(\tilde{\nu}_i) + A_B(\tilde{\nu}_i) + A_{AB}(\tilde{\nu}_i) \tag{8.5}$$

Similar to the homocomplexes each contribution could be transformed into a term in function of the absorbance at reference wavenumbers $\tilde{\nu}_{mA}$ and $\tilde{\nu}_{mB}$:

$$\begin{aligned} A_{exp}(\tilde{\nu}_i) = {} & a_{\mathrm{A}}(\tilde{\nu}_i, \tilde{\nu}_{mA,}\tilde{\nu}_{mB})A_A(\tilde{\nu}_{mA}) \\ & + a_{\mathrm{B}}(\tilde{\nu}_i, \tilde{\nu}_{mA,}\tilde{\nu}_{mB})A_B(\tilde{\nu}_{mB}) \\ & + a_{\mathrm{AB}}(\tilde{\nu}_i, \tilde{\nu}_{mA,}\tilde{\nu}_{mB})A_A(\tilde{\nu}_{mA})A_B(\tilde{\nu}_{mB}) \end{aligned} \tag{8.6}$$

In the first part of study on heterocomplex this adjusted model was validated by analyzing spectra of mixtures containing dimethyl ether (DME) and the trifluoromethyl halides CF_3I and CF_3Br in liquid argon. Apart from the bands assigned to the monomers, bands due to 1:1 complexes were observed for a variety of modes localized in the DME or CF_3X moiety. The results yielded monomer and dimer spectra similar to those in earlier studies.[8]

The second part of the study involved the application of the model towards the complexes formed between acetone and CF_3I in liquid krypton. Such complexes have not been reported before. To analyze the spectra of acetone and CF_3I the model in Eq. (8.6) needed to be further extended with terms to account for 1:2 and 2:1 trimers and acetone dimers:

$$\begin{aligned} A_{exp}(\tilde{\nu}_i) = {} & a_{\mathrm{A}}(\tilde{\nu}_i, \tilde{\nu}_{mA,}\tilde{\nu}_{mB})A_A(\tilde{\nu}_{mA}) \\ & + a_{\mathrm{B}}(\tilde{\nu}_i, \tilde{\nu}_{mA,}\tilde{\nu}_{mB})A_B(\tilde{\nu}_{mB}) \\ & + a_{\mathrm{AB}}(\tilde{\nu}_i, \tilde{\nu}_{mA,}\tilde{\nu}_{mB})A_A(\tilde{\nu}_{mA})A_B(\tilde{\nu}_{mB}) \\ & + a_{A_2B}(\tilde{\nu}_i, \tilde{\nu}_{mA,}\tilde{\nu}_{mB})A_A(\tilde{\nu}_{mA})^2A_B(\tilde{\nu}_{mB}) \\ & + a_{AB_2}(\tilde{\nu}_i, \tilde{\nu}_{mA,}\tilde{\nu}_{mB})A_A(\tilde{\nu}_{mA})A_B(\tilde{\nu}_{mB})^2 \\ & + a_{A_2}(\tilde{\nu}_i, \tilde{\nu}_{mA})A_A(\tilde{\nu}_{mA})^2 \end{aligned} \tag{8.7}$$

The analysis showed that clear heterodimer features are present in all studied regions. It also showed many signals for (acetone)$_2$·CF_3I but only a few for acetone·$(CF_3I)_2$. *Ab initio* calculations predicted the optimized geometries of the (acetone)$_2$·CF_3I and acetone·$(CF_3I)_2$ trimers and determined that the former has a complexation energy that is 10 kJ mol^{-1} larger than the latter, stating that the (acetone)$_2$·CF_3I is more likely to formed in the solution in comparison to the acetone·$(CF_3I)_2$. Figure 8.3 shows the results of the analysis of the $\nu_{\mathrm{C–C\ as}}$ mode at 1222.7 cm^{-1} for which blue-shifted complex bands were observed originating from the (acetone)$_2$, acetone·CF_3I, (acetone)$_2$·CF_3I and acetone·$(CF_3I)_2$ complexes.

8.3 Conclusions and outlook

The new methodology based on least-squares fitting of polynomials allowed us to analyze spectra of the self-associating molecules For all studied systems the new methodology showed added value as it made it possible to observe and identify the features due oligomers in liquid noble gasses, which was impossible with the earlier subtraction procedures. The results of HCl, ND_3 and pyrrole complemented the existing data and led to more complete characterization of the self-association and the effects on the obtained vibrational spectra. Although acetone has extensively been used several previous infrared studies in liquid noble gases, its dimer bands have always escaped detection and were therefore never observed before. The use of the new methodology now results in a separated monomer and dimer contribution which proves that polynomial regression pushes the boundaries of cryospectroscopy as it extracts more detailed data from the recorded data than before. The observation of the acetone dimer is also the first observation in cryosolvents of a complexes held together by dipole-dipole interactions. The boundaries were further explored by the analysis of spectra recorded for a mixture of acetone and the halogen bond donor CF_3I. To conclude, it can be stated that least-squares fitting of polynomials to data recorded at constant temperature can be seen as a valuable tool for studying the formation of complexes held together by weak intermolecular interactions.

After successfully observing the first complex held together by dipole-dipole interactions the developed approach shall in principle be used to observe the first stacked complex held together by π···π interactions. The simplest prototype of π···π interactions is the self-associated benzene dimer. Because of its low estimated dimerization energy it is known to only be stable at low temperatures[9] yet it has not been observed in cryosolutions. The gathering of data set of infrared spectra for the benzene solutions is not that straightforward as for previously studied systems. Because of the large infrared intensity of the out-of-plane bending mode, the MCT detector is saturated even at low concentrations, making it impossible to record reliable intensities. A technique that may provide a solution to this problem is the use of isotopic dilutions, in which a small amount of a molecule is mixed with a large amount of the same

molecule but with a different isotopic composition, like e.g. benzene and benzene-d_6. Therefore observing benzene dimer features is a future challenge that could push the boundaries of cryospectroscopy one step further.

References

[1] J. J. Dom, *Anaesthetics directed via weak hydrogen bonds? An infrared and Raman spectroscopic study towards target molecules and computational accuracy,* PhD thesis, University of Antwerp, 2011.

[2] in MATLAB 8.3, The MathWorks Inc., Natick, MA, USA, 2014.

[3] G. Schwarz, The Annals of Statistics, 6 (1978) 461-464.

[4] B. J. van der Veken and F. R. De Munck, J. Chem. Phys., 97 (1992) 3060-3071.

[5] T. D. Klots, R. D. Chirico and W. V. Steele, Spectrochim. Acta A, 50 (1994) 765-795.

[6] A. Gómez-Zavaglia and R. Fausto, J. Phys. Chem. A, 108 (2004) 6953-6967.

[7] G. Dellepiane and J. Overend, Spectrochim. Acta, 22 (1966) 593-614.

[8] D. Hauchecorne, R. Szostak, W. A. Herrebout and B. J. van der Veken, ChemPhysChem, 10 (2009) 2105-2115.

[9] M. O. Sinnokrot, E. F. Valeev and C. D. Sherrill, J. Am. Chem. Soc., 124 (2002) 10887-10893.

Samenvatting

In dit doctoraatsonderzoek werden nieuwe numerieke methoden ontwikkeld om monomeer- en complexbijdragen in overlappende spectra die opgenomen werden met infraroodspectroscopie van cryo-oplossingen in vloeibare edelgassen. Door de recentelijke toevoeging van een PID-regulator ontwikkeld door J. Dom[1] aan de experimentele opstelling werd het mogelijk om spectra op te nemen van verschillende concentraties bij constante temperatuur. Het onderzoek bestond uit twee grote delen. In het eerste deel worden de vorderingen besproken die gemaakt werden in het analyseren van spectra van uit zichzelf associërende moleculen, die ook wel homocomplexen genoemd worden. In het tweede deel worden deze vorderingen gebruikt om gecompliceerde spectra te interpreteren van mengsels van twee moleculen.

Homocomplexen

In Hoofdstuk 3 tot 6 ontwikkelen we een nieuwe numerieke methode die het mogelijk maakt spectra te onderzoeken waarin spectrale elementen zitten die te wijten zijn aan monomeren en homocomplexen die gelijktijdig in de oplossing aanwezig zijn en waarin de monomeerbijdrage niet nauwkeurig bepaald kan worden met traditionele substractie procedures. In deze methode kunnen de monomeer- en de verschillende oligomeerbijdragen bij elk golfgetal bekomen worden door de gemeten absorbanties te fitten aan de monomeer absorbanties met hogeregraads polynomen. De nieuwe benadering is gebaseerd op het feit dat cryo-oplossingen zich in thermodynamisch evenwicht bevinden. De evenwichtsconstante van de vorming van homocomplexen kan geschreven worden als

$$pA \rightleftharpoons A_p \qquad\qquad K_p = \frac{C_{A_p}}{C_A^p} \tag{9.1}$$

met de evenwichtsconcentratie C en p als het aantal moleculen in een complex.

De spectra van de mengsels van moleculen in cryo-oplossingen kunnen beschouwd worden als een superpositie van monomeerspectra en spectra van mogelijke homocomplexen. Daardoor kan de gemeten absorbantie bij een bepaald golfgetal $\tilde{\nu}_i$, $A_{exp}(\tilde{\nu}_i)$, gelijkgesteld worden aan de som van individuele bijdragen die in verband

staan met monomeren, A_1 of met één van de oligomeren zoals dimeren A_2, trimeren A_3, tetrameren, A_4, enz.

$$A_{exp}(\tilde{\nu}_i) = A_1(\tilde{\nu}_i) + A_2(\tilde{\nu}_i) + A_3(\tilde{\nu}_i) + A_4(\tilde{\nu}_i) + \cdots \quad (9.2)$$

De experimentele absorbantie voor elk golfgetal $\tilde{\nu}_i$, die voortkomt uit alle aanwezige verbindingen in de oplossing kan dan uitgedrukt worden als een polynoom van de monomeerabsorbantie bij een gekozen referentie golfgetal $\tilde{\nu}_m$ met graad 1, 2, 3, 4 of 5 met de intercept gelijk aan nul.

$$A_{exp}(\tilde{\nu}_i) = \sum_{p=1}^{n} a_{\mathrm{p}}(\tilde{\nu}_i, \tilde{\nu}_m)\,[A_{mon}(\tilde{\nu}_m)]^p \quad (9.3)$$

De coëfficiënt $a_{\mathrm{p}}(\tilde{\nu}_i, \tilde{\nu}_m)$ is een constante, verbonden met de evenwichtsconstante K_p van de oligomerisatiereactie, die gefit kan worden door gebruikt te maken van de methode van kleinste kwadraten.

De spectra van vier uit zichzelf associërende moleculen werden geanalyseerd met de nieuwe methodologie met behulp van Matlab.[2] De eerste molecule die gebuikt werd om de methode te testen was waterstofchloride (HCl). De spectra van HCl werden opgemeten van oplossing van vloeibaar argon bij 103 K. Dit toonde aan dat het fitten van hogeregraads polynomen met kleinste kwadraten geneigd is om te overfitten en ook leidt tot fysisch onmogelijke compensatie-effecten, waarbij een positieve bijdrage afkomstig van een verbinding wordt gecompenseerd wordt door een negatieve bijdrage van een andere verbinding. Deze zaken kunnen gecorrigeerd worden door enerzijds een procedure te implementeren die de gepaste polynoom selecteert bij elk golfgetal met het B informatie criterium (*BIC*)[3]. In dit criterium wordt de selectie gebaseerd op de verschillen tussen opeenvolgende fits bij systematische verhoging van de graad van het polynoom model. Anderzijds worden bijkomende beperkingen ingevoerd die het voorkomen van negatieve absorbanties voor de monomeren en oligomeren. Uiteindelijk kan elke term van de gefitte polynoom geplot worden voor elk golfgetal om zo de oligomeerbanden te verkrijgen. Deze werkwijze wordt geïllustreerd in Figuur 9.1. Het resultaat zijn goed gescheiden oligomeerbanden die voortkomen uit dimeren, trimeren, tetrameren.[4]

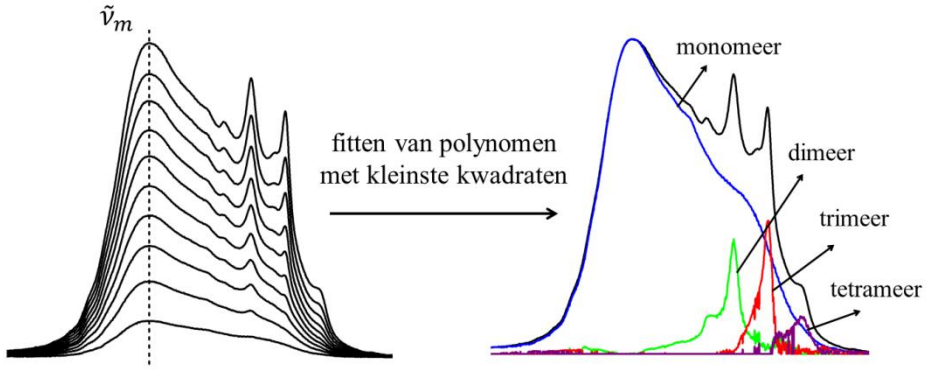

Figure 8.1 Samenvatting van de analyse van HCl opgelost in vloeibaar argon. Het resultaat toont de aanwezigheid van monomeer-, dimeer-, trimeer- en tetrameerbijdragen.

De tweede dataset die werd onderworpen aan een de nieuwe methodologie was een set van spectra van ammoniak (NH_3) opgelost in vloeibaar xenon. Het uit zichzelf associërende gedrag van deze molecule werd al eerder opgemerkt maar het was toen niet mogelijk om de tevoorschijn komende banden in detail toe te wijzen. Omdat zulke banden nog niet eerder beschreven werden voor ammoniak-d_3 (ND_3) werden ook datasets van ND_3 opgelost in vloeibaar xenon geanalyseerd. Bij het verhogen van de concentraties verschenen er voor beide verbindingen oligomeerbanden in de spectra. Maar jammer genoeg werd de analyse bemoeilijkt door tijdsafhankelijke artefacten, die veroorzaakt worden door de aanwezigheid van ijskristallen, die volledig overlapten met het N–H rekgebied. Dit maakte een eenduidige toewijzing onmogelijk. Omdat de artefacten geen overlap vertoonden met het N–D rekgebied was het wel mogelijk om de ND_3 spectra te analyseren. In dit geval werden oligomeerbanden geobserveerd afkomstig van dimeren, trimeren en tetrameren.

In een derde luik werd het uit zichzelf associërende gedrag van pyrrool beschreven wanneer het opgelost wordt in vloeibaard xenon. Bij het analyseren van de data werd het duidelijk dat door het fitten van polynomen, spectrale data afkomstig van pyrrool monomeren, dimeren, trimeren en zelfs tetrameren gescheiden kon worden. De toewijzing van de vibratiemodes van het monomeer waren gelijkaardig aan voorgaande toewijzingen bij gasvormig of vast pyrrool.[5,6] In elke spectrale regio werden er intense absorptie banden waargenomen die veroorzaakt worden door de pyrrool trimeren. Banden die die duiden op de aanwezigheid van dimeren en tetrameren zijn eerder

schaars en zwak. Het ontbreken van duidelijke dimeer signalen is verrassend omdat ze al wel geobserveerd werden in de gasvormige en vaste fase in voorgaande onderzoeken in de literatuur. Maar dit versterkt wel de suggestie dat door de aanwezigheid van sterke coöperatieve effecten in trimeren, bij chemisch evenwicht een dimeer geneigd is een extra pyrrool molecule op te nemen om het meer stabiele trimeer te vormen en bijgevolg de dimeer concentratie laag blijft. De toewijzing van tetrameer banden is voorlopig omdat vergelijkbare resultaten uit de literatuur eerder beperkt zijn. In het algemeen, zijn de resultaten die bekomen werden met de recent ontwikkelde methode consistent met de gegevens uit de literatuur maar er werden ook vele nieuwe oligomeerbanden toegewezen die nog niet eerder beschreven werden.

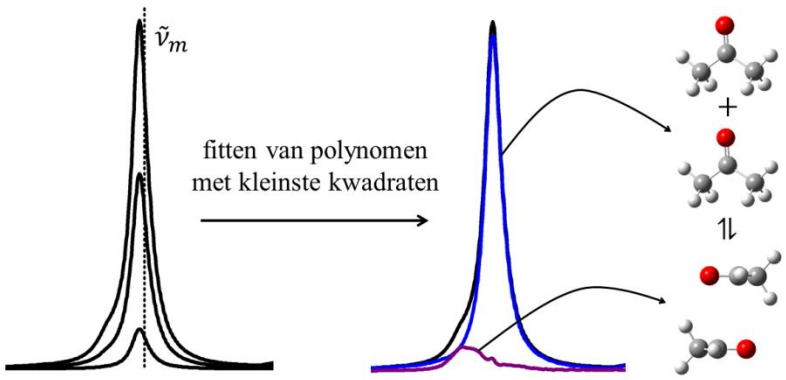

Figure 9.2 Samenvatting van de analyse van aceton opgelost in vloeibaar argon. Het resultaat toont de aanwezigheid van een monomeer- (blauw) en dimeerbijdrage (paars).

De vierde uit zichzelf associërende molecule die bestudeerd werd was aceton. Er werden infrarood spectra opgenomen van aceton opgelost in vloeibaar krypton bij constante temperatuur. Het vibratiespectrum werd ontbonden in een monomeer- en dimeerbijdrage. De toewijzingen van aceton in de gasfase die gevonden werden in de literatuur[7] werden ondersteund door onze toewijzing in vloeibaar krypton. Er werd opgemerkt dat in alle spectrale regio's dimeerbanden worden teruggevonden die volledig overlappen met de overeenkomstige monomeerbanden behalve voor de $\nu_{\mathrm{C–Cas}}$ mode bij 1222,7 cm^{-1} waarbij een complexband wordt waargenomen met een blauwverschuiving van 5,3 cm^{-1}, zoals voorgesteld in Figuur 9.2. Het is de eerste keer dat het volledige dimeerspectrum van aceton kon worden toegewezen. Door spectra op te nemen bij temperaturen tussen 134 en 142 K, kon berekend worden dat de

experimentele dimerisatie-enthalpie gelijk is aan -10.8 ± 1.1 kJ mol^{-1}. *Ab initio* berekeningen voorspelden een gestapelde en planaire dimeer geometrie waarbij de gestapelde geometrie 13.3 kJ mol^{-1} meer stabiel is met een CCSD(T) dimerisatie-energie van -28.4 kJ mol^{-1}. Met behulp van Monte Carlo Free Energy Perturbation (MC-FEP) simulaties en statistische thermodynamica werd berekend dat de theoretische dimerisatie-enthalpie gelijk is aan -13.7 kJ mol^{-1}.

Heterocomplexen

Het aantonen van de vorming van aceton dimeren beïnvloedt het gebruik van aceton als Lewis base met een carbonyl groep in studies naar heterocomplexen. Om spectra te kunnen analyseren van gemengde oplossingen van aceton en een waterstof of halogeenbrug donor moleculen is het niet voldoende om een substractie procedure uit te voeren, maar is het nodig om een gerichte aanpak uit te denken die gebaseerd is op de methodologie gebruikt in het geval van homocomplexen. Daarom werden in Hoofdstuk 7 de bestaande vergelijkingen werden aangepast zodat ze gebruikt konden worden voor de analyse van gemengde oplossingen waarbij twee verbindingen A en B zich in evenwicht bevinden met een complex met 1:1 stoichiometrie

$$\mathrm{A} + \mathrm{B} \rightleftharpoons \mathrm{AB} \qquad\qquad K_{AB} = \frac{C_{AB}}{C_A \cdot C_B} \tag{9.4}$$

Gebaseerd op dit evenwicht kan er een uitdrukking afgeleid worden waarin voor elk golfgetal $\tilde{\nu}_i$ de gemeten absorbantie A_{exp} kan geschreven worden als de som van absorbantiebijdragen die voortkomen uit de monomeren A en B, A_A en A_B, en de heterocomplexen zoals bv. het dimeer AB, A_{AB}:

$$A_{exp}(\tilde{\nu}_i) = A_A(\tilde{\nu}_i) + A_B(\tilde{\nu}_i) + A_{AB}(\tilde{\nu}_i) \tag{9.5}$$

Gelijkaardig aan de homocomplexen, kan elke bijdrage omgezet worden in een term in functie van de absorbantie bij de referentie golfgetallen $\tilde{\nu}_{mA}$ en $\tilde{\nu}_{mB}$:

$$\begin{aligned} A_{exp}(\tilde{\nu}_i) = {} & a_{\mathrm{A}}(\tilde{\nu}_i, \tilde{\nu}_{mA,}\tilde{\nu}_{mB})A_A(\tilde{\nu}_{mA}) \\ & + a_{\mathrm{B}}(\tilde{\nu}_i, \tilde{\nu}_{mA,}\tilde{\nu}_{mB})A_B(\tilde{\nu}_{mB}) \\ & + a_{\mathrm{AB}}(\tilde{\nu}_i, \tilde{\nu}_{mA,}\tilde{\nu}_{mB})A_A(\tilde{\nu}_{mA})A_B(\tilde{\nu}_{mB}) \end{aligned} \tag{9.6}$$

In het eerste deel van deze studie werd het aangepaste model gevalideerd door spectra te analyseren van mengsels van dimethylether (DME) en de

trifluoromethylhalides CF_3X (met X=I of Br) in vloeibaar argon. Naast de banden die toegewezen werden aan monomeer, werden er ook banden waargenomen voor 1:1 dimeren. We verkregen monomeer en dimeer spectra vergelijkbaar met voorgaande studies.[8]

In het tweede deel van de studie werd het model toegepast op complexen tussen aceton en CF_3I in vloeibaar krypton. Deze complexen werden nog niet eerder besproken in de literatuur. Om de spectra van aceton en CF_3I te analyseren was het nodig om het model in vergelijking (9.6) uit te breiden met term die rekening houden met 1:2 en 2:1 trimeren en acetondimeren:

$$\begin{aligned} A_{exp}(\tilde{\nu}_i) = {} & a_{\mathrm{A}}(\tilde{\nu}_i, \tilde{\nu}_{mA,}\tilde{\nu}_{mB})A_A(\tilde{\nu}_{mA}) \\ & + a_{\mathrm{B}}(\tilde{\nu}_i, \tilde{\nu}_{mA,}\tilde{\nu}_{mB})A_B(\tilde{\nu}_{mB}) \\ & + a_{\mathrm{AB}}(\tilde{\nu}_i, \tilde{\nu}_{mA,}\tilde{\nu}_{mB})A_A(\tilde{\nu}_{mA})A_B(\tilde{\nu}_{mB}) \\ & + a_{A_2B}(\tilde{\nu}_i, \tilde{\nu}_{mA,}\tilde{\nu}_{mB})A_A(\tilde{\nu}_{mA})^2A_B(\tilde{\nu}_{mB}) \\ & + a_{AB_2}(\tilde{\nu}_i, \tilde{\nu}_{mA,}\tilde{\nu}_{mB})A_A(\tilde{\nu}_{mA})A_B(\tilde{\nu}_{mB})^2 \\ & + a_{A_2}(\tilde{\nu}_i, \tilde{\nu}_{mA})A_A(\tilde{\nu}_{mA})^2 \end{aligned} \tag{8.7}$$

De analyse toonde aan dat er heterodimeerbanden aanwezig zijn in alle bestudeerde regio's. Er werd ook de aanwezigheid aangetoond van vele $(aceton)_2{\cdot}CF_3I$-signalen en slechts enkele $aceton{\cdot}(CF_3I)_2$-signalen. *Ab initio* berekeningen voorspelden geoptimaliseerde geometrieën van de $(aceton)_2{\cdot}CF_3I$ en $aceton{\cdot}(CF_3I)_2$ trimeren waarbij de eerste een complexatie-energie heeft die 10 kJ mol^{-1} hoger is dan die van de laatste. Daardoor wordt er gesteld dat het meer waarschijnlijk is dat het $(aceton)_2{\cdot}CF_3I$ trimeer zal in vergelijking met het $aceton{\cdot}(CF_3I)_2$ trimeer. Figuur 9.3 toont de resultaten voor de analyse van de $\nu_{\mathrm{C-Cas}}$ mode bij 1222,7 cm^{-1}. In deze regio werden blauwverschoven complexbanden waargenomen die voortkomen uit de aanwezigheid van $(aceton)_2$, $aceton{\cdot}CF_3I$, $(aceton)_2{\cdot}CF_3I$ and $aceton{\cdot}(CF_3I)_2$ complexen.

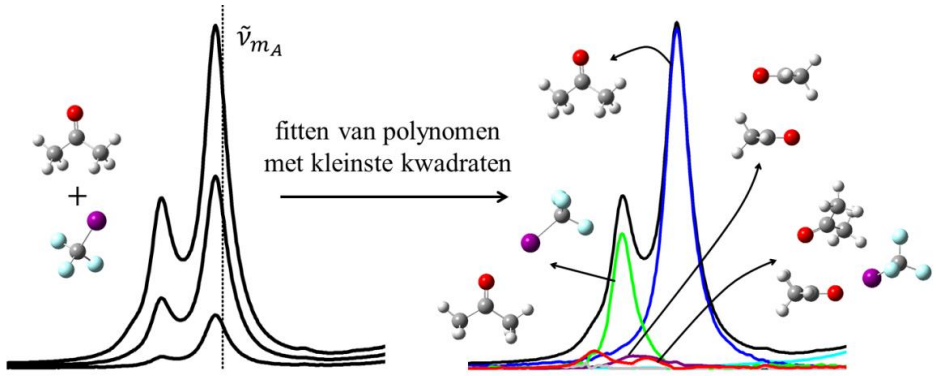

Figure 9.3 Samenvatting van de analyse van mengsels van aceton en CF_3I opgelost in vloeibaar krypton. Het resultaat toont de aanwezigheid van monomeer aceton (blauw) en CF_3I (cyaan) en van de complexen $(aceton)_2$ (paars), aceton·CF_3I (groen) en $(aceton)_2$·CF_3I (rood) in dit spectraal gebied.

Conclusies

In dit doctoraatsonderzoek werd aangetoond dat het mogelijk is om spectra van uit zichzelf associërende moleculen kunnen geanalyseerd worden door polynomen te fitten met kleinste kwadraten methode. Voor alle bestudeerde systemen werd het daardoor mogelijk om signalen waar te nemen en te identificeren die voortkomen uit de aanwezigheid van oligomeren. De resultaten van HCl, ND_3 en pyrrool vulden de bestaande data aan en leidden tot een meer volledige karakterisering van het zelf-associërende gedrag en de effecten ervan op de vibratiespectra. Hoewel aceton al uitgebreid bestudeerd werd in voorgaande studies naar intermoleculaire interacties in vloeibare edelgassen, zijn de dimeerbanden steeds buiten de detectie gevallen en werden ze nooit eerder waargenomen. Door gebruik te maken van de nieuwe methode kunnen de monomeer en dimeerbijdragen nu gescheiden worden wat bewijst dat het fitten van polynomen de grenzen van cryospectroscopie verlegd en er nu meer gedetailleerde data uit spectra afgeleid kan worden dan voorheen. Het waarnemen van het aceton dimeer is ook de eerste waarneming in cryo-oplossingen van een complex dat samen wordt gehouden door dipool-dipool interacties. De grenzen werden verder afgetast door de analyse van spectra die opgenomen werden voor een mengsel van aceton en de halogeenbrugdonor CF_3I. In dit onderzoek slaagden we erin om

overlappende spectra te scheiden van vier verschillende complexen. Tot slot kunnen we stellen dat het fitten van polynomen aan data die opgenomen werd in cryo-oplossingen bij constante temperatuur een waardevol middel is om de vorming van complexen te bestuderen die samengehouden worden door zwakke intermoleculaire interacties.

Referenties

[1] J. J. Dom, *Anaesthetics directed via weak hydrogen bonds? An infrared and Raman spectroscopic study towards target molecules and computational accuracy*, PhD thesis, University of Antwerp, 2011.

[2] in MATLAB 8.3, The MathWorks Inc., Natick, MA, USA, 2014.

[3] G. Schwarz, The Annals of Statistics, 6 (1978) 461-464.

[4] B. J. van der Veken and F. R. De Munck, J. Chem. Phys., 97 (1992) 3060-3071.

[5] T. D. Klots, R. D. Chirico and W. V. Steele, Spectrochim. Acta A, 50 (1994) 765-795.

[6] A. Gómez-Zavaglia and R. Fausto, J. Phys. Chem. A, 108 (2004) 6953-6967.

[7] G. Dellepiane and J. Overend, Spectrochim. Acta, 22 (1966) 593-614.

[8] D. Hauchecorne, R. Szostak, W. A. Herrebout and B. J. van der Veken, ChemPhysChem, 10 (2009) 2105-2115.

Academic CV

Liene De Beuckeleer
lienedebeuckeleer@gmail.com

Education

- **Ph.D. in Chemistry**, University of Antwerp 2010 -2015
  "Exploring the boundaries of cryospectroscopy: A new approach towards separating monomer and complex spectra"

- **M.Sc. in Chemistry,** University of Antwerp 2008-2010
  "*N-H···π interacties met pyrrool: een cryospectroscopisch onderzoek*"

- **B.Sc. Chemistry,** University of Antwerp 2005-2008

- **Bachelor of Conservation/Restoration**, Hogeschool Antwerpen 2003-2005

- **High School**, Science-Mathematics, KVR-Instituut, Vorselaar 1997-2003

Publications

- De Beuckeleer, L. I.; Herrebout, W. A., *Exploring the Limits of Cryospectroscopy: Least-Squares Based Approaches for Analyzing the Self-Association of HCl.* Spectrochim. Acta A (2016), 154, 89-97. doi:10.1016/j.saa.2015.10.012

- De Beuckeleer, L. I.; Herrebout, W. A., *The Self-Associating Behavior of Pyrrole in Liquid Xenon*. J. Mol. Struct. (2016), 1108, 71-79. doi: 10.1016/j.molstruc.2015.11.067

- De Beuckeleer, L. I.; Herrebout, W. A., *The Self-Associating Behavior of Acetone in Liquid Krypton*. J. Phys. Chem. A. (2016). doi: 10.1021/acs.jpca.5b10405

- De Beuckeleer, L. I.; Herrebout, W. A., *The self-associating behavior of NH_3 and ND_3 in liquid xenon*. Submitted to J. Mol. Struct. 07/12/2015

- De Beuckeleer, L. I.; Herrebout, W. A., *Dimers or higher associations ? A cryosolution infrared characterization of the halogen bonded complexes (dimethylether)n.(CF_3X)m and (acetone)n.(CF_3X)m with X = Br or I.* In preparation

Oral presentations

- *Pyrrole in Liquid Xenon, an N-H···π Bonding Situation* at the PhD student workshop of *Hydrogen Bonds between Disciplines* preceding the 19th International Conference on Horizons in Hydrogen Bond Research on September 12th 2011 in Göttingen, Germany.

- *Decomposing Infrared Spectra of Self-Associating Species Dissolved in Cryosolutions* at the CUSO Summer School about "Hydrogen Bonding" on August 20th-24th, 2012 in Villars sur Ollon, Switzerland.

- *Decomposing Infrared Spectra of Self-Associating Species Dissolved in Cryosolutions* during ChemCYS 2014, the 12th Chemistry Conference for Young Scientists on February 27th -28th, 2014 in Blankenberge, Belgium. Award for best oral presentation in the field of Physical and Theoretical Chemistry.

Poster presentations

- *Pyrrole in Liquid Xenon, an N-H···π Bonding Situation* during the 19th International Conference on Horizons in Hydrogen Bond Research on September 12-17, 2011 in Göttingen, Germany.

- *My Name is Bond, N-H···π Hydrogen Bond* during ChemCYS 2012, the 11th Chemistry Conference for Young Scientists on March 1st-2nd, 2012 in Blankenberge, Belgium.

- *Decomposing Infrared Spectra of Self-Associating Species Dissolved in Cryosolutions* at the CUSO Summer School about "Hydrogen Bonding" on August 20th-24th, 2012 in Villars sur Ollon, Switzerland.

- *Decomposing Infrared Spectra of Self-Associating Species Dissolved in Cryosolutions* during the 20th International Conference on Horizons in Hydrogen Bond Research on September 15th-20th 2013 in Antwerp, Belgium.

Dankwoord

Doctor L. De Beuckeleer is in the house! Jaja, het is me gelukt. ☺ Maar ik moet toegeven, ik vind het wel een beetje jammer dat mijn tijd als doctoraatsbursaal erop zit, want het was eigenlijk wel plezant. Experimenteren, labo geven, congressen, … het waren leuke tijden. En omdat een beeld meer zegt dan 1000 woorden heb ik op de volgende bladzijden een fotografisch overzicht geplaatst van enkele van mijn belevenissen van de afgelopen jaren. Naast al de vreugde was er natuurlijk het occasionele dal waar ik door moest zien te geraken. Maar gelukkig kon ik daarbij rekenen op de steun van een geweldige onderzoeksgroep, een liefdevolle familie en een fantastische vriendenkring.

Wouter, het was een voorrecht om met jou te mogen werken. Echt bedankt voor alles wat je voor mij en de onderzoeksgroep gedaan hebt. Verder kon ik altijd terecht bij mijn mededoctorandi Johan Dom (het omgekeerde van slim), Bart & De Bever, Dieter ~~met de snor~~, Playboygirl Elena, Nick Nasty Noodles, Ewoud edgussem, oh Sam Jacobs, Yannick R., Carlos Jazzhands, Evelien Van de Wondel en busy bee Roberta. Maar de groep was niet compleet zonder beerloving Christian, levendige Linny, Filip de knutselaar, Spanish Pilar en de studenten die bij ons een bachelor en/of masterproef gemaakt hebben. Ik ben blij dat jullie in mijn team zaten. En dan zijn er nog de collega's met wie ik samen heb getracht om de toekomstige generatie iets bij te leren, ik vond het zelf alvast heel leerrijk.

Mama en papa, broertjes, schoonzussen en schoonfamilie bedankt om te luisteren en mij op tijd het nodige advies te geven, ik zie jullie graag! Lieve vriendinnetjes en vriendjes, bedankt om mijn leven zoveel interessanter te maken. Jullie zijn een bron van inspiratie voor mij.

Save the best for lest. Liefste Nils. Samen aan onze doctoraten werken en elkaar motiveren om ervoor te blijven gaan. Het was een avontuur, maar het is ons gelukt! Bedankt voor jouw onvoorwaardelijke steun in alles wat ik doe. Je bent mijn liefje.

Liene De Beuckeleer 26 februari 2016

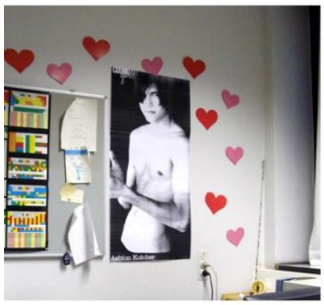

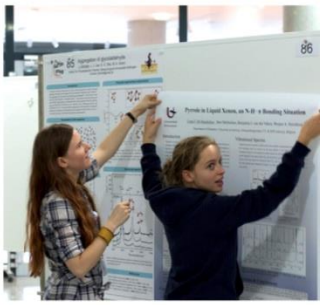


kvcv


Universiteit Antwerpen


kvcv


HAPPY BIRTHDAY
30


ie-net


Registration
N-Z